A Submillimetre Study of Nearby Star Formation using Molecular Line Data

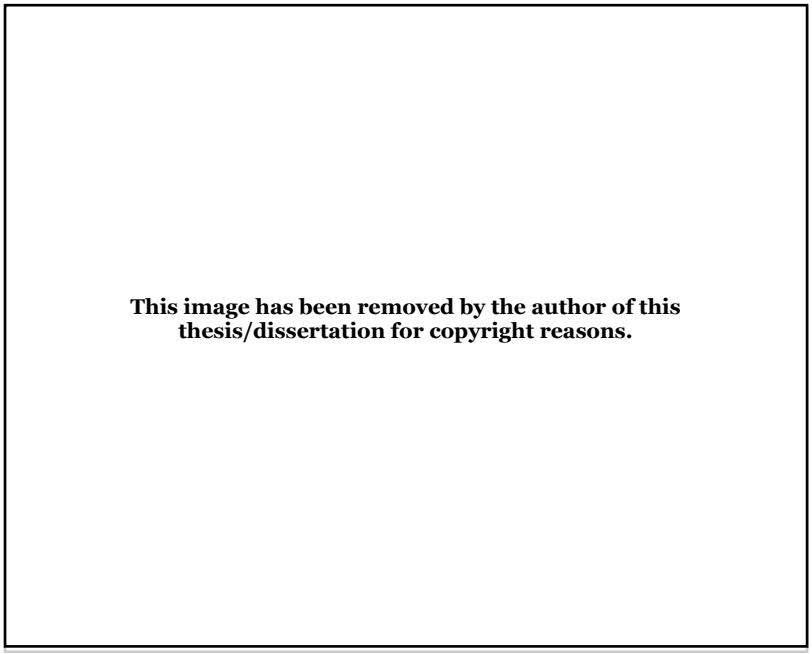

Emily R. Drabek-Maunder

For David.

Aut quam sidera multa, cum tacet nox,
furtivos hominum vident amores.
Catullus, VII

And for my parents, Ed and Rhonda.

Acknowledgements

There are a great number of people without whom this thesis would not have been possible and it is my pleasure to thank each one of them. I'm still in a state of disbelief that I have come to the end of my third year and am about to submit this thesis. To say that three years have gone by quickly is an understatement.

First and foremost, I would like to thank my supervisor, Jenny Hatchell, for her guidance and support over the three year period. Without her knowledge and 'nudges' in the right direction, this thesis would have never come together.

I would also like to thank Chris Brunt for useful conversations, especially regarding log-normal PDF density profiles from Chapter 5. He somehow managed to put up with me wandering into his office every week or so and asking questions starting with 'this is probably a stupid question, but....'.

The Exeter astrophysics group has been a pleasure to be a part of. Science discussions at coffee time always proved to be useful and 'Sporcle' on Friday afternoons was a nice distraction. Particularly, I thank everyone in my current PhD year; you were the first friends I made when I moved to the United Kingdom (Alex, Cat, Paul and Tom). The group has expanded now (and some people have moved on), so I would also like to thank: Claire, Lee, Moncho, Damian, Jon, Darryl, Jo, Joe and Andrew.

A special thank you to my officemate Hannah. She managed to curtail my constant worrying that I would never finish my thesis. Hopefully, I managed to help her as well (with an outside perspective of comments from journal referees). Similarly, my housemate Maria kept me sane

when my research wasn't quite going right. She was always there for helpful distractions and great sarcastic comments.

I also thank my parents for their support over the years, especially when I'm thousands of miles from my hometown in America.

Similarly, my science teacher and high school science research supervisor Ms. Sharon McElroy was one of the first people who encouraged my enthusiasm and interest in science. Without her, I'm not sure my pursuit of one day becoming a scientist would have ever materialised.

Lastly, I want to thank my husband, David, for his support and patience. Living separately in Exeter and London wasn't easy and we became very accustomed to the Exeter St Davids to London Waterloo train journey. Without our weekends together, my time as a PhD student would have been empty and not as enjoyable. Though I'm sad to leave Exeter, I'm finally happy to say that we can start our lives together in London.

Abstract

This thesis primarily uses submillimetre molecular line data from HARP, a heterodyne array on the James Clerk Maxwell Telescope (JCMT), to further investigate star formation in the Ophiuchus L1688 cloud. HARP was used to observe CO $J = 3 \rightarrow 2$ isotopologues: ^{12}CO, ^{13}CO and C^{18}O; and the dense gas tracer HCO+ $J = 4 \rightarrow 3$.

A method for calculating molecular line contamination in the SCUBA-2 450 and 850 μm dust continuum data was developed, which can be used to convert ^{12}CO $J = 6 \rightarrow 5$ and $J = 3 \rightarrow 2$ maps of integrated intensity (K km s^{-1}) to molecular line flux (mJy beam^{-1}) contaminating the continuum emission. Using HARP maps of ^{12}CO $J = 3 \rightarrow 2$, I quantified the amount of molecular line contamination found in the SCUBA-2 850 μm maps of three different regions, including NGC 1333 of Perseus and NGC 2071 and NGC 2024 of Orion B. Regions with 'significant' (i.e. $> 20\%$) molecular line contamination correspond to molecular outflows. This method is now being used to remove molecular line contamination from regions with both SCUBA-2 dust continuum and HARP ^{12}CO map coverage in the Gould Belt Legacy Survey (GBS).

The Ophiuchus L1688 cloud was observed in all three CO $J = 3 \rightarrow 2$ isotopologues. I carried out a molecular outflow analysis in the region on a list of 30 sources from the *Spitzer* 'c2d' survey [Evans et al., 2009]. Out of the 30 sources, 8 had confirmed bipolar outflows, 20 sources had 'confused' outflow detections and 2 sources did not have outflow detections.

The Ophiuchus cloud was found to be gravitationally bound with the turbulent kinetic energy a factor of 7 lower than the gravitational binding energy. The high-velocity outflowing gas was found to be only 21% of the

turbulence in the cloud, suggesting outflows are significant but not the dominant source of turbulence in the region. Other factors were found to influence the global high-velocity outflowing gas in addition to molecular outflows, including hot dust from nearby B-type stars, outflow remnants from less embedded sources and stellar winds from the Upper Scorpius OB association.

To trace high density gas in the Ophiuchus L1688 cloud, HCO+ $J = 4 \rightarrow 3$ was observed to further investigate the relationship between high column density and high density in the molecular cloud. Non-LTE codes RADEX and TORUS were used to develop density models corresponding to the HCO+ emission. The models involved both constant density and peaked density profiles. RADEX [van der Tak et al., 2007] models used a constant density model along the line-of-sight and indicated the HCO+ traced densities that were predominantly subthermally excited with densities ranging from 10^3–10^5 cm^{-3}. Line-of-sight estimates ranged from several parsecs to 90 pc, which was unrealistic for the Ophiuchus cloud. This lead to the implementation of peaked density profiles using the TORUS non-LTE radiative transfer code. Initial models used a 'triangle' density profile and a more complicated log-normal density probability density function (PDF) profile was subsequently implemented. Peaked density models were relatively successful at fitting the HCO+ data. Triangle models had density fits ranging from 0.2–2.0$\times10^6$ cm^{-3} and 0.1–0.3$\times10^6$ cm^{-3} for the 0.2 and 0.3 pc cloud length models respectively. Log-normal density models with constant-σ had peak density ranges from 0.2–1.0 $\times10^5$ cm^{-3} and 0.6–2.0$\times10^5$ cm^{-3} for 0.2 and 0.3 pc models respectively. Similarly, log-normal models with varying-σ had lower and upper density limits corresponding to the range of FWHM velocities. Densities (lower and upper limits) ranged from 0.1–1.0 $\times10^6$ and 0.5–3.0 $\times10^5$ cm^3 for the 0.2 and 0.3 pc models respectively.

The result of the HCO+ density modelling indicated the distributions of starless, prestellar and protostellar cores do not have a preference for higher densities with respect to the rest of the cloud. This is contrary

to past research suggesting the probability of finding a submillimetre core steeply rises as a function of column density (i.e. density; Belloche et al. 2011; Hatchell et al. 2005). Since the majority of sources are less embedded (i.e Class II/III), it is possible the evolutionary state of Ophiuchus is the main reason the small sample of Class 0/I protostars do not appear to have a preference for higher densities in the cloud.

Contents

List of Figures

LIST OF FIGURES

Chapter 1

Introduction

"We are all in the gutter, but some of us are looking at the stars."

— Oscar Wilde, Lady Windermere's Fan

Though stars are tranquil in appearance from the clear night sky, their formation is a turbulent process occurring at the centre of cores in the depths of molecular clouds. Regions of star formation are not easily studied in optical wavelengths due to the dust and gas enveloping the young protostars, often obscuring background starlight and creating 'dark' areas that seem to be devoid of stars (see Figure 1.1). Longer wavelengths (i.e. infrared, submillimetre, millimetre and radio) can penetrate the obscuring dust in these clouds and reveal the newborn stars. These early stages of star formation are still not well understood even though our knowledge has improved since the construction of detectors observing with longer wavelength ranges. In this thesis, I primarily use submillimetre wavelengths which detect the dust in the clouds as continuum emission and rotational transitions of various molecules as spectral lines. I focus on observations of carbon monoxide CO and the formyl cation HCO+ to investigate nearby star formation in the Gould Belt.

In this introduction, I present a current overview of star formation in our Galaxy. I then describe the process of submillimetre observing and instruments used in the detection of dust and molecular gas in star forming regions. Lastly, radiative transfer theory is used to derive useful quantities for tracing star formation properties in the cloud (e.g. excitation temperature, column density and gas mass).

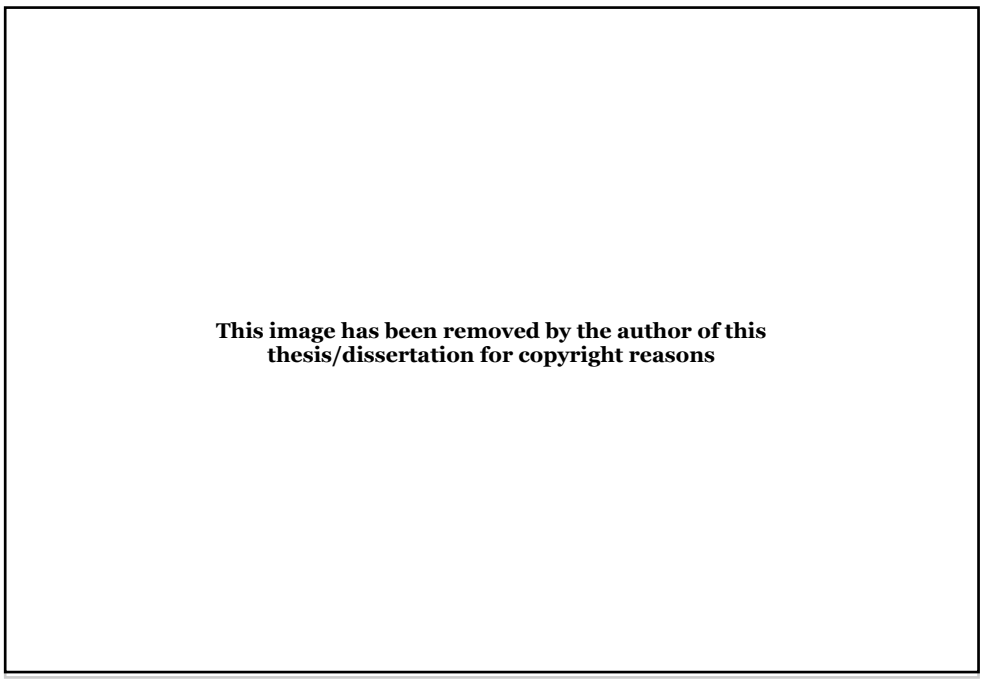

Figure 1.1: The constellation Orion in visible and infrared light. *Left:* Optical image, Akito Fujii. *Right:* Infrared image composed of 12 μm, 60 μm and 100 μm, taken by Infrared Astronomical Satellite (IRAS).

1.1 Star formation

In this section, the current understanding of nearby 'low mass' star formation (< 2 $M_\odot$) is discussed, including molecular clouds and the formation of cores. Protostellar evolution and classification are then presented followed by a more detailed description of molecular outflows.

1.1.1 Molecular clouds: nurseries for star formation

Molecular clouds act as stellar nurseries, rife with the dust and gas used to form stars. These clouds are cold (T ∼8–30 K), dense regions forming part of the interstellar medium (ISM). The ISM is filled with neutral, ionised and molecular hydrogen and helium as well as other heavier atoms [Tielens, 2009]. In star forming regions, the density of atomic hydrogen is substantial enough to form molecular hydrogen H_2 with number density $n_{H_2} \geq 10^3$ cm^{-3}.

The Gould Belt is a nearby active ring of star formation in the Galaxy, inclined by roughly 20 deg to the Galactic Plane [Herschel, 1847]. It consists of a ring of O-type stars with a radius of ∼350 pc and centred on a distance ∼200 pc from the Sun. Most of the local star forming regions are associated with the Gould Belt, shown in Figure 1.2. Star forming regions in this area range from small clouds to giant molecular clouds (GMCs) with sizes from ∼ 1–100 pc and masses from ∼10–10^6 $M_\odot$.

Molecular gas formation in clouds can be primarily explained in two different ways. First, shorter distances between atomic gas and dust grains could lead to more collisions in these dense regions, resulting in the formation of molecules. Additionally, ultraviolet (UV) radiation may not be able to easily dissociate already formed molecules due to higher dust extinction, a process known as self-shielding [Frerking et al., 1982; Ward-Thompson, 2002]. The most abundant gas in these clouds is molecular hydrogen H_2. H_2 is difficult to observe because it is a homonuclear diatomic molecule without a permanent electric dipole [Hildebrand, 1983b]. The lowest observable rotational transition for H_2 is $J = 2 \rightarrow 0$, corresponding to an excitation energy of 500 K [Rohlfs and Wilson, 2000]. Therefore, this transition is only observable in clouds with regions heated by shocks or UV radiation fields. The second most abundant molecule ^{12}CO is typically used to trace star formation in molecular clouds due to its abundance and lower critical density. The main dis-

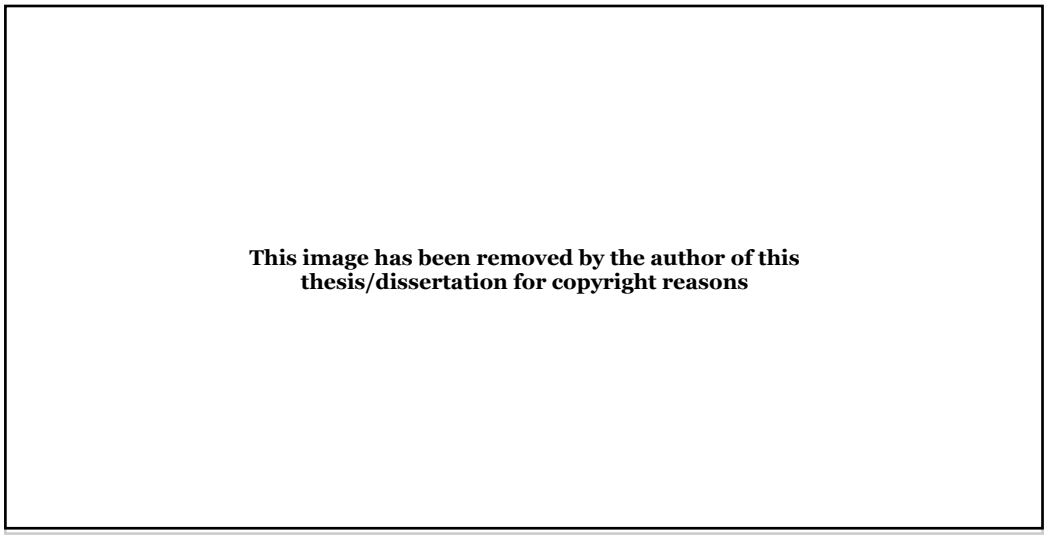

Figure 1.2: Diagram of the Gould Belt showing the projection of the ring plotted on the Galactic Plane. The 20 deg inclination can be seen [Ward-Thompson et al., 2007b]. Commonly observed molecular clouds are shown.

advantages of this molecule is that it can easily become optically thick at modest column densities and it has a tendency to freeze onto dust grains at lower temperatures and higher densities which causes depletion. Rarer isotopologues of CO (i.e. ^{13}CO and C^{18}O) can be used to study denser regions of the cloud due to their lower optical depth and lower abundances. Similarly, molecules with higher critical densities (e.g. HCO+, H^{13}CO+ and NH_3) can also be used to trace denser regions of the cloud [Hartmann, 2009b].

1.1.2 Core collapse: the birth of a protostar

Dense concentrations of molecular gas form in areas of decreased turbulence inside molecular clouds [Goodman et al., 2009]. These denser regions are known as 'cores' which are typically detected using dust continuum ($N(H_2) \geq 10^3$ cm^{-2}). Cores are typically categorised as either starless, prestellar or protostellar. 'Starless' is a loose term for all dense cores that may or may not form protostars and prestellar cores are gravitationally bound and will form protostars in the future. A protostar is thought to form from the gravitational collapse of a prestellar core. In a simple scenario, cores will form in areas of low turbulence and low magnetic fields. The cloud or a portion of a cloud will collapse to form a core when the kinetic energy is overcome

by its gravitational force. The stability of the cloud or core can can be described by the virial theorem,

$$\Omega_{\rm G} + 2K = 0, \tag{1.1}$$

where $\Omega_{\rm G}$ is the self-gravitational potential energy of the cloud and K is the kinetic energy of the cloud due to both thermal motions and turbulence. For a spherical object of mass $M_{\rm cl}$, radius $R_{\rm cl}$ and three-dimensional velocity dispersion σ,

$$K = \frac{1}{2} M_{\rm cl} \sigma^2 \tag{1.2}$$

$$\Omega_{\rm G} \sim -\frac{G M_{\rm cl}^2}{R_{\rm cl}}. \tag{1.3}$$

The virial mass is naturally the result of the virial theorem, describing the critical mass for the cloud to be in equilibrium,

$$M_{\rm vir} \sim \frac{\sigma^2 R_{\rm cl}}{G}. \tag{1.4}$$

For the cloud to collapse, the potential gravitational energy must satisfy the condition $\Omega_{\rm G} > 2K$, or the cloud mass must be greater than the virial mass. Similarly, the cloud will disperse under internal motions if the cloud mass is less than the virial mass.

The mass of the smallest clump that is thermodynamically viable to collapse can be predicted (in the case of no competing processes). This mass is known as the Jeans Mass $M_{\rm J}$, named after Sir James Jeans, who examined gravitational collapse of spherical nebula (Jeans 1902). Thermal energy causes the cloud to expand. The critical mass (and radius) of a clump or cloud where the gravitational force is able to counteract the thermal energy is,

$$M_{\rm J} \simeq \frac{4}{3} \rho_{\rm o} \pi R_{\rm J}^3 \tag{1.5}$$

$$R_{\rm J} \simeq \left(\frac{15}{4\pi G \rho_{\rm o}} \right)^{1/2} a_{\rm o}, \tag{1.6}$$

where $R_{\rm J}$ is the Jeans radius (critical radius corresponding to Jeans mass), ρ is the

density and a_o is the isothermal sound speed $\left(a_o^2 = \frac{kT}{\mu m_H}\right)$. Regions with higher mass (i.e. in higher density regions) or longer size scales will collapse under gravity and cannot support themselves only with thermal pressure.

The collapse lifetime of a core under gravity or the dispersion of a core with a mass less than the virial mass can be predicted. A collapsing core will have a free-fall timescale t_{ff},

$$t_{ff} = \left(\frac{3\pi}{32G\rho}\right)^{1/2}, \tag{1.7}$$

where ρ is the density. Similarly, the dispersion timescale is t_{disp} is,

$$t_{disp} \simeq \frac{R_{core}}{\sigma}, \tag{1.8}$$

where R_{core} is the core radius and σ is the internal velocity dispersion. Timescales based on the gravitational collapse for GMCs (i.e. the free-fall timescale) are estimated to be 2–4 Myr, where the best estimates of cloud lifetimes are either comparable to or up to five times larger than these free-fall times.

The current estimate of the star formation rate in the Galaxy is ~ 1 $M_\odot$ yr^{-1} [Robitaille and Whitney, 2010]. This is contradictory to the estimate of the free-fall timescale (2–4 Myr) and H_2 mass in the Galaxy (1–3$\times 10^9$ $M_\odot$; see Evans 1999 and references therein), which estimates a star formation rate of $\sim$200 $M_\odot$ yr^{-1}. This also shows star formation is a surprisingly inefficient process for our Galaxy using the predicted free-fall timescales. The star formation efficiency ϵ (see Elmegreen and Efremov 1997) is denoted as the ratio of the star formation rate and lifetime of the region to the mass (i.e. H_2 mass). The estimated star formation efficiency of the Galaxy is only a few percent [Zuckerman and Evans, 1974] using the free-fall timescale. The low star formation efficiency and disagreement between observations and predictions of the star formation rate suggests it is necessary to investigate potential cloud support mechanisms (e.g. turbulence and magnetic fields).

1.1.3 Core stability

The details about the cloud collapse and formation of the core are still disputed. In clustered regions, triggers for stellar formation can including anything from su-

pernova explosions, stellar winds, molecular outflows and shock waves. In the more isolated star forming regions, the potential factors for initiating core collapse are not always so obvious. Cores can either form in a static or dynamic scenario, where the two main theories for the physical mechanism of cloud support involve magnetic fields and turbulence.

The static scenario assumes minimal influence from turbulence. In this scenario, cores will form in areas with decreased turbulence in the cloud by the influence of gravitational forces and magnetic fields [Mouschovias and Ciolek, 1999; Myers, 2000; Myers and Mardones, 1998]. Clouds with a mass to magnetic flux ratio (M/ϕ) that is subcritical have a magnetic field strong enough to support the core against gravity, while supercritical clouds have a magnetic field that is too weak to support the cloud against gravity. Using these two cases, the contraction of the cores in a more static manner can either be sub or supercritical. For subcritical clouds, star formation can occur by ambipolar diffusion, which is the decoupling of molecules from the ions and electrons in the plasma (where the plasma is the main component behind the resistive magnetic field). Relatively, the timescale for ambipolar diffusion is several factors higher than the dynamical timescales which would make star formation rates (and thus efficiencies) low [Shu et al., 1987]. For supercritical clouds, the magnetic field is too weak to support the clump of material and the material gravitationally collapses to form a core (most likely in an area with little turbulence). Even if the magnetic fields do not prevent core collapse, they can still support large portions of the cloud by becoming the main source of internal pressure [Price and Bate, 2008].

In the dynamic scenario, supersonic turbulence supports the molecular cloud against gravitational collapse, where turbulence could generate an internal pressure preventing gravitational collapse in the cloud. Turbulence can be described as the random motions of material on a variety of length scales. Both the kinematics and structure of molecular clouds can be influenced by supersonic turbulence. Kolmogorov [1941] characterised a turbulent flow as a cascade of energy across a hierarchy of scales for high Reynolds numbers. A Reynolds number is defined as the ratio of internal to viscous forces, where high Reynolds numbers indicate the presence of turbulent flows (inertial forces dominate) and often produce instabilities like eddies or vortices. Kolmogorov [1941] indicated the smallest turbulent scales are universal and depend on the average dissipation rates of turbulent kinetic energy

per mass and the kinematic viscosity of the fluid. Similarly, Larson [1981] found a correlation between the internal velocity dispersion of the cloud (i.e. turbulence as measured from the non thermal molecular line widths) σ and the length L or mass M of star forming regions. The relation between the velocity dispersion and cloud size was first noted to be $\sigma = 1.10L^{0.38}$. The clouds also appeared to be gravitationally bound and in approximate virial equilibrium where the velocity dispersion-mass relation was $\sigma = 0.42M^{0.20}$. This work argued against a simplistic picture of gravitational collapse and fragmentation, where the cloud structures observed were at least partially influenced by supersonic turbulence.

Simulations have shown that turbulence can support the global cloud while allowing local regions of collapse (see Mac Low and Klessen 2004). However, there is an issue that hydrodynamic and magneto-hydrodynamic (MHD) turbulence decays quickly [Mac Low, 1999; Stone et al., 1998]. These turbulent motions must be continually driven if clouds are assumed to be stable and long-lived structures supported by supersonic turbulence. Possible turbulent driving sources may including stellar feedback (e.g. protostellar molecular outflows) or external turbulence from the ISM (e.g. supernova). While the kinetic energy in the supersonic turbulent motions often compares to the gravitational potential energy [Larson, 1981], it is still unknown if turbulent motions either impede the formation of stars by creating a pressure that is able to resist gravitational collapse or assist star formation by adding mass to less dense areas [Hartmann, 2009a]. For purposes of this thesis, I focus on better understanding turbulence in molecular clouds. The importance of molecular outflows is further discussed in Chapter 4, which investigates turbulence and sources of turbulence in the Ophiuchus molecular cloud.

1.1.4 Protostellar classification and links to evolution

A protostar is a young stellar object (YSO) in the process of collecting the matter needed for it to reach main-sequence [Andre et al., 1993]. This high density central object is detectable at both IR and submillimetre wavelengths depending on its evolutionary stage. The collapsing core begins to rotate due to small amounts of angular momentum. The rotation assists in the formation of a protoplanetary (circumstellar) disc around the protostar, where material from the disc accretes

onto the central object. Additionally, angular momentum is carried away from the system by a jet or stellar wind emitted by the protostar, known as a molecular outflow. Outflows are characteristic of embedded YSOs. As the protostar becomes less embedded in the surrounding dust and gas of the molecular cloud, the process of outflow and inflow cease and the disc evolves further into a planetary system. The protostar eventually evolves into a main-sequence star.

The protostellar lifecycle was initially defined using a classification system, labelling observed protostars as Class I–III [Lada, 1987]. Andre et al. [1993] revised the classification system by adding a category of sources less evolved than the Class I objects as Class 0. The spectral energy distributions (SEDs) are used to determine these classifications of protostars [Whitney et al., 2003]. Classifications are based on the slope of the SEDs, or their spectral index α [Lada, 1987]:

$$\alpha = \frac{d\log(\lambda F_\lambda)}{d\log(\lambda)}, \tag{1.9}$$

where λ is the wavelength over a range of IR and submillimetre wavelengths and F_λ is the flux density of the source. The spectral index α is the slope calculated in the wavelength interval 2.2–20 μm (near to mid-IR range). According to the system based on SEDs, the classification of the source would be as follows:

YSO Class	**Range**	**Source**
Class 0/I	$\alpha > 0$	Embedded
Class II	$-2 < \alpha < 0$	Disk
Class III	$\alpha < -2$	Optically thin without disk

The 'flat spectrum' classification was added between Classes I and II to better correspond to physical stages of YSO evolution. Flat spectrum sources are defined as $0.3 > \alpha \geq -0.3$ [Greene, 2004].

The four classes of protostars (shown in Figure 1.3) are further described as:

- **Class 0 source:** Class 0 protostars correspond to early protostellar collapse with a lifespan of ∼0.1 Myr [Evans et al., 2009]. In observations, their SEDs resemble blackbodies, $T \leq 30$ K, and more than half of their mass is located in the infalling envelope [Whitney et al., 2003]. Observations show an IR source

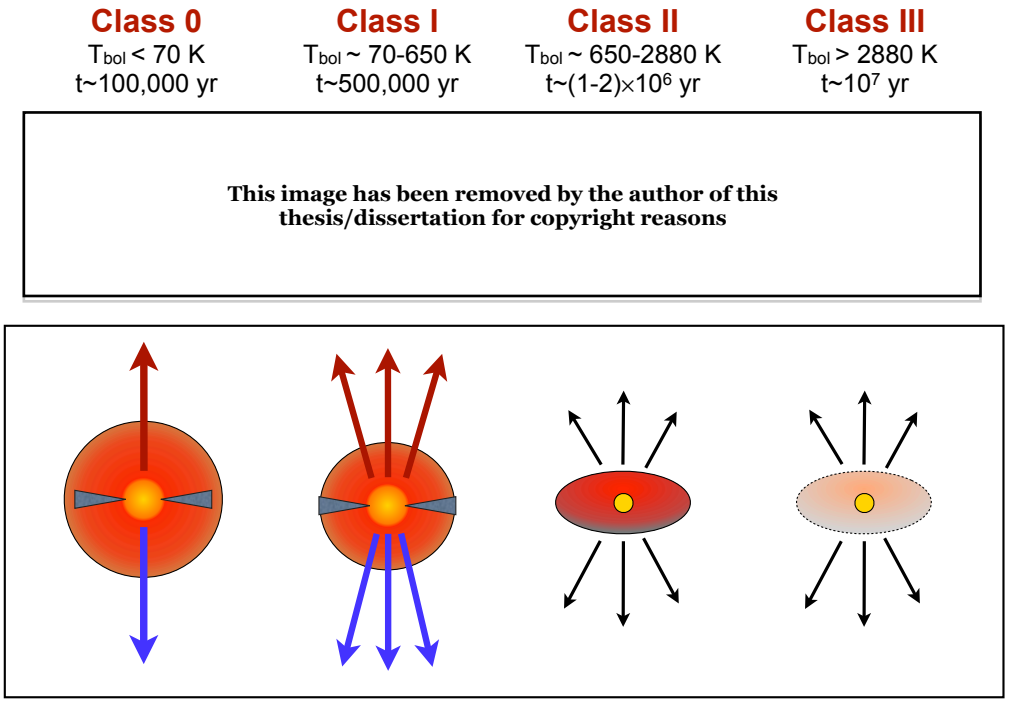

Figure 1.3: Classes of protostars. *Top:* SEDs are models from Whitney et al. [2003]. *Bottom:* Cartoon illustrating the stags of protostars. Adapted from Curtis (PhD Thesis, 2009) and originally obtained from Visser (PhD Thesis, 2000).

and corresponding submillimetre continuum emission. Additionally, outflows can be seen in molecular line data. The protostar is embedded in a thick envelope of dust and gas and they are actively undergoing accretion from the surrounding envelope [Hartmann, 2005].

- **Class I source:** The lifetime of the Class I protostar is ∼0.5 Myr [Evans et al., 2009] and is identified by broad SEDs peaking at around 100 μm. These objects have formed accretion disks and their envelopes have bipolar cavities excavated by outflows. IR emission increases at this stage with lower submillimetre emission because some of the envelope has been cleared by accretion.

- **Class II source:** The SED emission peak at this stage is falling in the near-IR and there is an excess IR emission occurring higher than the expectations for a stellar photosphere. The duration of this stage is $\sim 10^6 - 10^7$ yr [Whitney et al., 2003]. Cloud infall has stopped and the envelope eventually collects into a flattened disc in revolution around the central protostar due to angular momentum. This circumstellar disc is both dusty and optically thick, which are two characteristics used to identify Class II objects [Hartmann, 2009b]. These are typical characteristics of a classical T-Tauri star with an accretion disc surrounding it [Whitney et al., 2003].

- **Class III source:** The central star becomes the only observable emission due to the dispersion (or coagulation into planetary objects) of the dust [Hartmann, 2009b]. At this point, the SEDs have the same properties of a stellar photosphere. Class III sources are also called weak-line T-Tauri stars and become a main-sequence star of zero-age after $\sim 10^7$ yr. It is still uncertain if Class III objects are more evolved than Class II sources. It is possible that Class III sources have simply lost the majority of their circumstellar matter in a shorter amount of time [Whitney et al., 2003].

According to Robitaille et al. [2006], the spectral index may not always directly relate to the evolutionary stage of the object. For example, a disc that is being observed edge-on may be classified as Class I due to a positive spectral index, when its evolutionary stage is Class II. A more physically based method of identifying the evolutionary stages of objects instead of the observational characteristics involves

the following, where M_* is a sampled stellar mass, $M_{\rm env}$ is the envelope accretion rate, and $M_{\rm disk}$ is the disk mass is: Stage 0/I involves significant falling envelopes and possible disks when $M_{\rm env}/M_* > 10^{-6}$ yr^{-1}, Stage II involves optically thick disks and potential remnants of infalling envelopes when $M_{\rm env}/M_* < 10^{-6}$ yr^{-1} and $M_{\rm disk}/M_* > 10^{-6}$, and Stage III involves optically thin disks when $M_{\rm env}/M_* < 10^{-6}$ yr^{-1} and $M_{\rm disk}/M_* < 10^{-6}$ [Robitaille et al., 2006].

Many studies have been completed on the stellar initial mass function (IMF), which is the production frequency of stars with a given mass and helps determine both the photometric aspects of galaxies and dynamical and chemical aspects of the galactic ISM [Padoan and Nordlund, 2004; Padoan et al., 2001]. The number of stars N of mass M seems to follow a collection of power-law shapes when a logarithmic bin is applied, $s = d\log N/d\log M$ for different masses [Hennebelle and Chabrier, 2008, 2009; Kroupa, 2001; Miller and Scalo, 1979; Salpeter, 1955]. Similarly, Motte et al. [1998] first reported the submillimetre continuum cores had a similar structure to the IMF, known as the clump mass function (CMF). Past work from Padoan and Nordlund 2002, Padoan and Nordlund [2004] and Chabrier and Hennebelle [2011] predicts that turbulence generates overdensities in star forming regions leading to the formation of low-mass objects. In addition, Chabrier and Hennebelle [2011] predicts the turbulence in bound overdense regions act as support against collapse and allow the core to collect more mass, leading to the shape of the prestellar CMF.

1.1.5 Protostellar mass loss: molecular outflows

Molecular outflows are a ubiquitous part of star formation and act as a form of mass loss for young protostars. As a protostar collapses and accretes matter from surrounding material in the cloud, the object will also eject mass through a bipolar outflow. Two recent reviews of outflow processes include Bally et al. [2007] and Arce et al. [2007]. I further use molecular emission to identify outflows in Chapter 3, including ^{12}CO $J = 3 \rightarrow 2$ and the near-IR H_2 2.122 μm $v = 1 \rightarrow 0$ $S(1)$ ro-vibrational line. In this section, I focus on outflows from low-mass protostars.

Low-mass protostars with outflows have been extensively studied across wavelengths from UV to radio. These outflows typically have 0.1–1 pc length flows with corresponding velocities 10–100 km s^{-1} [Arce et al., 2007]. There appears to be a

power law dependence of the flow mass as a function of velocity as measured by CO, $M_{\rm CO}(\rm v) \propto \rm v^{-\gamma}$. The factor γ is typically $\sim$1.8 and will steepen at velocities greater than 10 km $\rm s^{-1}$ from the central velocity of the cloud (see Richer et al. 2000 and references therein).

The youngest outflows show observational evidence for being driven by a highly collimated jet, typically seen from Class 0 sources. An example of this is VLA 1623 in the L1668 cloud of Ophiuchus (see Chapter 3 and references: Andre et al. 2000; Nakamura et al. 2011; Ward-Thompson et al. 2011). The CO jet is lined with H_2 knots, or shocks seen in H_2 2.122 μm $v = 1 \rightarrow 0$ $S(1)$ ro-vibrational line. Outflows are expected to evolve over time. Older outflows are found to have wider opening angles and may be potentially wind driven [Arce et al., 2007]. Some YSOs can be further complicated by episodic ejection, potentially due to variations in accretion rates [Dunham et al., 2008]. Additionally, there is evidence for quadrupolar outflows and precessing outflow directions (see Chapter 3 regarding Ophiuchus protostars EL 29 and IRS 54).

There are several proposed models to explain the chemistry and physical mechanism driving the outflow. These models can be separated into four main categories [Arce et al., 2007; Cabrit et al., 1997], and depicted in Figure 1.4:

- **Turbulent Jet:** This model suggests the outflow is driven by an underlying jet. Kelvin-Helmholtz instabilities along the boundary between the jet and surrounding gas generate a turbulent layer that entrains molecular gas (e.g. Raga and Cabrit 1993; Stahler 1994).

- **Jet Bow Shock:** This model describes a highly collimated jet that pushes through the ambient material and entrains gas along a thin outflow shell [Masson and Chernin, 1993; Raga and Cabrit, 1993]. Two shocks are produced when the jet impacts the ambient material and high pressure gas is expelled sideways, forming the outflow shell which encircles the jet. This model mainly differs from the previous model by the manner molecular gas is entrained.

- **Wide-angle Wind:** In this model, a wide-angle radial wind pushes into the ambient material. An outflow shell is created when the wind sweeps up a shell of gas. This model predicts outflows with low collimation and wide opening angles, more characteristic of older outflows.

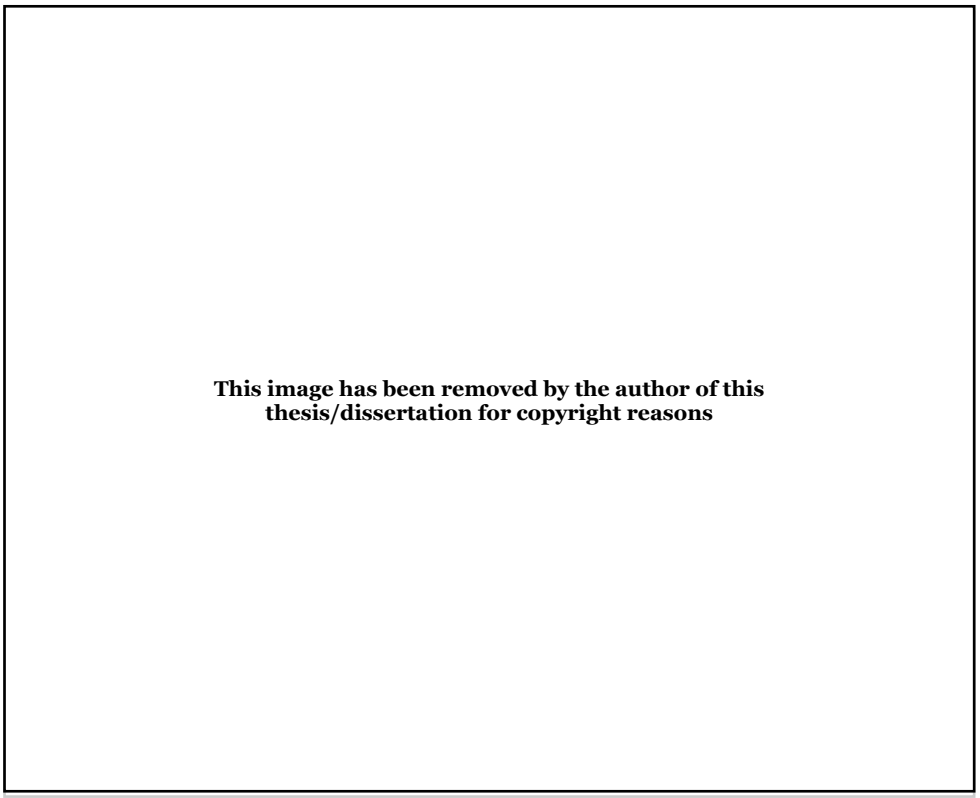

Figure 1.4: Outflow models described by Arce et al. 2007.

- **Circulation:** This model does not depict gas entrainment by a jet or underlying wind. The flow is instead formed by material that is infalling onto a protostar and is deflected by high MHD pressure. This model produces a quadrupolar circulation pattern. Local heating allows material to be accelerated above escape speeds [Fiege and Henriksen, 1996a,b].

There is a possibility these outflows can have an influence on the overall cloud [Nakamura and Li, 2007]. Even though intermediate and high mass YSOs have larger and more powerful outflows, multiple outflows from numerous low-mass YSOs in the cloud can be as equally disruptive. These groups of YSOs may be scattered throughout the cloud and interact with a sizeable portion of the star forming region. Turbulence generated from the outflows can additionally be comparable or larger than the turbulent and gravitational energies of the cloud (e.g. Buckle et al. 2010; Curtis et al. 2010b; Graves et al. 2010). If the outflows are well coupled to the cloud, they may be a considerable though not always a dominant source of turbulence in the cloud and could act as a form of support against gravitational collapse [Mac Low and Klessen, 2004]. In this thesis, the impact of outflows on turbulence in the Ophiuchus cloud is further discussed in Chapter 4.

1.2 Submillimetre observing

The physical conditions of the molecular cloud must be observed before and during the stellar formation process to address the current scientific questions. Near-IR detection images the results of this process but the sources are too evolved to determine the cloud conditions leading to formation. Additionally, optical data is problematic due to the high dust extinction found in these clouds. At submillimetre and millimetre frequencies, this dust emits blackbody radiation corresponding to the temperatures found in the molecular cloud (i.e. $\sim$8–30 K) and many molecular lines have rotational transitions at these frequencies. Therefore, this particular wavelength range is useful for tracing the initial conditions leading to star formation.

There are some limitations to observing in the submillimetre wavelength range. Contraints from water vapour absorption tend to be the most significant. Many instruments operating in the submillimetre must take advantage of 'atmospheric

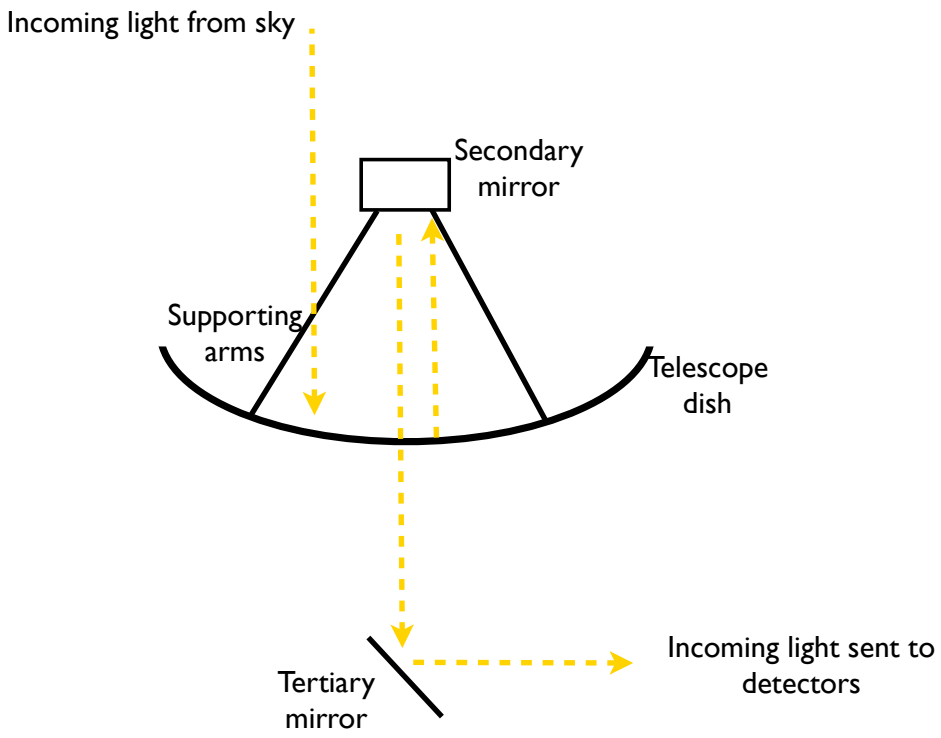

Figure 1.5: Basic diagram of the JCMT. Incoming light is gathered by the dish and reflected from to the secondary mirror. The light then travels to the tertiary mirror where it is sent to various detectors.

windows,' or wavelengths between these absorption bands. To account for potential absorption and radio interference, submillimetre telescopes tend to be located in high-altitude and dry environments away from urban populations. There are only a handful of locations that are suitable for this type of observing, including Mauna Kea Observatory in Hawaii, USA and the Llano de Chajnantor Observatory on the Atacama Plateau, Chile. Mauna Kea Observatory is home to the James Clerk Maxwell Telescope (JCMT)[1] at an altitude of 4092 m. With a 15 m dish, this submillimetre telescope has been observing regions of the solar system, the interstellar medium and distant galaxies for the past 26 years. All of the maps presented in this thesis have been observed with the JCMT. A basic diagram of how the JCMT gathers light is shown in Figure 1.5.

[1] I was pleased to find out the JCMT and I share birthdays; the telescope took its first light on the same week and year in April 1987 on which I was born.

1.2.1 Submillimetre Common User Bolometer Array - 2 (SCUBA-2)

Primarily Chapter 2 of this thesis involves the use of the instrument SCUBA-2, a new 10,000 bolometer submillimetre camera on the JCMT that began operations in 2010 and is expected to improve submillimetre astronomy by carrying out wide-field surveys to unmatched depths. The telescope beams are ~ 8.5 and ~ 14.5 arcsec for the 450 and 850 μm wavelengths respectively. I primarily focus on the details of the instrument filters, specifically understanding how molecular lines can contaminate dust continuum emission maps produced by the instrument.

For detailed explanations of the SCUBA-2 instrument, see Holland et al. [2013] and Dempsey et al. [2013]. Light gathered by the JCMT passes from the tertiary mirror to a beam splitter and through bandpass filters, which illuminate and define the filter ranges for the 450 and 850 μm focal planes. Each focal plane is made up of four subarrays consisting of bolometers in 32 columns and 42 rows (i.e. 1280 bolometers in each array). These bolometers act as thermal absorbers that are coupled to transition edge sensors (TESs). TESs detect temperature changes as a varying current which also cause the magnetic field to vary. These currents are both detected and amplified using superconducting quantum interference devices (SQUIDs) and output currents are then digitised. Flat field observations are used to establish the relationship between the digitised current and the input power. The emission is corrected for atmospheric extinctions and can be converted from power to astronomical flux units using a flux conversion factor (FCF) calculated from standard calibrators [Chapin et al., 2013]. FCFs are calculated from astronomical sources of known flux in a range of atmospheric conditions. Variations in FCFs tend to be dominated by optical effects from thermal distortions of the dish (primarily in early evening; Dempsey et al. 2013). See Chapter 2 for more details of FCFs.

SCUBA-2 uses a routine scanning mode with scanning patterns that depend on the field size observed. For small-field observations, the 'DAISY' scan is preferred for sources within a 3 arcmin or less diameter. This observing pattern is created by moving the telescope in a pseudo-circular pattern with the target kept on the arrays during integration. For the astronomical signal to be kept at a constant frequency, the telescope moves at a constant speed. For larger field observations, the 'PONG'

pattern is used in the scan model. The map area is initially defined as a square and the telescope begins to fill the square within the defined sky area. The map is rotated once a single pattern is complete and a new pattern begins. The result is a map with rounded corners. PONG patterns are available for a range of larger fields, including 15 arcmin, 30 arcmin, 1 deg and 2 degree maps [Holland et al., 2013].

1.2.2 Heterodyne Array Receiver Programme for B-band (HARP)

HARP is a heterodyne focal plane array used for mapping spectral lines with a higher sensitivity at the 325–375 GHz atmospheric window and uses 16 heterodyne receivers in a 4×4 array. The 16 pixels have receiver temperatures ranging from 94–165 K and an angular resolution of ∼14 arcsec, which matches the 850 μm SCUBA-2 resolution. Each receiver has an on-sky beam separation of ∼30″ and therefore an under sampled field of view of $104 \times 104''$ [Buckle et al., 2009; Ward-Thompson et al., 2007a].

For a detailed explanation of HARP, see Buckle et al. [2009]. Incoming light from the JCMT is reflected by the tertiary mirror (like SCUBA-2) to the K mirror where it is rotated, refocused and sent to the calibration system. The light passes through a Mach Zehnder interferometer in the cryogenically cooled optics section, where it is cooled to ∼60 K for sideband separation. The local oscillator produces a reference frequency that is mixed with the signal and is sent to the imaging array which operates at ∼4 K. Once the signal is amplified, it is passed to the Auto-Correlation Spectral Imaging System (ACSIS) which digitises the signal into a specific resolution and waveband (resulting in a spectrum). Output files are produced in a 3D format (two spatial dimensions and a velocity dimension). Used with HARP, ACSIS offers either wide bandwidth (up to 1.9 GHz or 0.8 km s^{-1} at 345 GHz) or high spectral resolution with channel spacing as small as 31 kHz or 0.03 km s^{-1} at 345 GHz.

There are three main observing modes for HARP, including ‘Scan,’ ‘Jiggle’ and ‘Stare.’ The scan (raster) mode generates rectangular maps of large regions that have been fully sampled (i.e. Nyquist sampled). Co-adding multiple maps of the regions is the common method used to increase the signal-to-noise ratio. The telescope scans back and forth along rows and observes a reference position at the end of a row. The

jiggle mode is used for mapping regions that are smaller than the field-of-view (FOV) of the array. This mode fills in the gaps by either 'jiggling' the secondary mirror (jiggle-chop) or by moving the entire telescope (grid position-switch) by observing different offsets around the source. Lastly, the stare mode (also known as a 'sample observation') is a fairly sparse map spanning the footprint of HARP. This mode does not provide a Nyquist sampled map.

It is particularly important to calibrate the measurements and remove unwanted atmospheric attenuation from the maps (i.e. from water vapour aborption in the atmosphere). A warm or a cold load is used for calibration. The warm load is heated to ∼40 K above ambient temperatures. Similarly, the cold load is cooled to ∼10 K below ambient temperatures to approximately the same temperature as water vapour in the atmosphere. There are two- or three-load calibration measurements that can then be taken. The two-load calibration measures the power from the sky and the cold load, which should accurately remove the attenuation from the atmosphere. Additionally, the three-load calibration measures the power from the warm load and provides measurements of the receiver temperature [Buckle et al., 2009].

The output from the instrument is a standard Rayleigh-Jeans brightness temperature scale, known as the corrected antenna temperature T_A^* which has been corrected for absorption by Earth's atmosphere. The Rayleigh-Jeans brightness temperature describes the power emission (per area, frequency interval and solid angle) of an object following the Rayleigh-Jeans law (in low frequencies or large wavelengths). The Rayleigh-Jeans approximation is not necessarily applicable to the frequencies and physical temperatures being measured in observations at sub-millimetre wavelengths. However, it is useful to use the law as a temperature scale because it is directly proportional to intensity. The brightness temperature is then related to the physical temperature of a blackbody by,

$$T_{\mathrm{B}} = \frac{h\nu}{k}\left(\exp\left[\frac{h\nu}{kT_{\mathrm{phys}}}\right] - 1\right)^{-1}, \tag{1.10}$$

where T_{phys} is the physical temperature of the blackbody and T_B is the Rayleigh-Jeans brightness temperature.

The temperature scale of the telescope T_A^* (corrected antenna temperature) must

be corrected for telescope and instrumental inefficiencies. These efficiencies are typically the main-beam efficiency $\eta_{\rm MB}$ and forward spillover and scattering efficiency $\eta_{\rm fss}$. The spectrum of a planet (of known intensity and comparable size to the beam FWHM) is used to determine the main-beam telescope efficiency $\eta_{\rm MB}$. The main-beam efficiency primarily measures the extent to which the beam is non-Gaussian (i.e. fraction of power contained within the main lobe of the beam pattern). The intensity of the planet measured by the instrument is calibrated to its known intensity. The forward spillover and scattering efficiency $\eta_{\rm fss}$ is the correction for radiation scattered from large angles by spillover (some radiation will not reflect off the subreflector into the detector) and scattering (by support legs; see Figure 1.5). This efficiency is typically measured from the Moon, which is a much larger source than the beam ($\sim 0.5^{\rm o}$ diameter) and comparing the intensity to the known intensity. The telescope beam is dependent on its wavelength and the telescope aperture, $\theta_{beam} = 1.22\lambda/D$, where θ_{beam} is the telescope beam width, λ is the wavelength of observation and D is the diameter of the telescope aperture [Rohlfs and Wilson, 2004]. Therefore to increase the angular resolution for the observation wavelength, it is necessary to increase the size of the telescope aperture.

In this study, I apply the commonly used main-beam efficiency $\eta_{\rm MB}$ to calibrate my HARP maps in main-beam brightness temperature $T_{\rm MB}$, which has been the standard in other Gould Belt Survey papers. Typically, $\eta_{\rm fss}$ would be used when studying extended sources where the source is much larger than the beam size. Conversely, $\eta_{\rm MB}$ is used for more point-like sources or sources that are comparable or smaller than the beam size. If $\eta_{\rm fss}$ was used instead of $\eta_{\rm MB}$, then brightness temperatures in the HARP data cubes would increase by a factor of 1.26 (average efficiencies across HARP detectors from Buckle et al. 2009). Efficiencies are further discussed in Chapter 2 (relating molecular line intensities to SCUBA-2 dust continuum). Since my maps are calibrated as a main-beam temperature, for extended sources where the size of the source is larger than the beam size ($\Omega_s > \Omega_{beam}$), $T_{\rm MB} = T_B$ (optically thin conditions). For less extended sources where $\Omega_s < \Omega_{beam}$, the main-beam temperature is related to the brightness temperature by $T_{\rm MB} = T_B \left(\frac{\Omega_s}{\Omega_{beam}}\right)$.

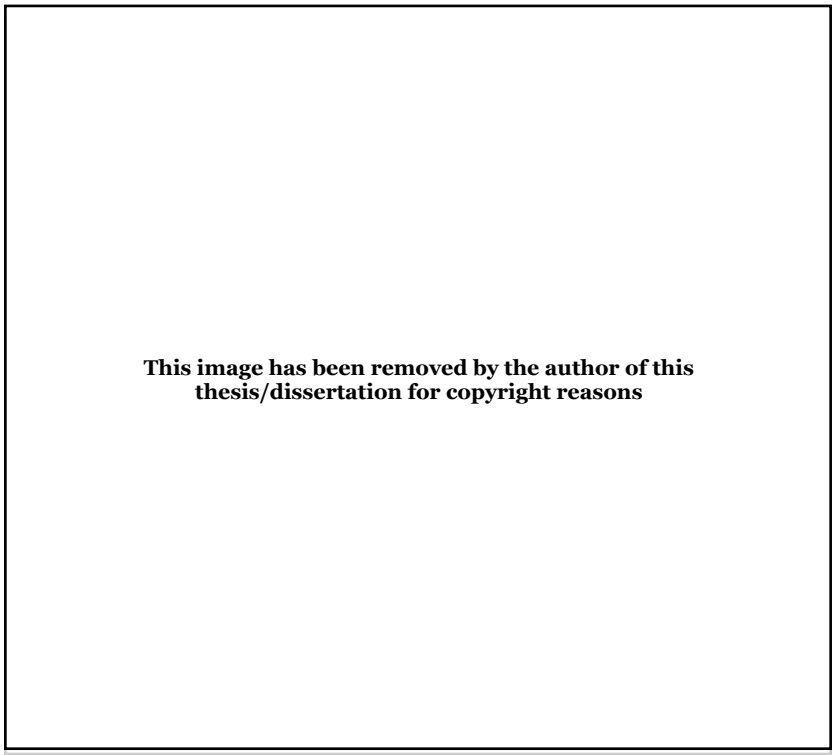

Figure 1.6: Diagram of the Gould Belt showing the centre of the Belt in relation to the Sun. Well-known molecular clouds are shown [Ward-Thompson et al., 2007b].

1.2.3 Gould Belt Legacy Survey (GBS)

The SCUBA-2 continuum data (Chapter 2) and the CO data (Chapter 3) for this thesis have been taken as a part of the Gould Belt Legacy Survey (GBS). The GBS aims to use the JCMT to take ∼500 hours of observations of Gould Belt clouds within 500 pc of the Sun, including regions like Taurus, Orion, Ophiuchus, Scorpius, Serpens and Perseus (see Figure 1.6). This survey is expected to lead to a better understanding of turbulence and emission from dust and molecular lines in these clouds.

The JCMT instruments used for the GBS include SCUBA-2 and HARP. SCUBA-2 is being used to map dust continuum emission at 450 and 850 μm. SCUBA-2 began full operations in late 2011 and has successfully started mapping the majority of the target regions. Additionally, HARP observations have been taken for a select number of regions in molecular clouds, including Ophiuchus, Taurus, Serpens, Orion A, Orion B and Perseus (see Chapter 4; Buckle et al. 2010; Davis et al. 2010a; Graves

et al. 2010).

This survey is important in our ability to understand a variety of star forming environments in the Galaxy and investigate many issues in star formation today. In particular, a large range of sources will be defined, including cores, protostars, disc sources (i.e. less embedded protostars) and molecular outflow candidates. These sources can be analysed and compared between their different environments and further observed by more powerful telescopes (e.g. the new interferometer ALMA - Atacama Large Millimeter Array).

1.3 Radiative transfer for a two-level system

Molecular line emission is useful for tracing the underlying properties of star formation, including the cloud excitation temperature, column density and mass. In this section, I introduce radiative transfer theory and the methods used to determine cloud properties using molecular line emission. Full derivations can be found in Stahler and Palla [2005] and Rohlfs and Wilson [2004].

1.3.1 Rotational emission: Carbon Monoxide (CO)

In this work, I mainly refer to the carbon monoxide (CO) molecule used to study star formation in molecular clouds. Carbon monoxide is a simple linear rotor molecule, where the kinetic energy is approximated by a dumbbell with a rotational axis through the centre of mass is given by,

$$E_{\rm rot} = \frac{L^2}{2I}, \tag{1.11}$$

where I is the moment of inertia and L is the angular momentum. Using quantum mechanics, this is rewritten as

$$E_J = \frac{\hbar^2}{2I} J(J+1) = \frac{h\nu_o J(J+1)}{2}, \tag{1.12}$$

where the above angular momentum L is now $L^2 = J(J+1)\hbar^2$, J is the level of transition and ν_o is the frequency of the lowest transition (i.e. from $J = 1 \rightarrow 0$). I

note that T_o is sometimes used to symbolise $h\nu_o/k$.

For this thesis, rotational transition $J = 3 \rightarrow 2$ are analysed for ^{12}CO, ^{13}CO and C^{18}O isotopologues. These are further discussed in Chapter 3.

1.3.2 Radiative transfer

Radiative transfer is the interaction of radiation through a medium as it travels along the line-of-sight to an observer. A simplified model describing the variation in the specific intensity of radiation I_ν as it passes through a medium along the line of sight (path length ds) is

$$\frac{dI_\nu}{ds} = -\alpha_\nu I_\nu + j_\nu, \tag{1.13}$$

where α_ν is the absorption coefficient in cm^{-1} and j_ν is the emission coefficient in energy per volume per time per frequency per solid angle (J cm^{-3} s^{-1} Hz^{-1} sr^{-1}). The absorption coefficient $\alpha_\nu = \rho\kappa_\nu$ where ρ is the total mass density (g/cm^3) and κ_ν is the opacity of the medium (cm^2/g). The emission coefficient is denoted by $j_\nu = \epsilon_\nu\rho/4\pi$ where ϵ_ν is the emissivity or the energy spontaneously emitted per unit frequency per time per mass (J Hz^{-1} s^{-1} g^{-1}), ρ is the mass density of the emitting medium (g/cm^3) and 4π is the solid angle (sr). A change in radiation intensity is only detected if the radiation is absorbed or emitted as it passes through a medium. The first term on the right side of the equation represents the effective absorption, which will include both true absorption and stimulated emission because both are proportional to the intensity of the incoming beam. The net absorption may be positive or negative depending on whether stimulated emission or true absorption dominates. The second term represents the increase in intensity (emission) by spontaneous emission in the medium.

The optical depth describes the transparency of the medium, or how much absorption occurs when radiation travels through the medium. The optical depth is defined by

$$\mathrm{d}\tau_\nu(s) = \alpha_\nu \mathrm{d}s \tag{1.14}$$

$$\tau_\nu(s) = \int_{s_o}^{s} \alpha_\nu(s')\mathrm{d}s' \tag{1.15}$$

where an optically thick medium will be $\tau_\nu >> 1$ and an optically thin medium will

be $\tau_\nu << 1$. The equation for radiative transfer (Equation 1.13) can be rewritten with the optical depth and source function $S_\nu \equiv \frac{j_\nu}{\alpha_\nu}$,

$$\frac{\mathrm{d}I_\nu}{\mathrm{d}\tau_\nu} = -I_\nu + S_\nu. \tag{1.16}$$

Solved as a differential equation, the radiative transfer equation becomes

$$I_\nu(\tau_\nu) = I_\nu(0)\ \exp(-\tau_\nu) + \int_0^{\tau_\nu} S_\nu(\tau'_\nu)\ \exp\left[-(\tau_\nu - \tau'_\nu)\right]\ \mathrm{d}\tau'_\nu, \tag{1.17}$$

where the first term on the right side of the equation is the fraction of the background radiation that is able to get through the medium and the second term is the radiation emitted by the medium that manages to escape. The background radiation $I_\nu(0)$ is typically assumed to be the cosmic microwave background (CMB).

1.3.3 Limiting case: LTE

According to Kirchhoff's law, the source function S_ν is simply the Planck function $S_\nu = B_\nu = \frac{j_\nu}{\alpha_\nu}$ in local thermodynamic equilibrium (LTE). The source function is a function of optical depth and temperature. Assuming an isothermal medium (constant temperature) with constant optical depth, Equation 1.17 becomes

$$\Delta I_\nu(s) = I_\nu(s) - I_\nu(0) = (B_\nu - I_\nu(0))(1 - \exp(-\tau)), \tag{1.18}$$

where the background emission $I_\nu(0)$ is subtracted from the spectral line measurement (typically in the form of baseline subtraction to remove continuum from the CMB). It is more convenient to replace the incident intensity and source function with their corresponding temperatures using the blackbody spectrum discussed in Section 1.2.2. Temperature of the background radiation is derived from the CMB as T_{CMB} and the source function $S_\nu = B_\nu$ is denoted as the excitation temperature where the excitation temperature is equal to the kinetic (physical) temperature under LTE assumptions ($T_{\mathrm{kin}} = T_{\mathrm{ex}}$). The equation of the brightness temperature

(sometimes referred to as the radiation temperature or $T_{\rm R}^{*}$) is then

$$T_{\rm B} = \frac{h\nu}{k}\left[\frac{1}{\exp\left(\frac{h\nu}{kT_{\rm ex}}\right)-1} - \frac{1}{\exp\left(\frac{h\nu}{kT_{\rm CMB}}\right)-1}\right](1-\exp\left(-\tau_\nu\right)). \tag{1.19}$$

Using the Rayleigh-Jeans approximation, the equation becomes

$$T_B = (T_{\rm ex} - T_{\rm CMB})(1-\exp(-\tau_\nu)). \tag{1.20}$$

Neglecting the CMB background radiation in the case of optically thin emission ($\tau_\nu << 1$), the brightness temperature becomes $T_B = \tau_\nu T_{\rm ex}$ (continuing to assume the Rayleigh-Jeans approximation under LTE conditions). In the optically thick limit ($\tau_\nu >> 1$) neglecting the CMB radiation, the brightness temperature is roughly equivalent to the excitation temperature $T_{\rm B} = T_{\rm ex}$. LTE is further discussed in Section 1.3.5.

1.3.4 Molecular line radiation

Until this point, I have expressed radiative transfer as a function of the macroscopic emission and absorption coefficients. However, I will now consider a species of atom, ion or molecule that has two energy levels separated by ΔE. This species will have number density n ($\rm cm^{-3}$) distributed through a gas of total number density $n_{\rm tot}$ and homogeneous composition ($\rm g/cm^{-3}$).

Upward transitions (excitation) take place under numerous processes. Collisional excitation transfers populations at a total rate per unit volume ($\rm cm^{-3}\ s^{-1}$) equal to $\gamma_{\rm lu} n_{\rm tot} n_{\rm l}$, where $\gamma_{\rm lu}$ is the collisional excitational coefficient. Radiative excitation transfers populations at a rate per unit volume equal to $B_{\rm lu}\overline{J}n_{\rm l}$ which is the probability per unit time of a species being excited radiatively, which must be proportional to the radiation intensity $\overline{J}$ and $B_{\rm lu}$ is the Einstein coefficient for absorption.

Similarly, downward transitions (de-excitation) between energy levels take place under collisional and radiative processes. Collisional de-excitation transfers populations downward at a rate per unit volume given by $\gamma_{\rm ul} n_{\rm tot} n_{\rm u}$ where $\gamma_{\rm ul}$ is the collisional de-excitation coefficient. There are two types of radiative downward transitions, including spontaneous and stimulated emission. Spontaneous emission

or spontaneous radiative de-excitation transfers population downward at a rate per unit volume equal to $A_{\rm ul}n_{\rm u}$ where $A_{\rm ul}$ is the Einstein coefficient for spontaneous emission. Stimulated emission or induced radiative de-excitation has a volumetric rate of transition given by $B_{\rm ul}\overline{J}n_{\rm u}$ where $B_{\rm ul}$ is the Einstein coefficient for stimulated emission.

In order for the populations of upper and lower levels to remain constant, the excitation and de-excitation rates must be equal,

$$\gamma_{\rm lu}n_{\rm tot}n_{\rm l} + B_{\rm lu}\overline{J}n_{\rm l} = \gamma_{\rm ul}n_{\rm tot}n_{\rm u} + B_{\rm ul}\overline{J}n_{\rm u} + A_{\rm ul}n_{\rm u}. \tag{1.21}$$

Expressions can be derived for the collisional and Einstein A and B coefficients assuming either collisional or radiative transitions dominate (see Stahler and Palla 2005 full details). When collisional transitions dominate over radiative ones, the two level system achieves local thermodynamic equilibrium (LTE) where the Boltzmann relation can be used to describe the level populations using the kinetic temperature $T_{\rm kin}$,

$$\frac{n_{\rm u}}{n_{\rm l}} = \frac{\gamma_{\rm lu}}{\gamma_{\rm ul}} = \frac{g_{\rm u}}{g_{\rm l}}\exp\left(\frac{-\Delta E}{kT_{\rm kin}}\right), \tag{1.22}$$

where $g_{\rm u}$ and $g_{\rm l}$ are the degeneracies of the upper and lower levels respectively. Similarly, assuming radiative transitions dominate ($n_{\rm tot}$ is negligible), the system reaches thermodynamic equilibrium. The level populations can also be described with the Boltzmann relation using a radiation temperature $T_{\rm rad}$ and the radiation $\overline{J}$ obeys Planck's law, yielding the relation between the Einstein coefficients:

$$A_{\rm ul} = \frac{2h\nu^3}{c^2}B_{\rm ul} \tag{1.23}$$

$$g_{\rm l}B_{\rm lu} = g_{\rm u}B_{\rm ul}, \tag{1.24}$$

where ν is the frequency of of the transition from the upper state $J+1$ to the lower state J and g is the degeneracy of the transition level. I note the Einstein A and B coefficients have been calculated using the mean intensity $\overline{J}$ [erg cm^{-2} s^{-1} Hz^{-1} sterad^{-1}]. These coefficients can also be calculated using the energy density u_ν instead of the mean intensity which would cause the A coefficient to differ by a factor of $4\pi/c$.

The Einstein A coefficient (s^{-1}) can be expressed more formally for a linear, rigid rotor model with rotation transition $J+1 \rightarrow J$,

$$A_{\rm ul} = \frac{64\pi^4}{3hc^3}\nu_{\rm ul}^3\mu^2\frac{J+1}{2J+3}, \tag{1.25}$$

where μ is the permanent electric dipole moment (e.g. CO). Additionally, the absorption coefficient from Equation 1.13 can now be defined using the Einstein coefficients,

$$\alpha_\nu = \frac{h\nu_{\rm ul}}{4\pi}\left(n_{\rm l}B_{\rm lu} - n_{\rm u}B_{\rm ul}\right)\phi(\nu), \tag{1.26}$$

where $B_{\rm lu}$ is the Einstein coefficient for absorption, $B_{\rm ul}$ is the Einstein coefficient for stimulated emission and $\phi(\nu)$ is the normalised intrinsic linewidth with $\int_0^\infty \phi(\nu){\rm d}\nu = 1$. The coefficient for stimulated emission is included in the absorption coefficient and can be viewed as 'negative absorption' because it is proportional to the ambient radiation intensity.

These parameters can now be incorporated into Equation 1.21. Using the excitation temperature $T_{\rm ex}$ which describes the level populations in terms of $T_{\rm ex}$ assuming Boltzmann's law:

$$\frac{n_{\rm u}}{n_{\rm l}} = \frac{g_{\rm u}}{g_{\rm l}}\exp\left(\frac{-\Delta E}{kT_{\rm ex}}\right), \tag{1.27}$$

the relationship between $T_{\rm ex}$, $T_{\rm kin}$, and $T_{\rm rad}$ becomes

$$\exp\left(\frac{-\Delta E}{kT_{\rm ex}}\right) = f_{\rm ul}\exp\left(\frac{-\Delta E}{kT_{\rm kin}}\right) + (1-f_{\rm ul})\exp\left(\frac{-\Delta E}{kT_{\rm rad}}\right), \tag{1.28}$$

where $f_{\rm ul}$ denote the fraction of collisional downward transitions or $f_{\rm ul} = n_{\rm tot}/[n_{\rm tot} + n_{\rm crit}(1 + c^2\overline{J}/2h\nu^3)]$ and $n_{\rm crit}$ is the critical density $n_{\rm crit} = A_{\rm ul}/\gamma_{\rm ul}$. The critical density denotes the density needed for collisions to depopulate the upper state instead of radiation. The excitation temperature $T_{\rm ex}$ or the level populations are always determined by the collisional and radiative processes, where $T_{\rm ex}$ is constrained by $T_{\rm kin}$ and $T_{\rm rad}$ in the equation above. When collisions are negligible and radiation dominates ($n_{\rm tot}$ is small so that $f_{\rm ul} << 1$), $T_{\rm ex} \rightarrow T_{\rm rad}$ or the level populations approach equilibrium with the radiation field. Similarly when collisions dominate so that $n_{\rm tot} >> n_{\rm crit}$ ($f_{\rm ul} \rightarrow 1$), $T_{\rm ex} \rightarrow T_{\rm kin}$ or the system is in LTE.

In the optically thick regime, each individual collision does not necessarily result

in detectable emission, i.e. a photon escaping the cloud. Photons may become reabsorbed and enhance the upper level populations, leading to a higher excitation temperature. This is a process known as 'radiative trapping.' The critical density decreases with the increasing optical depth by a factor of $1/\tau$. Therefore, the density needed to thermalise the line decreases for optically thick transitions.

1.3.5 Derivation of cloud properties (LTE)

For my analysis of the Ophiuchus molecular cloud, I assume the molecular line excitation is dominated by collisions and in a local thermodynamic equilibrium (LTE) state. LTE requires the environment to change slowly enough to essentially sustain its local Boltzmann distribution of molecular velocities. I will continue to assume LTE conditions for the derivation of various properties of the molecular cloud, including excitation temperature, column density and mass. This section does not include non-LTE modelling techniques used in Chapter 5, where more complex radiative transfer models can be used to numerically solve the temperature and density variations along the line-of-sight.

1.3.5.1 Excitation temperature

Under LTE conditions, the excitation temperature of the molecule is equivalent to the kinetic temperature. Using Equation 1.19 and assuming the sources observed are larger than the beam size (i.e. $T_{\rm MB} = T_{\rm B}$), the following relation can be calculated for the excitation temperature:

$$T_{\rm ex} = \frac{T_{\rm ul}}{\ln\left[T_{\rm ul}\left(T_{\rm peak} + \left(\frac{T_{\rm ul}}{\exp\left(T_{\rm ul}/T_{\rm CMB}\right)-1}\right)\right)^{-1} + 1\right]} \tag{1.29}$$

where ν is the frequency corresponding to the rotational transition, $T_{\rm ul}$ denotes $h\nu/k$, $T_{\rm peak}$ is the peak main-beam temperature of the molecule, and $T_{\rm CMB}$ is the background temperature corresponding to the CMB (2.73 K). This equation also assumes a high optical depth ($\tau >> 1$) so that $[1 - \exp -(\tau_\nu)] \rightarrow 1$ in Equation 1.19. I further discuss the excitation temperatures in Chapter 4 where I use optically thick isotopologues ^{12}CO and ^{13}CO to further investigate this parameter in the Ophiuchus

molecular cloud.

1.3.5.2 Column density

Molecular line intensities can be further used to calculate the total column density of regions in the molecular cloud using only the rotational transitions. Using the relations between the Einstein coefficients (Equations 1.23, 1.24 and 1.25), the excitation temperature definition (assuming LTE) and $\alpha_\nu = -\frac{\mathrm{d}\tau}{\mathrm{d}s}$, Equation 1.26 can be rewritten to show a definition for the upper-level density n_u:

$$n_\mathrm{u}\phi(\nu) = \frac{3hc}{8\pi^3\nu_\mathrm{ul}\mu^2}\left(\frac{2J+3}{J+1}\right)\frac{1}{\exp\left(h\nu/kT_\mathrm{ex}\right)-1}\left(-\frac{\mathrm{d}\tau}{\mathrm{d}s}\right). \tag{1.30}$$

Using the Rayleigh-Jeans approximation, the excitation (physical) temperature can be approximated as a brightness temperature as in Equation 1.10, denoted as T'_ex. The column density of the upper-limit is calculated by integrating the density n_u over the line of sight $\mathrm{d}s$ and the frequency ν. To make this calculation more relatable to molecular line observations, the frequency dependence can be changed to a velocity dependence by $\mathrm{d}\nu = -\nu_\mathrm{ul}/c\ \mathrm{dv}$. The upper-level column density therefore becomes,

$$N_\mathrm{u} = \frac{3k}{8\pi\nu_\mathrm{ul}^2\mu^2}\left(\frac{2J+3}{J+1}\right)T'_\mathrm{ex}\int\tau\mathrm{dv}. \tag{1.31}$$

To obtain the total column density, it is necessary to sum over all the energy levels of the molecule. This is done using a fractional population that has been defined by the Boltzmann distribution and Partition function, assuming all levels have the same excitation temperature (i.e. LTE),

$$\frac{N_\mathrm{u}}{N(\mathrm{total})} = \frac{g_u}{Q}\exp\left[-\frac{h\nu_o(u)(u+1)}{2kT_\mathrm{ex}}\right], \tag{1.32}$$

where u is the level, g_u is the degeneracy $(2J+3)$ and Q is the Partition function. The Partition function is defined as

$$Q = \sum_{u=0}^{\text{all states}} g_x\exp\left[-\frac{T_o(u)(u+1)}{2T_\mathrm{ex}}\right], \tag{1.33}$$

where $T_o = h\nu_o/k$. This function can be approximated using the assumption $T_\mathrm{ex} \gg$

T_o. The Partition function becomes $Q \approx 2T_{\rm ex}/T_o$. Solving Equation 1.32 for the total column density $N(\text{total})$ is then

$$N(\text{total}) = \frac{3k^2}{4\pi h\nu_o^2(J+1)^2\mu^2} \frac{T_{\rm ex}}{\exp\left[-\frac{(J+1)(J+2)h\nu_o}{2kT_{\rm ex}}\right]} T'_{\rm ex} \int \tau \mathrm{dv}. \tag{1.34}$$

The column density is derived from observations using the main-beam temperature using Equation 1.20. The Rayleigh-Jeans excitation temperature $T'_{\rm ex}$ is described as $T_{\rm MB}/\left(1-\exp(-\tau_\nu)\right)^{-1}$, where I assume $T_{\rm B} = T_{\rm MB}$. The full column density equation becomes

$$N(\text{total}) = \frac{3k^2}{4\pi h\nu_o^2(J+1)^2\mu^2} \frac{T_{\rm ex}}{\exp\left[-\frac{(J+1)(J+2)h\nu_o}{2kT_{\rm ex}}\right]} \frac{\tau_o}{1-\exp -\tau_o} \int T'_{\rm ex} \mathrm{dv}, \tag{1.35}$$

where I assume a constant optical depth. In the case of optically thin emission ($\tau << 1$), $\frac{\tau_o}{1-\exp -\tau_o} \rightarrow 1$. In this thesis I primarily use CO $J = 3 \rightarrow 2$ isotopologues. Assuming optically thin emission, the corresponding total column densities are:

$$N(\mathrm{C^{18}O}) = 5.82 \times 10^{12} \frac{T_{\rm ex}}{\exp\left(-31.6\ [\mathrm{K}]/T_{\rm ex}\right)} \frac{\int T_{\rm MB}\mathrm{dv}}{[\mathrm{K\ km\ s^{-1}}]} \left[\mathrm{cm^{-2}}\right], \tag{1.36}$$

$$N(\mathrm{^{13}CO}) = 5.77 \times 10^{12} \frac{T_{\rm ex}}{\exp\left(-31.7\ [\mathrm{K}]/T_{\rm ex}\right)} \frac{\int T_{\rm MB}\mathrm{dv}}{[\mathrm{K\ km\ s^{-1}}]} \left[\mathrm{cm^{-2}}\right], \tag{1.37}$$

$$N(\mathrm{^{12}CO}) = 5.27 \times 10^{12} \frac{T_{\rm ex}}{\exp\left(-33.2\ [\mathrm{K}]/T_{\rm ex}\right)} \frac{\int T_{\rm MB}\mathrm{dv}}{[\mathrm{K\ km\ s^{-1}}]} \left[\mathrm{cm^{-2}}\right]. \tag{1.38}$$

1.3.5.3 Mass

The column density calculation is particularly important in calculating the mass of a molecular cloud. The mass of the total cloud can be inferred from the sum of the column densities in a cross-sectional area (i.e. pixel area), correcting for the relative abundance of the observed molecule in reference to H_2 and accounting for the average mass of a particle. The relation for mass is therefore,

$$M = \mu_{\rm mol} m_{\rm p} X_{\rm mol}^{-1} A_{\rm pixel} \sum_j N_j, \tag{1.39}$$

where $\mu_{\rm mol}$ is the relative molecular mass (accounting for He and H_2 is 2.72), $m_{\rm p}$ is the mass of a proton (1.67×10^{-24} g), $A_{\rm pixel}$ is the cross-sectional area of a pixel (i.e. the area of a pixel in square-radians multiplied by the square-distance to the cloud) and $X_{\rm mol}$ is the relative abundance of the molecule to H_2. This calculation is applied in Chapter 4 of the Ophiuchus molecular cloud using the CO $J = 3 \rightarrow 2$ isotopologues.

1.4 Thesis outline

The work of this thesis uses both early SCUBA-2 850 μm and HARP CO $J = 3 \rightarrow 2$ and HCO+ $J = 4 \rightarrow 3$ observations from the JCMT:

- **Chapter 2** introduces a method for calculating molecular line contamination in the SCUBA-2 data. Using HARP maps of ^{12}CO $J = 3 \rightarrow 2$, I quantify the amount of molecular line contamination found in SCUBA-2 maps of three different regions, including NGC 1333 of Perseus and NGC 2071 and NGC 2024 of Orion B. This method is now being used to remove molecular line contamination for regions with both SCUBA-2 dust continuum and HARP ^{12}CO map coverage in the Gould Belt Survey.

The remaining chapters focus on HARP observations of the Ophiuchus molecular cloud:

- **Chapter 3** introduces CO $J = 3 \rightarrow 2$ data of the Ophiuchus L1668 cloud, which is a part of the Gould Belt Survey. I examine protostellar sources for the presence of molecular outflows in this region and attempt to shed light on some confused sources.

- **Chapter 4** looks at the physical conditions of the gas in the Ophiuchus cloud, including the excitation and optical depths of the region. The mass and energetics of the cloud are calculated to investigate if the cloud is gravitationally bound. The mass and energetics of the global outflows are also calculated to investigate the driving source of turbulence in the region.

- **Chapter 5** presents HCO+ $J = 4 \rightarrow 3$ observations of the Ophiuchus L1668 cloud. A comparison between HCO+ and various column density tracers is made to further investigate the relationship between column density and density in the cloud. Non-LTE models are developed to model the densities HCO+ is tracing in the cloud. The density profiles included: constant density, a 'triangle' density (densities increased at a constant gradient to a maximum peak and then decreased at a constant gradient) and a 'lognormal PDF' density model (based on the lognormal probability density function).

- **Chapter 6** summarises the conclusions of this thesis and how this work could lead to future research.

Chapter 2

Line contamination in the SCUBA-2 dust continuum

This chapter is based on work initially published as Drabek et al. [2012], *Molecular line contamination in the SCUBA-2 450 and 850 μm continuum data*. Using the SCUBA-2 filter profiles, I calculated 'conversion' factors used to convert maps of molecular line integrated intensity (K km s^{-1}) to molecular line flux (mJy beam^{-1}) contaminating the dust continuum emission. These conversion factors were calculated for ^{12}CO $J = 3 \rightarrow 2$ contributions to the 850 μm SCUBA-2 dust continuum emission and for ^{12}CO $J = 6 \rightarrow 5$ contributions to the 450 μm SCUBA-2 continuum. Conversion factors were then applied to HARP ^{12}CO maps of NGC 1333, a region in the Perseus molecular cloud complex, and NGC 2071 and NGC 2024, regions in the Orion B molecular cloud complex, to calculate the line contamination directly by measuring fluxes and masses of a list of sources. Once the ^{12}CO contamination to the source fluxes were calculated, the sources with the highest contamination were analysed in more detail to determine the cause of the molecular flux contribution, e.g. molecular outflows or hot molecular gas from nearby stars.

This work has since been applied in SCUBA-2 studies of Perseus NGC 1333 (Hatchell et al. 2013, including Drabek, E) and B1 (Sadavoy et al. 2013, including Drabek, E). I detail improvements to the conversion factors and their applications in these works.

2.1 Molecular line contamination

As discussed in Chapter 1, dust emission detected in the submillimetre range is a useful tracer of star formation, identifying filamentary structure, Class 0 protostars, prestellar cores and disks in molecular clouds as well as tracing the mass of dust and gas in galaxies. To quantify the flux from the submillimetre dust continuum, the heat generated by this radiation is measured using bolometers with the detected wavelength range defined by wide-band filters [Holland et al., 2002]. These observations of broadband continuum emission from the dust can be contaminated by molecular line flux, particularly from ^{12}CO, which is the second most abundant molecule in the interstellar medium (after H_2) with strong emission lines in the submillimetre [Hatchell and Dunham, 2009; Johnstone et al., 2003; Seaquist et al., 2004; Zhu et al., 2003]. Since the molecular line contamination depends explicitly on the bandwidth and wavelength of the bolometer, it is important to quantify the contribution from molecular lines to make accurate flux measurements of the submillimetre dust emission used in mass calculations.

The CO line contribution can be quantified by comparing observations of the dust continuum emission and the CO line emission [Gordon, 1995]. Past research [Davis et al., 2000; Johnstone and Bally, 1999; Papadopoulos and Allen, 2000; Tothill et al., 2002] has focused on the Submillimetre Common User Bolometer Array (SCUBA) at the James Clerk Maxwell Telescope (JCMT), where line contribution from the ^{12}CO $J = 3 \rightarrow 2$ line was found to range from little to tens of per cent in the 850 μm band. Other studies have examined contamination in various bolometer instruments, including MAMBO-II, Bolocam, and SHARC-II. The Submillimetre High Angular Resolution Camera II (SHARC-II) operates at the same wavelength range as SCUBA (450 μm and 850 μm), but also includes a 350 μm filter (780 to 910 GHz). The 350 μm SHARC-II continuum could be potentially contaminated by the ^{12}CO $J = 7 \rightarrow 6$ line (806 GHz) up to $\sim$20%, similar to the ^{12}CO $J = 3 \rightarrow 2$ contamination to the SCUBA 850 μm continuum [Hatchell and Dunham, 2009]. While Bolocam (operated at Caltech at 1.1 mm with a 250 to 300 GHz filter) has been designed to exclude ^{12}CO line contamination, the Max Planck Millimetre Bolometer II (MAMBO-II; operated by the Max Planck Institut für Radioastronomie at 1.2 mm with a $\sim$210 to 290 GHz filter) includes ^{12}CO $J = 2 \rightarrow 1$ (230 GHz) molecular line

emission which could potentially increase flux at most a few per cent [Aguirre et al., 2011]. Other possible contamination for Bolocam and MAMBO-II could result from other known molecular lines in clouds, including SiO $J = 6 \rightarrow 5$ ($\sim$260 GHz) and HCN $J = 3 \rightarrow 2$ ($\sim$258 GHz).

The successor to SCUBA is SCUBA-2, which can be as susceptible to significant molecular line contamination as the above bolometers. In regards to ^{12}CO, both SCUBA-2 bandpass filters have a central transmission peak near a ^{12}CO line: the 850 μm bandpass filter centre is at 347 GHz near the ^{12}CO $J = 3 \rightarrow 2$ line at 345.796 GHz and the 450 μm bandpass filter centre is 664 GHz near the ^{12}CO $J = 6 \rightarrow 5$ line at 691.473 GHz. The proximity of the ^{12}CO line frequencies to the centres of the transmission peaks makes significant CO contamination in SCUBA-2 maps likely.

2.2 Method for calculating the ^{12}CO line contamination

As detailed in Section 1.2.2, molecular line emission is typically measured as an intensity or surface brightness in terms of the Rayleigh-Jeans (R-J) brightness temperature (in Kelvin) while the dust continuum fluxes are given in Janskys measured over the telescope beam area (Jy beam^{-1}). In order to convert ^{12}CO line intensities to pseudo-continuum fluxes, the intensity of a molecular line must be converted into the flux of the line using the following relation

$$F = \int I \, \mathrm{d}\Omega \approx I\Omega, \tag{2.1}$$

where I is the intensity and Ω is the telescope beam area. The intensity is measured as a main-beam brightness temperature T_{MB} in Kelvin and converted to intensity using

$$I_\nu = \frac{2\nu^2}{c^2} k T_{\mathrm{MB}} = \frac{2k}{\lambda^2} T_{\mathrm{MB}}, \tag{2.2}$$

where ν is the frequency, λ is the wavelength, and k is the Boltzmann constant.

A narrow molecular line within a filter contributes flux over a smaller frequency range (ν_{line}) than continuum emission across the filter. To obtain the flux from the

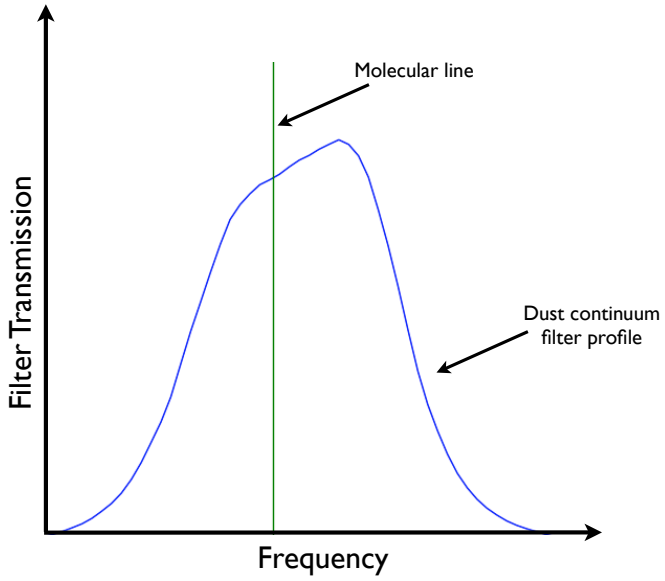

Figure 2.1: Diagram of the dust continuum filter profile. The frequency of a molecular line is shown that could potentially cause contamination. The parameter $g_\nu(line)$ corresponds to the filter transmission at the molecular line frequency.

molecular line, the average intensity $\langle I \rangle$ must be calculated over the full filter band, i.e.

$$\langle I \rangle = \frac{\int I_\nu(\text{line})\ g_\nu(\text{line})\ d\nu}{\int g_\nu\ d\nu}, \tag{2.3}$$

where $I_\nu(\text{line})$ is the intensity of the molecular line, $g_\nu(\text{line})$ is the filter passband (transmission) at the frequency of the molecular line, and $\int g_\nu\ d\nu$ is the integrated filter passband (transmission) across the full range of filter frequencies. An example of the continuum profile with the frequency of the molecular line is shown in Figure 2.1. Using Equation 2.2 and the Doppler shift, $\Delta\nu/\nu = \Delta \text{v}/c$, Equation 2.3 can be converted to T_{MB}:

$$\langle I \rangle = \frac{\frac{\nu}{c}\int I_\nu(\text{v})\ g_\nu(\text{v})\ d\text{v}}{\int g_\nu\ d\nu} = \frac{2k\nu^3}{c^3}\frac{g_\nu(\text{line})}{\int g_\nu\ d\nu}\int T_{\text{MB}}\ d\text{v}, \tag{2.4}$$

where $\int T_{\text{MB}}\ d\text{v}$ is the velocity integrated main-beam brightness temperature, or integrated intensity. Using these calculations of intensity, it follows from Equation 2.1

that

$$\frac{F_\nu}{\text{mJy beam}^{-1}} = \frac{2k\nu^3}{c^3}\frac{g_\nu(\text{line})}{\int g_\nu\, d\nu}\Omega_B \int T_{\text{MB}}\, d\text{v} \tag{2.5}$$

A similar calculation was used in Seaquist et al. [2004].

The main-beam brightness temperature T_{MB} is used rather than the antenna temperature T_{A}^* for analysing small-scale emission as long as the continuum calibration accounts for the same beam efficiencies as the molecular line emission. This is true for the SCUBA-2 and HARP pairing at the JCMT. The beam efficiencies are discussed further in Section 2.4. T_{A}^* is related to T_{MB} by the following:

$$T_A^* = \eta_{\text{MB}} T_{\text{MB}}, \tag{2.6}$$

where η_{MB} is the main-beam efficiency factor. The efficiency factor that takes into account emission at larger scales is discussed in Section 2.2.2. At ~345 GHz with HARP on JCMT, η_{MB} is 0.61 [Buckle et al., 2009]. The telescope beam area, also discussed further in Section 2.2.2, is measured in steradians (sterad) and obtained from the full-width-half-maximum (FWHM) θ_B of a Gaussian beam using $\Omega_B = 2\pi\sigma^2$ where the FWHM $\theta_B = 2\sqrt{2\ln 2}\sigma$:

$$\frac{\Omega_B}{\text{sterad}} = \frac{\pi}{4\ln 2}\left(\frac{\theta_B}{''}\right)^2\left(\frac{\pi}{180\times 3600}\right)^2 \tag{2.7}$$

Using Equation 2.5, a molecular line conversion factor, C, can be calculated to convert molecular line maps, measured in the velocity integrated main-beam temperature $\int T_{\text{MB}}\, d\text{v}$ (K km s^{-1}), into maps of line flux (mJy beam^{-1}) that contributes to the observed continuum emission,

$$\begin{aligned}\frac{C}{\text{mJy beam}^{-1}\text{ per K km s}^{-1}} &= \frac{F_\nu}{\int T_{MB}\, d\text{v}} \\ &= \frac{2k\nu^3}{c^3}\frac{g_\nu(\text{line})}{\int g_\nu\, d\nu}\Omega_B\end{aligned} \tag{2.8}$$

where frequencies are measured in GHz and 1 Jy = 10^{-26} W m^{-2} Hz^{-1} = 10^{-23} erg s^{-1} cm^{-2} Hz^{-1}. Note that the beam size is wavelength dependent, where $\Omega_B \propto \lambda^2$. The difference in beam size between the ^{12}CO and the SCUBA-2 measurements is not taken into account.

2.2.1 Line conversion factors

To calculate the conversion factor C from Equation 2.9, the SCUBA-2 filter profiles and the added atmospheric transmission were used to find $\int g_\nu \, d\nu$ and g_ν(line). The SCUBA-2 850 μm and 450 μm filter profiles are shown in the bottom plot of Figures 2.2 and 2.3 (obtained from Per Friberg, private communication in June 2011). The SCUBA-2 filter profiles are a result of stacking all of the filters (thermal and bandpass filters as well as the cryostat window and dichroic) that form the continuum bandpasses when combined with the atmosphere. The bandpasses are the main filters defining the transmission window, where passbands are the range of frequencies with a signal passing through the filter and stopbands define frequency ranges with a signal attenuated by the filter. The main infrared (IR; thermal) blocking filters are designed to block transmission at higher frequencies (IR and optical). For this study, a constant value for these filters has been assumed due to the high transmission in the frequency range. For further information, see the JCMT website regarding the cryostat window, filter and dichroic specification and measurements[1].

The JCMT has a system that describes the atmospheric conditions ranging from weather grades 1-5. The atmospheric conditions are based on precipitable water vapour (PWV) levels (in mm) that correspond to different sky opacities at 225 GHz, or τ_{225}. The relation between PWV and τ_{225} is the following (JCMT Telescope Overview website)[2]:

$$\tau_{225} \approx 0.01 + (0.04 \times \mathrm{PWV}) \tag{2.9}$$

The JCMT weather grades are defined as:

- **Grade 1:** PWV: < 1 mm, τ_{225}: < 0.05
- **Grade 2:** PWV: 1 to 1.75 mm, τ_{225}: 0.05 to 0.08
- **Grade 3:** PWV: 1.75 to 2.75 mm, τ_{225}: 0.08 to 0.12
- **Grade 4:** PWV: 2.75 to 4.75 mm, τ_{225}: 0.12 to 0.20

[1] http://www.jach.hawaii.edu/JCMT/continuum/scuba2/filter/
[2] www.jach.hawaii.edu/JCMT/overview/tel_overview

- **Grade 5:** PWV: > 4.75 mm, τ_{225}: > 0.20

The continuum bandpass transmission of the filter profile and atmosphere combined varies depending on atmospheric conditions. Therefore, the CO contamination was calculated based on these five weather grades. Plots of atmospheric transmission corresponding to these conditions can be found in the top half of Figures 2.2 and 2.3 and are labelled according to the respective water vapour levels (for more detail, see CSO Atmospheric Transmission Interactive Plotter website).[1] The SCUBA-2 850 μm and 450 μm filter profiles were multiplied by each individual atmospheric transmission profile to produce continuum bandpass profiles at each weather grade, shown in the bottom of Figures 2.2 and 2.3.

In Equation 2.5, $\int g_\nu \, d\nu$ is the integrated SCUBA-2 continuum bandpass and is calculated as the the sum of $g_\nu \times \delta\nu$ (where $\delta\nu$ is 0.01 GHz) at each corresponding frequency with units in GHz. The transmission of ^{12}CO, g_ν(line), is the transmission of the SCUBA-2 850 μm continuum bandpass at 345.7960 GHz (the rest frequency of the ^{12}CO $J = 3 \rightarrow 2$ line) and the transmission of the SCUBA-2 450 μm continuum bandpass at 691.4731 GHz (the rest frequency of the ^{12}CO $J = 6 \rightarrow 5$ line). To calculate conversion factors for redshifted lines, the frequency ν and transmission g_ν(line) (from Figures 2.2 & 2.3) in Equation 2.9 must be changed appropriately. The SCUBA-2 beam size is calculated using Equation 2.7 assuming the main-beam FWHM θ_B is 13.8″ at 850 μm and 8.3″ at 450 μm, measured 2012 January (Per Friberg, private communication). The possibility of an associated secondary beam is discussed in Section 2.2.2.

2.2.2 Telescope beam area

The beam profile of the original SCUBA instrument diverged from a single Gaussian and displayed a beam profile of two combined Gaussians: a primary beam roughly corresponding to the assumed FWHM and a secondary beam of 40″ FWHM [Di Francesco et al., 2008]. For the 450 μm maps, the primary beam had a 8.5″ FWHM with a 0.90 relative amplitude and the secondary beam had a 0.10 relative amplitude. For the 850 μm maps, the primary beam had a 13.5″ FWHM with a 0.96 relative amplitude and the secondary beam had a 0.04 relative amplitude.

[1] http://www.submm.caltech.edu/cso/weather/atplot.shtml

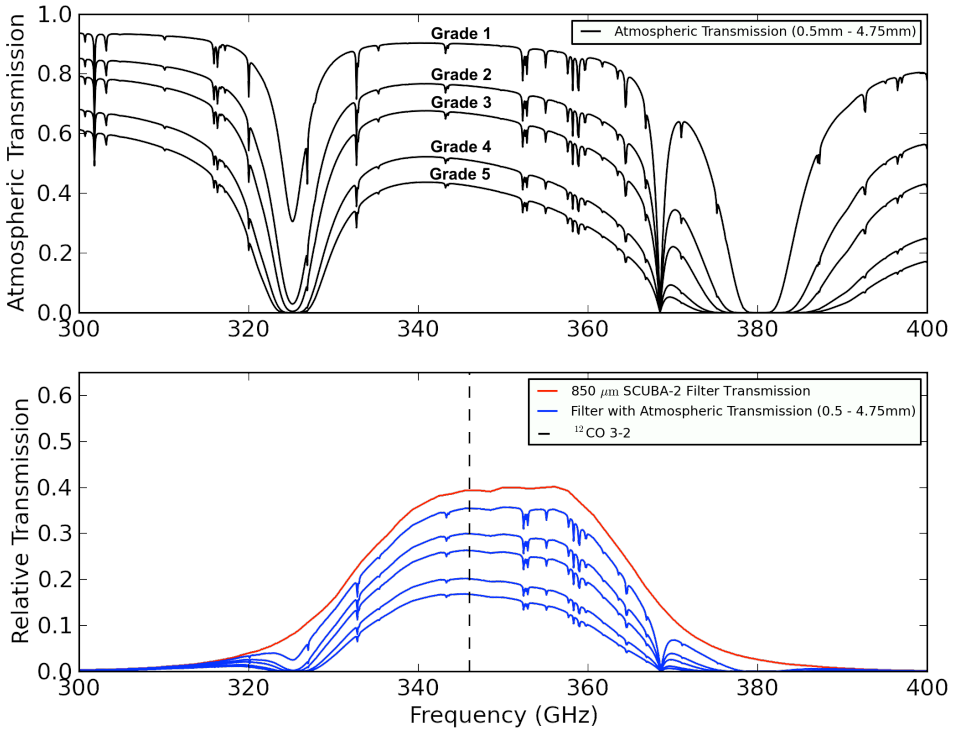

Figure 2.2: *Upper:* Plots of the atmospheric transmission at 300 to 400 GHz, given 0.5 to 4.75 mm of precipitable water vapour. *Lower:* The upper line is the profile of the SCUBA-2 850 μm filter, and the lines beneath represent the SCUBA-2 filter with the addition of the atmospheric transmission at varying water vapour levels. The ^{12}CO $J = 3 \rightarrow 2$ line is plotted at 345.7960 GHz. As shown in Table 2.1, the atmospheric transmission corresponds to different bands of weather used for observations.

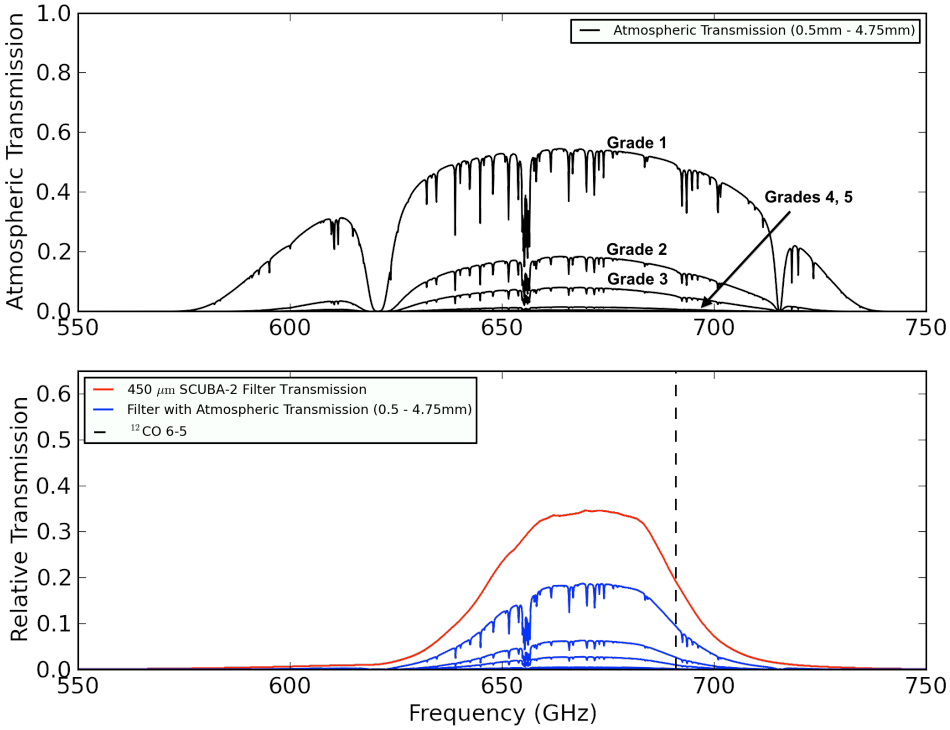

Figure 2.3: *Upper:* Plots of the atmospheric transmission at 550 to 750 GHz, given 0.5 to 4.75 mm of precipitable water vapour. *Lower:* The upper line is the profile of the SCUBA-2 450 μm filter, and the lower lines represent the SCUBA-2 filter with the addition of the atmospheric transmission at varying water vapour levels. The ^{12}CO $J = 6 \rightarrow 5$ line is plotted at 691.4731 GHz.

Band	Filter with Atmos. Trans. (PWV in mm)	$\int g_\nu d\nu$ GHz	θ_B $''$	Line	ν GHz	g_ν(line)	τ_{225}	Weather Grade	C mJy beam^{-1} per K km s^{-1}
850 μm	0.5	19.79	13.8	^{12}CO $J = 3 \rightarrow 2$	345.7960	0.58	0.03	1	0.63
	1.5	15.63	13.8	^{12}CO $J = 3 \rightarrow 2$	345.7960	0.49	0.07	2	0.68
	2.25	13.24	13.8	^{12}CO $J = 3 \rightarrow 2$	345.7960	0.43	0.10	3	0.70
	3.75	9.56	13.8	^{12}CO $J = 3 \rightarrow 2$	345.7960	0.33	0.16	4	0.74
	4.75	7.71	13.8	^{12}CO $J = 3 \rightarrow 2$	345.7960	0.28	0.20	5	0.77
450 μm	0.5	8.49	8.3	^{12}CO $J = 6 \rightarrow 5$	691.4731	0.09	0.03	1	0.64
	1.5	2.64	8.3	^{12}CO $J = 6 \rightarrow 5$	691.4731	0.02	0.07	2	0.57
	2.25	1.10	8.3	^{12}CO $J = 6 \rightarrow 5$	691.4731	0.01	0.10	3	0.51
	3.75	0.19	8.3	^{12}CO $J = 6 \rightarrow 5$	691.4731	< 0.01	0.16	4	0.41
	4.75	0.06	8.3	^{12}CO $J = 6 \rightarrow 5$	691.4731	< 0.01	0.20	5	0.35

Table 2.1: Line contribution factors for ^{12}CO lines in the SCUBA-2 850 μm & 450 μm continuum bands. Beam sizes, introduced in Section 2.2.1, were early measurements from 2012 January by Per Friberg and only include the primary beam.

The total SCUBA-2 beam also includes a broader secondary component [Dempsey et al., 2013]. As explained in Section 2.2.1, the telescope beam areas for this study were calculated assuming FWHMs of 8.3″ and 13.8″ for the 450 μm and 850 μm SCUBA-2 beams respectively. The primary beam is appropriate for studying the CO contamination in compact sources (small-scale emission), e.g. protostars and small outflows. However, if the CO emission is both bright and extended, then it may be necessary to include the secondary beam in the calculation (i.e. on scales much larger than the beam size). By fitting a two component Gaussian to coadded SCUBA-2 maps of Uranus (Per Friberg, private communication), the 450 μm primary FWHM is 8.7″ (relative amplitude 0.83) and secondary FWHM is 20.4″ (relative amplitude 0.17) and the 850 μm primary FWHM is 13.9″ (relative amplitude 0.97) and secondary beam FWHM is 39.1″ (relative amplitude 0.03).[1] The effective FWHM is described using

$$\theta_{\mathrm{E}} = \sqrt{\alpha_{\mathrm{prim}}(\theta_{\mathrm{prim}})^2 + \alpha_{\mathrm{sec}}(\theta_{\mathrm{sec}})^2}, \tag{2.10}$$

where θ_{E} is the effective FWHM, α_{prim} is the relative amplitude of the primary beam, α_{sec} is the relative amplitude of the secondary beam, θ_{prim} is the FWHM of the primary beam and θ_{sec} is the FWHM of the secondary beam. The effective FWHM becomes 11.6″ and 15.3″ for 450 μm and 850 μm beams respectively. This would cause the total beam area for 450 μm to be higher by a factor of 2.0 and the 850 μm total beam area to be higher by a factor or 1.2.

If it is necessary to incorporate the secondary beam into the beam area calculation, then a new conversion factor can be calculated using Equation 2.9. The conversion factors are directly proportional to the telescope beam area. Assuming C' is the the conversion factor with the inclusion of both a primary and secondary beam (Ω'_B) and C is the relation shown in Equation 2.9, then it follows from Equation 2.9:

$$C' = C\,\frac{\Omega'_B}{\Omega_B} = C\,\left(\frac{\mathrm{FWHM}'}{\mathrm{FWHM}}\right)^2, \tag{2.11}$$

where FWHM′ is the effective FWHM. For large-scale and extended emission on scales significantly larger than the size of the telescope beam (greater than 13.8″,

[1] Measured primary beam sizes are slightly larger than the sizes quoted in Section 2.2.1. This is potentially due to small pointing shifts between coadded maps (Per Friberg, private communication).

the 850 μm FWHM), it is also more appropriate to use $\eta_{\rm fss}$, the forward spillover and scattering efficiency, to calibrate the CO emission instead of the main-beam efficiency $\eta_{\rm MB}$. The forward spillover and scattering efficiency measures the amount of coupling to an extended source up to a 30′ diameter (measured by observing the Moon). Equation 2.11 becomes

$$C' = C \left(\frac{\rm FWHM'}{\rm FWHM}\right)^2 \frac{\eta_{\rm MB}}{\eta_{\rm fss}} \tag{2.12}$$

The increase of telescope beam area caused from the inclusion of the secondary beam is somewhat counterbalanced by the use of $T_{\rm R}^* = T_{\rm A}^*/\eta_{\rm fss}$ rather than $T_{\rm MB}$, accounting for the more efficient telescope coupling to large-scale emission ($\eta_{\rm fss} = 0.71$ compared to $\eta_{\rm MB} = 0.61$).

The secondary beam and potential changes in conversion factors for large-scale emission are further discussed in Section 2.5.

2.3 Results

The ^{12}CO conversion factors, C, for SCUBA-2 are listed in Table 2.1. The ^{12}CO $J = 3 \rightarrow 2$ conversion factors (in mJy beam^{-1} per K km s^{-1}) range from 0.63 (Grade 1) to 0.77 (Grade 5) with a mid value of 0.70 (Grade 3). The conversion factors change depending on the atmospheric conditions that affect the continuum bandpass profile. Since each increase in τ_{225} causes the 850 μm continuum bandpass profile to become narrower with less overall transmission, $\int g_\nu d\nu$ in Equation 2.5 shrinks faster than the transmission of ^{12}CO, g_ν(line). Therefore, the ^{12}CO $J = 3 \rightarrow 2$ line contribution to the flux is lowest in Grade 1 weather and steadily increases with each step to Grade 5 weather.

For the 450 μm continuum bandpass profile, the opposite trend is seen. The ^{12}CO line contribution to the 450 μm flux is highest in Grade 1 but steadily decreases with each step to Grade 5 weather. In most cases, observations using SCUBA-2 450 μm would only be taken in Grade 1 to 3 weather due to the decreased transmission in higher weather grades. The ^{12}CO $J = 6 \rightarrow 5$ conversion factors range from 0.64 (Grade 1) to 0.35 (Grade 5) with a mid value of 0.51 (Grade 3).

I note that the contamination is expected to have different behaviour between

the 450 μm and 850 μm filters. The ^{12}CO $J = 3 \rightarrow 2$ line is in the centre of the 850 μm filter with the bulk of the transmission while the ^{12}CO $J = 6 \rightarrow 5$ line is close to the edge of the 450 μm filter with lower transmission. The molecular line contribution to the 450 μm band decreases with weather grade because of the increasing attenuation of the ^{12}CO $J = 6 \rightarrow 5$ line.

2.4 Applications to observations

The conversion factors calculated in Section 2.3 were applied to HARP ^{12}CO $J = 3 \rightarrow 2$ maps and compared to SCUBA-2 850 μm dust emission maps to measure the ^{12}CO contamination directly. Three different regions were used for this study: NGC 1333, NGC 2071, and NGC 2024. By quantifying the percentage of contamination to the dust continuum flux, the regions more likely to be contaminated by CO can be determined (i.e. regions with molecular outflows or nearby stars).

2.4.1 Flux calculations

The continuum observations were taken with SCUBA-2 at 450 μm and 850 μm in each region in 2010 during the SCUBA-2 Shared Risk Observing (S2SRO) campaign when SCUBA-2 had two science grade arrays (one at 450 μm and one at 850 μm) installed. Observations were taken in Grade 2 weather conditions. The S2SRO observations were the best dust continuum data from SCUBA-2 that was available at the time. See Section 2.6 to see more recent applications of the understanding ^{12}CO contamination in the dust continuum.

I initially tested the above ^{12}CO contamination technique on ^{12}CO $J = 3 \rightarrow 2$ data from HARP for NGC 1333 was observed in January 2007 using raster mapping techniques. The ^{12}CO $J = 3 \rightarrow 2$ data cubes for NGC 2071 and NGC 2024 were observed in November 2007 using raster mapping techniques as well (see Buckle et al. 2010). Both datacubes were rebinned to 0.42 km s^{-1} velocity channels and converted to $T_{\rm MB}$ using a main-beam efficiency $\eta_{\rm MB}$ of 0.61.

Similar to other ground-based bolometer arrays, the limited, single-subarray version of SCUBA-2 available for S2SRO reproduced maps that are not sensitive to large-scale emission, in this case on scales larger than the single subarray field-of-

view ($\sim$4′). However, the HARP ^{12}CO maps still contain this large-scale flux. A simple application of the CO conversion factors from Table 2.1 to the HARP maps would retain the large-scale structure and overestimate the CO contamination. In order to account for the spatial filtering inherent in bolometer array reconstruction in a simple way and subtract the large-scale flux from the maps, a Gaussian smoothing mask (GSM) filter was applied to both the ^{12}CO HARP integrated intensity maps (in K km s^{-1}) and the 850 μm maps (mJy beam^{-1}) of the regions. The GSM filter was designed to minimise emission from structure on scales inaccessible to SCUBA-2 at this time. For the HARP maps, GSM filters were created by convolving a HARP ^{12}CO contamination map directly with a Gaussian a few arc minutes FWHM in size and subtracting the resulting smoothed map from the original map. For the SCUBA-2 maps, it was necessary to first create a thresholded map for masking bright protostars and convolve the thresholded map with a Gaussian the same FWHM in size. The resulting smoothed map was then subtracted from the original map.

A 1′ FWHM Gaussian was chosen for generating GSM maps after analysing 1′ to 3′ GSM filter sizes, further discussed in Section 2.4.1.4. Figure 2.4 shows examples of the SCUBA-2 GSM processed maps for protostellar cores LBS-MM18 (NGC 2071-IRS) in NGC 2071 (see Motte et al. 2001), FIR 1-7 in NGC 2024(see Buckle et al. 2010; Richer et al. 1989), and SVS13 in NGC 1333 (see Hatchell et al. 2007b). The brightest CO features in the maps are the result of molecular outflows driven by the dense cores in the regions. Dust emission contours in the outflows of these regions clearly follow the ^{12}CO $J = 3 \rightarrow 2$ emission, indicating the CO contamination is strong enough to be directly detected in the dust continuum.

To study the CO contamination quantitatively, aperture photometry with a 15″ radius was applied to lists of known submillimetre sources, listed in Table 2.4 and further discussed in Sections 2.4.1.1, 2.4.1.2, and 2.4.1.3. A 15″ aperture radius was chosen based on source proximity and the possibility of the aperture diameter extending to a neighbouring source. Integrated flux densities are calculated by assuming a sky background of zero with flux uncertainties based on the sky RMS and include a correction for the Gaussian beam [Enoch et al., 2006]. Therefore, a point-source has the same integrated flux density in any size aperture.

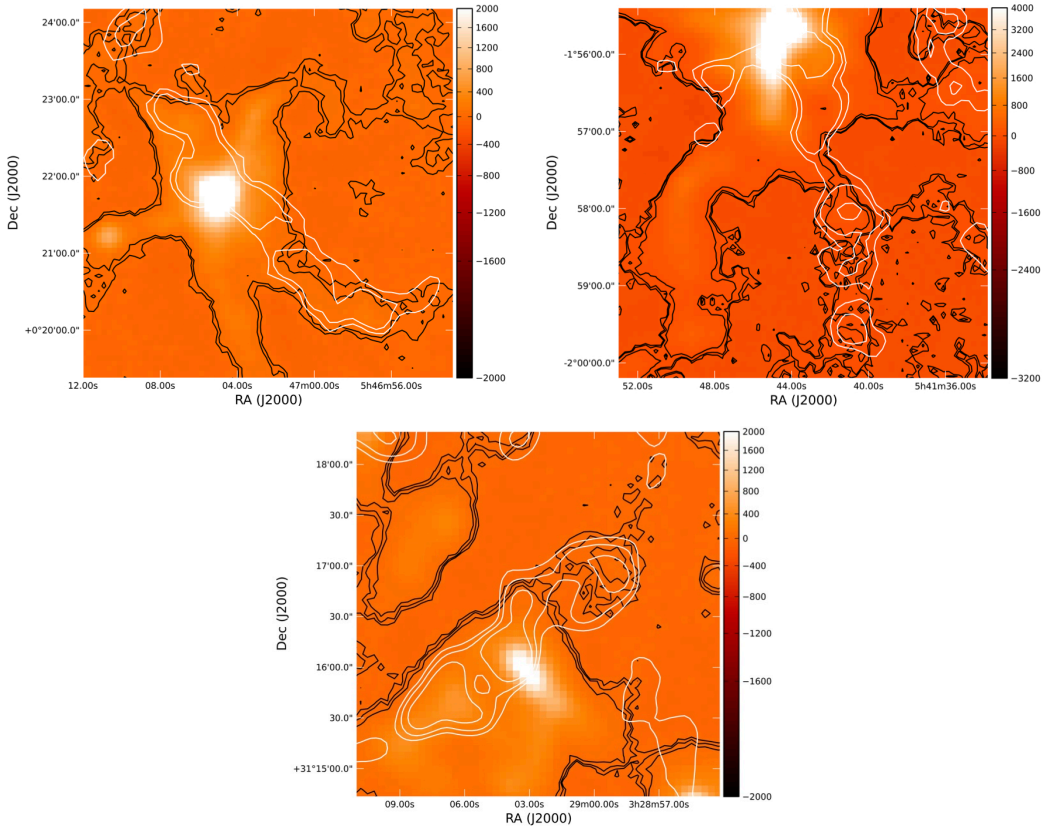

Figure 2.4: Regions in the SCUBA-2 850 μm GSM-filtered maps of NGC 2071, NGC 2024, and NGC 1333 where ^{12}CO emission contributes strongly to the 850 μm flux. Black contours correspond to the SCUBA-2 850 μm dust continuum maps and white contours correspond to HARP ^{12}CO $J = 3 \rightarrow 2$ contamination maps. *Top Left:* Close-up of LBS-MM18 (NGC2071-IRS) and corresponding outflow. Both sets of contours correspond to flux at 20 and 45 mJy beam^{-1}. Noticeable ^{12}CO flux contribution in the lower right lobe of the molecular outflow. *Top Right:* Close-up of FIR 1-7 and corresponding outflow. Both contours correspond to flux at 10, 20, and 45 mJy beam^{-1}. Noticeable ^{12}CO flux contribution in the lower lobe of the molecular outflow. *Bottom:* Close-up of SVS13 and corresponding outflow. Both sets of contours correspond to flux at 10, 20, and 35 mJy beam^{-1}. Noticeable ^{12}CO flux contribution in the right lobe of the molecular outflow.

2.4.1.1 Application to NGC 1333

NGC 1333 is a reflection nebula in the Perseus molecular cloud and is characterised by early stage star formation of age less than 1 Myr [Lada et al., 1996; Wilking et al., 2004]. The flux calibration for the S2SRO maps of this region was the CRL618 nebula and pointing checks were from the active galactic nucleus 3C84. A flux conversion factor (FCF) of 500 Jy beam^{-1} pW^{-1} was used for NGC 1333 to convert the maps into mJy beam^{-1}. Sources were chosen from a list of cores in NGC 1333 [Hatchell et al., 2007b] that had been previously identified in the submillimetre using SCUBA [Hatchell et al., 2005] and Bolocam [Enoch et al., 2006] with a total of 35 sources in the area covered by the SCUBA-2 map. These sources include a mixture of protostellar and starless cores. For further information regarding HARP observations, see Curtis et al. [2010b].

Figure 2.5 shows the source fluxes from the SCUBA-2 850 μm and ^{12}CO $J = 3 \rightarrow 2$ Grade 2 contamination maps and the percentage contribution of ^{12}CO $J = 3 \rightarrow 2$ flux to 850 μm SCUBA-2 flux. I note that all of the sources have ^{12}CO contributions less than 20% and every source except one (source 21) has a contribution less than 10%. Source 21 is further discussed in Section 2.4.3.

2.4.1.2 Application to NGC 2071

NGC 2071 is a region in the Orion B molecular cloud. Sources were chosen from a list of young stellar objects that had been previously identified using SCUBA [Nutter and Ward-Thompson, 2007] with a total of 50 sources in the area covered by the SCUBA-2 map. A flux conversion factor of 685 Jy beam^{-1} pW^{-1} was used for NGC 2071 as well as NGC 2024 (FCF value valid for October 2010 reduction, equivalent to Nutter et al, *in prep.*). For further information on HARP observations of NGC 2071, see Buckle et al. [2010].

Figure 2.6 shows the source fluxes from the SCUBA-2 850 μm and ^{12}CO $J = 3 \rightarrow 2$ Grade 2 contamination maps and the percentage contribution of ^{12}CO $J = 3 \rightarrow 2$ flux to SCUBA-2 850 μm flux. I note that the majority of sources have ^{12}CO contributions of less than 20% in Grade 2 weather. Four sources (sources 70, 74, 88, and 91) have ^{12}CO contributions greater than 20% (ranging from 34 to 79%). Sources with a higher ^{12}CO contamination are further discussed in Section 2.4.3.

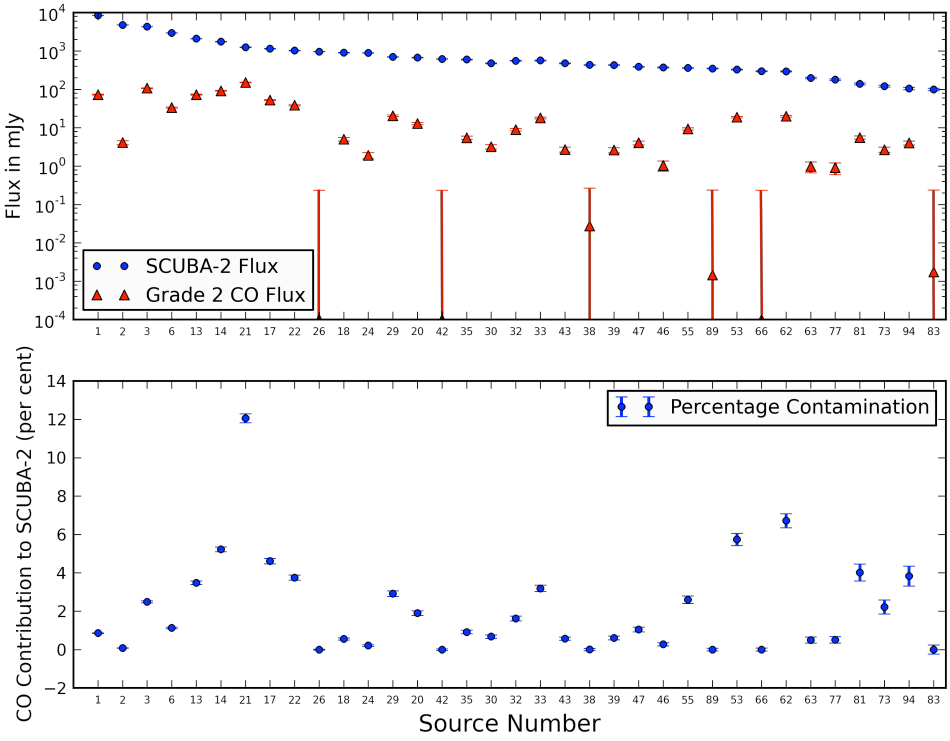

Figure 2.5: *Top:* The SCUBA-2 source fluxes calculated from the 850 μm continuum and ^{12}CO $J = 3 \rightarrow 2$ contamination maps (Grade 2 weather) of NGC 1333. Note several sources (26, 42, and 66) have ^{12}CO flux contributions of 0 mJy beam^{-1}. *Bottom:* The percentage contribution to the SCUBA-2 fluxes from the ^{12}CO contamination maps. Numbers are given arbitrarily to the sources and were based on the original list of SCUBA and Bolocam cores [Hatchell et al., 2007b].

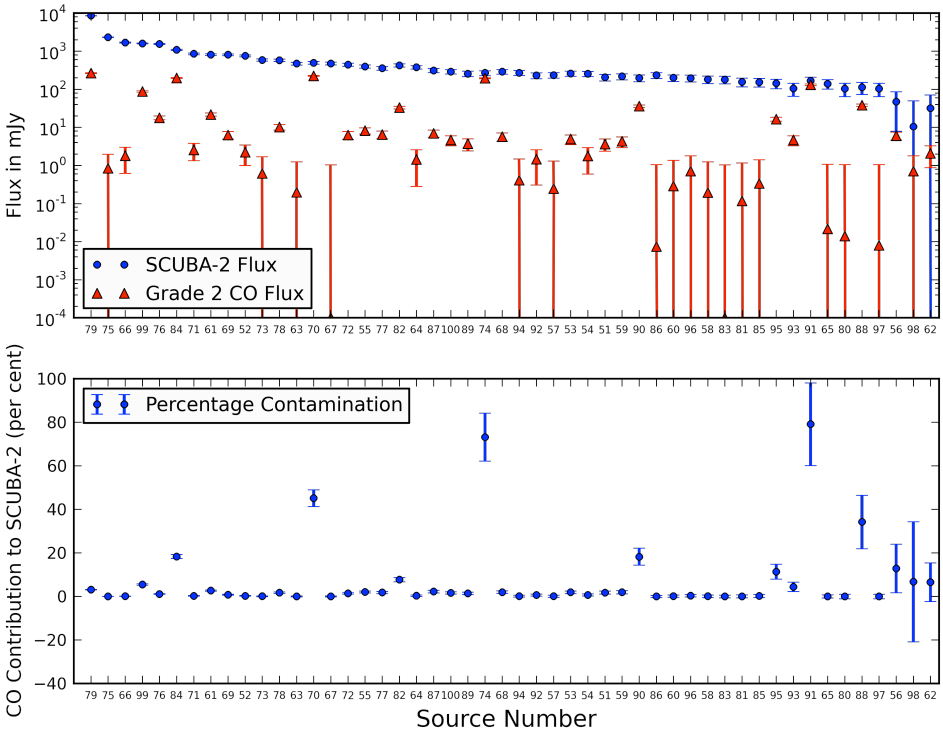

Figure 2.6: *Top:* The SCUBA-2 source fluxes calculated from the 850 μm continuum and ^{12}CO $J = 3 \rightarrow 2$ contamination maps (Grade 2 weather) of NGC 2071. Note source 67 has a ^{12}CO flux contribution of 0 mJy beam^{-1}. *Bottom:* The percentage contribution to the SCUBA-2 fluxes from the ^{12}CO contamination maps. Numbers are given arbitrarily to the sources and were based on the original list of cores from Nutter and Ward-Thompson [2007].

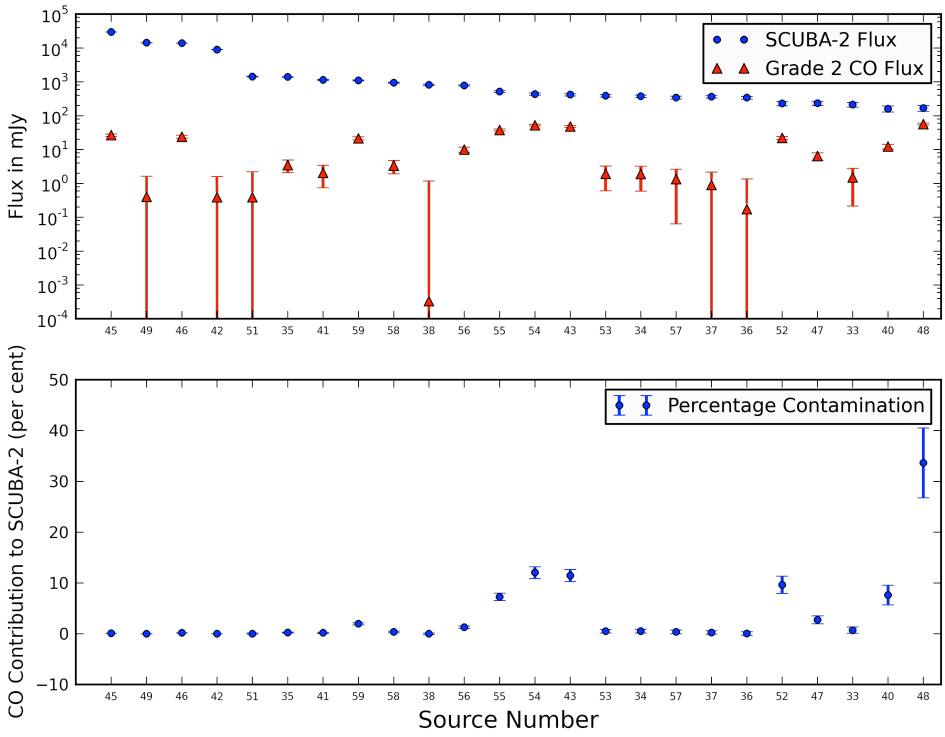

Figure 2.7: *Top:* The SCUBA-2 source fluxes calculated from the 850 μm continuum and ^{12}CO $J = 3 \rightarrow 2$ contamination maps (Grade 2 weather) of NGC 2024. *Bottom:* The percentage contribution to the SCUBA-2 fluxes from the ^{12}CO contamination maps. Numbers are given arbitrarily to the sources and were based on the original list of cores from Nutter and Ward-Thompson [2007].

2.4.1.3 Application to NGC 2024

NGC 2024 is another emission nebula in the Orion B molecular cloud. Sources were chosen from a list of young stellar objects in NGC 2024 that had been previously observed using SCUBA [Nutter and Ward-Thompson, 2007] with a total of 24 sources in the area covered by the SCUBA-2 map. As stated in Section 2.4.1.2, a FCF of 685 Jy beam^{-1} pW^{-1} was used to correspond with current studies of Orion B (FCF value valid for October 2010 reduction, equivalent to Nutter et al, *in prep.*). For further information on HARP observations of NGC 2024, see Buckle et al. [2010].

Figure 2.7 shows the source fluxes from the SCUBA-2 850 μm and ^{12}CO $J = 3 \rightarrow 2$ Grade 2 contamination maps and the percentage contribution of ^{12}CO $J = 3 \rightarrow 2$ flux to SCUBA-2 850 μm flux. I note that the majority of sources have ^{12}CO

contributions of less than 20%. One source (source 48) has a ^{12}CO contribution more than 20% (34% contamination), further discussed in Section 2.4.3.

2.4.1.4 GSM analysis

For SCUBA-2, GSM filters were created by applying upper thresholds to the original SCUBA-2 maps which acted as a mask for source emission and convolving the thresholded maps with a Gaussian a few arcminutes in FWHM size (similar to Kirk et al. 2006; Reid and Wilson 2005); this is a standard technique for the SCUBA-2 data. Negative regions of flux, known as negative 'bowls,' surround very strong sources in the SCUBA-2 maps and are produced in the map reconstruction process (see Johnstone et al. 2000). SCUBA-2 thresholding was necessary to prevent introducing new negative bowls in the image caused by smoothing and subtracting bright continuum sources. Without thresholding, artificial negative bowling would have been further added to the map, causing negative flux to lower source fluxes and increase the calculated ^{12}CO 3-2 contamination. To test the effects of changing the filter size, S2SRO maps were analysed with an upper threshold of 15 mJy beam^{-1} for NGC 1333 and 30 mJy beam^{-1}for NGC 2071 and NGC 2024 (used to mask out bright sources) and 1′ to 3′ FWHM Gaussian smoothing. Aperture fluxes from each of the GSM maps (1′, 2′, and 3′) and the original, unsmoothed S2SRO maps were found to agree within uncertainties, indicating that the emission on scales which would have been affected by the GSM filter had been filtered out by the SCUBA-2 map reconstruction. The 1′ and 2′ GSM filters were further analysed with application to the HARP ^{12}CO maps based on the similarity between S2SRO and SCUBA maps, for which scales greater than 2′ are known to be poorly reproduced [Hatchell et al., 2007b].

For the HARP ^{12}CO maps, thresholding was not required because ^{12}CO mainly traces molecular outflows which have bright, extended structures on scales not fully reproduced by SCUBA-2. To generate the ^{12}CO GSM maps, GSM filters with 1′ and 2′ FWHM Gaussians were directly applied and subtracted from the original maps. Negative flux regions in the final HARP maps resulting from the oversubtraction of background flux estimated by the GSM filter was set to 0 mJy beam^{-1} to prevent biasing the source fluxes in the aperture photometry process. The S2SRO 1′ and

2′ GSM maps were subtracted from the corresponding ^{12}CO GSM maps (Grade 2 contamination) to analyse the GSM filter effectiveness in matching the spatial filtering of the SCUBA-2 maps. Positive flux in the residuals indicates higher ^{12}CO flux than 850 μm dust continuum flux, suggesting that the GSM filter size should be scaled down to subtract smaller scale emission. In each of the regions, the 2′ GSM residuals were found to overestimate the ^{12}CO flux contribution to the dust continuum. On average, the 2′ GSM map residuals were 1.4 to 1.5 times greater than the 1′ GSM. The 1′ GSM filters were applied to both the S2SRO and HARP maps for consistency in eliminating flux on scales of 1′ and above.

With the full complement of subarrays, SCUBA-2 is likely to recover more large-scale structure and continuum fluxes may increase further. A comparison of ^{12}CO contamination on scales of 1′ or greater will have to wait for full SCUBA-2 operations.

2.4.2 Mass calculations

The calculation of the dust continuum flux from pre- and protostellar sources in a molecular cloud can be used to obtain source masses [Hildebrand, 1983a]. Depending on the molecular cloud environment surrounding the sources, contamination from the ^{12}CO line emission may affect low- and high-mass sources, leading to a varying level of source contamination. Therefore, the masses of sources were calculated using the relation between the dust and gas mass and the total source dust continuum flux (e.g. Enoch et al. 2006; Seaquist et al. 2004),

$$M = \frac{S_{850} D^2}{\kappa_{850} B_{850}(T_{\rm d})}, \tag{2.13}$$

where S_{850} is the flux from 15″ radius aperture photometry at 850 μm, D is the distance to the source, κ_{850} is the dust opacity at 850 μm and $B_{850}(T_{\rm d})$ is the Planck function at 850 μm for the dust temperature $T_{\rm d}$.

2.4.2.1 Mass calculations for NGC 1333

For NGC1333, a distance of 250 pc was assumed for the mass calculations. Hatchell et al. [2007b] used a distance of 320 pc, which would increase masses by a factor of

1.6. A temperature of 10 K was used as an estimate of the dust temperature, where dense regions that do not have internal heating are colder on the inside and warmer on the outside [Evans et al., 2001]. Cores with internal heating are warmer in the inner regions. For example, Class 0 and Class I protostars are found from models to have $\sim T_{\rm d} = 15$ K [Shirley et al., 2002; Young et al., 2003], but most of the dust mass is found in areas of lower temperatures. To cover pre- and protostellar sources, $T_{\rm d} = 10$ K is a commonly used average. It should be noted that this value can overestimate the masses of protostellar sources by a factor of 2 to 3 if the temperature is warmer [Enoch et al., 2006].

The dust opacity κ_{850} is also uncertain for individual regions. Hatchell et al. [2007b] assumed a dust opacity of 0.012 cm^{2}g^{-1} for the 850 μm SCUBA dust emission maps of NGC 1333 based on a gas/dust ratio of 161 (see Ossenkopf and Henning 1994). This dust opacity is at the low end of the assumed values and a dust opacity of 0.02 cm^{2}g^{-1} at 850 μm could have been used [Kirk et al., 2006]. Here, I choose a dust opacity of 0.012 cm^{2}g^{-1}. If 0.02 cm^{2}g^{-1} was used, then our masses would decrease by a factor of 1.7.

Masses were calculated from source fluxes obtained from continuum emission with and without ^{12}CO contamination taken into account. The bottom portion of Figure 2.8 shows the ratio between these masses. Due to the CO flux contamination, the calculated source masses are being overestimated by up to a factor of 1.2.

2.4.2.2 Mass calculations for NGC 2071 and NGC 2024

For NGC 2071 and NGC 2024, parameters from past mass estimates [Nutter and Ward-Thompson, 2007] were used to calculate source masses. A distance of 400 pc was assumed for both regions [Brown et al., 1994] and a temperature of 20 K was assumed as an estimate of the dust temperature [Johnstone and Bally, 2006; Launhardt et al., 1996; Mitchell et al., 2001]. An 850 μm dust opacity of 0.01 cm^2 g^{-1} was used [Andre et al., 1996; André et al., 2003; Ward-Thompson et al., 1999], similar to the dust opacity used for NGC 1333. As in NGC 1333, the assumption of a single temperature for each source does introduce a potential bias in the masses. If 10 K was assumed, as for NGC 1333, then masses for NGC 2071 and NGC 2024 sources would be larger by a factor of 2.

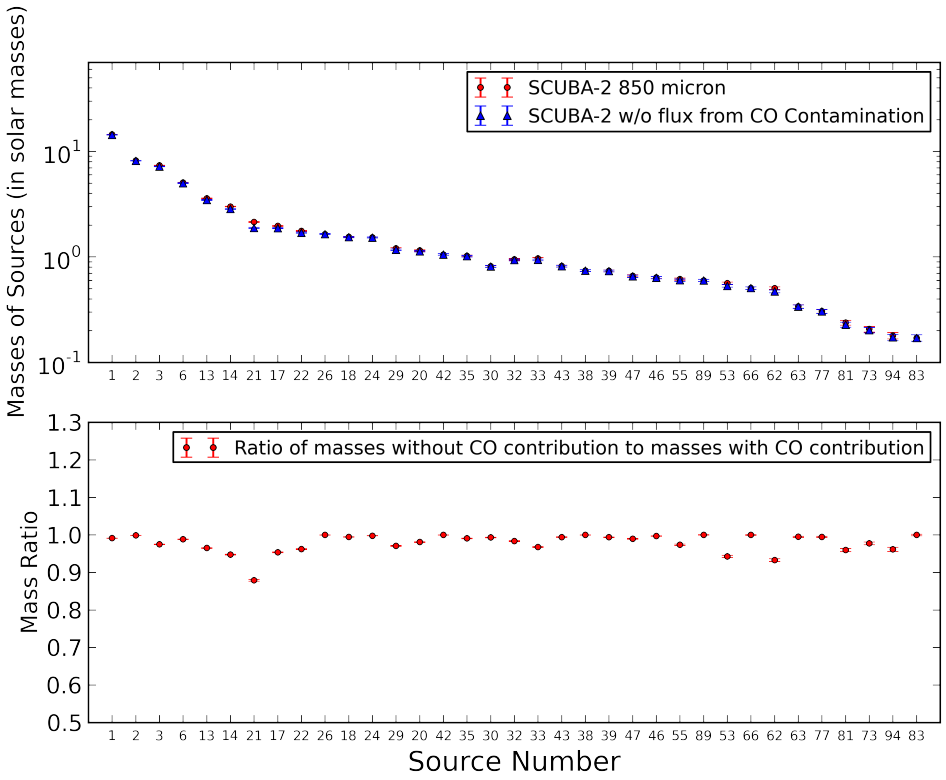

Figure 2.8: *Top:* Mass calculations (in solar masses) of the different sources in NGC 1333. The masses were calculated using the SCUBA-2 850 μm map and then recalculated excluding the flux contribution from ^{12}CO in different atmospheric conditions. *Bottom:* Ratio of the masses calculated from the flux without to with the ^{12}CO contribution. In both plots, uncertainties are calculated only from the source fluxes and do not include absolute calibration uncertainties.

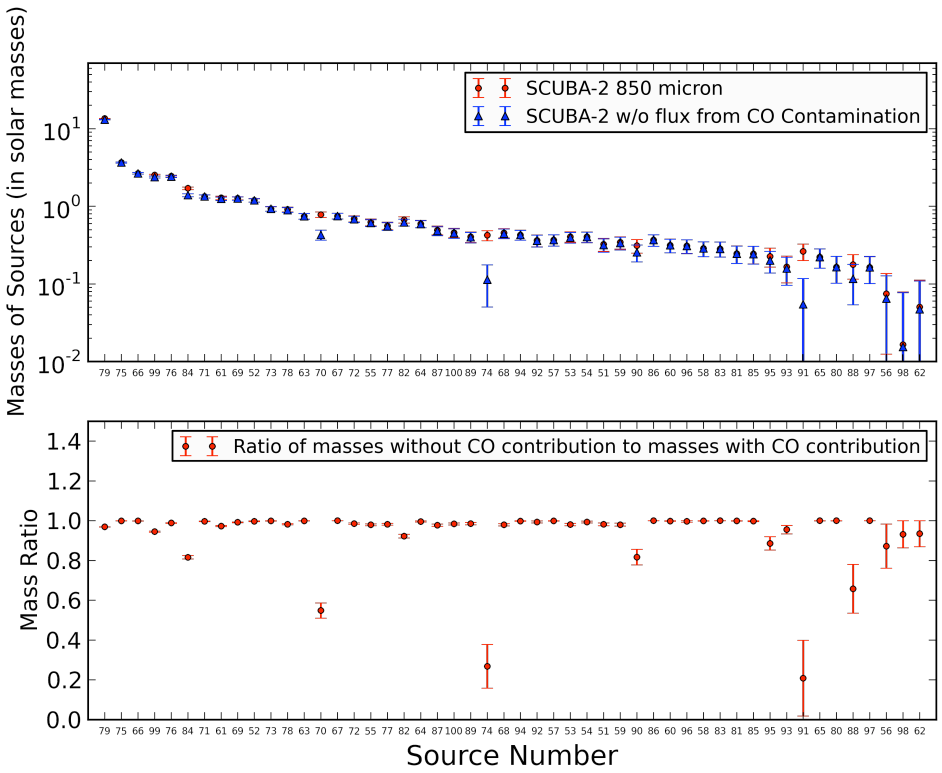

Figure 2.9: *Top:* Mass calculations (in solar masses) of the different sources in NGC 2071. The masses were calculated using the SCUBA-2 850 μm map and then recalculated excluding the flux contribution from ^{12}CO in different atmospheric conditions. *Bottom:* Ratio of the masses calculated from the flux without to with the ^{12}CO contribution. In both plots, uncertainties are calculated only from the source fluxes and do not include absolute calibration uncertainties.

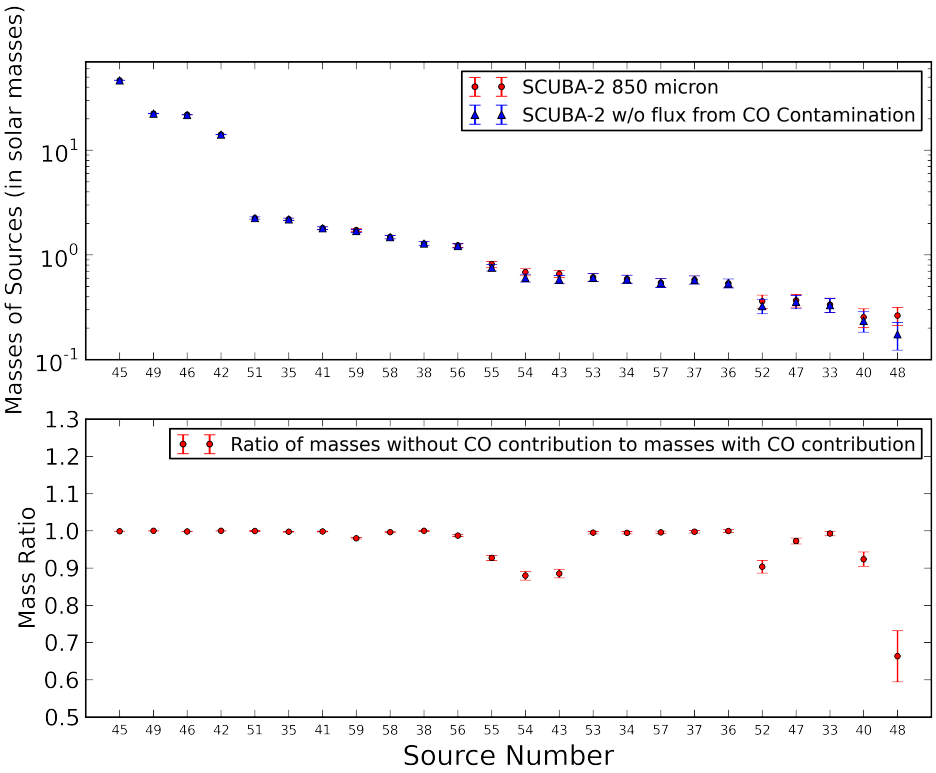

Figure 2.10: *Top:* Mass calculations (in solar masses) of the different sources in NGC 2024. The masses were calculated using the SCUBA-2 850 μm map and then recalculated excluding the flux contribution from ^{12}CO in different atmospheric conditions. *Bottom:* Ratio of the masses calculated from the flux without to with the ^{12}CO contribution. In both plots, uncertainties are calculated only from the source fluxes and do not include absolute calibration uncertainties.

Masses were calculated from the source fluxes of the 850 μm continuum emission (see Section 2.4) with and without ^{12}CO $J = 3 \rightarrow 2$ contribution taken into account. The bottom portion of Figures 2.9 and 2.10 show the ratio between these masses for NGC 2071 and NGC 2024 respectively. Due to the CO flux contamination, the calculated source masses are being overestimated by a factor up to 4.8 for NGC 2071 and 1.5 for NGC 2024.

2.4.3 Molecular outflow analysis

The location of protostellar sources can help identify the potential causes of ^{12}CO contamination. The presence of protostellar molecular outflows and hot ambient gas from nearby stars results in bright ^{12}CO emission, making regions with these characteristics rife with contamination.

Sources with high ^{12}CO contamination were examined in further detail using the HARP data cubes. In each of the three regions, sources with greater than 20% contamination were defined as 'sources with high contamination.' For NGC 1333, there were no sources with greater than 20% contamination, excluding it from this portion of the high contamination study. In NGC 2071, four sources fulfilled the high contamination criterion and one source in NGC 2024 fulfilled the criterion. In order to identify the cause of high contamination, the ^{12}CO spectra were extracted and analysed for molecular outflows.

For NGC 2071 and NGC 2024, the linewing criterion used to identify a molecular outflow candidate was a linewing above 1.5 K (T_A^*) at $\pm$ 4 km s^{-1} from the core velocity, $v_{\rm LSR}$. This linewing criterion method follows the method in Hatchell et al. [2007a]. A core velocity of 10 km s^{-1} was used for all of the sources in NGC 2024 and NGC 2071 based on C^{18}O $J = 3 \rightarrow 2$ data [Buckle et al., 2010]. Linewing criteria were based on T_A^* RMS values for the regions (5σ).

The linewing criterion identifies not only protostars driving molecular outflows, but also sources which are contaminated by outflows along the line of sight. Outflow candidates were identified using the above criteria and examined further to determine if the source or another protostar was the outflow driving source. Sources with high contamination that were not outflow candidates were further analysed to determine if there were other causes behind the ^{12}CO contamination, such as a nearby

star heating the gas.

Highly contaminated sources are listed in Table 2.2. Table 2.2 includes the region, source number, RA and Dec, flux calculated from aperture photometry in mJy, ^{12}CO flux contamination in Grade 2 weather in mJy, percentage contamination from ^{12}CO, core velocity $v_{\rm LSR}$ in km s^{-1}, and the final molecular outflow candidate result. The outflow naming convention follows Hatchell and Dunham [2009], where a 'y' is given when an outflow is present and 'n' is given when an outflow is not present. Sources are marked '?' when there is confusion as to the source of the outflow. In this case, the potential source causing the outflow detection is listed in a footnote.

2.4.3.1 Sources in NGC 1333

Figure 2.11 shows the 850 μm SCUBA-2 map with blue contours tracing the blueshifted ^{12}CO HARP intensity $\int T_A^*\ dv$ (integrated from -2.5 to 4.5 km s^{-1}) and red contours tracing the redshifted ^{12}CO intensity (integrated from 10.5 to 16.5 km s^{-1}). Sources in NGC 1333 are denoted by the percentage contamination, where '×' denotes sources with 0 to 10% contamination and '+' denotes sources with 10 to 20% contamination. Source 21 had the highest percentage contamination at 12%. According to the linewing criteria used to identify a molecular outflow candidate (linewing above 1.5 K for T_A^* at ± 3 km s^{-1} from the core velocity 7.9 km s^{-1}, following the criterion for NGC 1333 used in Hatchell et al. 2007a), source 21 is a molecular outflow candidate that could potentially be the result of a source at (J2000) 03:29:03.2, 31:15:59.0 (SVS13) or source at (J2000) 03:29:08.8, 31:15:18.1 (SK-16) [Hatchell and Dunham, 2009]. A ^{12}CO spectrum for this source is included in Figure 2.14.

2.4.3.2 Sources in NGC 2071

Figure 2.12 shows 850 μm SCUBA-2 map with blue contours tracing the blueshifted ^{12}CO HARP intensity $\int T_A^*\ dv$ (integrated from -2.0 to 6.0 km s^{-1}) and red contours tracing the redshifted ^{12}CO intensity (integrated from 14.0 to 22.0 km s^{-1}). Sources in NGC 2071 are denoted by the percentage contamination, where '×' denotes sources with 0 to 10% contamination, '+' denotes sources with 10 to 20%

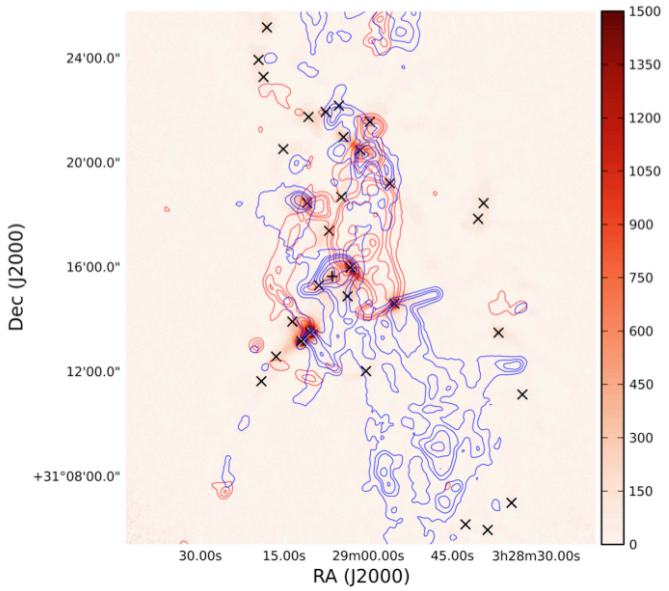

Figure 2.11: SCUBA-2 850 μm map of NGC 1333. The colour bar represents flux in mJy beam^{-1}. Blue contours correspond to blueshifted ^{12}CO $J = 3 \rightarrow 2$ HARP intensity $\int T_A^* \, dv$ (integrated from -2.5 to 4.5 km s^{-1}). Red contours correspond to redshifted intensity (integrated from 10.5 to 16.5 km s^{-1}). Contour levels are 5, 10, 15, 25, 45, 65, and 85 K km s^{-1}. Sources in NGC 1333 are denoted by percentage contamination, where '×' denotes sources with 0 to 10% contamination and '+' denotes sources with 10 to 20% contamination.

Region	Source	RA (J2000)	Dec (J2000)	Flux[a] mJy	^{12}CO (Grade 2) mJy	Percentage Cont. (Grade 2)	$v_{\rm LSR}$ km s^{-1}	Outflow?
NGC2071	70	05:46:57.6	00:20:09	495 ± 40	224 ± 6	46 ± 5	10.0	y
	74	05:47:01.0	00:20:42	268 ± 40	196 ± 6	73 ± 13	10.0	y
	88	05:47:06.7	00:23:14	112 ± 39	38 ± 3	34 ± 14	10.0	y? [b]
	91	05:47:08.9	00:23:56	166 ± 40	132 ± 5	79 ± 22	10.0	y?[b]
NGC2024	48	05:41:19.9	-01:54:16	168 ± 33	56 ± 3	34 ± 9	10.0	y

Table 2.2: List of sources categorised with high ^{12}CO contamination to the 850 μm dust continuum.

[a]SCUBA-2 fluxes appear to be lower than seen by SCUBA due to the subtraction of large-scale flux by SCUBA-2.

[b]Could be due to a large, central blue outflow from source at (J2000) 05:47:06.9, 00:22:39 (source 84; LBS-MM19) or a source at (J2000) 05:47:04.1, 00:21:58 (LBS-MM18; NGC2071-IRS), where LBS-MM18 was found to be responsible for driving the outflow in Motte et al. [2001] and both sources are confirmed Class 1 protostars detected using IRAC [Nutter and Ward-Thompson, 2007].

contamination, and 'O' denotes sources with greater than 20% contamination. According to the linewing criteria used, all four sources with high contamination are molecular outflow candidates. Even though sources 70 and 74 have clear blue- and redshifted spectral linewings, all four sources appear to trace a large central outflow that could be driven by a source at (J2000) 05:47:06.9, 00:22:39 (source 84; LBS-MM19) or a source at (J2000) 05:47:04.1, 00:21:58 (source 79; LBS-MM18; NGC2071-IRS), where LBS-MM18 was found to be responsible for driving the outflow in Motte et al. [2001] and both sources are confirmed Class 1 protostars detected using IRAC [Nutter and Ward-Thompson, 2007]. Note that sources 84 (LBS-MM19) and 90, both with 18% contamination, also correlate with the central outflow. The ^{12}CO spectra for these sources are displayed in Figure 2.14.

2.4.3.3 Sources in NGC 2024

Figure 2.13 shows 850 μm SCUBA-2 map with blue contours tracing the blueshifted ^{12}CO HARP intensity $\int T_A^* \, dv$ (integrated from -2.0 to 6.0 km s^{-1}) and red contours tracing the redshifted ^{12}CO intensity (integrated from 14.0 to 22.0 km s^{-1}). Sources in NGC 2024 are denoted by the percentage contamination, where '×' denotes sources with 0 to 10% contamination, '+' denotes sources with 10 to 20% contamination, and 'O' denotes sources with greater than 20% contamination. According to the linewing criteria used, the single source with a high contamination is a molecular outflow candidate. The ^{12}CO spectrum for this source is listed in Figure 2.14.

2.5 Discussion

Typical ^{12}CO contamination levels in the observed SCUBA-2 850 μm emission from NGC 1333, NGC 2071, and NGC 2024 are under 20% (this includes 95% of sources, and 88% of all sources have under 10% contamination). Similar results were found for SCUBA, where Johnstone et al. [2003] suggested that ^{12}CO line contamination is typically under 10% for submillimetre sources in Orion and Davis et al. [2000] suggested contamination was ∼10% near the source V380 Orion NE.

In locations where molecular outflows are present, ^{12}CO contamination can rise

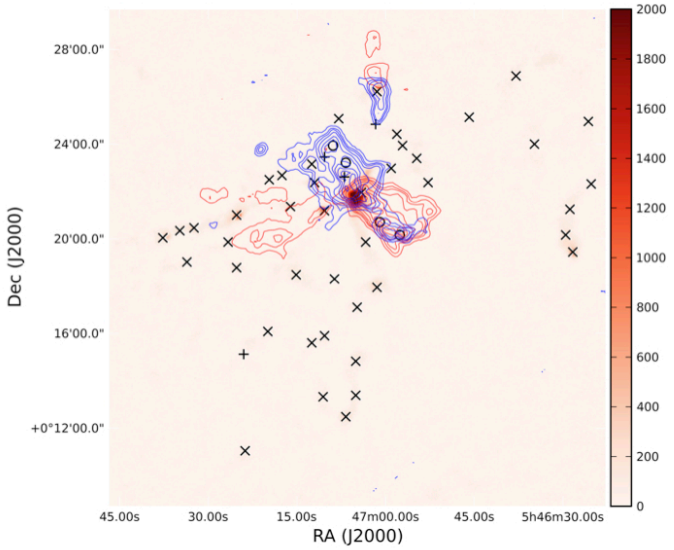

Figure 2.12: SCUBA-2 850 μm map of NGC 2071. The colour bar represents flux in mJy beam^{-1}. Blue contours correspond to blueshifted ^{12}CO $J = 3 \rightarrow 2$ HARP intensity $\int T_A^* \, dv$ (integrated from -2.0 to 6.0 km s^{-1}). Red contours correspond to redshifted intensity (integrated from 14.0 to 22.0 km s^{-1}). Contour levels are 5, 10, 15, 25, 45, 65, 85, 105, 125, and 145 K km s^{-1}. Sources in NGC 2071 are denoted by percentage contamination, where '$\times$' denotes sources with 0 to 10% contamination, '+' denotes sources with 10 to 20% contamination, and 'O' denotes sources with greater than 20% contamination.

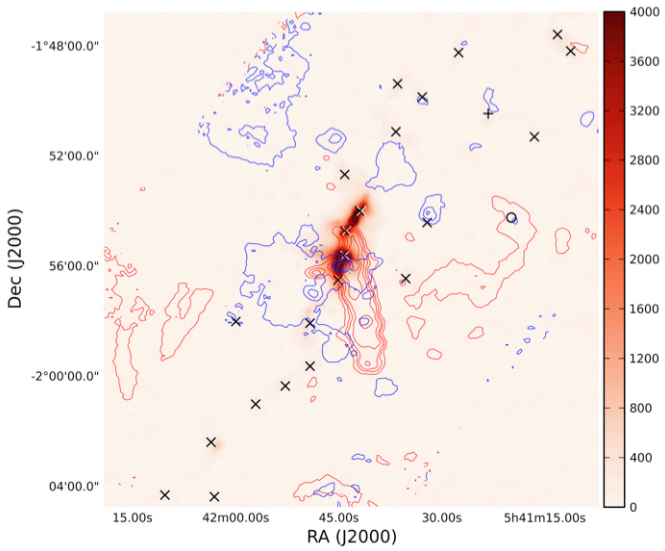

Figure 2.13: SCUBA-2 850 μm map of NGC 2024. The colour bar represents flux in mJy beam^{-1}. Blue contours correspond to blueshifted ^{12}CO $J = 3 \rightarrow 2$ HARP intensity $\int T_A^* \, dv$ (integrated from -2.0 to 6.0 km s^{-1}). Red contours correspond to redshifted intensity (integrated from 14.0 to 22.0 km s^{-1}). Contour levels are 5, 10, 15, 25, 45, 65, 85, 105, 125, and 145 K km s^{-1}. Sources in NGC 2024 are denoted by percentage contamination, where '$\times$' denotes sources with 0 to 10% contamination, '+' denotes sources with 10 to 20% contamination, and 'O' denotes sources with greater than 20% contamination.

above 20 per cent and dominate the dust continuum (up to 79 per cent contamination), corresponding to a CO contribution ranging from 16 to 68 mJy beam^{-1} for the sources analysed in this study. Peak ^{12}CO fluxes found in the molecular outflows of NGC 1333, NGC 2071, and NGC 2024 maps reach even higher fluxes of 84 mJy beam^{-1}, 154 mJy beam^{-1}, and 94 mJy beam^{-1} respectively. Our study suggests that molecular outflows can influence line contamination in sources with both low and high continuum fluxes ($\sim$ 100 to 500 mJy). This result agrees with that of Johnstone et al. [2003], where they concluded that the areas with warmer molecular gas temperatures and higher velocities (i.e. shocks and molecular outflows) were the only locations where ^{12}CO emission dominated the dust continuum flux due to the higher molecular line integrated intensities associated with such regions. In addition, Gueth et al. [2003] found a 20 per cent contamination for the well-known outflow source L1157. Hatchell and Dunham [2009] similarly found a 20 to 30 per cent ^{12}CO contamination level in the IRAS 03282+3035 outflow in Perseus.

The ^{12}CO contamination combined with contamination from other molecular lines allows outflows to potentially be seen in continuum maps with a similar appearance as protostellar cores or filamentary structure, which may be the case for SVS13 in NGC 1333 and the large, central outflows in NGC 2071 and NGC 2024 that have strong evidence of molecular outflow lobes detected in the dust continuum emission maps (see Figure 2.4). Other studies have suggested that regions involving molecular outflows can reach 50% ^{12}CO contamination, e.g. in the extended outflow lobes of V380 Orion NE [Davis et al., 2000], and even up to 100% contamination, e.g. the central blue outflow region in NGC 2071 driven by source LBS-MM18 (NGC2071-IRS; Motte et al. 2001).

The FCF uncertainty from calibrator observations for the 850 μm S2SRO maps is 18% (SMURF SCUBA-2 Data Reduction Cookbook)[1]. The calibration uncertainty of HARP observations at JCMT is estimated to be 20% by Buckle et al. [2009]. With contamination levels to SCUBA-2 850 μm less than or equal to 20% for the majority of the sources, the typical contamination is less than or equivalent to the calibration uncertainty. Problems arise when the contamination is greater than than calibration uncertainties, contributing a significant portion of flux and potentially dominating the dust continuum. For bright sources, it should be possible to use the

[1] http://star-www.rl.ac.uk/star/docs/sc19.htx/node40.html

subtracted ^{12}CO background to estimate the column density and hence the potential CO contamination to the 850 μm SCUBA-2 dust emission, as suggested by Tothill et al. [2002].

For faint sources, the insensitivity of SCUBA-2 to the large-scale dust emission introduces additional uncertainties. The spatially filtered maps created here do not appear to entirely subtract the total large-scale flux detected by HARP. Excess ^{12}CO flux seen as positive flux in residuals (Section 2.4.1.4) point to the need for a more detailed model of SCUBA-2 structure response. The large-scale reconstruction issues limit analysing contamination where the SCUBA-2 flux is faint. This analysis is something that has been considered for the full SCUBA-2 array, but not for the limited S2SRO data. See Section 2.6 for more details. If the SCUBA-2 and HARP maps were subtracted in order to account for the molecular line contamination, there is a possibility that an overcompensation for the molecular line flux would occur, creating regions of negative flux in the dust continuum map.

An additional uncertainty in the contamination due to large-scale CO emission is the inclusion of the secondary beam in the calculation of the telescope beam area in Equation 2.9, which increases the beam area by a factor of 1.2 at 850 μm (determined from a new FWHM calculated in Section 2.2.2). Large-scale emission couples to the telescope beam as the efficiency factor $\eta_{\rm fss}$ instead of $\eta_{\rm MB}$ (as in Equation 2.12). Therefore, the conversion factor for ^{12}CO $J = 3 \rightarrow 2$ would increase by a factor of 1.1, which is insignificant compared to other uncertainties. The scales of large-scale emission that could cause significant signal without being taken out by the S2SRO common-mode subtraction range from 13.8″ (the FWHM of the 850 μm beam) to 1′ (the Gaussian FWHM used in the GSM masking process). For the full SCUBA-2 array, CO emission on scales up to 8′ in size could contribute.

CO is not the only possible contributor in the 850 and 450 μm bands. Studies of other molecular lines found SCUBA 850 μm line contamination from HCN, HNC, CN and methanol add together to form roughly 40% of the total line contamination when observing other more energetic sources, like the shocked region SK1-OMC3 [Johnstone et al., 2003] . Similar contamination was found in the Kleinmann-Low nebula, from SO and SO_2 emission that was 28 to 50% of the total line contamination at 850 μm [Groesbeck et al., 1994; Serabyn and Weisstein, 1995]. Other studies have found the total line contamination by other molecular lines to be a factor of 2 to

3 times that from CO in outflows [Gueth et al., 2003; Tothill et al., 2002]. Since molecular line contamination from other molecules is also likely, some features with low flux in the dust continuum may entirely be the result of line emission.

2.5.1 ^{12}CO $J = 6 \rightarrow 5$ contamination

For the 450 μm band, there are no ^{12}CO $J = 6 \rightarrow 5$ maps with which to estimate the CO contamination directly. Using the line intensities from the ^{12}CO $J = 3 \rightarrow 2$ HARP maps, I can instead predict the potential line contamination from ^{12}CO $J = 6 \rightarrow 5$ to the SCUBA-2 450 μm dust continuum signal.

Assuming local thermodynamic equilibrium, the ratio of the main-beam brightness temperatures T_{MB} for ^{12}CO $J = 6 \rightarrow 5$ and ^{12}CO $J = 3 \rightarrow 2$ can be estimated. I assume the excitation temperature, T_{ex}, is equal to the kinetic temperature of the region, and is therefore the same for both ^{12}CO $J = 3 \rightarrow 2$ and ^{12}CO $J = 6 \rightarrow 5$. I also assume the partition function $Z \approx 2T_{ex}/T_0$ and the Gaussian line shape $\theta(\text{peak}) = 2c\sqrt{2\ln 2} \,/\, \nu\, \Delta v\sqrt{2\pi}$, yielding the relation (in CGS units):

$$\begin{aligned} T_{MB} &= \frac{8\pi^3}{3h}\mu^2(J+1)^2\frac{T_0^2}{2T_{ex}}\exp\left(\frac{-(J+1)(J+2)T_0}{2T_{ex}}\right) \\ &\times \frac{2\sqrt{2\ln 2}}{\Delta v\sqrt{2\pi}}\, N_{tot} \end{aligned} \tag{2.14}$$

where h is Planck's constant, μ is the permanent electric dipole moment of the molecule, J is the lower rotational level of a linear molecule, and T_0 is the ground-state temperature ($h\nu_0/k$) at 5.5 K. Using Equation 2.14, the ratio ^{12}CO $J = 6 \rightarrow 5/^{12}$CO $J = 3 \rightarrow 2$ is:

$$\begin{aligned} \frac{T_{MB}(6\rightarrow 5)}{T_{MB}(3\rightarrow 2)} &= \frac{(6)^2}{(3)^2}\frac{\exp\left(\frac{-21\ T_0}{T_{ex}}\right)}{\exp\left(\frac{-6\ T_0}{T_{ex}}\right)} \\ &= 4\exp\left(-15\frac{T_0}{T_{ex}}\right) \end{aligned} \tag{2.15}$$

where $J(6 \rightarrow 5) = 5$ for $T_{MB}(6 \rightarrow 5)$ and $J(3 \rightarrow 2) = 2$ for $T_{MB}(3 \rightarrow 2)$.

Assuming the source dust temperatures of 10 K, as in Section 2.4.2, are equal to the excitation temperature in the protostellar envelope, it follows from Equation 2.15 the ratio ^{12}CO $J = 6 \rightarrow 5/^{12}$CO $J = 3 \rightarrow 2$ is ∼0.001 in the optically thin case. The ratio between the two lines is low due to the low temperature of the region, indicating there is less likelihood of detecting ^{12}CO $J = 6 \rightarrow 5$ in cooler regions of the cloud. The sources analysed in NGC 1333, NGC 2071, and NGC 2024 with high ^{12}CO $J = 3 \rightarrow 2$ contamination correspond to molecular clouds at temperatures of 20 to 25 K. At 25 K, the ratio of ^{12}CO $J = 6 \rightarrow 5/^{12}$CO $J = 3 \rightarrow 2$ is 0.147 in the optically thin case. However, outflows can contain even higher temperatures, ranging from 50 to 150 K [Hatchell et al., 1999a; van Kempen et al., 2009]. At 50 K, the ratio is 0.769, indicating ^{12}CO $J = 6 \rightarrow 5$ is much more likely to be detected from outflows. If, on the other hand, both lines are optically thick, then the ratio tends to 1 as is known to be the case for ^{12}CO $J = 3 \rightarrow 2$ [Buckle et al., 2010; Curtis et al., 2010b].

Using the ratio ^{12}CO $J = 6 \rightarrow 5/^{12}$CO $J = 3 \rightarrow 2$, typical peak fluxes for ^{12}CO $J = 6 \rightarrow 5$ can be estimated: an excitation temperature of 25 K and a source with a typical ^{12}CO $J = 3 \rightarrow 2$ integrated intensity of 100 K km s^{-1} will produce a corresponding ^{12}CO $J = 6 \rightarrow 5$ flux contribution of 8 mJy beam^{-1} for Grade 2 weather in the 450 μm SCUBA-2 map. With the SCUBA-2 450 μm sensitivity for the Gould Belt Survey at an average RMS of ∼70 mJy beam^{-1} for the observed clouds in Grade 2 weather (Jane Buckle, private communication in July 2013), the ^{12}CO $J = 6 \rightarrow 5$ flux contribution would not be detected. Even in the case of optically thick emission where the ratio ^{12}CO $J = 6 \rightarrow 5/^{12}$CO $J = 3 \rightarrow 2$ is 1, the ^{12}CO $J = 6 \rightarrow 5$ is estimated to be 57 mJy beam^{-1}, which is under the noise level.

Using published observations, ^{12}CO $J = 6 \rightarrow 5$ contamination can be studied in further detail. ^{12}CO $J = 6 \rightarrow 5$ data were taken for IRAS 2A, 4A, and 4B in NGC 1333 by Yıldız et al. [2010]. These sources are particularly bright and possibly intermediate-mass protostars. ^{12}CO $J = 6 \rightarrow 5$ integrated intensities at the positions of the protostars were 57 K km s^{-1}, 122 K km s^{-1}, and 43 K km s^{-1} respectively. Using the ^{12}CO $J = 6 \rightarrow 5$ conversion factors calculated in this study for Grade 2 weather, the corresponding CO contamination to the SCUBA-2 450 μm dust continuum would be 32 mJy beam^{-1} (IRAS 2A), 70 mJy beam^{-1} (IRAS 4A), and 25 mJy beam^{-1} (IRAS 4B) for the CO contam-

ination to the SCUBA-2 450 μm dust continuum. Peak fluxes from SCUBA were 2355 mJy beam^{-1}, 7000 mJy beam^{-1}, and 3025 mJy beam^{-1} respectively [Hatchell et al., 2005]. The SCUBA-2 450 μm dust emission peaks are a factor of several hundred times larger than the ^{12}CO $J = 6 \rightarrow 5$ contribution. For these bright protostars, the CO contamination is insignificant at 450 μm.

Dust continuum fluxes in the 450 μm SCUBA-2 band are estimated to be a factor of 6 to 12 higher than fluxes in the 850 μm band. In the Rayleigh-Jeans approximation, the dust optical depth increases as $\lambda^{-\beta}$ with β between 1 and 2 and the corresponding flux density increases as λ^{-3} to λ^{-4} [Wilson, 2009]. The increase in continuum flux at 450 μm clearly outweighs the expected contribution from ^{12}CO $J = 6 \rightarrow 5$. At most the ^{12}CO $J = 6 \rightarrow 5$ integrated main-beam emission is the same as the ^{12}CO $J = 3 \rightarrow 2$ emission assuming optically thick emission. This situation corresponds to a molecular line ratio of 1 and a contamination flux ratio of 0.84 (assuming Grade 2 weather). Since 450 μm continuum fluxes increase with respect to the 850 μm continuum, 450 μm continuum measurements would more likely be contaminated by strong molecular outflows instead of other means, i.e. nearby stars or ambient cloud emission. Nonetheless, potential contamination could occur in particularly low flux sources with nearby molecular outflows, such as the sources in NGC 2071 that were near to confirmed outflow candidates (see Section 2.4.3).

In the case of large-scale ^{12}CO $J = 6 \rightarrow 5$ emission, it is also necessary to include the secondary beam in the calculation of the 450 μm telescope beam (Equation 2.9). The total beam area for 450 μm increases by a factor of 2.0 (determined from an effective FWHM calculated in Section 2.2.2). Using Equation 2.12 with the the efficiency factor $\eta_{\rm fss}$, the ^{12}CO $J = 6 \rightarrow 5$ conversion factor would increase by a factor of 1.7. The increase in the expected 450 μm dust continuum flux still exceeds any change in the ^{12}CO line conversion factors. Therefore, my conclusion that there is little CO contamination in the 450 μm maps, as discussed above, still holds.

2.6 Improvements and other work

Some improvements have been made to beam size estimates [Dempsey et al., 2013] and the CO contamination spatial filtering since the publication of Drabek et al.

Weather Grade	$C_{\rm old}$ (13.8″ FWHM)	$C'_{\rm prim}$ (13″ FWHM)	$C'_{\rm sec}$ (14.6″ FWHM)
1	0.63	0.56	0.71
2	0.68	0.60	0.76
3	0.70	0.62	0.78
4	0.74	0.66	0.83
5	0.77	0.68	0.86

Table 2.3: Line contribution factors for the old primary FWHM 13.8″ from Section 2.2.1 and new FWHM values from Dempsey et al. [2013] for the ^{12}CO $J = 3 \rightarrow 2$ line in the SCUBA-2 850 μm continuum band. $C'_{\rm prim}$ is the line contribution factor calculated using the new primary beam FWHM only. $C'_{\rm sec}$ is the line contribution factor calculated using the new effective beam FWHM (i.e. the primary and the secondary beam).

[2012]. Corrections to the spatial filtering are incorporated in Hatchell et al. [2013] and Sadavoy et al. [2013]. Additionally, Sadavoy et al. [2013] includes updated beam size estimates. In this section, I discuss the improvements to the CO contamination factors and applications to these recent studies.

2.6.1 Beam measurements

Beam sizes from Section 2.2.1 were initially measured in January 2012 (Per Friberg, private communication). These beam measurements were finalised in Dempsey et al. [2013], who found a 13.0″ (relative amplitude 0.98) primary beam for the 850 μm maps with a secondary beam 48″ (relative amplitude 0.02), yielding an effective FWHM 14.6″. The old primary beam used in the initial calculation of the line conversion factor was a FWHM 13.8″. The old effective beam size from Section 2.2.2 had a FWHM 15.3″. These new beam sizes alter the conversion factors according to Equation 2.11. New conversion factors using the primary beam FWHM only and the effective beam FWHM are shown in Table 2.3. Using the new FWHM beam sizes, conversion factors decrease by a factor of 1.06 using the primary beam only and increase by a factor of 1.06 using the new effective beam sizes (i.e. the combined primary and secondary beams) from the listed conversion factors in Section 2.2.1.

Using the primary beam, the new conversion factors do not significantly change the results from Section 2.5. For example, the four sources in NGC 2071 with the

highest amounts of line contamination continue to have contamination values greater than 20%: source 70 (40%), source 74 (65%), source 88 (30%), and source 91 (70%). Additionally, source 48 in NGC 2024 has a contamination of 30%. The results still indicate that high contamination regions correspond primarily to regions with molecular outflows.

Similarly, the larger effective beam FWHM does cause conversion factors to increase but these also do not significantly change the results in Section 2.5. For example, the two sources in NGC 2071 (84 and 90) with 'moderate' line contamination (corresponding to ∼18%) will have 20% contamination using the increased effective beam sizes. Since these sources are located in the blueshifted outflow lobe of the central NGC 2071 outflow driven by LBS-MM18 (Motte et al. 2001; further discussed in Section 2.4.3.2), the results still suggest the high contamination regions correspond to regions with molecular outflows.

2.6.2 Related work

Subsequent publications have built upon and incorporated my work from Drabek et al. [2012]. My direct contribution to Hatchell et al. [2013] involves supplying the $^{12}CO\ J = 3 \rightarrow 2$ *'contamination' maps to be subtracted from the 850* μm *SCUBA-2 data. In Sadavoy et al. [2013], I supplied new line conversion factors to account for the different beam FWHM used and the* $^{12}CO\ J = 3 \rightarrow 2$ *'contamination' maps.*

The filtering process used to match the HARP CO contamination maps to the SCUBA-2 continuum maps (discussed in Section 2.4.1.4) is improved by the use of the the data reduction package `SMURF` (Jenness et al. 2011, version from 2012 May 2) in Hatchell et al. [2013] for NGC 1333. The S2SRO data was re-reduced in 2012 June for NGC 1333. Using this method, the CO contamination map was converted from mJy beam^{-1} to pW using a negative multiplying factor -1/FCF during the reduction process of the 850 μm map (where FCF has units mJy beam^{-1} pW^{-1}). The contamination was then input as a fake source which is subtracted from the 850 μm times series fluxes. This eliminates the potential issue with spatial filtering and matching the structure from the CO contamination map and continuum maps. The result is a 850 μm continuum map without the inclusion of the CO contamination. This process is also used by Sadavoy et al. [2013] in the reduction of the Science

Verification data (S2SV) observation of B1 from 2011 October.

As discussed in the above section, Hatchell et al. [2013] used the 450 and line contamination subtracted 850 μm continuum maps to trace dust temperatures in the NGC 1333 using the new CO subtraction technique. The same Grade 2 conversion factors are used (Section 2.2.1; 0.66 mJy beam^{-1} per K km s^{-1}) on the HARP data as described in Section 2.4.1.1. The dust temperatures were calculated from the ratio of 450 and 850 μm dust continuum flux (where line contamination was first subtracted from the 850 μm emission). An increased 850 μm flux from line contamination will result in smaller dust temperatures (or lower dust emissivity β). In NGC 1333, molecular line contamination for analysed sources was found to be primarily under 12% from Section 2.4.1.1 (this is lowered to 10% when the smaller primary beams are used from Section 2.6.1). Estimating the systematic uncertainty in the ratio maps from calibration to be $\sim$15%, the molecular line contamination is within the uncertainties for the calculation of dust temperature in the region. However, it was necessary to remove line contamination primarily due to outflows that could appear to be starless cores or filaments in the map (as evidenced in Figure 2.4 for source SVS13 driving an outflow in NGC 1333 with corresponding line contamination).

The new beam sizes, contamination factors and CO contamination subtraction process are incorporated in Sadavoy et al. [2013] for the B1 region of Perseus. The B1 data was taken as a part of the Science Verification (S2SV). Unlike S2SRO, the S2SV data has all eight science grade arrays (four arrays for 450 and 850 μm). This study focuses on constraining the dust emissivity β by fitting SEDs using *Herschel* PACS+SPIRE (70, 160, 250, 350 and 500 μm) and SCUBA-2 (450 and 850 μm). *Herschel* is widely free of molecular line contamination with the possible exception of ^{12}CO $J = 7 \rightarrow 6$ (806.652 GHz) contaminating the 350 μm dust continuum. However, this line contamination is ruled out for similar reasons as ^{12}CO $J = 6 \rightarrow 5$ in Section 2.5.1. To constrain β with the inclusion of 850 μm emission, it is therefore important to correct for the ^{12}CO $J = 3 \rightarrow 2$ line contamination in the continuum. Sadavoy et al. [2013] applied the Grade 1 CO conversion factors to HARP maps of B1 using an effective beam size 14.2″ (C = 0.67 mJy beam^{-1}). This beam size is similar to the effective beam size in Table 2.3. Dempsey et al. [2013] gives two possible effective FWHM beams, 14.1″ and 14.6″. The lower FWHM is determined

by fitting a linear relation between peak FCF and integrated FCF values at each wavelength and the higher FWHM is determined using the two-component model.

The results from the Sadavoy et al. [2013] study on the B1 region indicate there is significant ^{12}CO molecular line contamination in the 850 μm SCUBA-2 data. The contamination is primarily located along the northern bipolar outflow, contributing up to 90% of the flux (see Figure 3 of Sadavoy et al. [2013] for comparison of the dust continuum with and without molecular line flux subtraction). In the central region, contamination reaches 15% and the remainder of B1 has $\leq$1%, similar to results from NGC 1333, NGC 2071 and NGC 2024 in Section 2.5. It is therefore necessary to subtract line contamination from the continuum data for accurate calculations of β.

2.7 Conclusions

In this study, the ^{12}CO line contamination factors for the 450 μm and 850 μm SCUBA-2 continuum bands were calculated under different atmospheric conditions (weather grades 1 to 5). These contamination factors were then applied to three different regions, NGC 1333, NGC 2071, and NGC 2024, in order to study the HARP ^{12}CO $J = 3 \rightarrow 2$ flux contribution to the SCUBA-2 850 μm measurements using a list of sources for each region. Sources with high ^{12}CO contamination (greater than 20%) were analysed in further detail to determine the cause of the contamination. The following can be concluded from this study:

1. For the 850 μm SCUBA-2 filter profile, the ^{12}CO $J = 3 \rightarrow 2$ contamination factors increase as the sky opacity τ_{225} increases. The contamination factors (mJy beam^{-1} per K km s^{-1}) of ^{12}CO to the 850 μm dust emission are, by weather grade, (Grade 1) 0.63; (Grade 2) 0.68; (Grade 3) 0.70; (Grade 4) 0.74; (Grade 5) 0.77.

2. For the 450 μm SCUBA-2 filter profile, the ^{12}CO $J = 6 \rightarrow 5$ contamination factors decrease as the sky opacity τ_{225} increases due to the atmosphere transmission steeply declining at higher opacity grades. The contamination factors (mJy beam^{-1} per K km s^{-1}) of ^{12}CO to the 450 μm dust emission are, by

weather grade, (Grade 1) 0.64; (Grade 2) 0.57; (Grade 3) 0.51; (Grade 4) 0.41; (Grade 5) 0.35.

3. The ^{12}CO $J = 3 \rightarrow 2$ contribution to the 850 μm SCUBA-2 dust continuum is typically under 20% for all of the regions studied. However, in regions of molecular outflows, the ^{12}CO can reach a flux contribution of $\sim$ 68 mJy beam^{-1} for the sources studied, dominating the dust continuum in sources with both high and low continuum flux densities (up to 500 mJy beam^{-1}) with a contribution up to 79% contamination. Peak ^{12}CO fluxes in molecular outflows in the regions reached even higher levels, up to 154 mJy beam^{-1}. There is strong evidence that ^{12}CO $J = 3 \rightarrow 2$ contamination, while mostly minimal, is a major potential source of confusion that can be observed directly in the 850 μm dust continuum maps resembling protostellar cores or filamentary structure (as may be the case in NGC 1333, NGC 2071, and NGC 2024).

4. Even though there are no ^{12}CO $J = 6 \rightarrow 5$ molecular line maps to study in further detail, in hot (50 K) regions, e.g. molecular outflows, the ratio of main-beam temperature $T_{\rm MB}$ for ^{12}CO $J = 6 \rightarrow 5$/^{12}CO $J = 3 \rightarrow 2$ is $\sim$0.769. However, CO contamination to the 450 μm source fluxes is not expected to be as much of an issue because of the expectation for the 450 μm dust emission to be a factor of 6 to 12 times brighter than the 850 μm fluxes.

5. From Dempsey et al. [2013], the beam FWHM has been finalised at 13$''$ primary beam and 14.6$''$ effective beam at 850 μm. Using the primary beam FWHM there is a decrease in conversion factors by 1.06 and using the effective beam FWHM there is an increase in conversion factors by 1.06. For the 850 μm SCUBA-2 filter profile using the new primary beam only, the line conversion factors become: (Grade 1) 0.56; (Grade 2) 0.60; (Grade 3) 0.62; (Grade 4) 0.66; (Grade 5) 0.68. Using the effective beam size, the line conversion factors become: (Grade 1) 0.71; (Grade 2) 0.76; (Grade 3) 0.78; (Grade 4) 0.83; (Grade 5) 0.86. These changes to the conversion factors do not significantly effect the results of this study and the most significant regions with molecular line contamination appear to correspond to molecular outflows.

6. The CO conversion factors from this study have been applied to recent work

using SCUBA-2 by Hatchell et al. [2013] for re-reduced 850 μm maps of NGC 1333 and Sadavoy et al. [2013] for 850μm maps of B1 in Perseus. Results from Sadavoy et al. [2013] show similar line contamination as NGC 1333, NGC 2071 and NGC 2024 reaching 90% in regions directly corresponding to a molecular outflow in B1. The remainder of the region has contamination under 15%, similar to regions NGC 2071 and NGC 2024.

2.8 Appendix: Source list and molecular outflow analysis

Region	Source	RA (J2000)	Dec (J2000)	Other Source ID
NGC 1333	1	03:29:10.4	31:13:30	HRF41
	2	03:29:12.0	31:13:10	HRF42
	3	03:29:03.2	31:15:59	HRF43
	6	03:28:55.3	31:14:36	HRF44
	13	03:29:01.4	31:20:29	HRF45
	14	03:29:11.0	31:18:27	HRF46
	17	03:28:59.7	31:21:34	HRF47
	18	03:29:13.6	31:13:55	HRF48
	20	03:28:36.7	31:13:30	HRF49
	21	03:29:06.5	31:15:39	HRF50
	22	03:29:08.8	31:15:18	HRF51
	24	03:29:03.7	31:14:53	HRF52
	26	03:29:04.5	31:20:59	HRF53
	29	03:29:10.7	31:21:45	HRF54
	30	03:28:40.4	31:17:51	HRF55
	32	03:29:07.7	31:21:57	HRF56
	33	03:29:18.2	31:25:11	HRF57
	35	03:29:16.5	31:12:35	HRF59
	38	03:28:39.4	31:18:27	HRF60
	39	03:29:17.3	31:27:50	HRF61

Table 2.4: continued from previous page.

Region	Source	RA (J2000)	Dec (J2000)	Other Source ID
	42	03:29:07.1	31:17:24	HRF62
	43	03:29:18.8	31:23:17	HRF63
	46	03:29:25.5	31:28:18	HRF64
	47	03:29:00.4	31:12:02	HRF65
	53	03:29:05.3	31:22:11	HRF66
	55	03:29:19.7	31:23:56	HRF67
	62	03:28:56.2	31:19:13	HRF68
	63	03:28:34.4	31:06:59	HRF69
	66	03:29:15.3	31:20:31	HRF70
	73	03:28:38.7	31:05:57	HRF71
	77	03:29:19.1	31:11:38	HRF72
	81	03:28:32.5	31:11:08	HRF74
	83	03:28:42.6	31:06:10	HRF75
	89	03:29:04.9	31:18:41	Bolo44
	94	03:28:32.7	31:04:56	Bolo26
NGC 2071	51	05:47:23.7	00:11:02	BN-547237+01102
	52	05:47:06.8	00:12:30	BN-547068+01230
	53	05:47:10.6	00:13:18	BN-547106+01318
	54	05:47:05.1	00:13:21	BN-547051+01321
	55	05:47:05.0	00:14:49	BN-547050+01449
	56	05:47:23.9	00:15:07	BN-547239+01507
	57	05:47:12.4	00:15:37	BN-547124+01537
	58	05:47:10.4	00:15:53	BN-547104+01553
	59	05:47:19.9	00:16:03	BN-547199+01603
	60	05:47:04.8	00:17:07	BN-547048+01707
	61	05:47:01.5	00:17:55	BN-547015+01755
	62	05:47:08.7	00:18:17	BN-547087+01817
	63	05:47:15.2	00:18:30	BN-547152+01830
	64	05:47:25.3	00:18:48	BN-547253+01848

Table 2.4: continued from previous page.

Region	Source	RA (J2000)	Dec (J2000)	Other Source ID
	65	05:47:33.6	00:19:02	BN-547336+01902
	66	05:46:28.3	00:19:28	BN-546283+01928
	67	05:47:03.4	00:19:50	BN-547034+01950
	68	05:47:26.7	00:19:53	BN-547267+01953
	69	05:47:37.7	00:20:01	BN-547377+02001
	70	05:46:57.6	00:20:09	BN-546576+02009
	71	05:46:29.4	00:20:10	BN-546294+02010
	72	05:47:34.9	00:20:20	BN-547349+02020
	73	05:47:32.5	00:20:26	BN-547325+02026
	74	05:47:01.0	00:20:42	BN-547010+02042
	75	05:47:25.2	00:20:59	BN-547252+02059
	76	05:47:10.3	00:21:12	BN-547103+02112
	77	05:46:28.7	00:21:14	BN-546287+02114
	78	05:47:16.0	00:21:23	BN-547160+02123
	79	05:47:04.1	00:21:58	BN-547041+02158
	80	05:46:25.3	00:22:20	BN-546253+02220
	81	05:46:52.8	00:22:23	BN-546528+02223
	82	05:47:11.9	00:22:23	BN-547119+02223
	83	05:47:19.7	00:22:31	BN-547197+02231
	84	05:47:06.9	00:22:39	BN-547069+02239
	85	05:47:17.5	00:22:40	BN-547175+02240
	86	05:46:59.1	00:22:59	BN-546591+02259
	87	05:47:12.4	00:23:11	BN-547124+02311
	88	05:47:06.7	00:23:14	BN-547067+02314
	89	05:46:54.7	00:23:24	BN-546547+02324
	90	05:47:10.4	00:23:27	BN-547104+02327
	91	05:47:08.9	00:23:56	BN-547089+02356
	92	05:46:57.2	00:23:56	BN-546572+02356
	93	05:46:34.7	00:23:59	BN-546347+02359

Table 2.4: continued from previous page.

Region	Source	RA (J2000)	Dec (J2000)	Other Source ID
	94	05:46:58.0	00:24:26	BN-546580+02426
	95	05:47:01.7	00:24:52	BN-547017+02452
	96	05:46:25.7	00:24:56	BN-546257+02456
	97	05:47:08.0	00:25:05	BN-547080+02505
	98	05:46:45.9	00:25:07	BN-546459+02507
	99	05:47:01.4	00:26:14	BN-547014+02614
	100	05:46:38.0	00:26:53	BN-546380+02653
NGC 2024	33	05 42 03.0	-02 04 23	BS-542030-20423
	34	05 42 10.3	-02 04 20	BS-542103-20420
	35	05 42 03.5	-02 02 24	BS-542035-20224
	36	05 41 57.1	-02 01 00	BS-541571-20100
	37	05 41 52.9	-02 00 21	BS-541529-20021
	38	05 41 49.3	-01 59 38	BS-541493-15938
	40	05 42 00.0	-01 58 01	BS-542000-15801
	41	05 41 49.1	-01 58 03	BS-541491-15803
	42	05 41 45.2	-01 56 31	BS-541452-15631
	43	05 41 35.4	-01 56 29	BS-541354-15629
	45	05 41 44.5	-01 55 39	BS-541445-15539
	46	05 41 44.2	-01 54 43	BS-541442-15443
	47	05 41 32.1	-01 54 26	BS-541321-15426
	48	05 41 19.9	-01 54 16	BS-541199-15416
	49	05 41 42.0	-01 53 59	BS-541420-15359
	51	05 41 44.2	-01 52 41	BS-541442-15241
	52	05 41 16.6	-01 51 19	BS-541166-15119
	53	05 41 36.7	-01 51 06	BS-541367-15106
	54	05 41 23.4	-01 50 27	BS-541234-15027
	55	05 41 32.9	-01 49 53	BS-541329-14953
	56	05 41 36.4	-01 49 24	BS-541364-14924
	57	05 41 27.6	-01 48 13	BS-541276-14813

Table 2.4: continued from previous page.

Region	Source	RA (J2000)	Dec (J2000)	Other Source ID
	58	05 41 11.3	-01 48 12	BS-541113-14812
	59	05 41 13.3	-01 47 35	BS-541133-14735

Table 2.4: List of sources used for the study of ^{12}CO contamination to the SCUBA-2 850 μm dust continuum. Source numbers correspond to the arbitrary number assigned to sources for this study. Source numbers corresponding to original studies (NGC 1333 sources obtained from Hatchell et al. 2007b and NGC 2071 and NGC 2024 sources obtained from Nutter and Ward-Thompson 2007) are listed under 'Other Source ID'.

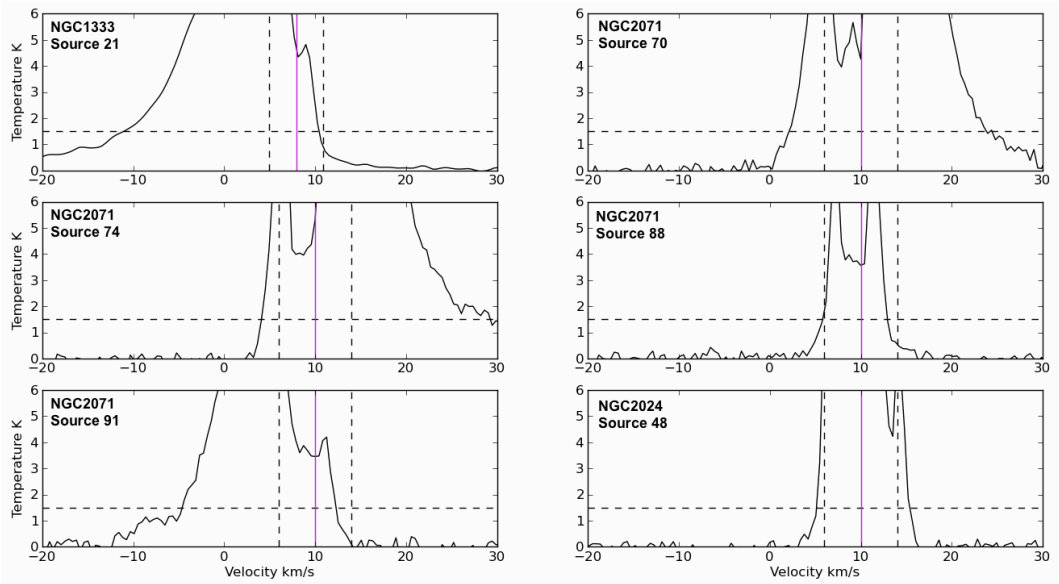

Figure 2.14: ^{12}CO $J = 3 \rightarrow 2$ spectra for sources further analysed in Section 2.4.3 regarding the molecular outflow analysis. The core velocities are listed in Section 2.4.3.1 for NGC 1333 and in Table 2.2 for NGC 2071 and NGC 2024. Parameters ± 3 km s^{-1} for NGC 1333 and ± 4 km s^{-1} for NGC 2071 and NGC 2024 at 1.5 K were used to classify the presence of outflows.

Chapter 3

Ophiuchus: molecular outflow detection

"...tenues volat illa per auras,
dumque volat, gemmae nitidos vertuntur in ignes
consistuntque loco, specie remanente coronae,
qui medius Nixique genu est Anguemque tenentis."

"...her crown flies through the unresisting breezes,
and while it flies the jewels are turned into shining fires,
yet the crown remains the same and they stop in a spot,
between Hercules on his knees and the Snake Handler, Ophiuchus."
— Ovid, Metamorphoses

As discussed in Section 1.1.5, the process of mass-loss through means of a molecular outflow appears to be an integral part of star formation. Molecular outflows are expected to have various roles and consequences in the star formation process, where the individual outflow lobes provide a record of the protostellar mass-loss history and potentially drive turbulence in the molecular cloud. Additionally, outflows may provide an explanation for problems with angular momentum. The outflow would need to carry away excess angular momentum in order for mass from the surrounding envelope to accrete onto the central protostar, indicating the possibility of a rotating jet (e.g. Bacciotti et al. 2002).

This chapter presents ^{12}CO, ^{13}CO and C^{18}O $J = 3 \rightarrow 2$ observations of the

Ophiuchus molecular cloud, which is a part of the Gould Belt Legacy Survey (GBS). Using the *Spitzer*'s c2d survey (Evans et al. 2009), I have identified 30 Class 0/I/II and flat spectrum sources that are analysed for molecular outflows. Outflow lobes are identified using the ^{12}CO $J = 3 \rightarrow 2$ data and suggestions for outflow orientations are further discussed using the 2.122 μm H_2 $v = 1 \rightarrow 0$ $S(1)$ ro-vibrational line. Understanding the locations and velocities associated with the outflow emission is fundamental for Chapter 4, where I investigate their contributions to turbulence in the Ophiuchus molecular cloud.

3.1 Ophiuchus molecular cloud

The ρ Ophiuchus molecular cloud complex is one of the closest star forming regions in the Gould Belt with a distance estimated to be 120–160 pc [Knude and Hog, 1998; Loinard et al., 2008; Lombardi et al., 2008; Mamajek, 2008; Rebull et al., 2004; Snow et al., 2008; Torres, 2010]. Recent observations by Lombardi et al. [2008] suggest the cloud is at the closer distance of $120.0^{+4.5}_{-4.2}$ pc and this distance was confirmed by Torres [2010]. From these studies, I adopt the distance of 120 pc to Ophiuchus for this thesis. The cloud has been a heavily studied region in millimetre, infrared, and optical wavelengths and provides an excellent example of intermediate mass star formation which links the study of low mass and isolated star forming regions (e.g. Taurus-Auriga) and high mass and clustered star formation (e.g. the Orion molecular cloud complex).

The Ophiuchus cloud complex is broken up into several dense clouds: L1729, L1712, L1689 (North and South), L1709, L1704, and L1688 [Lynds, 1962]. The focus of this study will be the main cloud in the complex, L1688. This cloud is split into six dense clumps: Oph A, Oph B, Oph C, Oph D, Oph E, and Oph F (shown in Figure 3.1 using 1.3 mm observations from Motte et al. 2001). Both prestellar cores and young stellar objects (YSOs) are found in the cores of L1688. The YSOs found in the region are at various evolutionary stages where the majority are more evolved T Tauri stars (Class II) and some Class 0/I protostars. This includes the well-known Class 0 source VLA 1623 [Andre et al., 1990]. On the western border of the L1688 cloud, near Oph A, lies an edge-on photodissociation region (photon dominated region - PDR) driven by the B2V star HD 147889. Large-scale dust heating is also

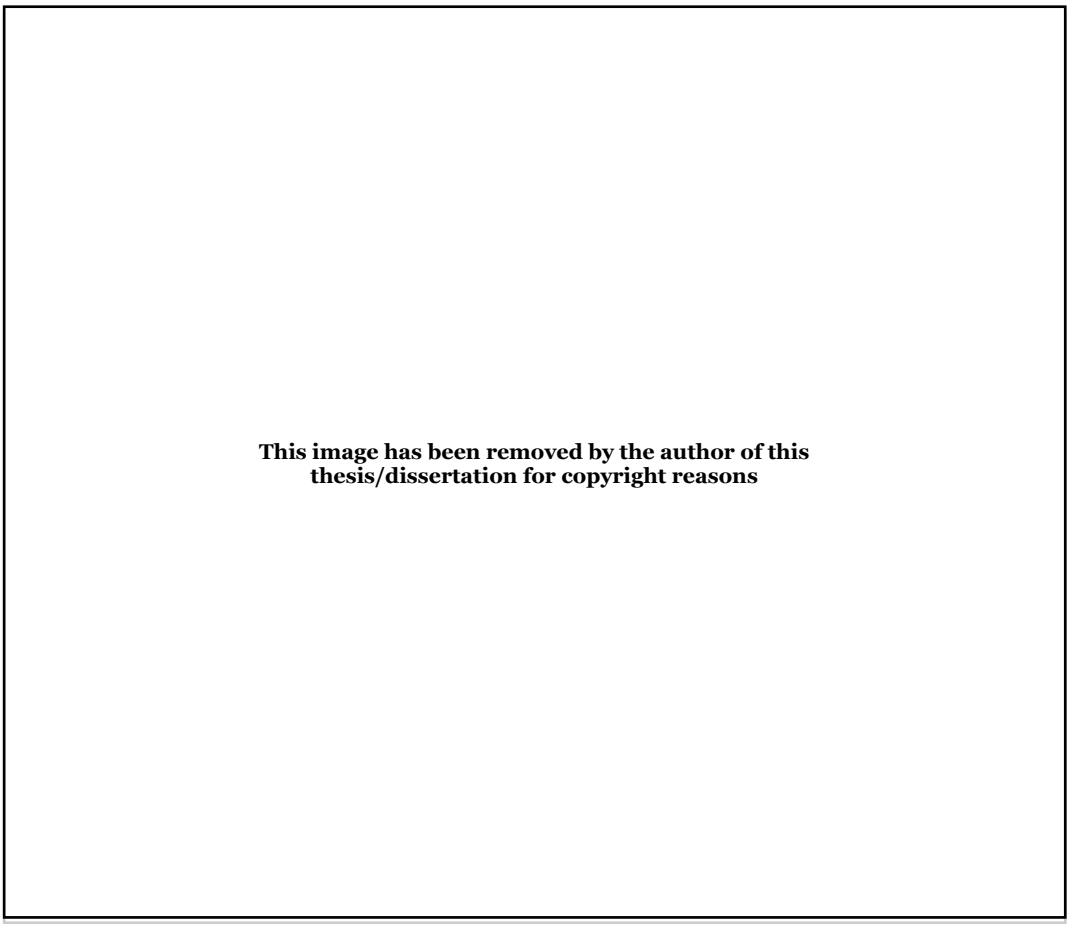

Figure 3.1: Observations of the 1.3 mm dust continuum for the L1688 Ophiuchus cloud (figure reproduced from Motte et al. 2001). Dense clumps Oph A, B, C, D, E, and F are shown. Contours range from 5 to 40 MJy str^{-1} in increments of 5 MJy str^{-1}, from 50 to 80 MJy str^{-1} in increments of 10 MJy str^{-1}, at 100 MJy str^{-1} and from 120 to 280 MJy str^{-1} in increments of 40 MJy str^{-1}.

dominated in this region of the cloud by B stars SR 3 and Oph Source 1 [Abergel et al., 1996; Casassus et al., 2008; Kulesa et al., 2005; Liseau et al., 1999].

Past studies indicate several prominent outflows, including Class 0 source VLA 1623, IRS 45/47, IRS 54, EL 29, WL 10, IRS 43, and IRS 44 [Andre et al., 1990; Bontemps et al., 1996; Jørgensen et al., 2009; Kamazaki et al., 2003; Nakamura et al., 2011; Sekimoto et al., 1997]. Additionally, recent work from van der Marel et al. [2013] provides a survey of 16 Class I sources in the region and indicates 13 of these sources drive outflows with 5 of these new outflow drivers.

3.2 Data reduction

The observations presented in this chapter primarily consist of the HARP ^{12}CO, ^{13}CO and C^{18}O $J = 3 \rightarrow 2$ maps from the Gould Belt Legacy Survey (GBS) and ancillary data of the H_2 2.122 μm $v = 1 \rightarrow 0$ $S(1)$ ro-vibrational line from the near-IR wide-field camera (WFCAM) on UK Infrared Telescope (UKIRT). In this section, I describe the data reduction process carried out for the HARP CO observations and the continuum-subtracted H_2 map.

3.2.1 CO $J = 3 \rightarrow 2$

Data reduction of the CO $J = 3 \rightarrow 2$ maps was completed by Malcolm Currie at the Joint Astronomy Centre and further cosmetic destriping algorithms were developed and implemented by Jon Gregson at Open University. In this section, I briefly describe techniques used to reduce the HARP maps of Ophiuchus. A more detailed description of reducing HARP data can be found in Section 5.1, where I describe my own reduction of HCO+ molecular line data of the Ophiuchus region.

The ^{12}CO $J = 3 \rightarrow 2$ emission maps (rest frequency of 345.796 GHz) were observed in February and March 2008 for 3.2 hours using a raster scan mode. Basket-weaving was used to even out noise variations due to missing receptors or poor performance from the receptors. This involved two independent maps scanned perpendicular to one another. The resulting velocity resolution of the observations was 0.050 km s^{-1} and effective FWHM beam size of 16.6″ after using a 9″Gaussian gridding kernel on 6″ pixels. ^{13}CO and C^{18}O maps were observed simultaneously

for 16.6 hours in March, July and August 2008 using the raster scan mode and basket-weaving. The resulting velocity resolution was 0.055 km s^{-1} and an effective FWHM beam size of 17.2″ after using a 9″ Gaussian gridding kernel on 6″ pixels for both maps. Main-beam efficiencies of $\eta_{\rm MB} = 0.61$ were used (345 GHz; Buckle et al. 2009).

The resulting maps showed noticeable striping effects, indicating that some detectors were systematically higher or lower relative to others. Similar issues were found in past HARP maps (e.g. Curtis et al. 2010a) and the cause of these systematic differences is unknown. To remove the cosmetic striping effects, the map was first binned to 0.1 km s^{-1} velocity channels. A 3σ clipped image mask in each velocity channel was used to search for striping by using a Hough transform to automatically search for straight ridges in the data. Striping was typically found to follow the array scan direction. A Fourier destriping technique was then implemented on the raw data cubes using the least squares difference between the original data and the array of stripes. The resulting map visibly had fewer stripes in the data without quantitatively altering the map (the correction in striping was ∼2% of the peak brightness level).

3.2.2 $\mathbf{H_2}$ $v = 1 \rightarrow 0$ $S(1)$

The narrow-band H_2 maps consisted of the 2.122 μm $v = 1 \rightarrow 0$ $S(1)$ ro-vibrational line that traces weaker and lower velocity shocks ranging from ∼100-1000 K temperatures. Maps were taken in June 2010 with effective pixel sizes ∼0.4″. Data reduction and K-band continuum emission subtraction were carried out by Glenn White at Open University. Reduced maps can be seen in Section 3.6. Some stars appear negative (white) in the images which is due to the imperfect continuum subtraction. However, H_2 emission clumps from the Ophiuchus Molecular Hydrogen Emission Line Objects (MHOs) detailed by Davis et al. [2010b] are visible and Herbig-Haro (HH) objects can also be seen [Davis and Eisloeffel, 1995; Dent et al., 1995; Gómez et al., 2003; Grosso et al., 2001; Wilking et al., 1997].

3.3 HARP CO $J = 3 \rightarrow 2$ observations

Figure 3.2 shows the integrated ^{12}CO $J = 3 \rightarrow 2$ emission from the JCMT Gould Belt Legacy Survey (GBS). The region covered by the map is centred at $16^{h}27^{m}32.0^{s}$ -24°33′00.0″ in L1688. HD 147889, Oph S1, and SR3 which drive the PDR can be seen in the Oph A region (respectively at [J2000] $16^{h}25^{m}24.32^{s}$, -24°27′56.6″; $16^{h}26^{m}34.17^{s}$, -24°23′28.3″; and $16^{h}26^{m}09.31^{s}$, -24°34′12.1″). The noise (RMS) of the map is found in Figure 3.3 on 1 km s^{-1} velocity channels. Even though the edges of the map have higher noise levels, the majority of protostellar sources and emission fall within a region of average noise value of 0.33 K. The ^{12}CO $J = 3 \rightarrow 2$ molecule traces densities of 10^{4}–10^{5} cm^{-3}. These densities are found to correspond to star forming regions, including high velocity emission driven by molecular outflows from Class 0/I protostars. With an upper state energy equivalent to a temperature of 33 K, the $J = 3 \rightarrow 2$ transition also traces temperatures found in molecular outflows ($\sim$50 K).

Figure 3.2 shows the integrated ^{13}CO and C^{18}O $J = 3 \rightarrow 2$ emission at 330.588 and 329.331 GHz respectively taken by the JCMT GBS. The regions covered by the maps are centred at the same position in the L1688 cloud as the ^{12}CO map. Noise maps of the main-beam temperature are shown in Figure 3.3 where average noise levels are 0.45 K on 0.1 km s^{-1} for both ^{13}CO and C^{18}O. Both ^{13}CO and C^{18}O are less abundant than the ^{12}CO molecule and therefore trace higher column density regions in the molecular cloud and are useful for determining bulk properties of the cloud (e.g. mass, gravitational energy, and turbulent kinetic energy). Section 4.1 discusses the Ophiuchus cloud properties in more detail, including the abundance ratios in the cloud, [^{12}CO]/[^{13}CO]= 77 [Wilson and Rood, 1994] and ^{13}CO/C^{18}O= 8 (8.4; Frerking et al. 1982).

3.4 CO $J = 3 \rightarrow 2$ spectral information

The averaged spectra for the cloud can be seen in Figure 3.4 for ^{12}CO, ^{13}CO, and C^{18}O $J = 3 \rightarrow 2$. Both ^{12}CO and ^{13}CO appear off centre in velocity compared to the C^{18}O spectrum. This asymmetry may be due to the noticeable self absorption in the ^{12}CO and ^{13}CO spectra. In addition, less dense blue and redshifted high

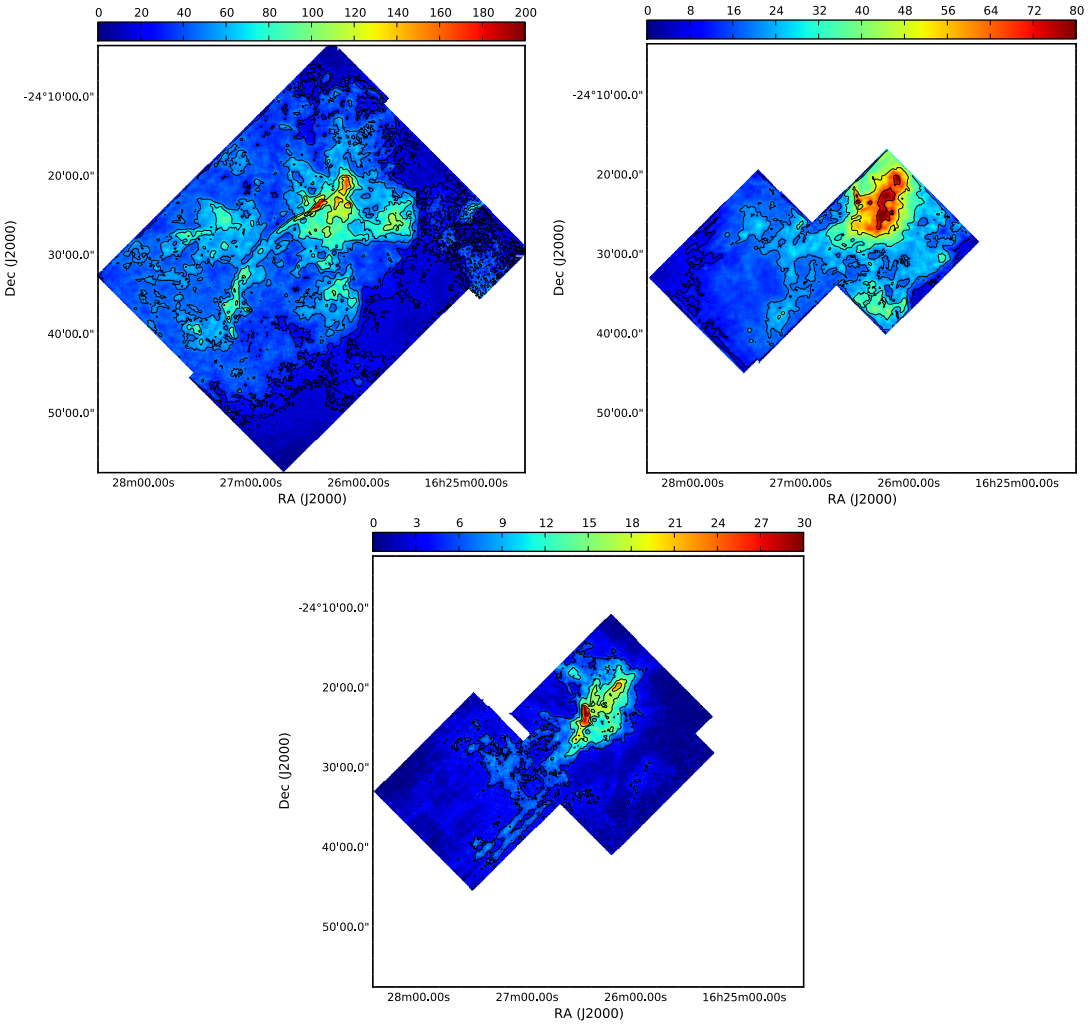

Figure 3.2: Integrated main-beam intensity maps of ^{12}CO (top), ^{13}CO (centre) , and C^{18}O (bottom) in K km s^{-1}. Contours trace 20, 30, 50, 70, 100, and 130 K km s^{-2} for ^{12}CO; 10, 20, 30, 50, 70 K km s^{-1} for ^{13}CO; 5, 10, 15, and 20 K km s^{-1} for C^{18}O.

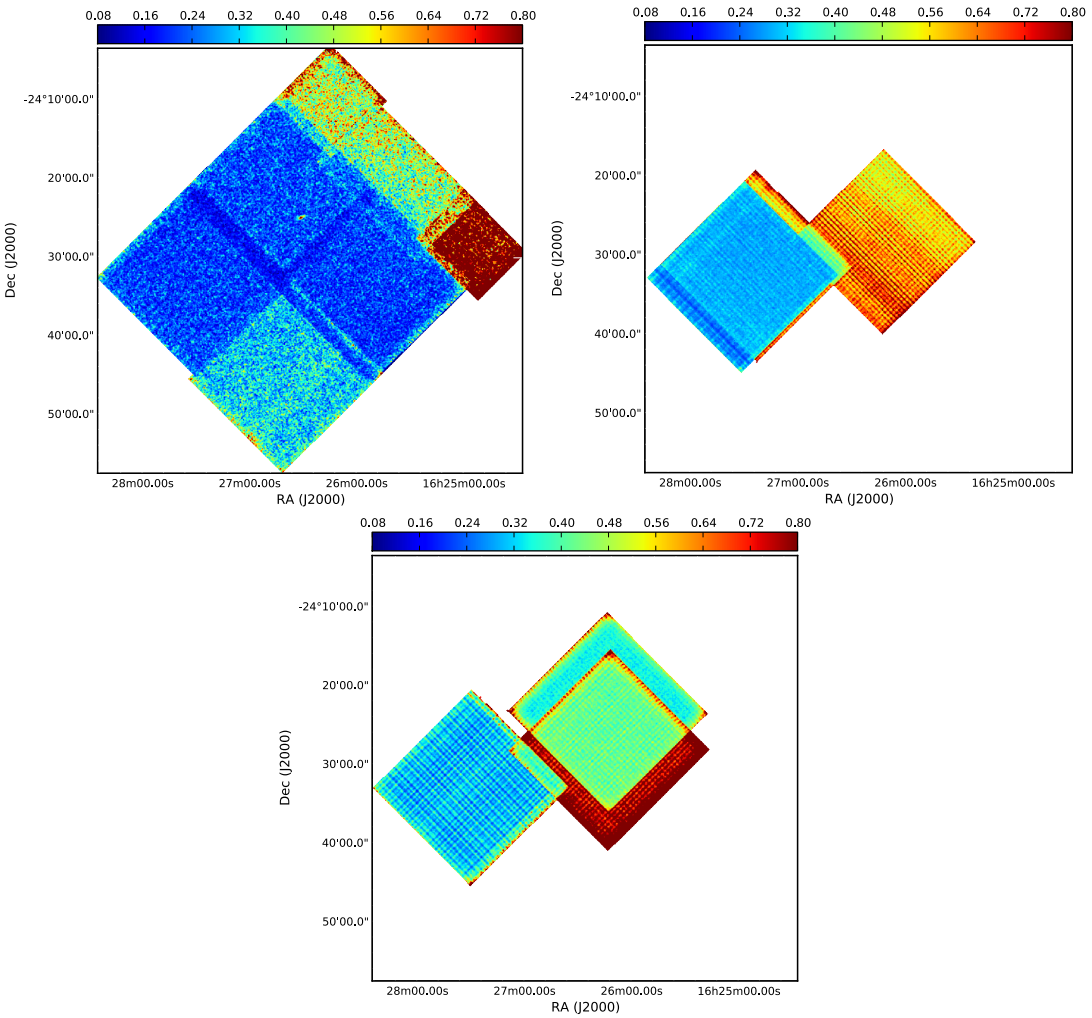

Figure 3.3: Noise maps of ^{12}CO (top) , ^{13}CO (bottom left) , and C^{18}O (bottom right). Values are in Kelvin where ^{12}CO is measured using 1.0 km s^{-1} channels and ^{13}CO and C^{18}O is measured using 0.1 km s^{-1} channels.

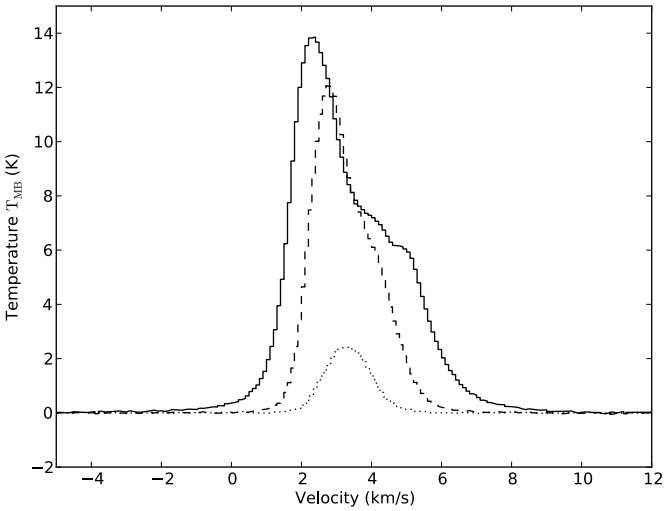

Figure 3.4: ^{12}CO (solid), ^{13}CO (dashed), and C^{18}O (dotted) spectra from the averaged spectra.

Spectrum	RA range	Dec range
Oph A	$16^h26^m00.1^s$ to $16^h26^m52.8^s$	-24°30′45.0″ to -24°17′46.3″
Oph B	$16^h26^m42.7^s$ to $16^h27^m16.3^s$	-24°30′37.86″ to -24°36′09.1″
Oph C	$16^h26^m42.7^s$ to $16^h27^m16.3^s$	-24°30′37.86″ to -24°36′09.1″
Oph E	$16^h26^m41.5^s$ to $16^h27^m22.2^s$	-24°36′11.2″ to -24°41′40.5″
Oph F	$16^h27^m25.5^s$ to $16^h27^m45.6^s$	-24°37′33.3″ to -24°44′32.3″

Table 3.1: Coordinates for regions used to average spectra in Figure 3.5.

velocity gas (i.e. due to outflows or winds from nearby B stars) can dominate the ^{12}CO emission and cause asymmetry.

Figure 3.5 shows the spatially averaged spectra of all three isotopologues for each of the cores as defined by Motte et al. [1998], coordinates listed in Table 3.1. Due to the prominent PDR and heating from nearby B stars, a mask was created from the ISOCAM 12 μm dust continuum data with at least a 45 MJy str^{-1} detection to define the region directly corresponding to hot dust (see Figure 4.2 for ISOCAM 12 μm data). The Oph A spectra are shown for the entire region, the region corresponding to hot dust emission from the B stars, and for Oph A region with the hot dust regions fully masked (labelled as 'Oph A, Hot Dust' and 'Oph A, without Hot

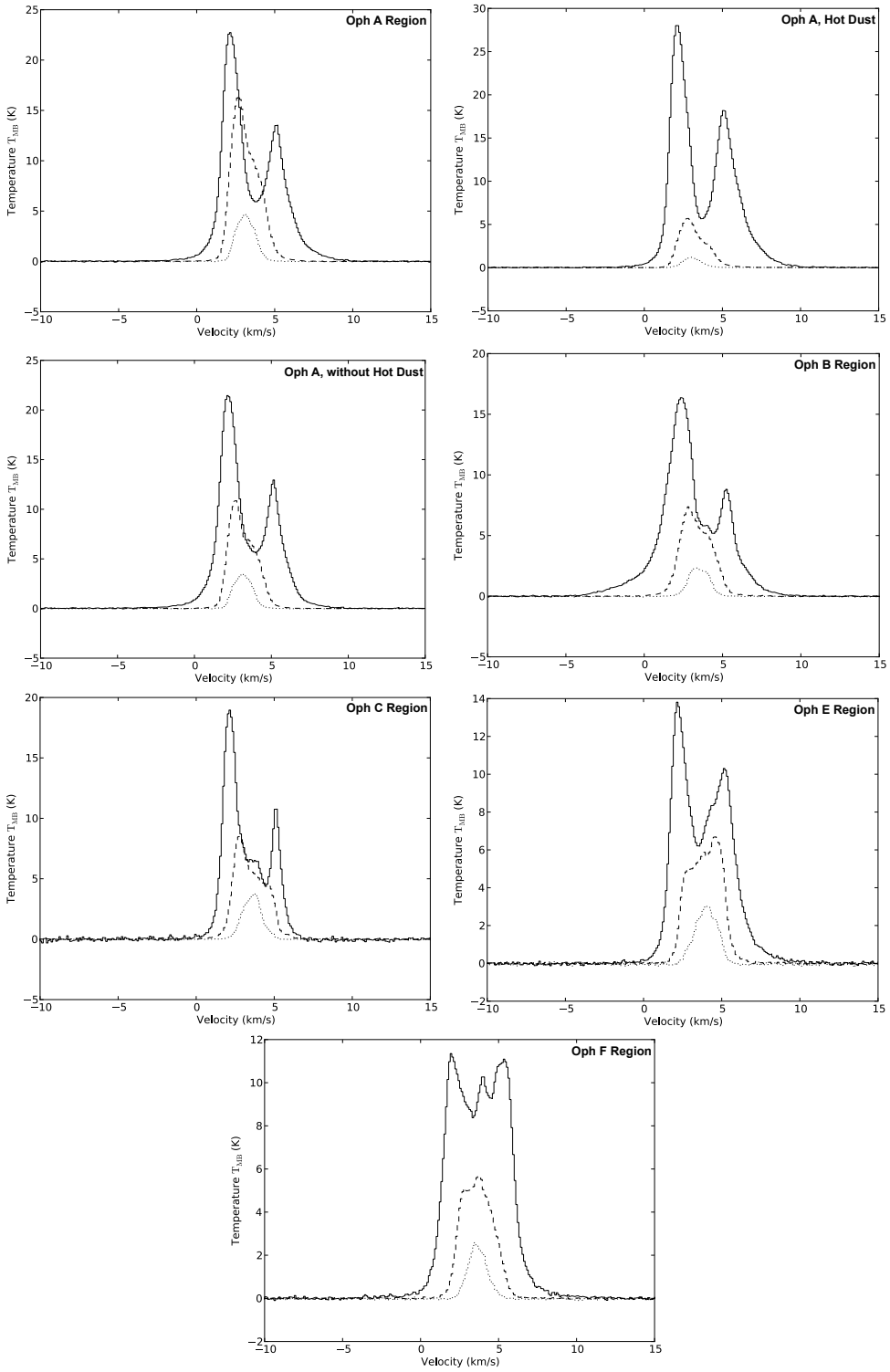

Figure 3.5: ^{12}CO (solid), ^{13}CO (dashed), and C^{18} (dotted) spectra from the individual Ophiuchus cores as defined by Motte et al. [1998].

Dust'). Comparison of these spectra indicate a strong redshifted emission that is caused by turbulence from the dust heating or emission from material at the front side of the cloud and a $C^{18}O$ peak that is offset from the other isotopologues.

The majority of the line shapes for both ^{12}CO and ^{13}CO are double-peaked or asymmetric Gaussians with dips in emission $\sim$2–3 km s^{-1} between peaks. Without corresponding $C^{18}O$ double-peaked emission, it is more likely these features are due to self absorption and not multiple velocity components. Using $C^{18}O$ emission, I calculate the central velocity of the averaged spectrum to be 3.3 km s^{-1} using a Gaussian fit. Over the cloud, averaged ambient velocities range from 3.1 km s^{-1} (Oph A) to 4.0 km s^{-1} (Oph E).

Both Figures 3.4 and 3.5 show evidence of linewing emission indicating the presence of bipolar outflows in the region. Linewing emission appears to reach velocities around 7 km s^{-1} from ambient velocities. Past studies indicate several prominent outflows, including Class 0 source VLA 1623, IRS 45/47, IRS 54, EL 29, WL 10, IRS 43, and IRS 44 [Andre et al., 1990; Bontemps et al., 1996; Jørgensen et al., 2009; Kamazaki et al., 2003; Nakamura et al., 2011; Sekimoto et al., 1997]. This data improves on past studies of the properties of the cloud, including molecular outflows in the region, by having a higher angular resolution (14.5 arcsec) or a larger mapping area in all three isotopologues. Many observations focused on lower transitions of CO $J = 2 \rightarrow 1$ and $J = 1 \rightarrow 0$ in the L1688 cloud. For example, Andre et al. [1990] observed both ^{12}CO transitions with a 12 and 21 arcsec size beam respectively and Bontemps et al. [1996] observed the $J = 2 \rightarrow 1$ transition of outflows in the cloud using a 30 arcsec beam. Additionally, there are other studies observing more specific regions of the cloud including Bussmann et al. [2007] of the Oph E with a 22 arcsec beam in the $J = 2 \rightarrow 1$ transition and Sekimoto et al. [1997] used the same tracer with a 34 arcsec beam to observe the Oph E/F region. More recent studies have examined to ^{12}CO $J = 3 \rightarrow 2$ transition. Kamazaki et al. [2003] observed Oph A and B2 using a 14 arcsec beam and Nakamura et al. [2011] observed most of the cloud using a 22 arcsec beam but excluded important sources in Oph B2 (e.g. IRS 54) and Oph F (IRS 44 and 43). The most recent study using ^{12}CO $J = 3 \rightarrow 2$ is van der Marel et al. [2013] observing 16 Class I sources in the cloud using a 14 arcsec beam from the HARP instrument. However, these observations only consist of small $2' \times 2'$ maps of each source.

3.5 Individual molecular outflow analysis of Ophiuchus

The molecular outflows in Ophiuchus can be further examined using the ^{12}CO $J = 3 \rightarrow 2$ data. This section provides a detailed analysis of molecular outflows driven by Class 0 and I protostars in this region.

3.5.1 Source classification and outflow detection

A total of 30 protostars were initially selected using *Spitzer* data from the survey "From Molecular Clouds to Planet-Forming Disks" (c2d; Evans et al. 2009) as potential drivers for molecular outflows. Using the data from the c2d survey, Padgett et al. [2008] assigned a spectra index $\alpha_{2-24\mu\mathrm{m}}$ to classify the sources following Greene et al. [1994]. I further analysed the sources with a spectral index $\alpha_{2-24\mu\mathrm{m}} > -0.3$, which correspond to Class 0 and I sources as well as flat spectrum objects, listed in Table 3.2. Sources were also required to have a bolometric temperature (Myers & Ladd 1993) $T_{\mathrm{bol}} < 750$ K to further distinguish between more evolved flat spectrum sources bordering the Class II stage, where Class II protostars typically have a bolometric temperature ranging from 650–2880 K [Andre et al., 2000; Chen et al., 1995]. The bolometric temperature cut-off was extended to 750 K in order to include flat spectrum sources IRS 45 and 47 which were previously studied for driving an outflow in the Oph B region [Kamazaki et al., 2003]. Class II source WL 10 was also added due to past studies [Sekimoto et al., 1997] suggesting the source drives an outflow visible in ^{12}CO.

The ^{12}CO $J = 3 \rightarrow 2$ map was used to search for molecular outflows in Ophiuchus. The method used to identify molecular outflow follows the objective criterion introduced by Hatchell et al. [2007a]: are linewings detected in the ^{12}CO spectra above 1.5 K at ± 3 km s^{-1} from the core/ambient cloud velocity, v_{LSR}? Core velocities were determined by fitting a Gaussian to the C^{18}O $J = 3 \rightarrow 2$ spectra at the source coordinates. Source spectra were plucked from both the ^{12}CO and C^{18}O maps using the KAPPA PLUCK command. Spectra are obtained from the two nearest pixel values along each axis and interpolated for the final source spectrum. The 1.5 K temperature criterion corresponds to T_{MB} RMS values of $\sim 5\sigma$ (depending on the

source location in the map). Temperature and velocity limits are used to identify significant high velocity emission from each source that is characteristic of molecular outflows. Figure 3.7 shows the individual ^{12}CO spectra rebinned to 1 km s^{-1} with the core velocities and outflow criterion.

Results of the outflow analysis are summarised in Table 3.2. I include the detection of either a blue or redshifted linewing for each source and the conclusion of the outflow analysis. The linewing criterion identifies not only protostars driving molecular outflows, but also sources which are confused by nearby outflows or multiple velocity components along the line of sight. Outflow candidates are identified with a blue and/or redshifted linewing and further examined to determine if the high-velocity emission detected is an outflow and if the source or another protostar is the outflow driving source. Sources with potential confusion are labeled 'y?c' and the source number that could potentially cause confusion.

3.5.2 H_2 knot analysis

Ancillary to investigating the ^{12}CO molecular outflow lobes, molecular hydrogen H_2 maps can be used to better trace the underlying jet potentially driving the molecular outflow. In the following sections, I also compare significant high-velocity CO emission to past studies of Herbig-Haro (HH) objects and H_2 knots in H_2 maps taken with WFCAM on UKIRT.

HH objects are shocks seen as optical nebulae in bipolar outflows and H_2 knots are shock-excited knots in the infrared. Both HH objects and H_2 knots can look like jets or bow shocks, curving in the direction the outflow is travelling which can make them useful outflow tracers. In Sections 3.6.1–3.6.3, I discuss the H_2 data region-by-region and highlight past research that has discussed the potential YSOs that drive lists of H_2 knots and HH objects in the Ophiuchus region. There are numerous studies identifying these objects in molecular hydrogen data, for example: Gómez et al. [2003], Grosso et al. [2001], Kamazaki et al. [2003], Caratti o Garatti et al. [2006], Eislöffel et al. [2000], Khanzadyan et al. [2004], and Ybarra et al. [2006].

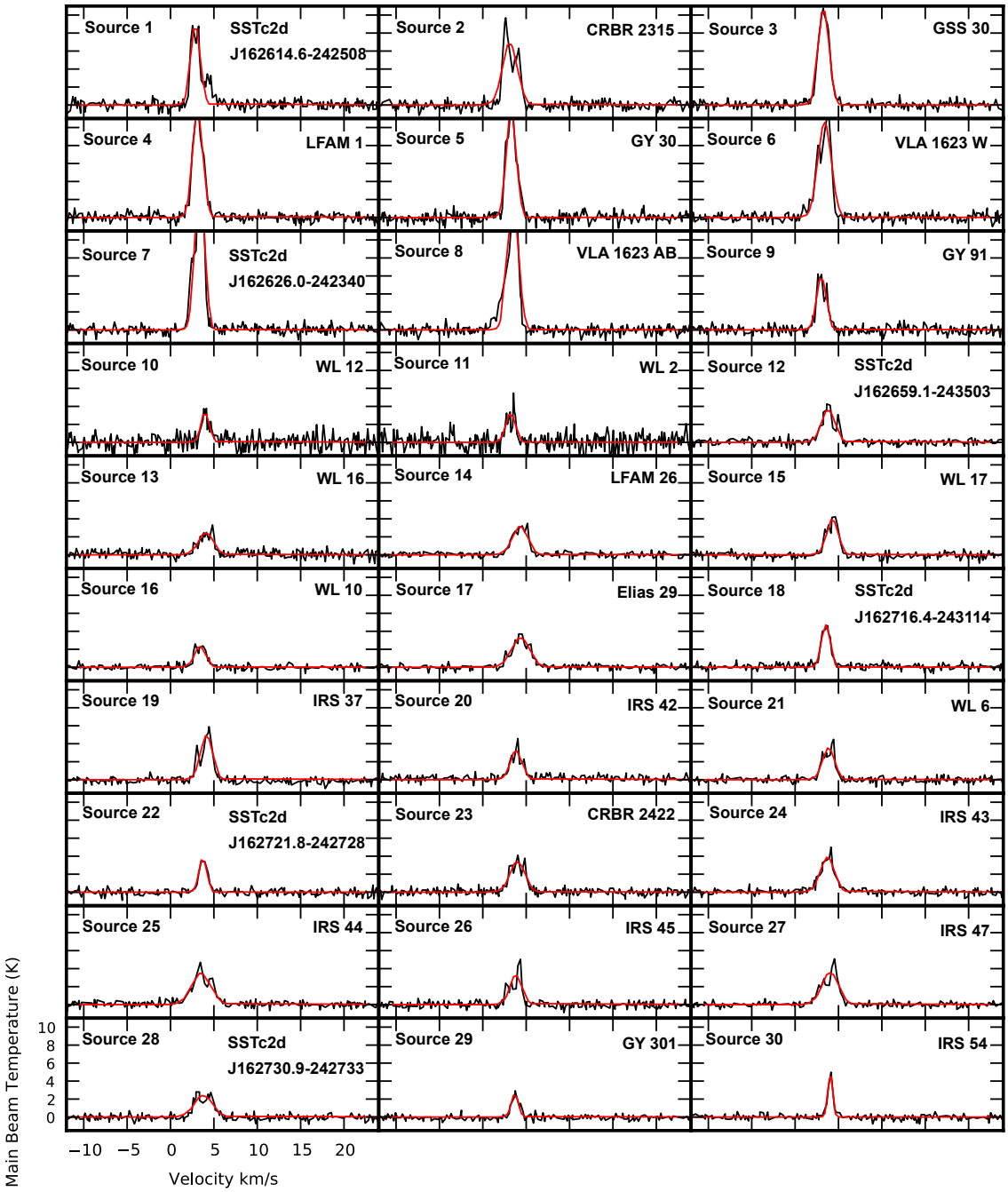

Figure 3.6: $C^{18}O$ spectra at protostellar positions.

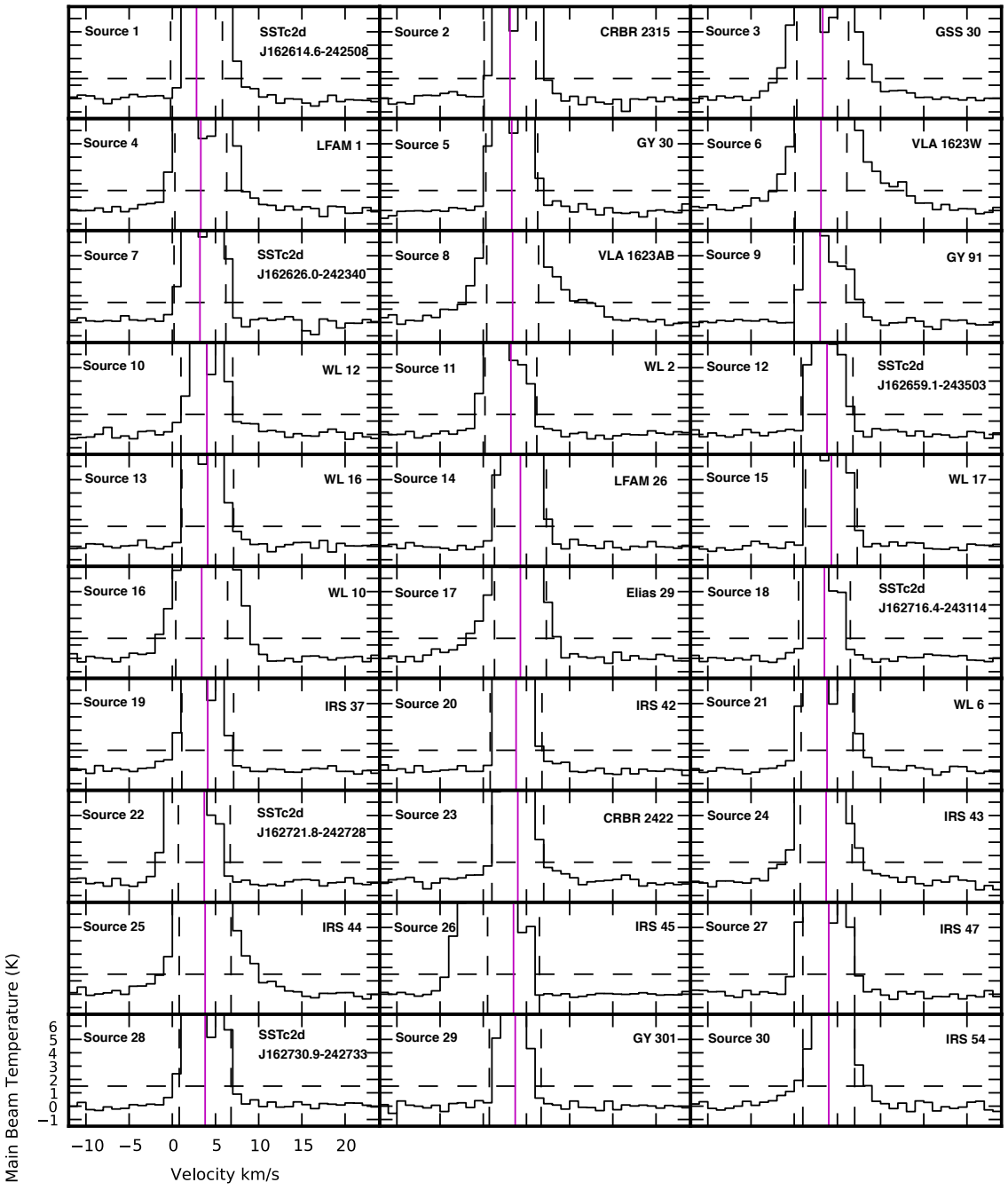

Figure 3.7: ^{12}CO spectra at protostellar positions.

Table 3.2: Outflow status for sources in Ophiuchus based on the criteria of outflow identification, discussed in Section 3.5.1.

Source	Right Ascension (J2000)	Declination (J2000)	Name[a]	Class[b]	v_{LSR} km s^{-1}	Red Lobe	Blue Lobe	Verdict
1	16:26:14.63	-24:25:07.5	SSTc2dJ162614.6-242508	0	2.8	y	n	y?c8
2	16:26:17.23	-24:23:45.1	CRBR 2315	I	3.1	y	y	y?c8
3	16:26:21.40	-24:23:04.1	GSS 30-IRS1 (GSS 30)	I	3.3	y	y	y?c8
4	16:26:21.70	-24:22:51.4	GSS 30-IRS3, LFAM 1	I	3.3	y	y	y?c8
5	16:26:25.46	-24:23:01.3	GY 30	I	3.3	y	y	y?c8
6	16:26:25.62	-24:24:28.9	VLA 1623W [c]	I	3.1	y	y	y?c8
7	16:26:25.99	-24:23:40.5	SSTc2dJ162626.0-242340	flat	3.2	y	y	y?c8
8	16:26:26.42	-24:24:30.0	VLA 1623(AB)	0	3.4	y	y	y
9	16:26:40.46	-24:27:14.3	GY 91	flat	3.0	y	n	y?PDR
10	16:26:44.19	-24:34:48.4	WL 12	I	4.0	y	n	y?
11	16:26:48.47	-24:28:38.7	WL 2, GY 128	flat	3.2	n	y	y?c4
12	16:26:59.10	-24:35:03.3	SSTc2d J162659.1-243503	I	3.8	y	n	y?
13	16:27:02.32	-24:37:27.2	WL 16, GY 182	I	4.1	n	y	y?
14	16:27:05.24	-24:36:29.6	LFAM 26, GY 197	I	4.3	y	y	y?c17
15	16:27:06.75	-24:38:14.8	WL 17, GY 205	I	4.3	n	y	y?c17
16	16:27:09.09	-24:34:08.3	WL 10	II	3.4	y	y	y
17	16:27:09.40	-24:37:18.6	Elias 29, GY 214	I	4.3	y	y	y
18	16:27:16.39	-24:31:14.5	SSTc2dJ162716.4-243114	flat	3.5	n	n	n
19	16:27:17.58	-24:28:56.2	IRS 37	I	4.1	n	y	y?c27
20	16:27:21.45	-24:41:43.0	IRS 42, GY 252	flat	3.8	y	n	y?
21	16:27:21.79	-24:29:53.1	WL 6	I	3.8	y	y	y
22	16:27:21.82	-24:27:27.6	SSTc2d J162721.8-242728	flat	3.7	n	y	y?c27
23	16:27:24.58	-24:41:03.1	CRBR 2422	I	4.0	y	n	y?24
24	16:27:26.91	-24:40:50.7	IRS 43, GY 265	I	3.7	y	y	y
25	16:27:27.99	-24:39:33.4	IRS 44, GY 269	I	3.8	n	y	y
26	16:27:28.44	-24:27:21.0	IRS 45, Elias 32	flat	3.5	n	y	y?c27
27	16:27:30.17	-24:27:43.7	IRS 47, Elias 33	flat	4.0	n	y	y
28	16:27:30.91	-24:27:33.2	SSTc2d J162730.9-242733	I	3.8	y	y	y?c27
29	16:27:37.23	-24:42:37.9	GY 301	flat	3.7	n	n	n
30	16:27:51.79	-24:31:45.4	IRS 54, GY 378, YLW 52	flat	4.0	y	y	y

[a] VLA: Andre et al. [1990] , GY: Greene and Young [1992], GSS: Grasdalen et al. [1973], IRS: Allen [1972], Elias: Elias [1978], CRBR: Comeron et al. [1993], WL: Wilking and Lada [1983], Leous et al. [1991], SSTc2d: Evans et al. [2009].

[b] Classifications follow Greene [2004], where the spectral index α is derived from Padgett et al. [2008].

[c] Enoch et al. [2009] denote this source as VLA 1623.

3.6 Discussion

Using the criterion above, I detected outflows towards 28 out of 30 sources (8 firm, 20 marginal), which is 93 % of sources. All protostars with firm outflow detections have been previously reported in other studies (VLA 1623 AB, WL 10, Elias 29, WL 6, IRS 43, IRS 44 and IRS 54) and the driver of the main Oph B outflow (IRS 47) is discussed in Section 3.6.2. Several new sources identified in the c2d survey have been analysed for molecular outflows, labelled 'SSTc2d' in Table 3.2. The majority of these sources have some evidence for red and/or blueshifted outflow lobes, but are confused by other nearby protostars. Non-detections are found from 2 flat spectrum sources in the Oph B and F regions. Flat spectrum objects are less embedded than Class 0/I sources and are less likely to have outflow detections. I discuss sources further analysed for outflows region-by-region in Sections 3.6.1–3.6.3. All plots with red and blue contours correspond to red and blueshifted ^{12}CO integrated intensities at 3, 5, 10, 15, 30 and 45 K km s^{-1} unless otherwise noted.

3.6.1 Oph A

Oph A contains two Class 0, five Class I and three flat spectrum protostars. The ^{12}CO outflow criteria have confirmed one outflow (expected to be driven by VLA 1623 AB) and potential outflows from SSTc2d J162614.6-242508, CRBR 2315, GSS 30, LFAM 1, GY 30, VLA 1623 W, SSTc2dJ1626.0-242340 and GY 91 with at least one high velocity outflow lobe. Figure 3.8 shows the H_2 2.122 μm $v = 1 \rightarrow 0$ $S(1)$ ro-vibrational line map of the Oph A region with blue contours tracing the blueshifted ^{12}CO intensity $\int T_{\rm MB}$ dv (integrated from -8.6 to 0.4 km s^{-1}) and red contours tracing the redshifted ^{12}CO intensity (integrated from 6.4 to 15.4 km s^{-1}). Protostellar sources are denoted by '$\times$'. H_2 knots, used to provide further evidence for source outflows, are labelled by $\triangle$. '[GSWC2003]XX' denotes knots from Gómez et al. [2003], 'fXX-XX' denotes knots from Khanzadyan et al. [2004], '[G01]XX' denotes knots from Grosso et al. [2001], and '[Y06]XX' denotes knots from Ybarra et al. [2006]. Figure 3.9 shows a channel map of the Oph A region, which provides further evidence of high-velocity blue and redshifted outflow lobes. This map is rebinned to 1 km s^{-1} channels and shows channels with high-velocity blue and redshifted emission based on the linewing criterion used for the ^{12}CO molecular outflow analysis.

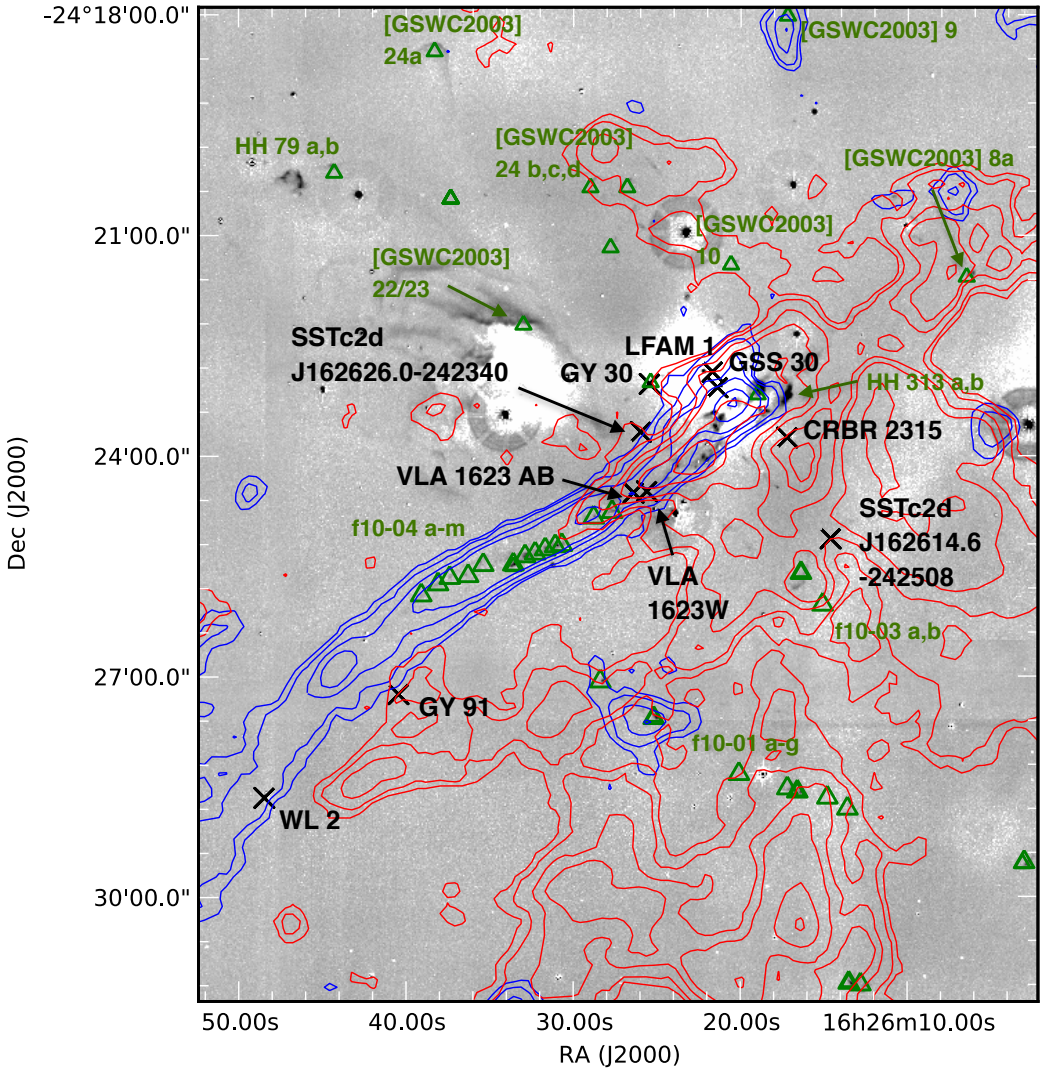

Figure 3.8: ^{12}CO 3-2 outflows in Oph A.

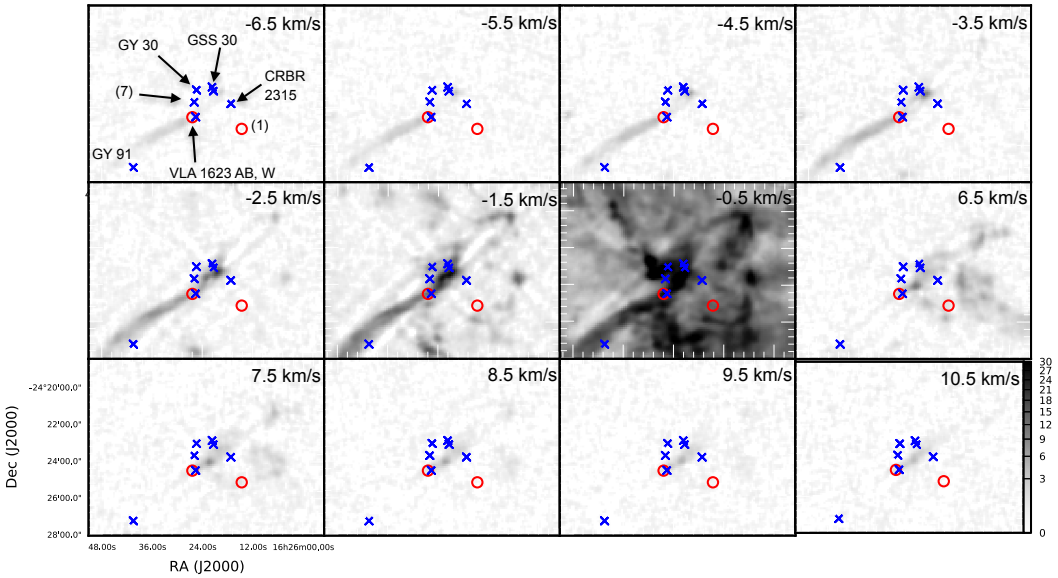

Figure 3.9: Channel map of Oph A. Channels are rebinned to 1 K km s^{-1} channels. Class 0 sources VLA 1623 AB and SSTc2d J162614.6-242508 are denoted as '○' and other sources are denoted as '×'.

Individual sources are further discussed in Sections 3.6.1.1–3.6.1.6.

3.6.1.1 VLA 1623

The highly collimated outflow from VLA 1623 can be clearly seen in Figure 3.8. The prominent blueshifted lobe of the outflow extends roughly 0.7 pc across Oph A, as found by Dent et al 1995. VLA 1623 is composed of three sources [Murillo and Lai, 2013; Ward-Thompson et al., 2011]: VLA 1623 A (Class 0), VLA 1623 B (suggested to be either between prestellar and Class 0 stages or a shocked knot in the jet) and VLA 1623 W (Class I). I refer to VLA 1623 A and B as one source because they are unresolved in the c2d survey [Evans et al., 2009]. The CO flow encompasses several H_2 knots labelled f10-04 (c-m) in the blueshifted emission and f10-04 (a,b) in the redshifted emission that are attributed to VLA 1623 by both Gómez et al. [2003] and Kamazaki et al. [2003]. The redshifted region is partially confused by hot dust and potentially the PDR located to the west of the source, but emission from the redshifted flow becomes clearer in channels 9.5 and 10.5 km s^{-1} of Figure 3.9. This redshifted emission is not as extended as the blueshifted lobe.

The less prominent redshifted lobe from VLA 1623 to the northwest causes confusion in the region for Class I sources GY 30, GSS 30, LFAM 1, CRBR 2315, VLA 1623 W and Class 0 sources SSTc2d J1626.0-242508. These sources are further discussed in Sections 3.6.1.2–3.6.1.4.

3.6.1.2 GSS 30

GSS 30 consists of two Class I sources (GSS 30-IRS1 and -IRS3, denoted as GSS 30 and LFAM 1 respectively) and one Class II source (GSS 30-IRS2). Only GSS 30 and LFAM 1 are considered for analysis in this study. Both red and blue linewings are detected for the sources in Figure 3.8, but the sources are located in a confused region due to their proximity to VLA 1623. To analyse further support for potential outflows driven by the sources, a H_2 2.122 μm $v = 1 \rightarrow 0$ $S(1)$ map of the region is shown in Figure 3.10 with relevant HH objects and H_2 knots labelled and the proposed axes for potential outflow driven by GSS 30. This figure also shows the blue and redshifted CO map of the Oph A region. The first proposed axis is in alignment with H_2 knots [GSWC2003] 22a and 23c which agrees with Gómez et al. [2003]. This axis also is in alignment with HH 313 (b), attributed by Caratti o Garatti et al. [2006] and Eislöffel et al. [2000] to GSS 30 and by Gómez et al. [2003] to VLA 1623. The shape of HH 313 (b) could indicate the H_2 knot travels to the west, which is consistent with the knot originating from GSS 30. HH 313 (b) can also be seen in optical wavelengths as a water maser [Gómez et al., 2003]. The second potential flow is traced by H_2 knot [GSWC2003] 9 and 10, discovered by Gómez et al. [2003]. These knots are found only to the north of the source and appear to continue travelling north. Lastly, the third potential flow travels through a region of H_2 knots [GSWC2003] 24b, 24c, and 24d [Gómez et al., 2003] and is in line with f10-03 a,b [Caratti o Garatti et al., 2006; Gómez et al., 2003; Khanzadyan et al., 2004]. The latter knots are roughly 2.5′ southwest of GSS 30 and align in a southwest motion.

Even though there is evidence from the ^{12}CO outflow criterion and H_2 knots, I cannot be certain that GSS 30 and LFAM 1 drive outflows in this portion of the confused Oph A region. This follows the conclusions from Bontemps et al. [1996], which also found that the outflow from VLA 1623 caused too much confusion in

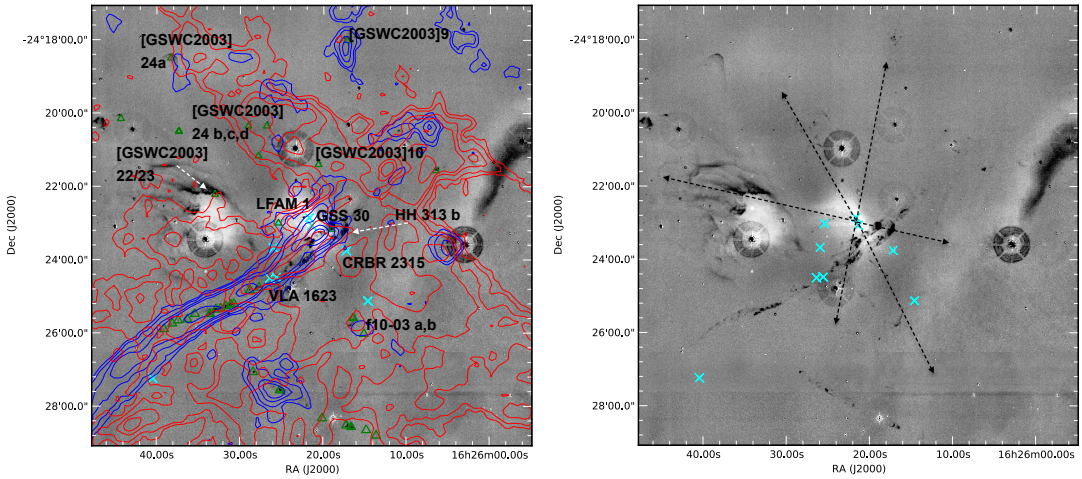

Figure 3.10: Left: Blue and redshifted contours of Oph A, same as Figure 3.8 with proposed H_2 knots corresponding to GSS 30- and LFAM1 labelled. Right: Proposed outflow axes for sources.

Oph A to conclude GSS 30 and LFAM 1 drive outflows.

3.6.1.3 GY 30

GY[92] 30 (GY 30) is located northeast of VLA 1623. Both blue and red linewings are detected for GY 30, but like GSS 30 and LFAM 1 the confusing effects of the VLA 1623 outflow complicate the analysis. Figure 3.11 depicts the high-velocity emission near GY 30, similar to Figure 3.10. Blue contours trace the blueshifted ^{12}CO integrated main-beam temperature (from -9.0 to 0.3 km s^{-1}) and red contours trace the redshifted ^{12}CO integrated main-beam temperature (from 6.3 to 16.0 km s^{-1}). Both red and blueshifted emission can be seen in Figure 3.11, but the region is heavily confused with the VLA 1623 outflow. Kamazaki et al. [2003] used ^{12}CO 1-0 to show that it is likely GY 30 is driving an outflow parallel to VLA 1623. An outflow driven by GY 30 is further supported by Figure 3.9, where there is noticeable bipolar blue and redshifted emission in channels -0.5 and 6.5 km s^{-1}. There is also a H_2 knot close to the source which seems to follow a bipolar outflow parallel to VLA 1623, shown in Figure 3.8, which could be potentially driven by an GY 30.

Like GSS 30 and LFAM 1, the confusion from VLA 1623 prevents a confirmation of a bipolar outflow driven by GY 30.

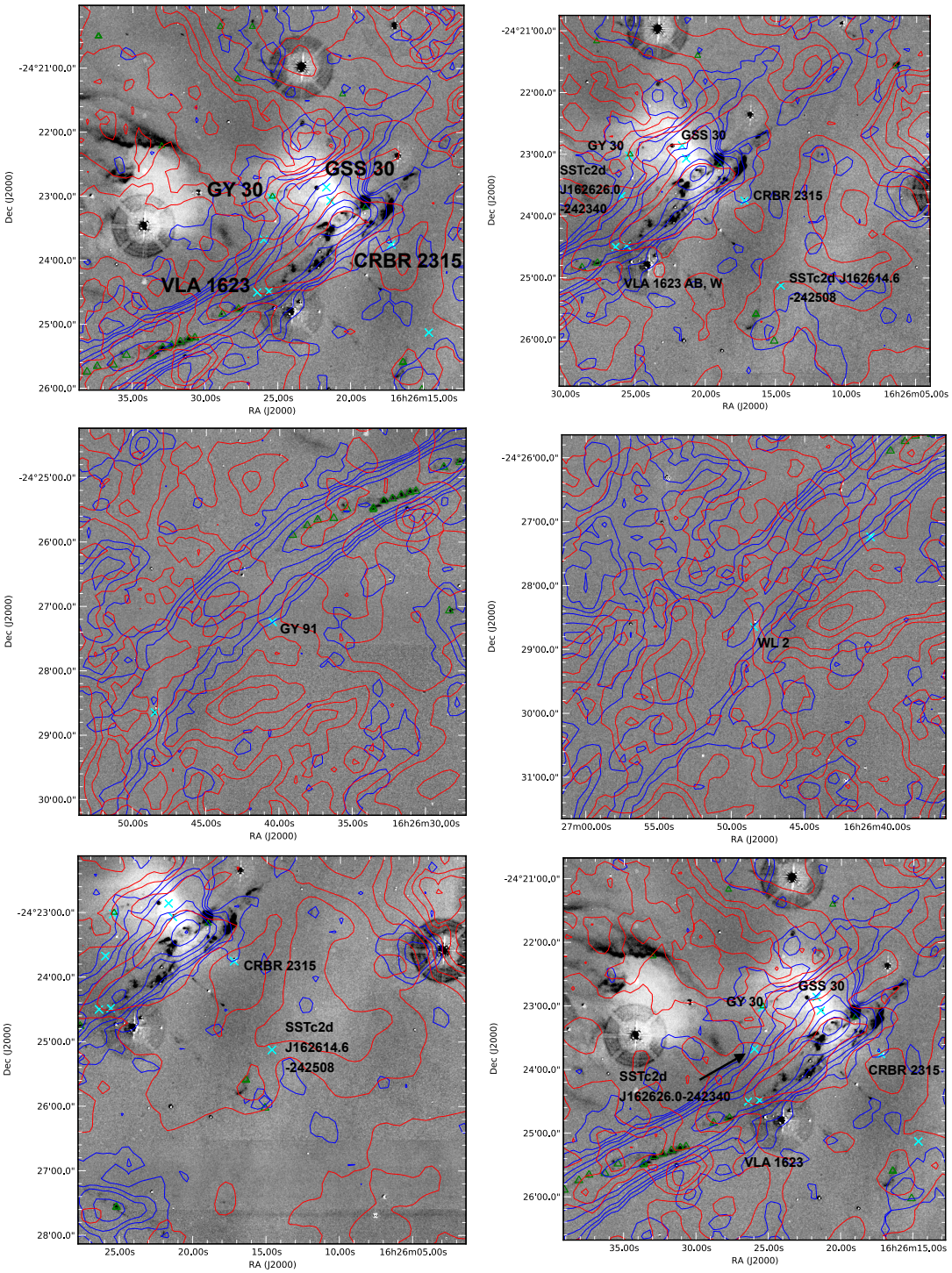

Figure 3.11: Top: Blue and redshifted contours of confused sources in Oph A.

3.6.1.4 CRBR 2315.8-1700

CRBR 2315.8-1700 (CRBR 2315) is located in Oph A, northwest of VLA 1623. Like the other Class I protostars in the region both blue and red linewings are detected for CRBR 2315, but these could be the result of confusion from the VLA 1623 outflow. Figure 3.11 shows a close-up of the source. Blue contours trace the blueshifted ^{12}CO integrated main-beam temperature (from -9.0 to 0.1 km s^{-1}) and red contours trace the redshifted ^{12}CO integrated main-beam temperature (from 6.1 to 16.0 km s^{-1}).

Both red and blue line wings can be seen near the source, but this emission could easily be the result of the VLA 1623 outflow. With the evidence from the CO outflow criteria, I cannot be certain that CRBR 2315 drives an outflow in the region due to this confusion with VLA 1623. I note that this region is known for many H_2 knots that are mainly attributed to GSS 30, LFAM 1, or VLA 1623. If CRBR 2315 does drive an outflow, then it is possible that some of these H_2 knots are driven by the source as well.

3.6.1.5 GY 91

GY[92] 91 (GY 91) is located southeast of the central Oph A core region. Using the outflow criterion, only a redshifted lobe is detected for the source. Figure 3.11 shows a close-up of the GY 91 source, similar to Figure 3.10. Blue contours trace the blueshifted ^{12}CO integrated main-beam temperature (from -9.0 to 0.0 km s^{-1}) and red contours trace the red shifted ^{12}CO integrated main-beam temperature (from 6.0 to 16.0 km s^{-1}). Only the redshifted emission can be seen for the source, which is near the blueshifted outflow from VLA 1623. It is possible any blueshifted emission from a high-velocity outflow is potentially obscured by VLA 1623. Without evidence of the blueshifted emission, I cannot be certain that GY 91 drives a bipolar outflow.

3.6.1.6 WL 2

WL 2 is located south of GY 91. Using the outflow criterion, only a blueshifted linewing is detected for the source. Confusion is caused in this region from the highly collimated, blueshifted outflow from VLA1623, which could be the source of the blue linewing for WL 2. Figure 3.11 shows a close-up of the blue and redshifted emission with the same velocity ranges as Figure 3.8. The redshifted emission to

the northwest of the source could potentially be remnants of outflow activity and the blueshifted emission may be obscured by VLA 1623. With only the blueshifted emission detected in the outflow criterion, the blue linewing is most likely due to the confusion from the VLA 1623 outflow.

3.6.1.7 SSTc2d J162614.6-242508

SSTc2d J162614.6-242508 is a new Class 0 source on the western edge of the Oph A clump (nearest to the PDR). Though a red linewing is detected using the outflow criterion, there is no corresponding blue linewing. This outflow detection is most likely the result of hot dust generated by nearby stars. Figure 3.11 shows a close-up of the blue and redshifted emission. Due to the confusion with the surrounding environment and lack of a blue outflow lobe, I cannot be certain if this source drives an outflow.

3.6.1.8 SSTc2d J162626.0-242340

SSTc2d J162626.0-242340 is a new flat spectrum source directly north of VLA 1623, close to star Oph S1. Though both red and blue linewings are detected towards this source, the confusion from VLA 1623 makes it difficult to decipher the origin of the emission. Figure 3.11 shows a close-up of the blue and redshifted emission, similar to Figure 3.10. Due to the confusion with VLA 1623, I label this source as 'confused.'

3.6.2 Oph B

Oph B contains three Class I and five flat spectrum protostars. Using the ^{12}CO outflow criteria, three sources (WL 6, IRS 54, and IRS 47) have been confirmed to drive outflows and four sources have been identified as marginal molecular outflow candidates. Figure 3.12 shows the H_2 maps with the outflows for this region. Blue contours trace the blueshifted ^{12}CO intensity $\int T_{\rm MB}$ dv (integrated from -6.0 to 1.0 km s^{-1}) and red contours trace the redshifted ^{12}CO intensity (integrated from 7.0 to 14.0 km s^{-1}). Additionally, Figure 3.13 shows a channel map of the Oph B region, which is further used to provide evidence of high velocity blue and redshifted outflow lobes. This map is rebinned to 1 K km s^{-1} channels and shows channels

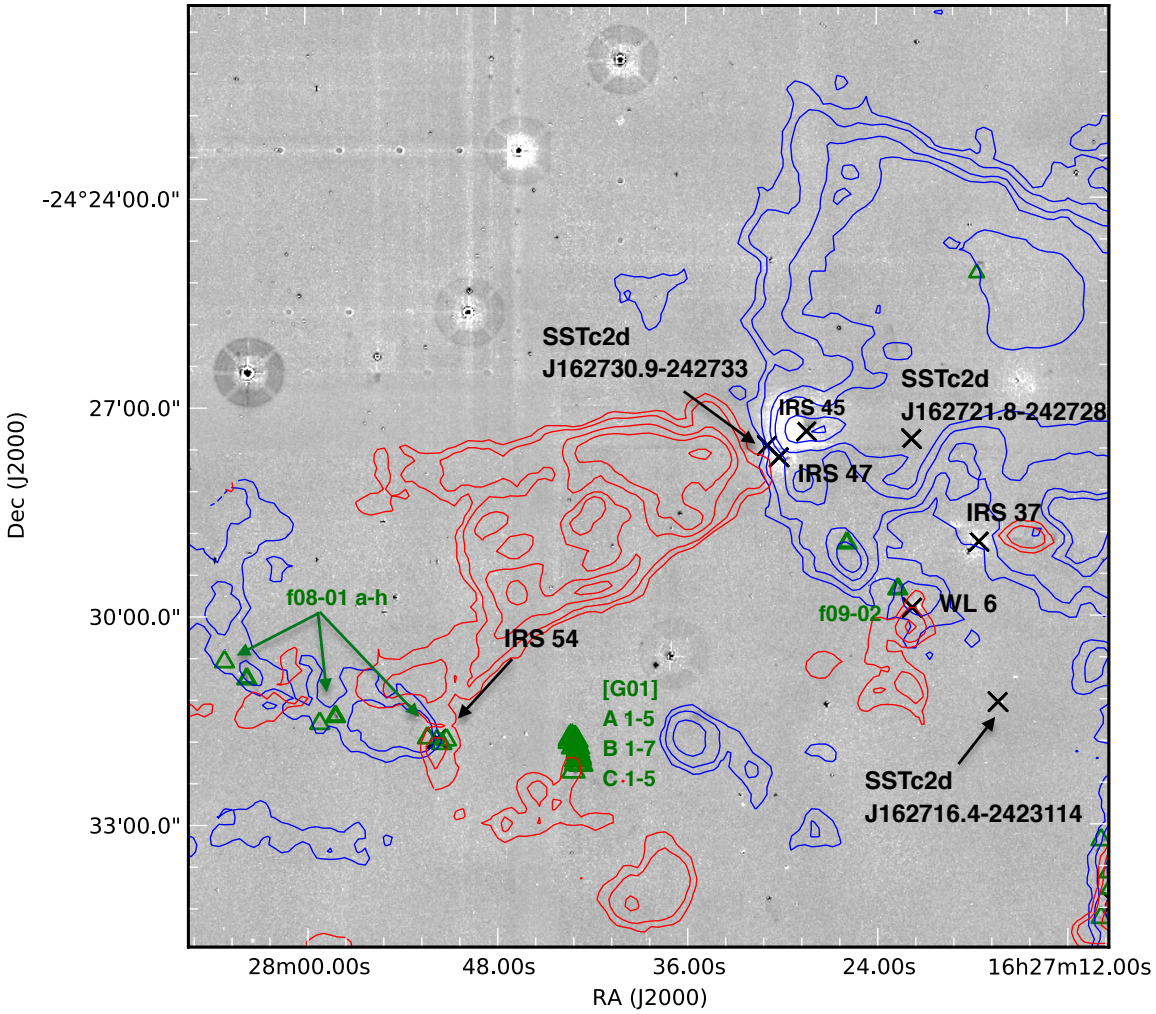

Figure 3.12: Contours of blue and redshifted ^{12}CO $J = 3 \rightarrow 2$emission in Oph B.

with high velocity blue and redshifted emission based on the linewing criterion used for the ^{12}CO molecular outflow analysis.

3.6.2.1 SSTc2d J162730.9-242733, IRS 45, IRS 47 and WL 6

Protostars SSTc2d J162730.9-242733, IRS 45, and IRS 47 can be seen in the central region of a large, clumpy outflow in Oph B (Figure 3.12). Kamazaki et al. [2001] attributed this outflow to IRS 45 due to its proximity to the strongest blueshifted emission in the lobe. The position-velocity diagram in Figure 3.14 clearly shows the redshifted lobe extending from the centre of IRS 47 and ∼0.3′ from IRS 45, also seen

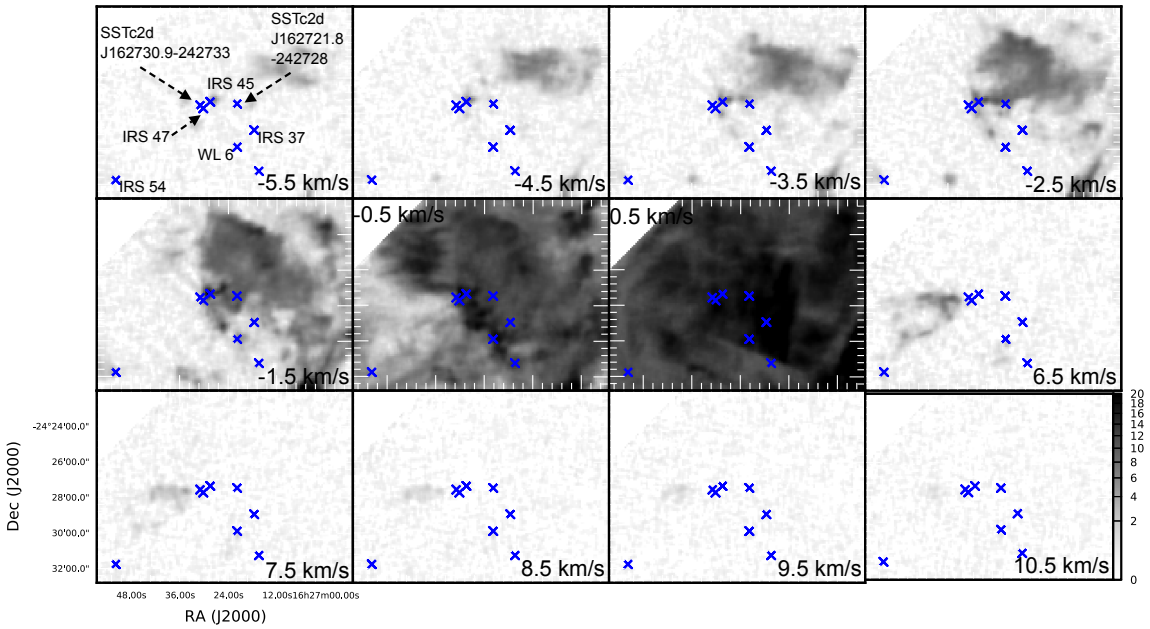

Figure 3.13: Channel map of Oph B. Channels are rebinned to 1 K km s^{-1} channels. Class I and flat spectrum sources are denoted as '×'.

in Figure 3.12. I assume that IRS 47 is the driving source for this region due to its more central location between the blue and redshifted lobes. This is in agreement with recent work from van der Marel et al. [2013] who also attributes this outflow to IRS 47. The bipolar outflow driven by Class I source WL 6 is located southwest of IRS 47. It has been suggested by Khanzadyan et al. [2004] this source drives the H_2 knot f09-02 from the blueshifted lobe of the outflow. This outflow detection agrees with Sekimoto et al. [1997]. The last firm bipolar outflow detection is from IRS 54 in the east of Oph B, which is further discussed in detail in Section 3.6.2.4. The remaining protostars located in Oph B are further discussed in Section 3.6.2.2–3.6.2.4.

3.6.2.2 IRS 37

IRS 37 is located to the west of IRS 45 and IRS 47 in Oph B. Only the blueshifted lobe is detected using the outflow criteria, which could be caused by confusion from the blueshifted lobe of the IRS 47 outflow. Figure 3.15 shows a close-up of the source. Blue contours trace the blueshifted ^{12}CO integrated main-beam temperature

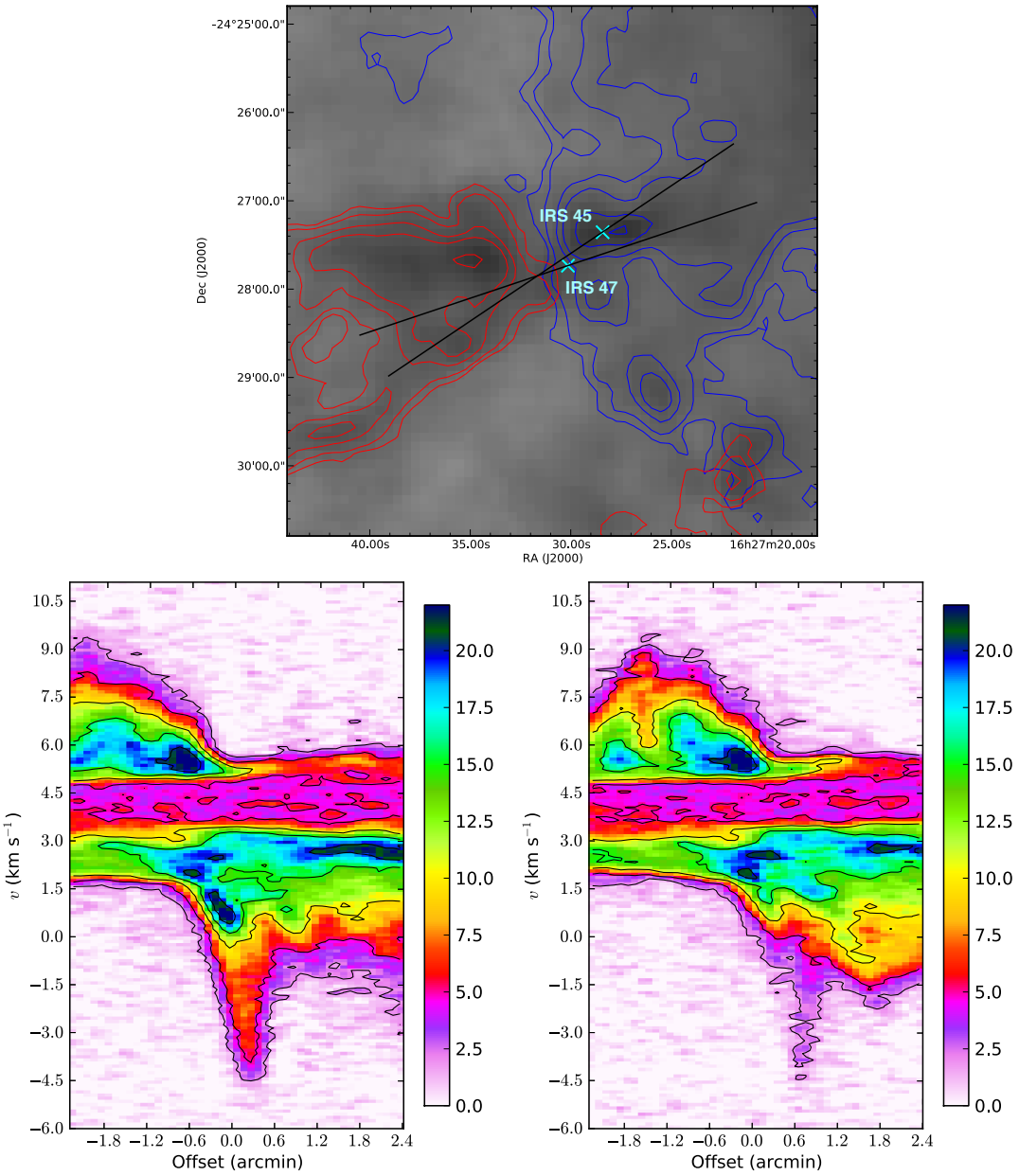

Figure 3.14: Position-velocity diagrams for sources IRS 45 (left) and IRS 47 (right). The positions used for the PV diagram are shown below. Colours are in main-beam temperature (K).

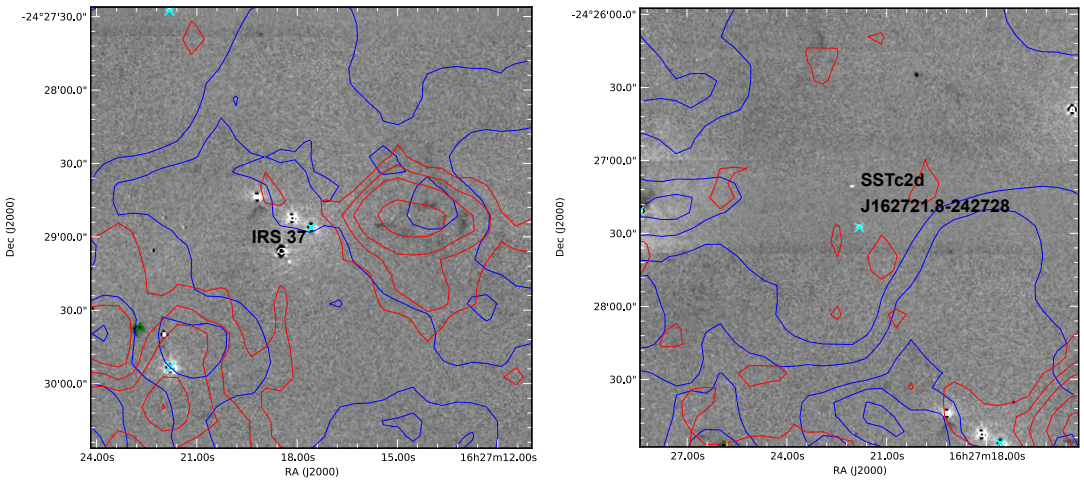

Figure 3.15: Top: Close-up images of confused sources in Oph B.

(from −6.0 to 1.2 km s^{-1}) and red contours trace the redshifted ^{12}CO integrated main-beam temperature (from 7.2 to 14.0 km s^{-1}). Only the blueshifted emission can be seen in this image. However, there is a 'bubble' of redshifted emission to the west of the source without an apparent driving source for the material. The lack of a redshifted component suggests the blueshifted emission is the result of the IRS 47 outflow. I note recent work from van der Marel et al. (2013) does conclude this source drives a molecular outflow at lower velocities than the $v_o \pm 2.5$ km s^{-1} ambient velocity criterion.

3.6.2.3 SSTc2d J162721.8-242728

SSTc2d J162721.8-242728 is located west of IRS 47 in Oph B. Only the blue lobe is detected for this source in the linewing criterion, which could be the result of the blueshifted emission of the IRS 47 outflow. Figure 3.15 shows a close-up of the source. Blue contours trace the blueshifted ^{12}CO integrated main-beam temperature (from −6.0 to 0.7 km s^{-1}) and red contours trace the redshifted ^{12}CO integrated main-beam temperature (from 6.7 to 14.0 km s^{-1}). The lack of a redshifted component suggests the blueshifted emission is the result of IRS 47. In conclusion, an outflow driven by the source cannot be confirmed.

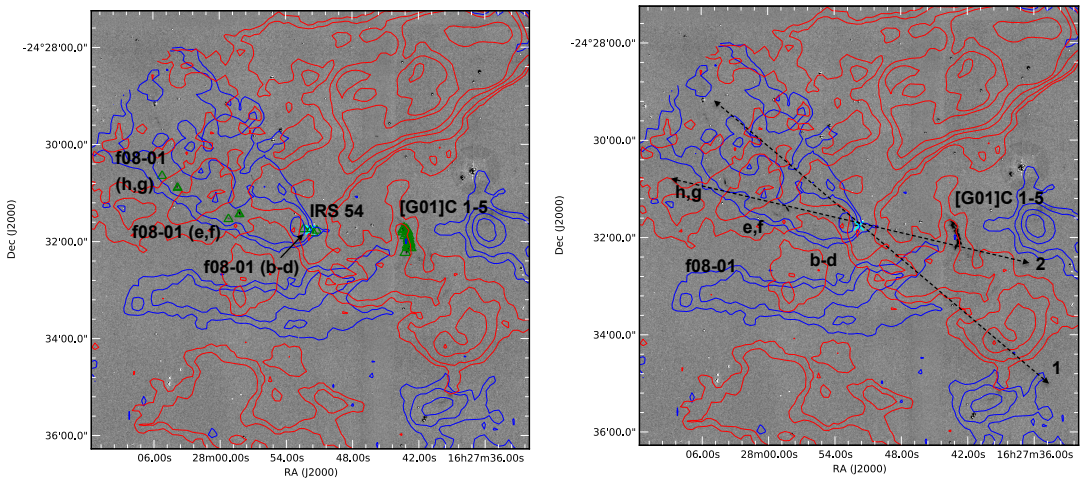

Figure 3.16: Proposed axis for the precessional outflow from IRS 54.

3.6.2.4 IRS 54

IRS 54 is binary with a separation measured to be 7″ using near-IR observations [Duchêne et al., 2004; Haisch et al., 2006] located on the edge of Oph B. Past studies [Jørgensen et al., 2009] have suggested the source drives a bipolar, precessional outflow. The clumpy east-west outflow driven by IRS 54 can be seen in Figure 3.12 and both blue and redshifted lobes are detected in the outflow criterion. The outflow also corresponds to several H_2 knots labelled [G01] C(1-5) [Grosso et al., 2001] and f08-01(a-h) [Gómez et al., 2003; Khanzadyan et al., 2004]. Figure 3.16 (right) shows the proposed outflow axes that depict the change in axis direction with the H_2 2.122 μm $v = 1 \rightarrow 0$ $S(1)$ map in the background. Figure 3.16 (left) shows a close-up of IRS 54. Blue contours trace the blueshifted ^{12}CO integrated main-beam temperature (from -5.0 to 1.0 km s^{-1}) and red contours trace the redshifted ^{12}CO integrated main-beam temperature (from 7.0 to 13.0 km s^{-1}). The first axis I label follows the more distant blue and redshifted ^{12}CO emission. The second axis I label follows the H_2 knots in the region and portions of the CO emission that are closer to the source. The change in outflow axis agrees with Jørgensen et al. [2009]. In conclusion, the outflow criterion confirms the bipolar outflow driven by IRS 54 and the precessional axes caused by the binary.

3.6.3 Oph C, E, and F

The Oph C and E regions make up the mid to southwestern portions of the L1688 cloud. Together, the regions contain six Class I protostars and one Class II protostar analysed for the outflow study. Using the ^{12}CO outflow criteria, two sources (Elias 29 and WL 10) are confirmed to drive outflows and five sources are identified as marginal molecular outflow candidates with one high velocity linewing detected. Figure 3.17 shows the H_2 maps with the outflows for Oph C, E, and F. Blue contours trace the blueshifted ^{12}CO intensity $\int T_{\rm MB}$ dv (integrated from -5.7 to 1.3 km s^{-1}) and red contours trace the redshifted ^{12}CO intensity (integrated from 7.0 to 14.3 km s^{-1}. Figures 3.18 and 3.19 show channel maps of the Oph C, E, and F regions, which are further used to provide evidence of high velocity blue and redshifted outflow lobes. These maps are rebinned to 1 km s^{-1} channels and shows channels with high velocity blue shifted and redshifted emission based on the linewing criterion used for the ^{12}CO molecular outflow analysis.

3.6.3.1 Elias 29

Elias 29 is located in Oph E near LFAM26, WL16, and WL17. This source is known for its s-shaped bipolar outflow [Bontemps et al., 1996; Sekimoto et al., 1997; van der Marel et al., 2013], which is potentially caused from its precessing axis without being a part of a binary [Ybarra et al., 2006]. The bipolar outflow can be clearly seen in Figure 3.17 and the outflow criterion detected both the blue and red outflow lobes. The outflow encompasses several H_2 knots, mainly in the southern redshifted lobe, which are labelled 2(a,b) and 3(a,b) from Ybarra et al. [2006]. The detection of the southern knots indicates that the outflow axis is currently a north-south alignment, but remnant CO emission located to the northeast of the source indicates that the outflow axis at one time may have been altered. The blueshifted outflow lobe extends to the north, also potentially driving several knots near WL 10 outflow (discussed further in Section 3.6.3.5, described by Khanzadyan et al. [2004]. Gómez et al. [2003] also suggests that knot [GSWC2003]2 is driven by Elias 29, aligning with the east-west CO emission and further supporting the poorly collimated shape of the outflow. The shape of [GSWC2003]2 indicates the knot travels to the west. The outflow criterion confirms the bipolar outflow driven by Elias 29 and supports the

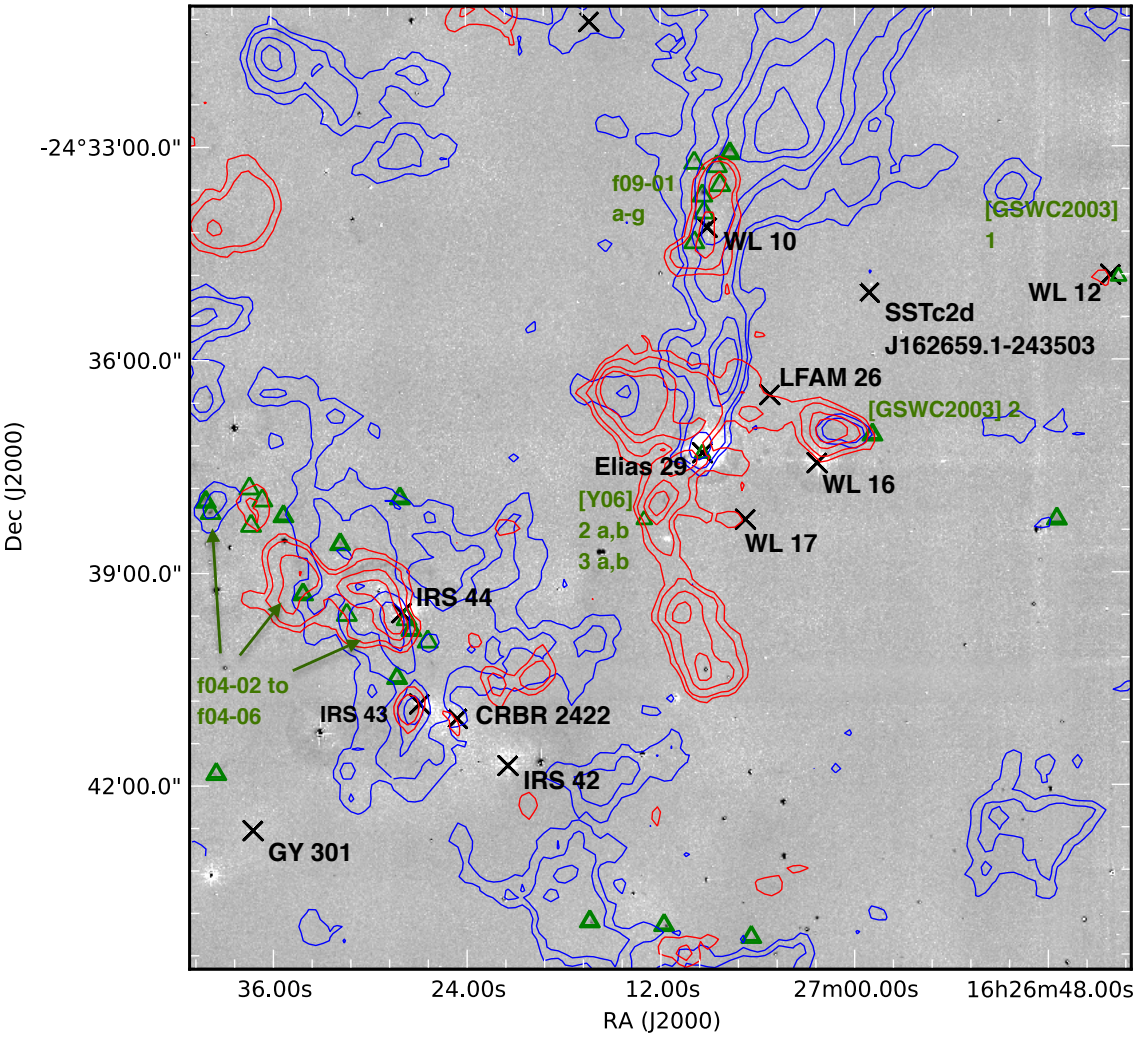

Figure 3.17: Contours of blue and redshifted ^{12}CO $J = 3 \rightarrow 2$ emission in Oph C, E, and F.

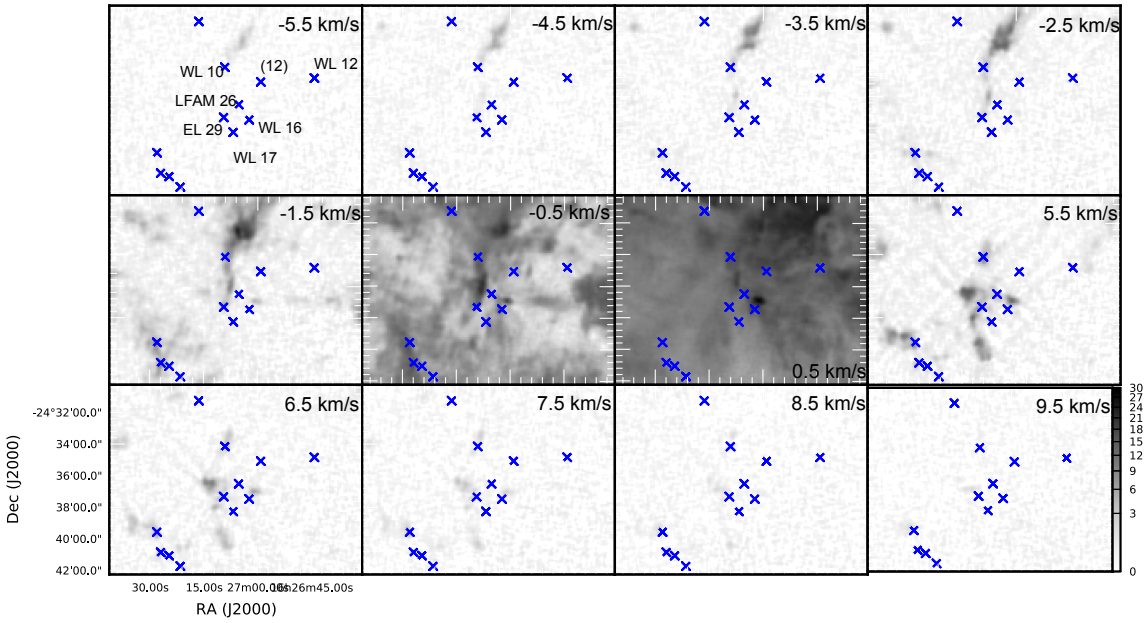

Figure 3.18: Channel map of Oph C and E. Channels are rebinned to 1 K km s^{-1} channels. Class I and flat spectrum sources are denoted as '×'.

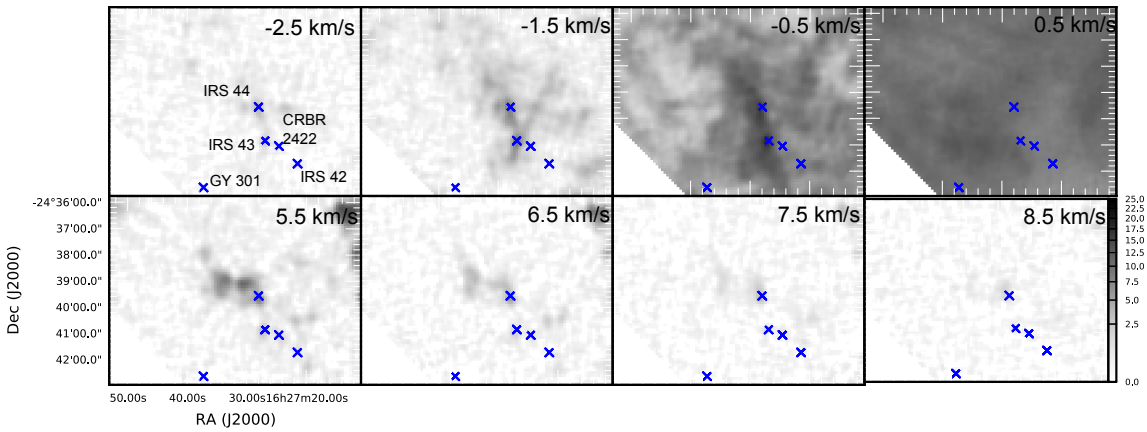

Figure 3.19: Channel map of Oph F. Channels are rebinned to 1 K km s^{-1} channels. Class I and flat spectrum sources are denoted as '×'.

outflow axis precession as indicated by multiple redshifted outflow lobes.

3.6.3.2 WL 16

WL 16 is located in Oph E west of Elias 29. Using the outflow criterion, a faint blue linewing is detected without redshifted emission. Figure 3.20 shows a close-up of WL 16. Blue contours trace the blueshifted ^{12}CO integrated main-beam temperature (from -5.7 to 1.2 km s^{-1}) and red contours trace the redshifted ^{12}CO integrated main-beam temperature (from 7.2 to 14.3 km s^{-1}). Blue and red contours begin at 1.5 K km s^{-1}. The blue lobe is detected at the source and borders a redshifted region that also includes a separate blueshifted emission along with a H_2 knot, [GWCS2003]2. The H_2 knot travels in a western direction but is further north to the source which may indicate the knot is not driven by WL 16. As discussed in Section 3.6.3.1, Gómez et al. [2003] concluded this knot is more likely driven by Elias 29 due to its location and known bipolar CO outflow. In Figures 3.17 and 3.21, Gómez et al. [2003] and Zhang et al. [2003] suggest WL 16 is the driver of f09-01(a,c,d), where f09-1a,c are thought to belong to the same flow. The shape of this knot suggests the flow travels to the northeast, potentially from the same direction of WL 16. However, the high velocity CO emission does not seem to follow the shape of this possible flow. There is a possibility that this source does drive a bipolar outflow, but I cannot conclude this using the ^{12}CO molecular line emission.

3.6.3.3 LFAM 26

LFAM 26 is located north of Elias 29. Past studies [Bussmann et al., 2007; Nakamura et al., 2011; van der Marel et al., 2013] have suggested this source drives an east-west oriented bipolar outflow. Both blue and red linewings are faintly found in the outflow criterion. Figure 3.17 shows the proximity of LFAM 26 to the blue outflow from Elias 29. Figure 3.20 shows a close-up LFAM 26. Blue contours trace the blueshifted ^{12}CO integrated main-beam temperature (from -5.7 to 1.4 km s^{-1}) and red contours trace the redshifted ^{12}CO integrated main-beam temperature (from 7.4 to 14.3 km s^{-1}). Blue and red contours begin at 1.5 K km s^{-1}. A small section of blueshifted emission can be seen in the image along with redshifted emission that is more than likely due to the northern portion of the Elias 29 outflow. It is mored

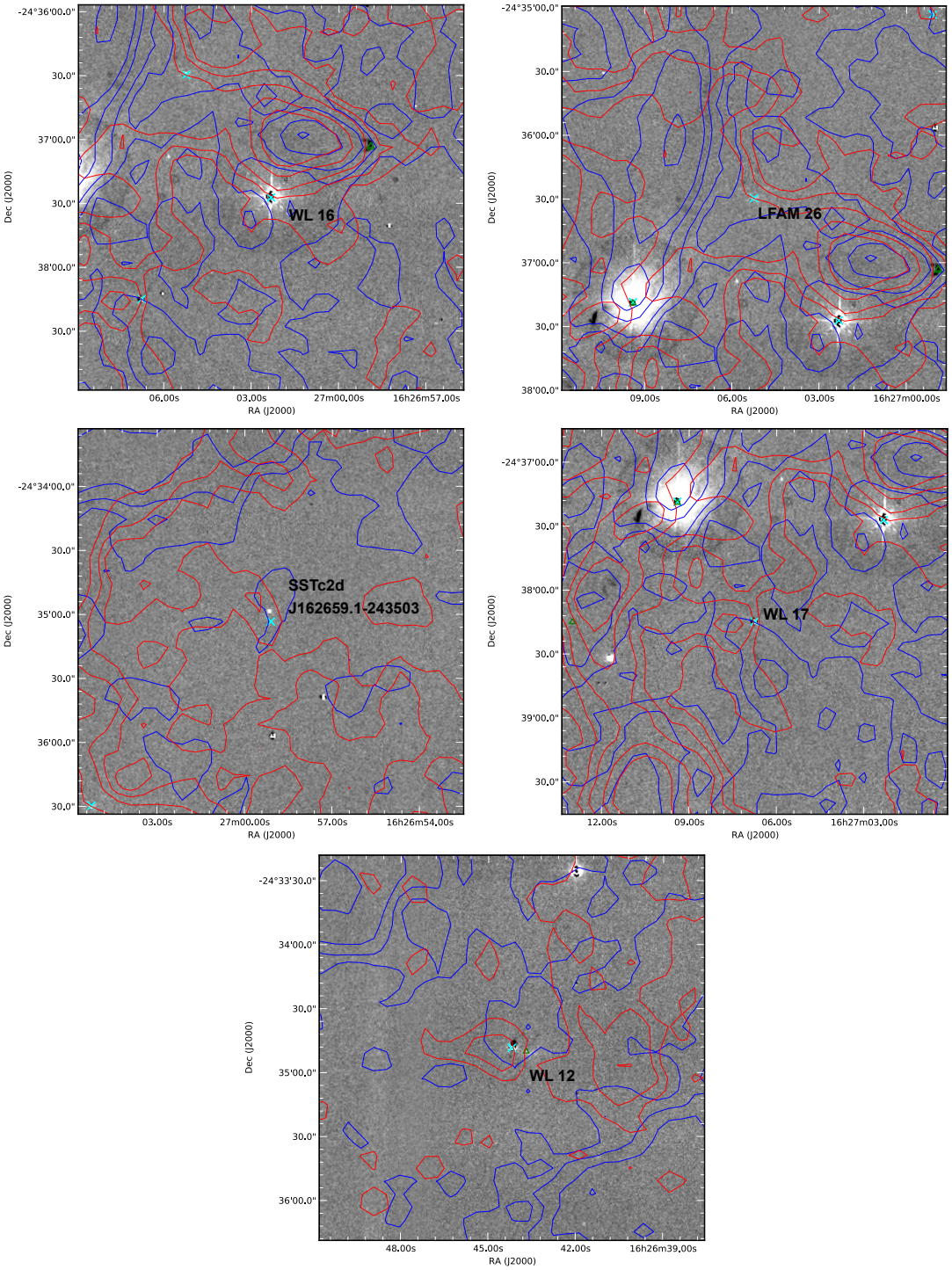

Figure 3.20: Close-up images of confused sources in Oph C and E.

likely the precessing Elias 29 outflow causes confusion in this region and falls into the path of LFAM 26. Due to this confusion, I cannot be certain that LFAM 26 drives an outflow.

3.6.3.4 WL 17

WL 17 is located in Oph E, south of WL 16. Using the outflow criterion, both blue and red linewings are detected. Figure 3.20 shows a close-up of WL 17, with blue contours trace the blueshifted ^{12}CO integrated main-beam temperature (from -5.7 to 1.3 km s^{-1}) and red contours trace the redshifted ^{12}CO integrated main-beam temperature (from 7.3 to 14.3 km s^{-1}). Blue and red contours begin at 1.5 K km s^{-1}. The blue and redshifted regions can be seen in a north-south orientation around the source at the 1.5 K km s^{-1} contour. There is a possibility that this source does have an outflow, but confusion from EL 29 to the east of the source could easily cause this blue and redshifted line emission. Due to this confusion, I cannot be certain that this source drives a bipolar outflow. I note van der Marel et al. [2013] concludes WL 17 drives an outflow, but this detection is at lower velocities than the $v_o \pm 2.5$ km s^{-1} ambient velocity criterion requires.

3.6.3.5 WL 10

WL 10 is a Class II protostar [Kamata et al., 1997] located in Oph C, north of Elias 29 at the end of the blueshifted VLA1623 outflow lobe. It is known for a bipolar outflow [Sekimoto et al., 1997] that can be seen in Figure 3.17. Both blue and redshifted linewings are detected in the CO outflow criterion. Figure 3.21 shows a close-up of WL 10. Blue contours trace the blueshifted ^{12}CO integrated main-beam temperature (from -9 to 0.3 km s^{-1}) and red contours trace the redshifted ^{12}CO integrated main-beam temperature (from 6.3 to 16 km s^{-1}). Figure 3.21 also shows the H_2 2.122 μm $v = 1 \rightarrow 0$ $S(1)$ map of the source with relevant H_2 knots labeled. The outflow encompasses several H_2 knots, labelled f09-01a-g (Khanzadyan et al 2004). Gómez et al. [2003] and Zhang et al. [2011] attribute f09-01b,e-g to the WL 10 outflow, shown as my first proposed axis for the WL 10 outflow. The second axis follows knots f09-01a,c,d which could also be related to the CO flow. As discussed in Section 3.6.3.2, these knots could be related to WL 16 (see Gómez

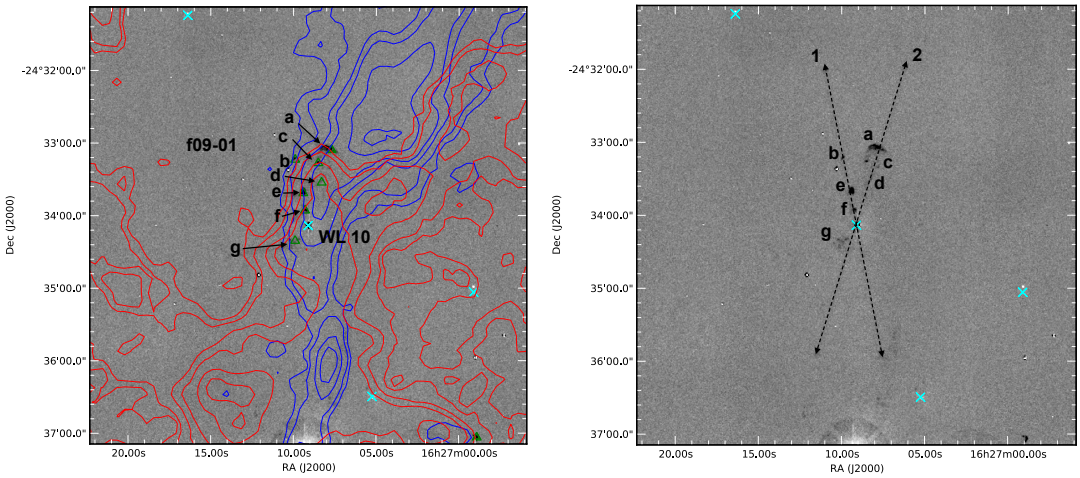

Figure 3.21: Left: Blue and redshifted contours of the Oph C region, including WL 10. Right: H_2 map of Oph C region. Proposed knots corresponding to the WL 10 outflow are labeled.

et al. 2003; Zhang et al. 2011). The combination of blue and reshifted outflow lobes and H_2 knots confirms the bipolar outflow driven by WL 10.

3.6.3.6 WL 12

WL 12 is located in the western portion of Oph C. Using ^{12}CO $J = 2 \rightarrow 1$ detections, Bontemps et al. [1996] classified the source as driving a molecular outflow because of its high velocity linewings (at least ± 5 K km s^{-1}). This study also noted that WL 12 is considered a more uncertain detection because it only fulfilled one of the criterion for being an outflow (i.e., the detection was not bipolar). Using the CO outflow criterion, only a slight redshifted lobe is detected and a high velocity blueshifted lobe is not detected. Figure 3.17 shows a close-up of the source. Blue contours trace the blueshifted ^{12}CO integrated main-beam temperature (from -5.1 to 0.9 km s^{-1}) and red contours trace the redshifted ^{12}CO integrated main-beam temperature (from 6.9 to 12.9 km s^{-1}). Blue and red contours begin at 1.5 K km s^{-1}. The image shows a faint blue and redshifted lobe at the 1.5 K km s^{-1} contour, which potentially indicates the presence of a bipolar outflow though this is a faint detection. The detected blue and redshifted emission also encompasses a H_2 knot, labelled [GSWC2003]1, which was attributed to WL 12 by Gómez et al. [2003]. The

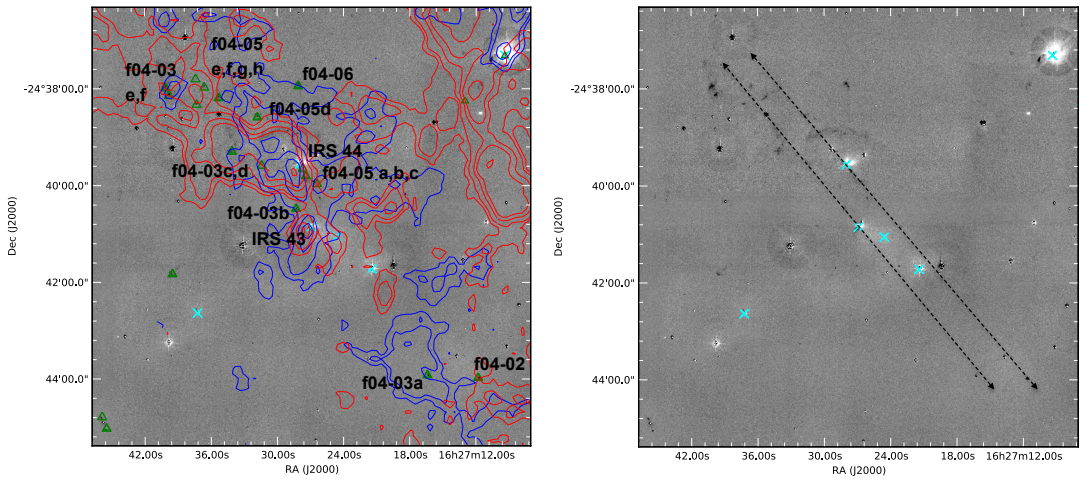

Figure 3.22: Maps of the Oph F region. Left: Blue and redshifted contours of the CO emission. Right: H_2 map of IRS 44 and IRS 43.

knot appears to be traveling to the west from the source in the opposite direction than the redshifted CO emission. Even though I cannot be certain that this source drives an outflow, it is possible that there is a bipolar outflow driven by WL 12.

3.6.3.7 IRS 43 and IRS 44

IRS 43 and IRS 44 are located in Oph F south of IRS 54. Both are known to drive a bipolar outflow (IRS 44: Bontemps et al. 1996; Bussmann et al. 2007; Terebey et al. 1989; IRS 43: Bontemps et al. 1996), which can be seen in Figure 3.22 depicting the Oph F region. Blue contours trace the blueshifted ^{12}CO integrated main-beam temperature (from -5.4 to 0.6 km s^{-1}) and red contours trace the redshifted ^{12}CO integrated main-beam temperature (from 6.6 to 13.6 km s^{-1}). Both blue and red linewings are detected in the CO outflow criterion for the sources. Several H_2 knots have been attributed to IRS 44 and IRS 43, labelled f04-02 to f04-6 [Khanzadyan et al., 2004]. The outflow axes have been labelled in Figure 3.22 over the H_2 2.122 μm $v = 1 \rightarrow 0$ $S(1)$ map of the region. Proposed axes, based on the H_2 knots, agree with Khanzadyan et al. [2004], where f04-02, f04-05 a,b,d–f,h have been attributed to IRS 44 and f04-03a–e have been attributed to IRS 43. In conclusion, the CO outflow criterion confirms the bipolar outflow driven by IRS 44 and IRS 43.

3.6.3.8 IRS 42

IRS 42 is southwest of IRS 43 and IRS 44. There is a small blue linewing detected in the CO outflow criterion without a red linewing. The source is not in a region that is particularly confused by surrounding outflow, like the outflows from IRS 43 and 44, but no high velocity emission is detected in Figure 3.17 of IRS 44 and IRS 43 or in Figure 3.23 which is a close-up of IRS 42. Blue contours trace the blueshifted ^{12}CO integrated main-beam temperature (from -6.0 to 1.2 km s^{-1}) and red contours trace the redshifted ^{12}CO integrated main-beam temperature (from 7.2 to 14.0 km s^{-1}). Blue and red contours begin at 1.5 K km s^{-1}. I cannot be certain that IRS 42 drives a bipolar outflow due to the lack of defined bipolar outflow lobes.

3.6.3.9 CRBR 2422.8-3423

CRBR 2422 is located southwest of IRS 43 and IRS 44. A small blue linewing is detected in the outflow criterion without a red linewing. Figure 3.23 shows a close-up of the source, similar to Figure 3.17. Blue contours trace the blueshifted ^{12}CO integrated main-beam temperature (from -5.4 to 1.1 km s^{-1}) and red contours trace the redshifted ^{12}CO integrated main-beam temperature (from 7.1 to 13.6 km s^{-1}). Blue and red contours begin at 1.5 K km s^{-1}. Blue and redshifted emission can be seen in the figure at the 1.5 K km s^{-1} contour. With the outflow driven by IRS 43 to the east of CRBR 2422, the faint high-velocity emission is potentially due to IRS 43. In conclusion, CRBR 2422 is in a confused region and I cannot be certain that it drives an outflow.

3.7 Conclusions

In this chapter, I introduced the HARP ^{12}CO, ^{13}CO and C^{18}O $J = 3 \rightarrow 2$ data of the Ophiuchus molecular cloud. This data (primarily ^{12}CO) was used to search for outflows and calculate the cloud mass and energetics of the region. The main conclusions can be summarised:

1. **Molecular outflow search.** Using *Spitzer* data from the survey "From Molecular Clouds to Planet-Forming Disks" or c2d [Evans et al., 2009], I identified 30 Class 0/I/II and flat spectrum sources that were further analysed for

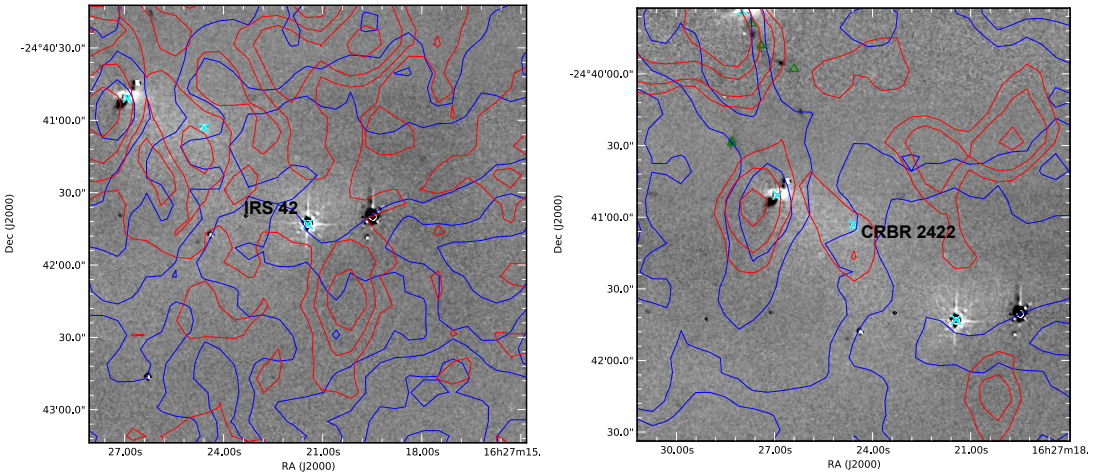

Figure 3.23: Close-up images of confused sources in Oph F.

molecular outflows. Out of the sources analysed, 8 had firm molecular outflow detections, 20 were 'confused' detections and 2 sources were non-detections.

2. **New sources.** Out of the 30 sources, 6 sources were newly identified from the c2d survey and analysed for outflows for the first time. These sources consisted of 1 Class 0, 2 Class I and 3 flat spectrum sources. All of these sources had detections for high-velocity emission but were classified as 'confused' due to confusion caused by nearby sources driving outflows.

3. **Identifying H_2 knots and outflow axes.** For sources with a blue and/or redshifted linewing detection, H_2 knots were further analysed to better understand possible directions of the outflow. This was particularly important for sources confused by the Class 0 VLA 1623 AB outflow in the Oph A region, IRS 54 with a precessing outflow axis and the Class II source WL 10 with confusion from the outflow VLA 1623 AB and EL 29. From this analysis, possible outflow directions from GSS 30 and LFAM 1 were discussed. Outflow directions from IRS 54 were examined and differing outflow directions detected by the H_2 knots and molecular outflow were reconciled. The source WL 16, initially thought to drive the H_2 knot f09-01 a,c [Gómez et al., 2003; Zhang et al., 2011], was ruled out for driving a molecular outflow because the high-velocity ^{12}CO emission corresponding to the H_2 knot does not seem to be driven by

the source. The Class II source WL10 was confirmed to drive an outflow with two possible axes, determined from the H_2 knots near the source and strong red and blueshifted linewings detected in the ^{12}CO spectrum. Lastly, IRS 44 and 43 were confirmed to drive outflows and their axes were further examined, where the location H_2 knots corresponds well with molecular outflow lobes.

Chapter 4

Ophiuchus: Global properties

As discussed in Section 2.4.3, cloud support against gravitational collapse is not fully understood. The two main theories for the physical mechanism of cloud support are magnetic fields and turbulence, where I focus on understanding turbulence in the cloud. It has been shown using simulations that turbulence can support the cloud while allowing local regions of collapse (e.g. Mac Low & Klessen 2004), where supersonic turbulence generates a pressure preventing gravitational collapse in the cloud. If turbulence does play a role in cloud support, then there must be a constant driving source replenishing the turbulence to help support the cloud. While it is possible radiative winds from nearby supernovae or main-sequence stars could drive turbulence in a molecular cloud, molecular outflows driven by young protostars may also be a dominant source of cloud turbulence (e.g. Li & Nakmura 2006).

The global properties of the cloud can be further investigated using the CO $J = 3 \rightarrow 2$ isotopologues introduced in Chapter 3. The $C^{18}O$ molecule is typically more accurate at tracing denser gas since it is less abundant and less optically thick than ^{12}CO and ^{13}CO. This makes $C^{18}O$ more useful for examining the mass and energetics (i.e. turbulent and gravitational energies) of the cloud. The optically thick and more abundant ^{12}CO molecule can be used to trace excitation temperatures and higher velocity emission associated with molecular outflows. Outflow mass and kinetic energy from ^{12}CO can then be compared to the turbulent cloud energy to examine the potential role of outflows driving turbulence in the cloud. The ^{13}CO molecule is less abundant than ^{12}CO (by a factor of $\sim$77; Wilson and Rood 1994) and more abundant than $C^{18}O$ (by a factor of 8; Frerking et al. 1982). ^{13}CO is particularly

useful for investigating the optical depths of ^{12}CO and C^{18}O to make appropriate optical depth corrections to cloud and outflow mass and energetics.

Using the HARP CO $J = 3 \rightarrow 2$ data presented in Chapter 3, the physical characteristics of L1688 Ophiuchus cloud are examined, including the excitation temperatures and optical depths. Additionally, I investigate the mass and energetics of the cloud in an attempt to understand the physical state of Ophiuchus (i.e. gravitationally bound or unbound) and the main driver of turbulence in the region (including outflow energy). This comparison of the outflow energy and cloud turbulence has been expanded to the other nearby Gould Belt clouds (including Ophiuchus, Serpens and Perseus), investigating the significance of outflow energy driving turbulence in star forming regions.

4.1 Cloud properties

In this section, the global cloud properties are examined in LTE conditions (see Section 1.3.5), where the excitation temperature and optical depths must first be determined using the CO isotopologues. Different methods are used to calculate the cloud and high-velocity outflowing mass/energetics to further investigate how the properties differ based on the initial assumptions and isotopologue used in the analysis. Similarly, the global high-velocity gas is further examined for potential drivers other than molecular outflows, e.g. hot dust from nearby B-type stars, outflow remnants from less embedded sources and stellar winds from the nearby Upper Scorpius OB association.

4.1.1 Excitation temperatures

In this section, I calculate the excitation temperature, $T_{\rm ex}$, of the ^{12}CO and ^{13}CO molecular gas assuming the emission is optically thick and in local thermodynamic equilibrium. The excitation temperature is calculated following the relation from Myers et al. [1983] described in Section 1.3.5.1,

$$T_{\rm ex}(^{12}{\rm CO}) = \frac{16.6\ {\rm K}}{\ln\left(\frac{16.6\ {\rm K}}{T_{\rm peak}+0.0377\ {\rm K}}+1\right)} \tag{4.1}$$

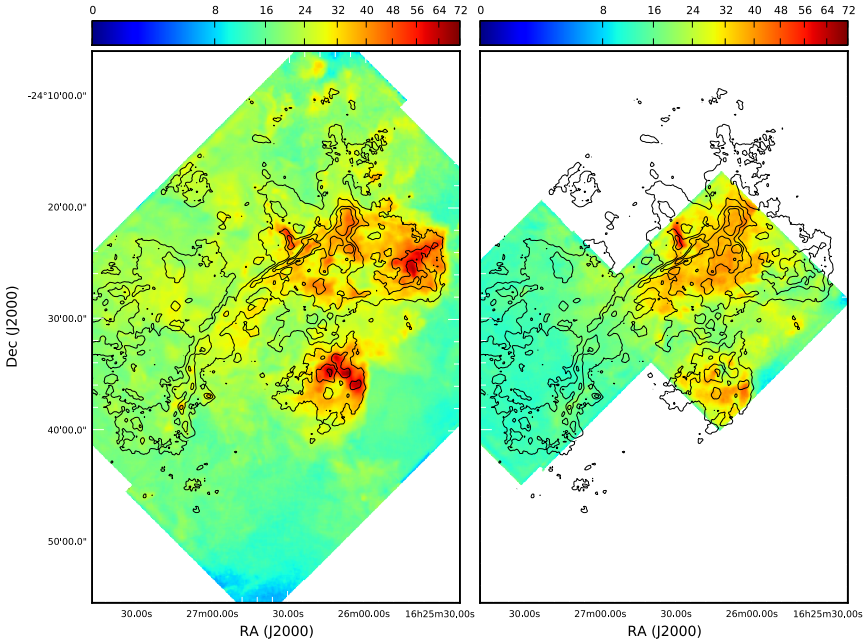

Figure 4.1: Excitation temperature maps (K) of $T_{\rm ex}(^{12}{\rm CO})$ (left) and $T_{\rm ex}(^{13}{\rm CO})$ (right) with contours from the ^{12}CO integrated main-beam intensity at levels 50, 75, 100, and 125 K km s^{-1}.

$$T_{\rm ex}(^{13}{\rm CO}) = \frac{15.9\ {\rm K}}{\ln\left(\frac{15.9\ {\rm K}}{T_{\rm peak}+0.0472\ {\rm K}}+1\right)}, \tag{4.2}$$

where $T_{\rm peak}$ is the peak main-beam temperature.

The results for ^{12}CO and ^{13}CO are shown in Figure 4.1. It is important to note that there are strong absorption features in the ^{12}CO emission ranging from $\sim$ 2.0–5.5 km s^{-1} and it is possible the excitation temperature has been underestimated for this transition. From past research, temperatures are expected to rise in protostellar outflows [Giannini et al., 2001; Hatchell et al., 1999a,b; Nisini et al., 2000]. Both $T_{\rm ex}(^{12}{\rm CO})$ and $T_{\rm ex}(^{13}{\rm CO})$ have typical ranges from 12–40 K.

The most noticeable feature in the maps is the warm gas that traces the hot dust caused by early-type B-type stars S1 and SR3 and the close binary HD 147889 (B2IV, B3IV; Casassus et al. 2008). Figure 4.2 compares ISOCAM 12 μm continuum data tracing the hot dust associated stars shown as yellow 'O's to the ^{12}CO excitation temperatures. The edge-on PDR can be seen as a filamentary-like feature in the

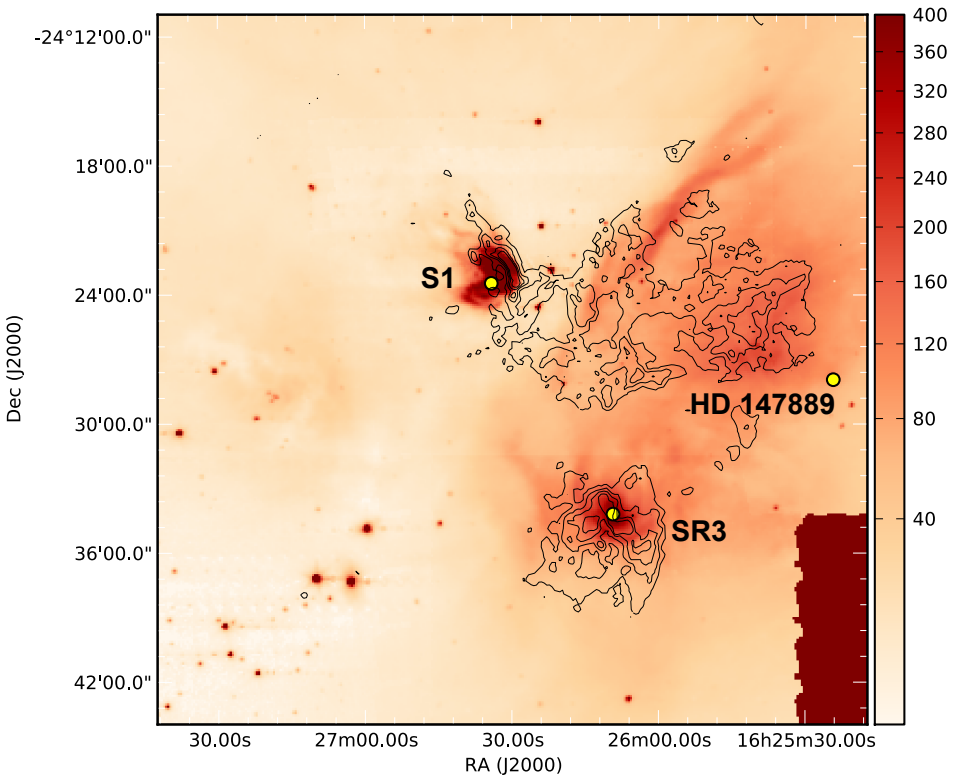

Figure 4.2: ISOCAM 12 μm map in MJy str^{-1} with ^{12}CO excitation temperature contours at levels 40, 50, 60, and 70 K. Stars HD 147889, S1, and SR3 shown.

north of Oph A. The excitation temperatures near the hot dust reach $\sim$ 70 K and $\sim$ 50 K for ^{12}CO and ^{13}CO respectively. These excitation temperatures are significantly higher than temperatures found in regions with molecular outflows. For example, near the VLA 1623 outflow in Oph A, ^{12}CO temperatures reach 30–40 K in the blueshifted flow and higher in the redshifted flow (40–50 K), where the redshifted flow has a closer proximity to the the star S1. The Elias 33 and WL 6 outflows in Oph B have ^{12}CO temperatures ranging from 20–30 K, which is similar to the temperatures found in the flows from Oph C, E, and F (including Elias 29, WL 10, IRS 44, and IRS 43).

I note the excitation temperatures for ^{13}CO are noticeably lower than ^{12}CO even though the ^{12}CO emission has the additional complication of self absorption in some portions of the cloud. This suggests the ^{13}CO is optically thin in some regions and temperature estimates based on this line must be corrected.

4.1.2 Optical depth

In this section, I calculate the optical depth of ^{13}CO and C^{18}O in Ophiuchus. Optically thin C^{18}O can be used as a tracer of the column density and mass in the cloud. It is important to calculate the C^{18}O optical depth to confirm the emission is optically thin for mass calculations. The optical depth is related to the intensity ratio of different CO isotopologues, I(^{13}CO)/I(C^{18}O), by the relation [Myers et al., 1983],

$$\frac{T_{^{13}\mathrm{CO}}}{T_{\mathrm{C}^{18}\mathrm{O}}} = \frac{1 - \exp\left(-\tau_{^{13}\mathrm{CO}}\right)}{1 - \exp\left(-\tau_{\mathrm{C}^{18}\mathrm{O}}\right)}, \tag{4.3}$$

where T is the peak brightness temperature and τ is the line centre optical depth of the corresponding isotopologues. The optical depths of the two isotopologues are related by $\tau_{^{13}\mathrm{CO}} = X\ \tau_{\mathrm{C}^{18}\mathrm{O}}$, where X is the abundance ratio for ^{13}CO/C^{18}O.

An issue with this method is the visible self absorption in the line profiles (which can be seen for the average regional spectra in Figure 3.4 of Chapter 3 for ^{12}CO and ^{13}CO and self absorption can be seen in C^{18}O for the source spectra in Figure 3.6 of Chapter 3). Another approach is to use the method in Ladd et al. [1998] which involves taking the ratio of ^{13}CO and C^{18}O integrated intensities to trace the optical depth of the cloud. Even though the self absorption will still lower the integrated intensities, this is a lower fractional error than the ratio between the peak main-beam temperatures. This method involves

$$\frac{\int_{-\infty}^{\infty} T_{^{13}\mathrm{CO}}(\mathrm{v})\ \mathrm{dv}}{\int_{-\infty}^{\infty} T_{\mathrm{C}^{18}\mathrm{O}}(\mathrm{v})\ \mathrm{dv}} = \frac{\int_{-\infty}^{\infty}(1 - \exp[-\tau_{^{13}\mathrm{CO}}(\mathrm{v})])\ \mathrm{dv}}{\int_{-\infty}^{\infty}(1 - \exp[-\tau_{\mathrm{C}^{18}\mathrm{O}}(\mathrm{v})])\ \mathrm{dv}}, \tag{4.4}$$

where $\tau_{\mathrm{C}^{18}\mathrm{O}} = \tau_{^{13}\mathrm{CO}}/X$. This equation can be further expanded so that $\tau_{^{13}\mathrm{CO}} = \tau_{^{13}\mathrm{CO}} \exp\left[-\mathrm{v}^2/2\sigma^2\right]$, which assumes a Gaussian velocity distribution and an optically thin line will have a Gaussian shape. Equation 4.4 can then be numerically minimised to determine the optical depth. I took $\sigma = 0.64$, corresponding to the average $\mathrm{v}_{\mathrm{fwhm}}$ of 1.5 km s^{-1} across the cloud. The abundance ratio was assumed to be the accepted value of $X = 8$ [Frerking et al., 1982]. Only spectra with a peak line detection of $3\sigma_{\mathrm{rms}}$ were used for the ^{13}CO and C^{18}O maps to create the ratio map, corresponding to peak line detections of 1.36 K in both maps.

Figure 4.3 shows the map of $\tau_{\mathrm{C}^{18}\mathrm{O}}$, where $\tau_{^{13}\mathrm{CO}}$ would be greater by the abun-

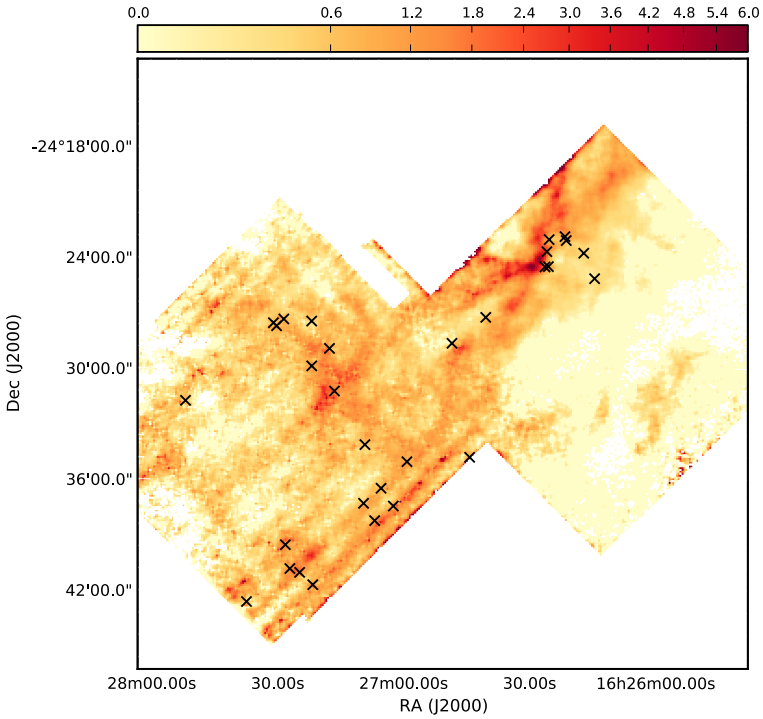

Figure 4.3: Optical depth map (τ) of $C^{18}O$. All sources examined for outflows are shown as '$\times$' . The ^{13}CO optical depth map is a factor of 8 larger than the $C^{18}O$ map.

dance factor of 8. In Oph A, typical integrated intensity ratios ^{13}CO/C^{18}O range from ∼2–7 at the sources, corresponding to $\tau_{^{13}\mathrm{CO}}$ of 2 to 16 and $\tau_{\mathrm{C}^{18}\mathrm{O}}$ of ∼0.3 to 2.0. Across the map, ^{13}CO is primarily optically thick with regions surrounding the main clump of dense gas optically thin. C^{18}O is optically thick in the regions that directly corresponding to the cores and the hot dust from S1. Near the S1 star, ^{13}CO is self-absorbed with a ^{13}CO/C^{18}O integrated intensity ratio as small as 1.2 at the region of greatest self-absorption and a corresponding high C^{18}O optical depth ($\tau_{\mathrm{C}^{18}\mathrm{O}} > 5$). Conversely, regions found to reach a ^{13}CO/C^{18}O ratio higher than the assumed abundance ratio due to systematic noise were manually set to low optical depths ($\tau_{\mathrm{C}^{18}\mathrm{O}} = 0.001$). Optical depths in Oph B, C, E, and F are more variable due to the quality of the observations (primarily striping effects that were discussed in Section 3.2.1). In these regions, the source C^{18}O optical depths can become optically thick and higher than the optical depths found for the Oph A sources which is likely from remnants of systematic striping.

4.1.3 Cloud mass

In this section, I calculate both the mass of the cloud using the C^{18}O integrated intensity and the virial mass of the cloud assuming a spherical cloud of uniform density [Rohlfs and Wilson, 2000]. Mass calculations are summarised in Table 4.1. From Section 4.1.2, the optical depth of C^{18}O emission is optically thick in some regions, indicating an optical depth correction needs to be applied when calculating the mass from the integrated C^{18}O emission. Only pixels with a peak T_{MB} of at least $3\sigma_{\mathrm{rms}}$ (1.36 K) were included in the calculation. The excitation temperature, T_{ex}, was calculated using the ^{13}CO peak temperature (Section 4.1.1). In regions without T_{ex} data, the average excitation temperature from ^{13}CO was used ($T_{\mathrm{ex}} = 20$ K). A ratio of C^{18}O to H$_2$ was taken to be $X_{\mathrm{C}^{18}\mathrm{O}} = 10^{-7}$ so the result could be compared directly with other work on GBS clouds [Curtis et al., 2010b; Graves et al., 2010], which is similar to the commonly used value from Frerking et al. [1982] of 1.7×10^{-7}. The distance to the cloud was assumed to be 120 pc. Assuming local thermodynamic

equilibrium, the mass was calculated using the relation from Section 1.3.5.3,

$$M_{\mathrm{C^{18}O}} = 2.29 \times 10^{-5} \left(\frac{\text{Pixel length}}{3.49 \times 10^{-3} \mathrm{pc}} \right)^2 \left(\frac{X_{\mathrm{C^{18}O}}}{10^{-7}} \right)^{-1} \times \sum_j \left(\frac{T_{\mathrm{ex},j}}{\exp\left(\frac{-31.6}{T_{\mathrm{ex},j}}\right)} \frac{\tau_{\mathrm{C^{18}O},j}}{1 - \exp(-\tau_{\mathrm{C^{18}O},j})} \int T_{\mathrm{MB},j} \ \mathrm{dv} \right) \ \mathrm{M}_\odot, \tag{4.5}$$

where X_{CO} is the relative abundance of $C^{18}O$ to H_2, pixel length is the length of one pixel in parsecs assuming the distance of the cloud at 120 pc, $\tau_{\mathrm{C^{18}O}}$ is the $C^{18}O$ optical depth (Section 4.1.2), $\int T_{\mathrm{MB}}$ dv is the integrated main-beam temperature of $C^{18}O$, and j is an index over map pixels. A mass of 515 $\mathrm{M}_\odot$ was calculated for the cloud. Without the optical depth correction, the mass of the cloud was 439 $\mathrm{M}_\odot$. Previous studies of star forming regions [Buckle et al., 2010; Curtis et al., 2010b; Graves et al., 2010] have assumed a constant excitation temperature of around 10–12 K based on the ^{13}CO average excitation temperature. Had the lower, constant excitation temperature been used, the mass would increase by a factor of ∼1.6–2.3.

The virial mass of the cloud can be calculated using the following relation [MacLaren et al., 1988],

$$M_{\mathrm{vir}} = \frac{3c \ \sigma^2 R}{G}, \tag{4.6}$$

where I assume σ is the 1D velocity dispersion $\Delta \mathrm{v}_{\mathrm{C^{18}O}}/\sqrt{8 \ln 2}$, $\Delta \mathrm{v}_{\mathrm{C^{18}O}}$ is the FWHM velocity in km s^{-1}, R is the radius of the cloud in parsecs, and G is the gravitational constant. The constant c is based on the density profile as a function of distance from the cloud centre, $\rho(r) = r^{-n}$,

$$c = \frac{5 - 2n}{3 - n}, \tag{4.7}$$

where $n = 2$, $\rho(r) = r^{-2}$ and $c = 1$. The FWHM velocity $\Delta \mathrm{v}_{\mathrm{C^{18}O}}$ was determined to be 1.5 km s^{-1} by fitting a Gaussian to the $C^{18}O$ average spectrum across the cloud. An effective radius of the cloud was determined from $A = \pi R_{\mathrm{eff}}^2$, where A is the total pixel area of the map with peak T_{MB} detections of at least $3\sigma_{\mathrm{rms}}$. This gave a radius of 14′ or 0.50 pc at a 120 pc distance. The virial mass was determined to be 141 $\mathrm{M}_\odot$.

The virial mass is 27 per cent of the calculated $C^{18}O$ mass, indicating the cloud is in a hugely overbound state, which is further discussed in the next section. Our study agrees with results from past studies using ^{13}CO 1–0 (Loren 1989; radius of 0.3 pc and 1.5 km s^{-1} velocity width) and $C^{18}O$ 1–0 (Tachihara et al. 2000; radius of 0.4 pc and 1.5 km s^{-1} velocity width) assuming a distance of 120 pc. The effective radius from the HARP $C^{18}O$ data is larger than the radius calculated by Tachihara et al. [2000] simply due to the larger map size of the HARP observations. Loren [1989] found the virial mass was 24 per cent of the total gas mass (475 $M_\odot$ gas mass and 113 $M_\odot$ M_{vir}) and Tachihara et al. [2000] found the virial mass to be 21 per cent of the cloud mass (455 $M_\odot$ gas mass and 97 $M_\odot$ M_{vir}. Similarly, Nakamura et al. [2011] calculated the virial mass to be 22 per cent of the mass for the total L1688 cloud (R21-22, R24-26) using the ^{13}CO data from Loren [1989] where a distance of 125 pc and a radius of 0.8 pc was used. My calculated virial mass is larger than many of these past studies due to the higher effective radius used in Equation 4.6.

To assess the reliability of the average cloud FWHM velocity, Figure 4.4 shows the FWHM (km s^{-1}) of each spectrum with a line peak of at least 3σ in $C^{18}O$. The FWHM is estimated by counting the number of velocity channels with half the peak intensity in the spectrum. I note the average FWHM of 1.5 km s^{-1} is not necessarily valid for the entire cloud and increases the uncertainty in this calculation.

4.1.4 Global energetics

To understand the energetics of the cloud better, the gravitational binding energy and the turbulent kinetic energy can be estimated assuming a uniform cloud density using the relations,

$$E_{\rm grav} = -\frac{3}{5}\gamma\frac{GM^2}{R} \tag{4.8}$$

$$E_{\rm kin} = \frac{3}{2}M\sigma^2, \tag{4.9}$$

where G is the gravitational constant, M is the mass of the cloud (Section 4.1.3), γ is typically 5/3 assuming a spherical cloud with density structure $\rho \propto r^{-2}$, R is the radius of the cloud (Section 4.1.3), and $\sigma = \Delta v_{C^{18}O}/\sqrt{8\ln 2}$ is the 1D velocity dispersion. As shown from Figure 4.9, the turbulent energy of the cloud is typically

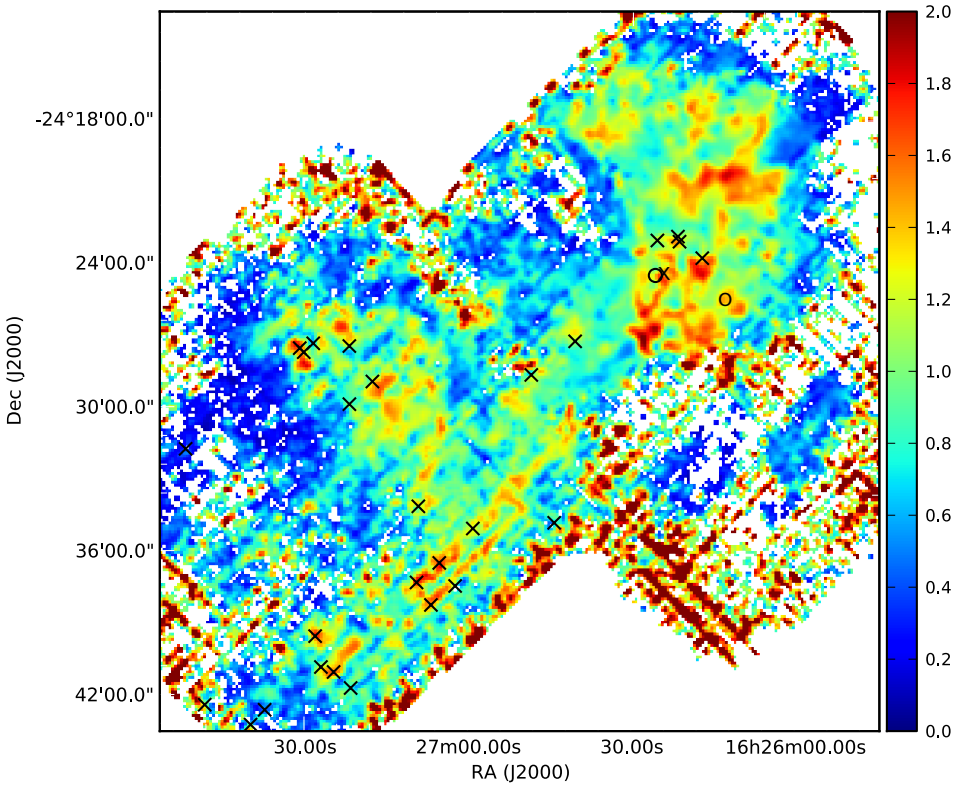

Figure 4.4: $C^{18}O$ FWHM of lines with 3σ peak intensity smoothed by 15 arcsec Gaussian. Protostellar sources from Section 3.5 are shown with Class 0 sources as '○' and Class I, flat spectrum and Class II sources as '×'.

Cloud	Total Mass ($M_\odot$)	E_{kin} (J)	E_{grav} (J)	Outflow Energy (J)
Ophiuchus	515	6.3×10^{38}	4.5×10^{39}	1.3×10^{38}

Table 4.1: Global mass and energetics.

measured using the line width of a molecular line. The $C^{18}O$ linewidth is used to trace the bulk motions of the dense cloud (i.e. turbulence) since the molecule is less optically thick than ^{12}CO which traces higher velocity outflowing gas (e.g. Curtis et al. 2010b; Graves et al. 2010).

For Ophiuchus, the gravitational binding energy was $4.5{\times}10^{39}$ J (2282 $M_\odot$ km^2 s^{-2}). Using v_{FWHM} from the average $C^{18}O$ spectrum across the cloud (Section 4.1.3), the turbulent kinetic energy was found to be 6.3×10^{38} J (320 $M_\odot$ km^2 s^{-2}). The global energetics are summarised in Table 4.5. The turbulent kinetic energy is roughly a factor of ∼7 smaller than the binding energy, which also suggests the the cloud is gravitationally bound as in Section 4.1.3.

The low virial mass calculated in the previous section suggests the cloud is overbound and potentially in a global state of collapse. Past research [Evans et al., 2009; Nakamura et al., 2011] suggests the virial ratio is small due to a lower star formation activity. Many of the YSOs in the region are older and less embedded (∼100 Class II sources), indicating more active cloud in the past. Outflows that may be a source of turbulence are not driven by less embedded sources. An alternative explanation is that the L1688 region may be compressed by an expanding shell created by stellar winds and supernovae from the Scorpius OB association [Loren and Wootten, 1986; Vrba, 1977]. According to Nakamura et al. [2011], this compression could lead to a higher gravitational energy and therefore a lower virial mass. Section 4.1.7 further investigates the global outflow energy of the region and compares the outflow and turbulent kinetic energies to better understand the main driver of turbulence in the region.

I note the mass and energetics of the cloud have nontrivial uncertainties from the input parameters and assumptions in the calculations. In Section 4.1.3, the largest sources of uncertainty on the mass include the $C^{18}O$ abundance and the assumption of LTE. Christie et al. [2012] further studied CO depletion in Gould Belt clouds by comparing $N(H_2)$ calculated from $C^{18}O$ and 850 μm data. For the

Ophiuchus region, $C^{18}O$ was found to have a higher average depletion or lower $C^{18}O$ abundance in bother starless and prestellar cores by factors of 7 and 4 respectively assuming $X_{C^{18}O} = 1.7 \times 10^{-7}$. Using the $C^{18}O$ abundance from Section 4.1.3 of $X_{C^{18}O} = 10^{-7}$, this corresponds to depletion factors of 4 and 2 respectively in the regions of starless and prestellar cores. Depending on varying depletion factors, the mass of the Ophiuchus cloud would change accordingly (i.e. higher depletion levels would increase the mass of the cloud by the depletion factor).

Uncertainties on the energetics involve the uncertainties of the mass, the assumption the cloud is a uniform density sphere (e.g. for the virial mass and gravitational binding energy calculations) and assuming a single velocity dispersion σ for the entire cloud. The velocity dispersion in particular is the combination between the thermal and non thermal motions where

$$\sigma^2 = \sigma_{\rm NT}^2 + \sigma_{\rm T}^2 \tag{4.10}$$

$$\sigma_{\rm T} = \frac{kT_{\rm ex}}{m_p \mu_{C^{18}O}} \tag{4.11}$$

where $\sigma_{\rm NT}$ is the non thermal dispersion and $\sigma_{\rm T}$ is the thermal dispersion. From Section 4.1.3, I assume $\sigma_{\rm T}$ is negligible (where $\sigma_{\rm T} = 0.07$ km s^{-1} for a cloud $T_{\rm ex} =$ 20 K, leading to $\sigma_{\rm NT} = 0.797$ km s^{-1} compared to the value I use in Section 4.1.3 of $\sigma = 0.798$ km s^{-1}).

4.1.5 Cloud mass and energetics using ^{13}CO

$C^{18}O$ has a lower abundance and optical depth than ^{13}CO and does not necessarily account for the mass and kinetic energy of less dense material in the cloud. To test the cloud mass calculation, I calculate the mass of the cloud using the ^{13}CO integrated intensity with a peak intensity of at least 3σ using the mass relation

assuming local thermodynamic equilibrium

$$\begin{aligned} \mathrm{M}_{^{13}\mathrm{CO}} &= 3.03 \times 10^{-8} \left(\frac{X_{^{13}\mathrm{CO}}}{1.4 \times 10^{-6}} \right)^{-1} \left(\frac{\mathrm{d}}{120 \text{ pc}} \right)^{2} \\ &\times \left(\frac{A_{\mathrm{pixel}}}{\mathrm{arcsec}^2} \right) \sum_{j} \left(\frac{T_{\mathrm{ex},j}}{\exp\left(\frac{-31.6}{T_{\mathrm{ex},j}} \frac{\tau_{^{13}\mathrm{CO},j}}{1-\exp\left(\tau_{^{13}\mathrm{CO},j}\right)} \right)} \int T_{\mathrm{MB},j} \, \mathrm{dv} \right) \mathrm{M}_{\odot}, \end{aligned} \tag{4.12}$$

where $X_{^{13}\mathrm{CO}}$ is the relative abundance of ^{13}CO to H_2, A_{pixel} is the pixel area (36 arcsec^2), T_{ex} is the ^{13}CO excitation temperature from Section 4.1.1, $\tau_{^{13}\mathrm{CO},j}$ is the ^{13}CO optical depth from Section 4.1.2 and j is an index over map pixels. The relative abundance $X_{^{13}\mathrm{CO}}$ I use is $1.4{\times}10^{-6}$ from Frerking et al. [1982] and Wilson and Rood [1994].

The mass calculation is similar to the relation used for the outflow mass and energetics in Section 4.1.7. Kinetic and gravitational energies were similarly calculated using Equations 4.8 and 4.9, where the radius of the cloud using an effective area from ^{13}CO emission was 13.6′ or 0.47 pc and the one-dimensional velocity dispersion for the averaged ^{13}CO spectrum across the cloud was based on $\mathrm{v}_{\mathrm{FWHM}} = 2.0$ km $^{-1}$. I note ^{13}CO isn't as likely to trace high velocity outflowing gas like ^{12}CO (e.g. Arce et al. 2007), but can potentially trace higher densities found in the flows. Only pixels with a line peak of 3σ (1.36 K) were used in the calculation.

The calculated mass of the cloud using the ^{13}CO data corrected for optical depth is 582 $\mathrm{M}_{\odot}$, which is a factor 1.1 larger than the mass calculated from C^{18}O. The kinetic energy of the cloud was 1.3 $\times 10^{39}$ J (630 $\mathrm{M}_{\odot}$ km^2 s^{-2}), which is a factor of $\sim$2 larger than the estimate of cloud turbulence using C^{18}O. The virial mass calculated from ^{13}CO is also roughly a factor of 1.7 larger due to the larger one-dimensional velocity dispersion value, increasing to 238 $\mathrm{M}_{\odot}$. The virial mass is $\sim$40% of the total cloud mass, indicating the ^{13}CO emission shows the cloud is 'less' bound than the C^{18}O emission but still gravitationally bound. The corresponding gravitational binding energy is 6.2 $\times 10^{39}$ J (3117 $\mathrm{M}_{\odot}$ km^2 s^{-2}). Using the ^{13}CO data, the gravitational energy is still $\sim$5 times larger than the kinetic energy.

The main difference between the measurements of cloud masses and energies calculated from C^{18}O and ^{13}CO is primarily due to the FWHM velocity. ^{13}CO has

a FWHM cloud velocity higher than the $C^{18}O$ by a factor of 1.3. This suggests there may be material with lower densities at higher velocities, which increases both the virial mass and turbulent kinetic energy of the cloud and results in the cloud being less bound than $C^{18}O$ calculations. However, there is also a possibility that the larger FWHM cloud velocity is biased by the high-velocity outflows that can potentially be traced by ^{13}CO. The cloud properties calculated by ^{13}CO emission still suggest the cloud is gravitationally bound and turbulence is not strong enough to surpass the gravitational binding energy.

4.1.6 ^{12}CO high-velocity optical depths

As discussed in Section 2.4.3, molecular outflows can potentially inject energy into the cloud and act as a substantial driving source for turbulence in a molecular cloud. ^{12}CO emission is often optically thick even in higher velocity regions. It is important to correct ^{12}CO emission for optical depth because high optical depths lead to underestimates of the masses and energetics of the molecular outflows. The ratio of ^{12}CO and ^{13}CO main-beam temperature was used to calculate the ^{12}CO opacity per velocity channel, $\tau_{12}(v)$. The maps are averaged into a single spectrum and clipped at $3\sigma_{rms}$ and $1\sigma_{rms}$ for ^{12}CO and ^{13}CO respectively. With this clipping, opacity could be calculated in the ^{12}CO linewings over a velocity range ~0–9 km s^{-1}.

The ^{12}CO optical depth is calculated using a similar relation to the one used in Section 4.1.5 (see also Curtis et al. 2010b; Graves et al. 2010; Hatchell et al. 1999a)

$$\frac{T_{12}}{T_{13}} = \left(\frac{\nu_{12}}{\nu_{13}}\right)^2 f \left(\frac{1-\exp(-\tau_{12})}{\tau_{12}}\right), \tag{4.13}$$

where T is the main-beam temperature of each CO transition, ν is the frequency of the isotopologues, f is the relative abundance of ^{12}CO to ^{13}CO ($f \approx 77$; Wilson and Rood 1994), and τ_{12} is the optical depth of ^{12}CO. Even though ^{12}CO is expected to become optically thin in the high velocity blue- and redshifted linewings, ^{13}CO does not extend as far in velocity range as ^{12}CO emission. Therefore, this equation was solved by assuming $\tau_{12} >> 1$ so that $1 - \exp(\tau_{12}) \approx 1$.

Figure 4.5 shows the ratio of ^{12}CO to ^{13}CO main-beam temperatures with the calculated ^{12}CO optical depth per velocity channel. The ^{12}CO emission is optically

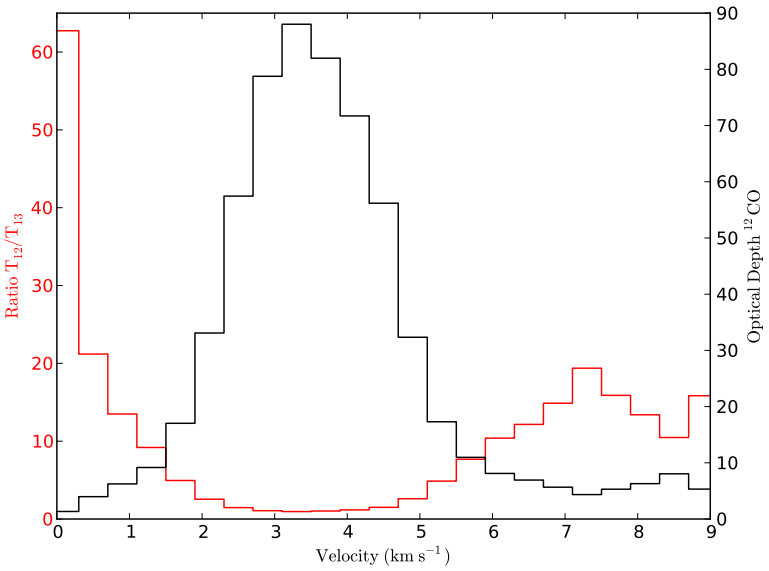

Figure 4.5: ^{12}CO optical depth variation with velocity, τ_{12}(v). The ratio of ^{12}CO to ^{13}CO is shown as a function of velocity (red) and the ^{12}CO optical depth is shown for the same velocity region (black).

thick ($\tau_{12} > 1$) in the velocity range $\sim$ 0–9 km s^{-1} with detectable ^{13}CO. The limit of the ^{12}CO optical depth measurement is $\tau_{12} \sim 3$. The ratio of ^{12}CO and ^{13}CO main-beam temperatures supports the suggestion that ^{12}CO is optically thick because the ratio only begins to approach the abundance ratio at the edges of the velocity range. I note the ratio at redshifted velocities ($\sim$7–9 km s^{-1}) does not fully reach the abundance ratio, indicating ^{12}CO is still optically thick in this range. The opacity correction applied to the ^{12}CO main-beam temperature is further discussed in Section 4.1.7.

4.1.7 Outflow energetics

The ^{12}CO $J = 3 \rightarrow 2$ gas traveling at high blue and redshifted velocities was used to calculate the global outflow mass and energetics of the cloud. To exclude ambient emission, the central velocity, v_0, was calculated using the average C^{18}O spectrum of the cloud and fit with a Gaussian to determine the line centre. The cloud velocity is measured to be 3.3 km s^{-1} and the line criterion used to determine the velocities of ambient gas was $v_0 \pm 2.5$ km s^{-1}. The line criterion used for the global energetics

is similar to the outflow criterion (Section 3.5.1) but it accounts for the change in the line centre up to 1 km s^{-1} that is seen across the cloud. However, some ambient emission will be included in these calculations because there is no fixed velocity boundary between outflow-driven gas and gas set in motion by ambient cloud turbulence. Unlike the cloud properties calculated from C^{18}O, the outflow mass and energetics are only calculated from the high velocity ranges associated with molecular outflows. The range of ambient velocities are further examined in Section 4.1.7.1 and a new ambient velocity is chosen based on ^{13}CO optical depths.

Assuming local thermodynamic equilibrium (LTE; as in Section 4.1.5), mass was calculated assuming a distance of 120 pc, optical depth corrections were included per velocity channel based on the calculations in Section 4.1.6, and a constant excitation temperature of 50 K was used [Curtis et al., 2010b; Graves et al., 2010; Hatchell et al., 2007a]. Mass was calculated using the relation

$$\begin{aligned} M_{^{12}\mathrm{CO}} &= 3.77 \times 10^{-8} \left(\frac{X_{\mathrm{CO}}}{10^{-4}}\right)^{-1} \left(\frac{\mathrm{d}}{120\ \mathrm{pc}}\right)^{2} \\ &\times \left(\frac{A_{\mathrm{pixel}}}{\mathrm{arcsec}^2}\right) \sum_j \left(\int T_{\mathrm{MB},j}\ \mathrm{dv}\right)\ \mathrm{M}_\odot, \end{aligned} \tag{4.14}$$

where X_{CO} is the relative abundance of CO to H_2 [Blake et al., 1987], A_{pixel} is the pixel area (36 arcsec^2) and j is an index over map pixels. To estimate the momentum and energy, $\int T_{\mathrm{MB}}\ \mathrm{dv}$ is replaced by $\int T_{\mathrm{MB}}|\mathrm{v}-\mathrm{v}_0|\ \mathrm{dv}$ and $\frac{1}{2}\int T_{\mathrm{MB}}(\mathrm{v}-\mathrm{v}_0)^2\ \mathrm{dv}$ respectively, where v_0 is the line centre for the cloud. With the correction for ^{12}CO optical depth discussed in Section 4.1.6 and similarly for ^{13}CO in Section 4.1.5, the integrated main-beam intensity becomes

$$\int T_{\mathrm{corr}}\ \mathrm{dv} = \int T_{\mathrm{MB}}\ \frac{\tau_{12}}{1-\exp\left(-\tau_{12}\right)}\ \mathrm{dv} \tag{4.15}$$

and the momentum and energy estimates are corrected similarly. Blue- and red-shifted main-beam temperatures are integrated from -8–0.8 and 5.8–15 km s^{-1} respectively and the opacity correction is applied to the corresponding velocity channels 0–9 km s^{-1} (Section 4.1.6). Velocity channel limits are based on detectable ^{12}CO emission at $1\sigma_{\mathrm{rms}}$.

The basic kinematics for the global outflowing gas in Ophiuchus are summarised

	Mass ($M_\odot$)	Momentum ($M_\odot$ km s^{-1})	Energy ($M_\odot$ km^2 s^{-2})
Thin			
Blue	0.20	0.74	1.49
Red	0.54	1.74	3.18
Opacity Corr.			
Blue	0.42	1.36	2.36
Red	4.30	12.67	19.85
Inclination Corr.			
Blue	–	2.72	7.08
Red	–	25.34	59.55

Table 4.2: Kinematics for the global outflowing gas assuming optically thin ^{12}CO linewing emission (thin), an optical depth correction (opacity corr.), and a correction for inclination (inclination corr.).

in Table 4.2. The mass, momentum, and energy increase substantially by factors of 6.4, 5.7, and 4.8 respectively when the optical depth of ^{12}CO is taken into account. I note the mass of the redshifted outflowing gas is substantially higher than the blueshifted gas, particularly seen in the opacity corrected values. This difference is the result of higher optical depths calculated in redshifted velocities (up to 9 km s^{-1}), which boosts the mass, momentum and kinetic energies in those channels. Effects involving outflow inclination angle can also greatly reduce the amount of momentum and energy observed. A correction for inclination can be applied to the blue- and redshifted velocities for momentum and energy calculations. The line of sight velocities should be corrected by a factor of $1/\cos(i)$, where i is the inclination angle. Assuming random inclinations to the line of sight with uniformly distributed outflows ($i \approx 57.3$ deg; Bontemps et al. 1996), the momentum will increase further by a factor 2 and the energy by a factor 3 [Curtis et al., 2010b].

The kinetic energy found at higher velocities gives an insight into the amount of turbulence generated by high-velocity molecular outflows. The outflow kinetic energy can be compared to the turbulent kinetic energy of the cloud to further examine the possibility for outflows to drive cloud turbulence and potentially unbind the cloud. When inclination is taken into account, the total outflow kinetic energy is 1.3×10^{38} J (67 $M_\odot$ km^2 s^{-2}). The total outflow kinetic energy is found to be 21% of the turbulent kinetic energy. This suggests that outflows are significant but

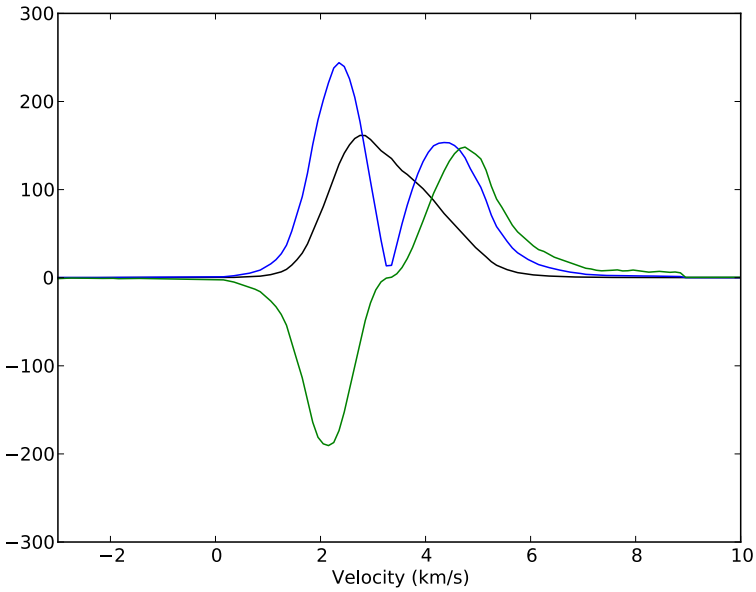

Figure 4.6: Integrated outflowing gas for Ophiuchus. Values are in: mass (black - $M_\odot$), momentum (blue - $M_\odot$ km s^{-1}), energy (green - $M_\odot$ km^2 s^{-2}).

not the dominant source of turbulence in Ophiuchus.

4.1.7.1 Global outflowing gas

The calculated energetics of the outflowing gas can vary with the channels chosen for the outflow velocity range. I further examine the relationship of the mass, momentum, and energy per velocity channel (opacity corrected) for the sum over the Ophiuchus cloud in Figure 4.6 to determine how these properties depend on the velocity range of the integrated emission. The bulk of the mass, momentum and kinetic energy are within the ambient velocity range, indicating these properties can significantly vary if the inner velocity boundaries are changed. In the outer velocities, the kinetic energy and to a lesser extent the moment can become more unreliable due to noise.

Figure 4.7 further examines the effects of the inner and outer velocity ranges on the outflow mass, momentum, and energy. This figure shows the total value of mass, momentum and kinetic energy using (left) varying outer velocities assuming a constant line centre and (right) varying inner velocities using a fixed outer veloc-

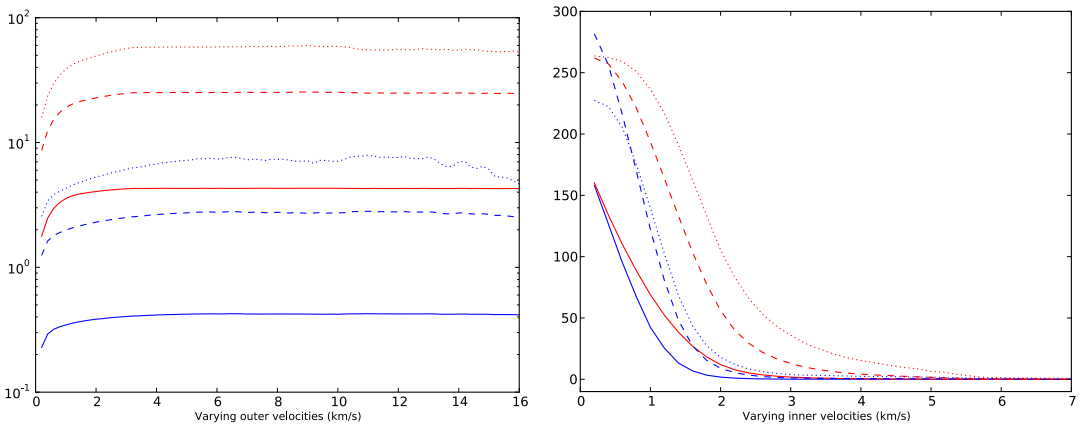

Figure 4.7: *Left:* Shows the total sum value with a constant line centre and varying outer velocities for the ^{12}CO outflow mass and energetics calculations. *Right:* Shows the total sum value with a constant outer velocity and varying line centres. Red and blue lines correspond to red and blueshifted emission. Values are in: solid line - mass ($M_\odot$), dashed line - momentum ($M_\odot$ km s^{-1}), dotted line - energy ($M_\odot$ km^2 s^{-2}).

ity. The variation of the outer channel with a constant inner velocity range (inner velocities - blue: 0.8 km s^{-1}; red: 5.8 km s^{-1}) does reinforce that the kinetic energy can be influenced by the choice of outer velocity for integration but only by up to 10$M_\odot$ km^2 s^{-2}. Specifically, when more channels are included in the kinetic energy calculation, the energy begins to decrease due to noise in the outer channels that is amplified by the factor $(v_o - v)^2$. The variation of the inner velocity with a constant outer velocity (outer velocities - blue: -8.0 km s^{-1}; red: 15.0 km s^{-1}) affects the mass and energetics to a greater extent than the variation of the outer velocities. The ambient velocity range is particularly important, causing either ambient emission to be included in the outflow emission (due to a small ambient velocity range) or excluding velocity channels with outflowing emission (due to a large ambient velocity range).

It is possible the criterion for ambient gas velocities used in the calculation of outflow energetics (3.3 $\pm$ 2.5 km s^{-1}) from Section 4.1.7 may have included lower velocity outflowing gas. To better examine the velocity range of global ambient emission, other factors can be used to determine ambient velocities including the optical depth of the ^{13}CO molecule which is expected to be optically thin in high-velocity 'outflowing' velocities. I calculate the ^{13}CO opacity per velocity channel

τ_{13}(v) using the ratio of ^{13}CO and C^{18}O emission (T_{13}/T_{18}). I use the relation

$$\frac{T_{13}}{T_{18}} = \frac{1 - \exp(-\tau_{13})}{1 - \exp(-\tau_{18})} \tag{4.16}$$

where $\tau_{18} = \tau_{13}/X$ assuming an abundance factor X of 8. The ^{13}CO and C^{18}O spectra at the positions of the eight sources with confirmed outflows (determined by Section 3.5 to be sources 8, 16, 17, 21, 24, 25, 27, 30) were averaged to calculate τ_{13}(v). This was done by increasing the pixel size to a 30 arcsec diameter to decrease noise and extracting the spectra for each source with at least a 3σ peak detection. Spectra were then cut at 1σ. Ambient emission was defined by velocity channels with optically thick ^{13}CO emission ($\tau_{13} > 1$). This is similar to the methods used in Sections 4.1.5 and 4.1.6, however there is no assumption that C^{18}O is optically thin. This is due to the possibility of optically thick C^{18}O emission in the immediate regions of the dense cores (see Section 4.1.2).

Figure 4.8 shows the T_{13}/T_{18} ratio and correspond τ_{13}. Optically thick emission spans $\sim$2 km s^{-1}, off centre from the ambient cloud emission of 3.3 km s^{-1}. It is possible that optically thick emission is off centre from the ambient cloud emission due to more sources with confirmed outflows in Oph B, C, E, F which are known to have higher ambient velocities (measured by C^{18}O in Section 3.5). The peak ^{13}CO optical depth corresponds to a velocity 3.8 km s^{-1}, which is 0.5 km s^{-1} greater than the central velocity measured by C^{18}O. Optically thick ^{13}CO ($\tau_{^{13}\mathrm{CO}} > 1$ is found at a velocity range from 2.5–4.7 km s^{-1}. I use this new velocity range from optically thick ^{13}CO to define ambient velocities in the cloud, which covers the ambient cloud central emission at 3.3 km s^{-1} from C^{18}O.

Using the new ambient velocity criterion and the same extreme velocity cuts from Section 4.1.7, I recalculate the global outflow mass, momentum, and kinetic energy, shown in Table 4.3. Mass, momentum, and energy increase by factors of 22, 11, and 6 respectively. This indicates a large percentage of the mass and energy is found in lower velocities of the cloud not originally included in the $v_o \pm 2.5$ km s^{-1} ambient velocity criterion. In relation to the cloud energetics, the total outflow energy (370 M$_\odot$ km^2 s^{-2}) is 1.2 times the turbulent energy of the cloud. This suggests the global outflows may drive turbulence in the cloud, assuming a 2.2 km s^{-1} ambient velocity range.

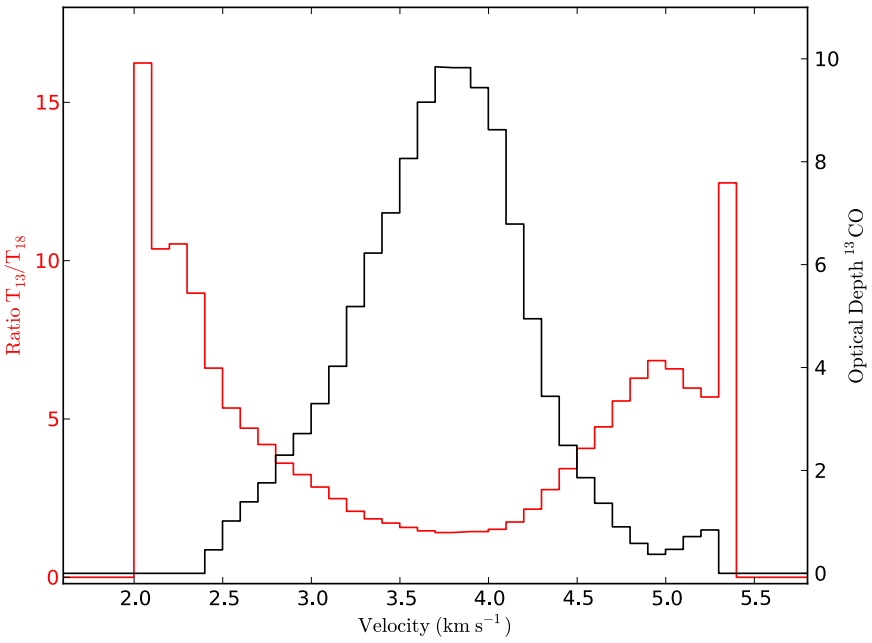

Figure 4.8: ^{13}CO opacity per velocity channel τ_{13}(v) with the ratio T_{13}/T_{18} used to define the ambient velocity range for the ^{13}CO cloud mass calculations.

	Mass ($M_\odot$)	Momentum ($M_\odot$ km s^{-1})	Energy ($M_\odot$ km^2 s^{-2})
Opacity Corr.			
Blue	67	86	59
Red	38	67	64
Inclination Corr.			
Blue	–	172	178
Red	–	133	192

Table 4.3: Global kinematics for the global outflowing gas assuming opacity corrected ^{12}CO linewing emission (opacity corr.) and with an a correction for inclination (inclination corr.). Ambient velocities were defined by the ^{13}CO opacity.

When compared to the turbulent kinetic energy calculated from ^{13}CO in Section 4.1.5 which includes energy from less dense gas in the cloud than the C^{18}O calculation, the global outflow energy is 59% of the cloud binding energy, which is higher than the 21% contribution calculated in Section 4.1.7, potentially indicating the outflows could be significant in regulating star formation in the cloud. Additionally, it is possible this ambient velocity range does not fully cover all of the ambient emission in the cloud, causing the increase in the global outflow energy. The influence of outflows on the global cloud turbulence is further discussed in Section 4.2.3, including the possibility for overlap between the ambient velocities defined using C^{18}O to calculate the cloud turbulence and outflow velocity ranges used in calculating outflow kinetic energies.

4.1.7.2 Mass-velocity relation

Past studies [Chandler et al., 1996; Downes and Cabrit, 2003; Lada and Fich, 1996; Masson and Chernin, 1993; Richer et al., 2000; Rodriguez et al., 1982; Stahler, 1994] indicate that molecular outflows have a power law dependence between the mass of the outflow $M(\mathrm{v})$ per velocity. This dependence characterised by $M(\mathrm{v}) \propto \mathrm{v}^{-\gamma}$ where $\gamma = 1.8$ is the typical value for low mass outflows. The slope steepens when $\Delta\mathrm{v} = |\mathrm{v} - \mathrm{v_o}| > 10$ km s^{-1} (where $\mathrm{v_o}$ is the ambient velocity) to values $\gamma \approx 3 - 7$. The mass-velocity relation is particularly important for understanding molecular outflow acceleration, e.g. through entrainment by a jet, and the various components of the outflow.

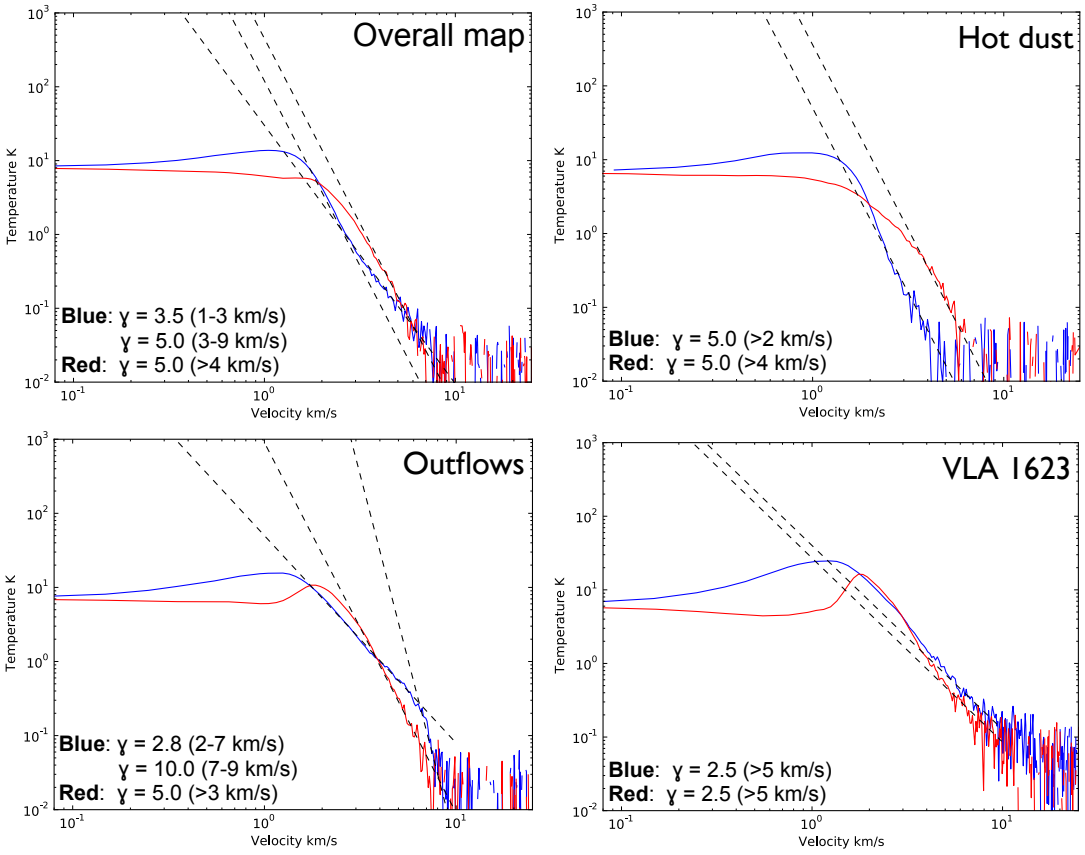

Figure 4.9: Plots of mass ($M(\mathrm{v}) \sim T_{\mathrm{MB}}(\mathrm{v})$) per velocity of the averaged ^{12}CO spectrum across the cloud, the region corresponding to the hot dust from ISOCAM 12μm, regions corresponding to red and blue outflow lobes and the VLA 1623 outflow. Dotted lines correspond to the fit v^{γ}, where the value of γ is shown for each region.

In Figure 4.9, I make a comparison between the sum of the main-beam emission (not corrected for ^{12}CO opacity) $\sum_j T_{\mathrm{MB},j}(\mathrm{v})$ where j is an index over map pixels per change in velocity Δv. I investigate γ from different regions of the cloud: (top left) the entire map, (top right) the region corresponding to hot dust from the ISOCAM 12 μm emission defined in Section 3.4, (bottom left) the region corresponding to outflow lobes identified in Section 3.5 and (bottom right) the region corresponding to the Class 0 outflow VLA 1623 AB. At velocities below 1–2 km s^{-1}, ambient emission dominates the main-beam temperature (i.e. mass). For the total cloud, there appears to be a power-law relation starting at 3 km s^{-1} for the blueshifted emission which is not present for the redshifted emission. The blueshifted emission shows $\gamma \approx 5.0$ at velocities less than 2–3 km s^{-1} and $\gamma \approx 3.5$ at velocities greater than 3 km s^{-1}. The redshifted emission shows $\gamma \approx 5.0$ at velocities greater than 3–4 km s^{-1}. For the region corresponding to hot dust, the slopes of both blue and redshifted emission corresponds to $\gamma \approx 5.0$. Regions corresponding directly to the 8 confirmed outflows in Section 3.5 show two power-law relations for the blueshifted emission that are not seen in the redshifted emussion. The blueshifted emission shows a slope that changes from $\gamma \approx 2.8$ to 10.0 at $\sim$7 km s^{-1}. The redshifted emission has a slope $\gamma \approx 5.0$. Lastly, the region corresponding to the Class 0 outflow VLA 1623 show $\gamma \approx 2.5$ for both the blue and redshifted emission.

One of the most noticeable differences between the regions in Figure 4.9 is the change in slope seen for the total molecular outflows. The slope is more pronounced for the blueshifted emission and becomes steeper at $\sim$7 km s^{-1}. A similar break can be seen for the total cloud, but the slope in blueshifted emission isn't as steep ($\gamma \approx 5.0$). VLA 1623 in unlike the other regions in the cloud where both blue and redshifted emission has a much shallower slope at high velocities > 5 km s^{-1}.

The slope found for the regions, particularly for the blueshifted emission, is much steeper than the typical $\gamma \approx 1.8$ that is found for outflows. It is possible the steeper slopes seen in the mass-velocity relationships may be due to the higher-J transition of ^{12}CO used for this study [Curtis, Ph.D. Thesis; Downes and Cabrit 2003]. Lower-J transitions are better at detecting high-velocity material at lower densities that produce flatter profiles. Stahler [1994] calculated γ for Class 0 source VLA 1623 and found the redshifted slope to be 1.83 and the blueshifted slope to be 1.98, which is inconsistent with the total mass-velocity relation I calculate for the VLA 1623

outflow or the total outflows. Out of the eight confirmed outflows in this region (Section 3.5), only VLA 1623 is a Class 0 source while the other outflows are driven by Class I, flat spectrum, and Class II sources. It is possible that older outflows in the region have a steeper mass-velocity relation compared to younger and more energetic outflows [Richer et al., 2000; Smith et al., 1997], which is supported by Figure 4.9 with VLA 1623 having a shallower slope than the total outflows.

4.1.8 Other drivers of high velocity emission

Turbulence can be produced by a variety of sources in a molecular cloud in addition to molecular outflows. Stellar winds from powerful main-sequence stars and outflow remnants from more evolved sources are other potential drivers of cloud turbulence. Even though outflows do not appear to be the dominant driver of turbulent energy in the Ophiuchius cloud as described in Section 4.1.7, the region is surrounded by nearby B-type stars S1 and SR3 and B2V star HD 147889 which drives a PDR near Oph A (as described in Chapter 1). Additionally, Ophiuchus lies south of the Upper Scorpius OB association region which bombards the the main Oph cloud L1688, L1689 and Oph North clouds with radiation and winds [de Geus, 1992; Hatchell et al., 2012; Nutter et al., 2006].

Using the molecular outflow analysis from Section 3.5 and the ISOCAM 12 μm data, masks can be created to quantify the kinetic energy of high velocity ^{12}CO emission associated directly with molecular outflows and winds from the nearby B stars in the Oph A region. This analysis is performed using the same method as Section 4.1.7 for the global high velocity 'outflowing' gas. Outflow masks are created using contour plots corresponding to the red and blue outflows lobes from Section 3.5, where rectangular sections are copied directly from the map. This gives an order of magnitude estimate of the kinetic energy in the outflow regions. A mask corresponding to the hot dust from the Oph A stars is created using a 45 MJy sterad^{-1} cut from the ISOCAM 12 μm data, similar to Section 3.4.

Table 4.4 details the results of the kinetic energy associated directly with outflow lobes, regions potentially corresponding to stellar wind from stars close to Oph A (hot dust) and regions that do not include either outflow lobes or hot dust. The energy has been calculated using the two different methods for identifying ambient

Scenario	Kinetic Energy ($M_\odot$ km^2 s^{-2})	
	$v_{amb} = \pm 2.5$ km s^{-1}	$v_{amb} = 2.5$–4.7 km s^{-1}
Global	67	370
Outflows	22	74
Hot dust	17	100
Other emission	27	196

Table 4.4: Kinetic energies for the global outflowing gas assuming opacity corrected ^{12}CO linewing emission and with a correction for inclination. Ambient velocities from Sections 4.1.7 and 4.1.7.1 are shown. Scenarios include global high velocity kinetic energy over the cloud, corresponding to outflow lobes, regions with hot dust emission and high velocity emission that does not correspond specifically to either outflow lobes or potential stellar winds.

velocities in the cloud (Sections 4.1.7 and 4.1.7.1), indicated by the v_{amb} range. For the ambient velocity range in Section 4.1.7 ($\Delta v = \pm 2.5$ km s^{-1}), the outflows are ∼33% of the global high velocity kinetic energy and the hot dust is ∼26% which leaves 41% of the high velocity kinetic energy unaccounted for. Using the smaller ambient velocity range derived from ^{13}CO opacity (Δv =2.5–4.7 km s^{-1}), the outflows are ∼20% of the high velocity kinetic energy and the hot dust is ∼27% of the energy which leaves 53% unaccounted for. In both scenarios, there is a significant amount of global high velocity energy that is not driven by embedded protostars through outflows or stellar winds from the stars near the Oph A region. Therefore, it is possible other sources are generating this turbulence at higher velocities, i.e. the Upper Sco OB association. Potential drivers of this high-velocity emission are further discussed in Section 4.2.3.

4.2 Discussion

In Section 4.1, the mass and energetics of the cloud and molecular outflows were presented using multiple CO $J = 3 \rightarrow 2$ isotopologues. The methods used to calculate these global properties suggest different results for the effect of outflows on turbulence. Additionally, the significant high-velocity emission could potentially result from other factors in the cloud (e.g. hot dust from near B-type stars or stellar winds). In this section, the global cloud properties are further discussed, including

the role of outflow kinetic energy in driving cloud turbulence. An attempt is made to better understand the source of global high-velocity emission in the cloud (e.g. molecular outflows, hot dust and stellar winds). Lastly, the global properties of the Ophiuchus L1688 cloud are compared to the Perseus and Serpens Main clouds to discuss the differences between star forming regions in the Gould Belt.

4.2.1 Methods for calculating outflow properties

As described in Sections 4.1.7 and 4.1.7.1, the outflow energetics were calculated using two different ranges for ambient velocities, the range based on a Gaussian fit to the $C^{18}O$ average spectrum ($v_o \pm 2.5$ km s^{-1}) and the range defined by the average ^{13}CO optical depth measurements across the cloud (2.5–4.7 km s^{-1}). These two methods result in outflow mass, momentum and kinetic energy calculations that differ by factors of 22, 11 and 6 respectively. Due to the variation in these calculations, the resulting influence over outflows on the overall global turbulence of the cloud is uncertain. The outflow kinetic energy calculated by the larger ambient velocity range determined from the $C^{18}O$ spectra suggests outflows are a significant source of turbulence but not the dominant source at 21% of the turbulent kinetic energy. The outflow kinetic energy derived from the smaller ambient velocity range defined by the ^{13}CO optical depth measurements suggests outflows are the dominant source of turbulence and exceed the turbulent kinetic energy (factor 1.2 larger). It is important to further examine the differences between these calculations and discuss the potential influence of outflows on the overall global turbulence.

It is possible the velocity ranges used to calculate the outflow properties include ambient material since it is not possible to completely exclude this emission from the outflow calculations. This is less likely for the larger ambient velocity range (defined by the $C^{18}O$ velocities) since a larger range was used to account for variations in the the central cloud velocity. However for the smaller ambient velocity range defined by ^{13}CO optical depths, this is particularly important since this method shows higher mass, momentum and kinetic energy for the molecular outflows. It is possible that some ambient velocity emission is optically thin in ^{13}CO and the primary velocity channels with optically thick emission correspond directly to the densest regions of the cloud (i.e. protostellar cores). In this case, I would be overestimating the

properties of the molecular outflows and underestimating the ambient velocity range. This would bias the comparison between the turbulent and outflow energies, leading to a higher percentage of turbulence driven by molecular outflows. In the future, this method can be revisited and a lower optical depth $\tau_{^{13}CO}$ could be explored as a limit for the ambient velocity range. Alternatively, since $C^{18}O$ is expected to trace the bulk motions of the cloud, the ambient velocity range could be defined as the range of velocities with at least a 3σ detectable $C^{18}O$ measurement (corresponding to $\sim$2.0–5.5 km s^{-1}).

Since the method described in Hatchell et al. (2005) has been used in past research involving Gould Belt clouds (e.g. Curtis et al. 2010; Graves et al. 2010), I continue to use the method with ambient velocity defined by the $C^{18}O$ data (i.e. $v_o \pm 2.5$ km s^{-1}) in the following sections. This allows me to compare the global properties of the Ophiuchus cloud to the other Gould Belt clouds in Section 4.2.4.

4.2.2 Comparison of energetics with Nakamura et al. [2011]

Contrary to the results presented in Section 4.1.7, Nakamura et al. [2011] suggested that protostellar outflows can drive turbulence in the region after finding the total outflow energy injection rate ($L_{tot} \sim 0.2\ L_\odot$) to be larger than the dissipation rate of the supersonic turbulence ($L_{turb} \sim 0.06$–$0.12\ L_\odot$) assuming optically thin emission. I use a similar method to calculate the global outflow energy injection rate $L_{global} = E_{out}/T_I$ where E_{out} is the global outflow kinetic energy and T_I is the lifetime of a Class I protostar ($\sim$ 0.5 Myr; Evans et al. 2009). This gives a global outflow energy injection rate $L_{global} = 0.02\ L_\odot$, which is a factor of 10 smaller than the injection rate from Nakamura et al. [2011]. The difference between the outflow energy injection rates is mainly due to my assumption of a longer outflow timescale that better reflects the age of Class I protostars as opposed to calculating dynamical timescales for individual outflows ($\sim 1.5\times10^4$ yr average). The majority of protostars in Ophiuchus driving outflows are Class I, which are expected to drive outflows on longer timescales (comparable to their lifetime). Additionally, the Ophiuchus molecular cloud has regions of high velocity gas that cannot always be assigned directly to an embedded protostar, but may be the result of jets or more evolved sources without a ^{12}CO outflow detection. It is important to use the longer timescale to account for this

material. Nakamura et al. [2011] calculates the turbulent dissipation rate from Mac Low (1999),

$$L_{\rm turb} = f\frac{\frac{1}{2}M{\rm v_{FWHM}}^2}{\lambda_{\rm d}/{\rm v_{FWHM}}}, \tag{4.17}$$

where $f \sim 0.33$ is a non dimensional coefficient, M is the cloud mass, $\rm v_{FWHM}$ is the FWHM velocity and $\lambda_{\rm d}$ is the driving scale of supersonic turbulence. Using the values calculated in Section 4.1.3, I calculate the turbulence dissipation rate to range from 0.05–0.12 $L_\odot$ on driving scales from the diameter of the cloud (1.0 pc) down to the size of an outflow (∼0.4 pc). There are increased turbulent dissipation rates potentially due to the optical depth correction on the $C^{18}O$ data. Comparing the injection rate using the longer timescale (0.02 $L_\odot$) to the turbulent dissipation rate suggests it is lower by a factor of 2.5–6.0 (depending on the driving scale). This result agrees with the conclusion that global outflows in the Ophiuchus region are significant but not necessarily the dominant driver of turbulence in the cloud.

Alternatively, the turbulent dissipation rate can also be derived from the ^{13}CO, similar to Section 4.1.5 where I calculate the mass and energetics of the cloud. ^{13}CO predicts dissipation rates ranging from 0.14–0.32 $L_\odot$ on driving scales from the size of the cloud (0.94 pc) to the length of an outflow (0.4 pc), which is higher than results from $C^{18}O$. Using these values, the outflow injection rate is a factor of 7–23 times smaller than the dissipation rates. Even using the smaller dynamical timescale, the outflow injection rates predicted by Nakamura et al. [2011] are comparable or less than the turbulent dissipation rates.

4.2.3 High-velocity emission

As described in Section 4.1.8, there is a substantial amount of high-velocity emission that does not appear to correspond to molecular outflows (classified in Chapter 3) or regions with hot dust corresponding to nearby B-type stars. Using the standard ambient velocity defined by the $C^{18}O$ spectra, ∼41% of the high-velocity material does not have an apparent source. It is possible the remaining turbulence in the region is the result of remnants from past outflows, high-velocity emission resulting from the H_2 knots or underlying jets from less embedded sources (i.e. Class II protostars) or stellar wind from the nearby Upper Scorpius OB association.

The lower outflow energy relative to the turbulent kinetic energy found in the Ophiuchus cloud could be indicative of the lower star formation activity in the region. The sheer number of Class II YSOs (∼60% of the YSO population) in Ophiuchus is potentially indicative of a burst in star formation activity that declined ∼0.1 Myr ago [Evans et al., 2009]. The decrease in star formation would lead to an eventual decrease in the ability for outflows to drive cloud turbulence since fewer protostars are at an age where powerful molecular outflows are produced (i.e. Class 0/I protostars).

Less embedded Class II sources found in the region could still drive some high-velocity emission. High-velocity remnants from outflows may remain or a jet interacting with cloud material may contribute to the overall cloud turbulence. A good example of this is found in Figure 3.8 of Chapter 3, located in the Oph A region. H_2 knots f10-01 a–g correspond directly to a Class II source [Gómez et al., 2003]. There is some corresponding blueshifted emission to the H_2 knots, potentially indicating the presence of a remnant outflow or an underlying jet interacting with surrounding molecular gas. Another example is H_2 knot [GSWC2003] 2 in the Oph CEF region (see Figure 3.17 in Chapter 3). As discussed in Section 3.6.3, this H_2 knot is near Class I source WL 16; however, the shape of the knot does not indicate it is being driven by the source. A noticeable 'bubble' of high-velocity blue and redshifted emission corresponds directly to the knot, north of the Class I source, but does not appear to be driven by the protostar. These cases of unexplained high-velocity molecular gas could indicate that protostars continue to contribute to turbulence in their natal cloud even as they become less embedded. There are numerous H_2 knots and HH objects found in the region that could contribute to turbulence in the cloud.

The Upper Sco OB association is a region to the north of the Ophiuchus cloud complex. Stellar winds and a potential supernova explosion of the ζ Oph binary companion is expected to create an expanding HI shell that surrounds Upper Sco [de Geus, 1992]. This shell impacts on the ambient material from the Ophiuchus cloud, including L1688 and other clouds located in Ophiuchus North. It has been suggested from past work [Loren and Wootten, 1986; Vrba, 1977] that star formation was initially triggered in L1688 from compression due to the OB association. It is possible that stellar winds driven by Upper Sco could generate high-velocity blue

and redshifted emission in the cloud, leading to turbulence that is unaccounted for by molecular outflows. This is consistent with Evans et al. [2009] work suggesting a burst of star formation activity triggered by Upper Sco that has subsequently declined, leading to less star formation activity (and fewer Class 0 protostars in the region). As discussed in Section 4.1.4, it is also possible this compression has lead to higher gravitational energy leading to the cloud being overbound (suggested by Nakamura et al. 2011). In this case, Upper Sco may still drive some turbulence in the region but not enough to support the cloud against collapse.

4.2.4 Comparison of Gould Belt clouds

A main goal of the Gould Belt Survey is to observe a number of nearby star forming regions in our Galaxy. This is particularly important for better understanding turbulence in a molecular cloud, the driving force behind turbulence and global cloud collapse. Using the GBS HARP observations, past studies [Buckle et al., 2010; Curtis et al., 2010b; Graves et al., 2010] have similarly calculated the mass, energetics and outflow energetics of molecular clouds in the Gould Belt (Perseus and Serpens). These regions can be compared to Ophiuchus to investigate the turbulent support mechanisms in a variety of environments.

Table 4.5 summarises the global mass, energetics, outflow energy turbulent dissipation rate and outflow injection rate in Ophiuchus compared to other nearby star forming regions. The Perseus molecular cloud includes regions NGC 1333, IC 348, L 1448 and L 1455. The Serpens molecular cloud only includes the 'Serpens Main' region. Outflow energies assume random inclination. All regions use $C^{18}O$ for calculating the total mass and kinetic energy and ^{12}CO for the global outflow energy. Turbulent dissipation and outflow injection rates are calculated using the method in Section 4.1.7, Equation 4.17. The range of turbulent dissipation rates are the result of a cloud and outflow driving scale and outflow injection rates are calculated assuming the 0.5 Myr driving timescale. Outflow driving scales are taken from Curtis et al. [2010b] and Graves et al. [2010], where Perseus clouds have a driving scale estimated at ∼0.15 pc and Serpens Main has a driving scale ∼0.23 pc.

In terms of energy, the molecular cloud ∼10 arcmin southwest of the cluster IC 348 is one of the most similar clouds to Ophiuchus. I note that I refer to the

bright molecular cloud as 'IC 348' as in Curtis et al. [2010b] even though it is more accurately associated with the 'Flying Ghost Nebula' [Boulard et al., 1995]. The outflow energies are ∼38% of the turbulence in the region which is slightly higher than the global outflow energy in Ophiuchus (21%), indicating that outflows are unlikely to drive turbulence in the cloud. Additionally, this is reflected by low outflow injection rates in comparison to turbulent dissipation rates. The majority of sources in IC 348 are starless cores and indicate the region is quite young [Curtis et al., 2010b] though there is evidence the region is a remnant of a larger cloud that formed the IC 348 cluster. It is possible that the nearby cluster triggered star formation in the molecular cloud. As discussed in Section 4.1.8, other factors can drive high velocity turbulence in molecular clouds including radiative wind from nearby stars. It is possible that both Ophiuchus and IC 348 have a significant fraction of the turbulence driven by these stellar winds. Additionally, both regions have low turbulent kinetic energy to gravitational binding energy, where IC 348 has a kinetic energy value less than 1% of its gravitational binding energy indicating the cloud is gravitationally bound like Ophiuchus.

Conversely NGC 1333, L1448, L1455, and Serpens Main have outflow energies comparable to the total kinetic energies of the regions, indicating a main driver of turbulence in these clouds is most likely high velocity outflows. NGC 1333 is the most active region in the Perseus molecular cloud with outflow energies ∼3 times the kinetic energy of the cloud. Knee and Sandell [2000] suggest the structure of the region is widely formed from cavities produced by these outflows and that it is likely the outflow can destroy the cloud. The outflow energies are around ∼16% of the gravitational binding energy, which indicates that outflows can regulate star formation and drive turbulence in the region if they can be efficiently coupled to the bulk motions of the cloud [Curtis et al., 2010b]. Both L1448 and L1455 have outflow energies greater than the kinetic energies. L1448 is particularly noticeable with an outflow energy a factor of 2 larger than the gravitational binding energy of the cloud. Though Curtis et al. [2010b] notes the outflows extend beyond the parent cloud, a portion of the outflow energy could be coupled to the cloud and potentially lead to its destruction. Additionally, L1455 has outflow energies that are roughly one-third of the overall binding energy of the cloud. Like L1448, Curtis et al. [2010b] notes that the outflows extend past the cloud and are upper energy limits.

Unlike the Perseus clouds that have outflow energies exceeding the turbulent energies, Serpens has outflow energies that are comparable to the turbulence measured in the cloud (∼68%) and ∼61% of the binding energy. The cloud appears to be weakly bound, which means on small scales there may be areas of collapse and other areas of expansion. Graves et al. [2010] concludes the outflows will have a strong influence on the structure in the region and fits with theories involving outflows driving supersonic turbulence in active star forming regions (i.e. Matzner 2007; Nakamura and Li 2007).

4.3 Conclusions

In this chapter, I examined the HARP ^{12}CO, ^{13}CO and C^{18}O $J = 3 \rightarrow 2$ data of the Ophiuchus molecular cloud. These data were used to search for outflows and calculate the cloud mass and energetics of the region. The main conclusions can be summarised:

1. **Cloud mass and energetics.** Using optical depth corrected C^{18}O emission, I calculated a total cloud mass of 515 $M_{\odot}$ and a virial mass of 141 M$_{\odot}$, indicating the cloud is gravitationally bound. These results are in agreement with past studies [Loren, 1989; Nakamura et al., 2011; Tachihara et al., 2000]. The turbulent kinetic energy was found to be 6.3 $\times 10^{38}$ J and gravitational binding energy 4.5 $\times 10^{39}$ J, where the turbulence in the region is a factor of 7 smaller than the gravitational energy. To test the possibility of C^{18}O not accounting for less dense material in the cloud, I also used ^{13}CO to calculate the mass and energetics. Mass increased by a factor of 1.1 (238 M$_{\odot}$). Additionally, the kinetic energy increased by a factor of 2 (1.3 $\times 10^{39}$ J) and the binding energy decreased to 3.8 $\times 10^{39}$ J, indicating the cloud is gravitationally bound but less bound than using C^{18}O emission.

2. **Outflow mass, momentum and energy.** The global outflow properties were calculated from the ^{12}CO data with a correction for optically thick emission in the line wings. The total mass in outflows was found to be 4.72 M$_{\odot}$, momentum was 28.06 M$_{\odot}$ km s^{-1} and kinetic energy was 66.63 M$_{\odot}$ km ^{2} s^{-2}. The outflow kinetic energy was found to be ∼21% of the turbulent energy in

Cloud	Mass ($M_\odot$)	$E_{\rm kin}$ (J)	$E_{\rm grav}$ (J)	Outflow Energy (J)	Turbulent Diss. Rate ($L_\odot$)	Injection Rate ($L_\odot$)
Ophiuchus	515	6.3×10^{38}	4.5×10^{39}	1.3×10^{38}	0.05–0.12	0.02
NGC 1333[a]	439	1.7×10^{38}	3.5×10^{39}	1.5×10^{39}	0.01–0.09	0.08
IC348[a]	196	2.6×10^{37}	1.2×10^{39}	1.0×10^{37}	0.002–0.008	0.002
L1448[a]	59	1.4×10^{37}	2.5×10^{38}	5.4×10^{38}	0.004–0.006	0.09
L1455[a]	19	3.6×10^{36}	5.5×10^{37}	1.5×10^{37}	0.001–0.002	0.002
Serpens[b]	203	4.4×10^{38}	4.9×10^{38}	3.0×10^{38}	0.006–0.020	0.05

Table 4.5: Comparison of the global mass and energetics of GBS clouds.

[a]Curtis et al. [2010b]
[b]Graves et al. [2010]

the region, indicating that outflows are a significant driver of turbulence but not necessarily the main source. This disagrees with Nakamura et al. [2011] that concluded outflows have a comparable or larger outflow energy injection rate than turbulent dissipation rate. Using longer outflow timescales, I show it can be misleading to use a dynamical timescale for these calculations and conclude the outflows are not the main driving source of turbulence in Ophiuchus. Additionally, I test an alternate method of defining ambient velocities using ^{13}CO opacity to examine the change in calculated outflow mass, momentum and energy which increase by factors of 22, 11 and 6 respectively. These results show the outflows have an outflow energy 1.2 times larger than the turbulent energy in the cloud and $\sim$59% of the gravitational binding energy.

3. **Cloud comparison.** Using HARP data, I compared a variety of regions observed by the Gould Belt Survey (Serpens Main and regions in Perseus: NGC 1333, IC 348, L1455 and L1448) to the Ophiuchus molecular cloud (see Curtis et al. 2010b; Graves et al. 2010). I find IC 348 to be most similar to Ophiuchus with a low outflow energy compared to the turbulent energy in the cloud. Both regions have stellar radiation bombarding the clouds (Upper Sco OB association for Ophiuchus, 'Flying Ghost Nebula' for IC 348) which may drive the turbulence calculated for the regions.

Chapter 5

Ophiuchus: HCO+ analysis and non-LTE modelling

HCO+ $J = 4 \rightarrow 3$ emission with a rest frequency of 356.73428 GHz is typically used to trace the warm, dense gas which is associated with active star formation ($n_{crit} \sim 8 \times 10^6$ cm^{-3}, $E_u \sim 43$ K). As a dense gas tracer, observations of HCO+ can be used to investigate the relation between high density regions and high column density in molecular clouds. Recent Herschel observations of Gould Belt clouds support a column density threshold for protostars at a level of $N(H_2) = 10^{22}$ cm^{-2} [André et al., 2010] originally suggested from CO observations of Taurus [Onishi et al., 1998]. This column density may be a result of filament fragmentation, as it corresponds to a critical mass per unit length in filaments [Ostriker, 1964] and/or it may link to thresholds in the density probability density function or PDF [Kainulainen et al., 2009]. Either way, it underlies the major issue in star formation of why so little of the mass of a molecular cloud ultimately ends up in stars, leading to global star-formation efficiencies (SFEs) of a few percent [Evans et al., 2009]. In addition to density calculations, HCO+ is often optically thick ($\tau_{HCO+} \approx 10^3\ \tau_{C^{18}O}$) making it a useful tracer of cores in a state of collapse through blue asymmetries in the line profile (e.g. Myers et al. 1996) and a tracer of outflows (e.g. van Kempen et al. 2009).

There have been several previous studies of dense gas tracers in the Ophiuchus L1688 cloud using a variety of molecules. Dense cores have been studied

across the cloud using $H^{13}CO+$ $J = 1 \rightarrow 0$ ($n_{\rm crit} \sim 10^5$ cm^{-3}; Maruta et al. 2010) and the Oph B region has been studied using N_2H^+ $J = 1 \rightarrow 0$ ($n_{\rm crit} \sim 2\times10^5$ cm^{-3}), NH_3 (1,1) ($n_{\rm crit} \sim 10^4$ cm^{-3}), N_2D^+ $J = 3 \rightarrow 2$ ($n_{\rm crit} \sim 8\times10^5$ cm^{-3}), H_2D^+ $J_{K_{-1}K_1} = 1_{11} - 1_{10}$ ($n_{\rm crit} \sim 10^5$ cm^{-3}) and N_2H^+ $J = 4 \rightarrow 3$ ($n_{\rm crit} \sim 7.7 \times 10^6$ cm^{-3}; Friesen et al. 2009, 2010a,b). Work from van Kempen et al. [2009] used both $C^{18}O$ $J = 3 \rightarrow 2$ and HCO+ $J = 4 \rightarrow 3$ to classify the evolutionary stages of protostars in the Ophiuchus main cloud. Similarly, Simpson et al. [2011] used large-scale maps of HCO+ $J = 4 \rightarrow 3$ in Ophiuchus to analyse prestellar cores, specifically investigating blue asymmetries in the line profile in comparison to the Jeans mass. These studies have mainly focused on core detection and properties rather than the potential relation between higher density and column density in the cloud.

In this chapter, I present the HCO+ $J = 4 \rightarrow 3$ observations of the main L1688 cloud in Ophiuchus using the JCMT under the proposals M11AU13 and M11BU11, which is the largest survey of a dense gas tracer at high angular resolution (PI John Richer). I examine the relationship between HCO+ as a dense gas tracer and column density tracers like $C^{18}O$, 850 μm continuum emission and visual extinction A_v. I then use non-LTE radiative transfer codes RADEX and TORUS to estimate the density traced by HCO+ emission in the cloud.

5.1 HARP HCO+ $J = 4 \rightarrow 3$ reduction and observations

As discussed in Chapter 1, HARP uses a digital spectrometer called ACSIS. This instrument generates raw data files in a three-dimensional format, where each spectral channel was written out with a time stamp from each receptor. The raw time-series cube was regridded to a position-position-velocity cube (PPV; RA × Dec × velocity) using the SMURF[1] data reduction package [Jenness et al., 2008].

Before the PPV cube was produced, some receptors needed to be fully or partially masked over a brief time period due to poorly performing receptors or bad baselines. To mask out these sections, the KAPPA chpix command was used to set

[1] http://www.starlink.ac.uk/docs/sun258.htx/sun258.html

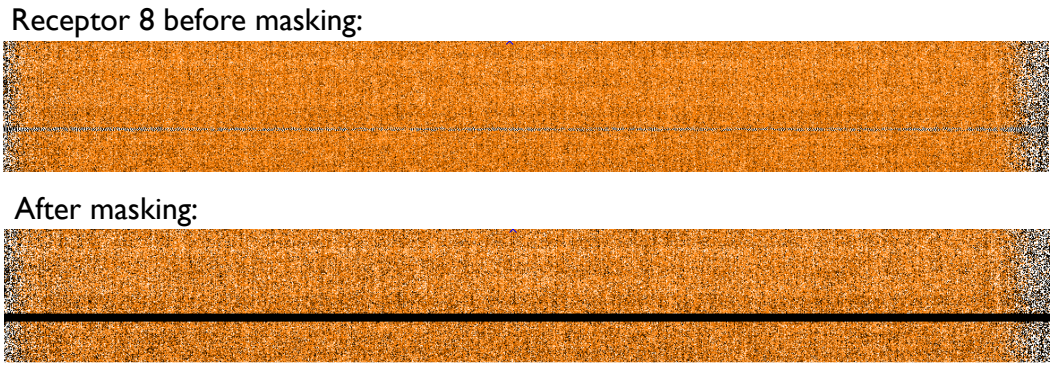

Figure 5.1: Example of poor performance by receptor number 8. The x-axis corresponds to the spectral channels and the y-axis corresponds to the time stamp. In the 'after' image, the section of time corresponding to the poor performance was set to BAD.

particular receptors to BAD. The HCO+ data for Ophiuchus had repeat poorly performing receptors from receptor numbers 8 and 10 (H07 and H09) that I partially or completely masked as they were found. An example of the poorly performing receptor number 8 can be seen in Figure 5.1 before and after masking techniques were applied. A large horizontal stripe extends across the length of the receptor, where the x-axis corresponds to the spectral channels and the y-axis is the time stamp. This indicates the receptor performed poorly at a certain point in time and this section of the receptor must be set to BAD.

Once bad receptors were removed from the data, the raw time-series cube was then converted into the three-dimensional PPV cube using the SMURF makecube command. Multiple raw time-series files were coadded using this command, allowing the resulting PPV cube to be created from multiple observations on various nights. The pixel size was specified to be 6 arcsec using a 9 arcsec FWHM Gaussian gridding kernel, which resulted in an equivalent FWHM beam size of 16.3 arcsec.

Once the PPV cube had been generated, I then removed the linear baseline using KAPPA mfittrend. This routine can fit up to a 15th order polynomial to a molecular line free portion of the data along the velocity axis. The baseline was subtracted from the original data cube. Using KAPPA sqorst, the data was then rebinned to a 0.2 km s^{-1} spectral resolution.

Figure 5.2 shows the integrated HCO+ $J = 4 \rightarrow 3$ emission. Like the CO $J =$

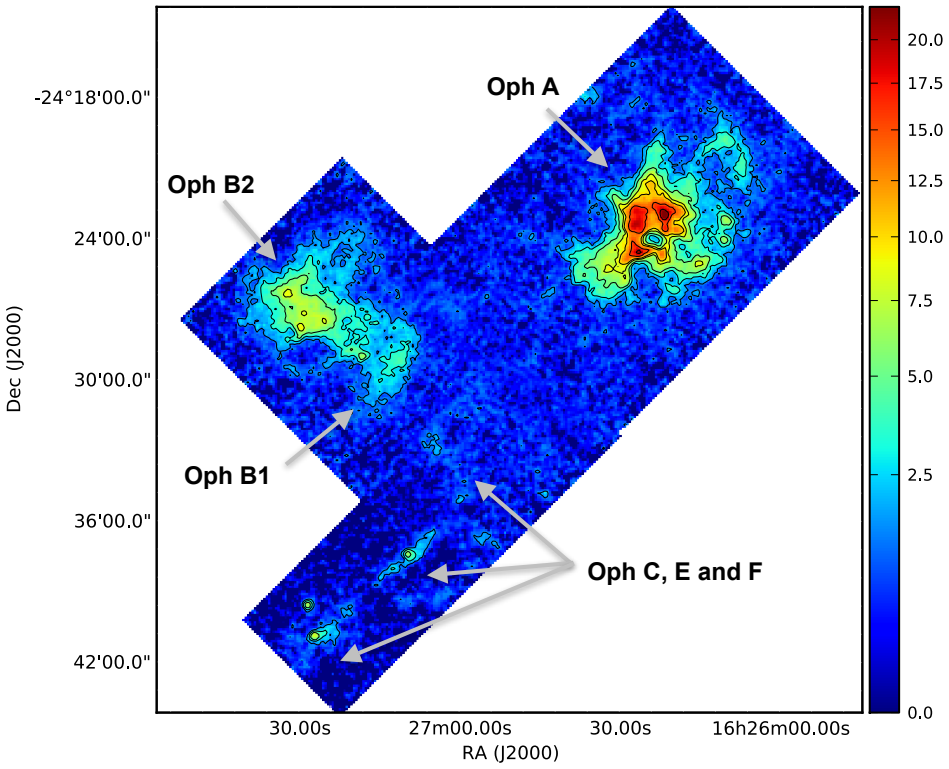

Figure 5.2: HCO+ integrated main-beam intensity map (K km s^{-1}) with contours at levels 1.5, 3, 5, 8, 10, 15 and 20 K km s^{-1}. Map has been integrated from -2 to 10 km s^{-2}.

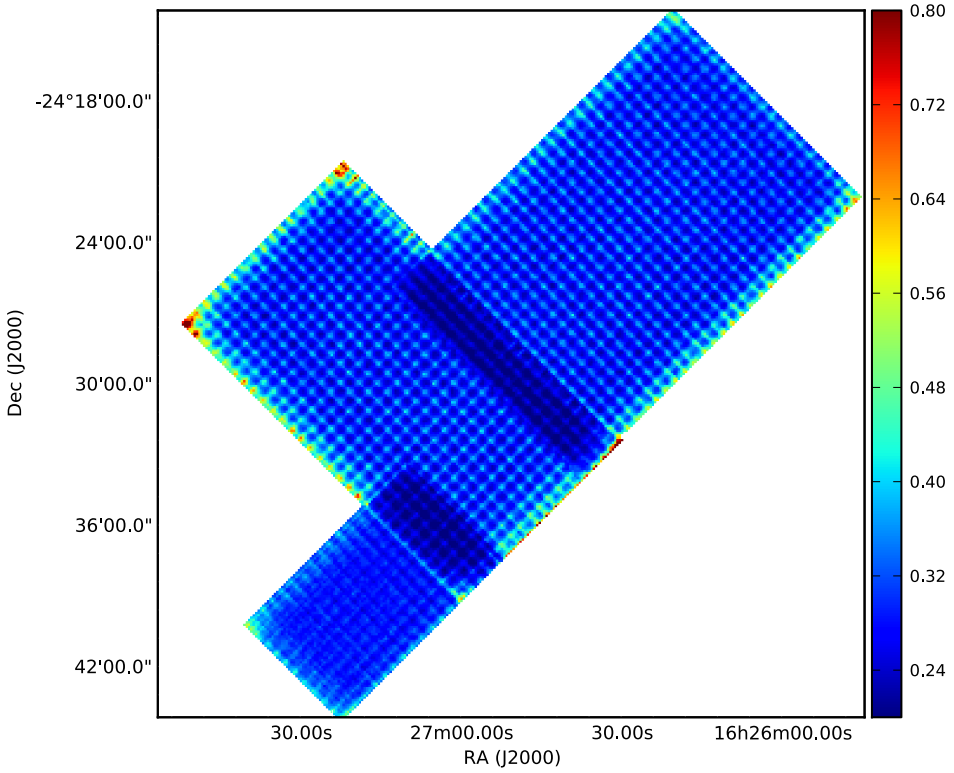

Figure 5.3: HCO+ noise maps in main-beam temperature (K).

$3 \rightarrow 2$ observations in Chapter 3, the map is centred on the L1688 main cloud of Ophiuchus at $16^{h}27^{m}32.0^{s}$ -24°33′00.0″. The map was planned in three sections, designed to cover the Oph A, B and CEF regions based on the $C^{18}O$ data from Chapter 3. Observations were taken between June and July 2011 in Grade 3 weather conditions. The noise (RMS) of the map is shown in Figure 5.3 for 0.2 km s^{-1} velocity channels with an average main-beam temperature noise 0.29 K. The edges of the map have been clipped due to increased noise. The average main-beam temperature noise values for the three different maps are 0.29 K for Oph A, 0.30 K for Oph B and 0.28 K for the Oph C, E, and F regions.

5.2 Source comparisons

Since HCO+ has a high critical density, it is possible HCO+ emission detected in molecular clouds indicates these regions have corresponding higher densities. Past

work from van Kempen et al. [2009] utilised this tracer and $C^{18}O$ in the Ophiuchus cloud to identify the evolutionary stages of protostars. Embedded protostars (i.e. Class 0 and I sources) were thought to have higher levels of HCO+ emission as opposed to less densely embedded 'disk' sources (i.e. flat spectrum or Class II protostars). Hatchell et al. [2005] showed that embedded sources (protostars and starless cores) also have a clear relation to column density, where the number of cores and embedded protostars increase with increasing column densities. Using the high density tracer HCO+, a similar relation may be found relating the number of cores to density.

Protostellar sources were identified using the *Spitzer* c2d survey, described in Chapter 3. The precursor to protostellar cores are pre-stellar or starless cores. Starless cores are thought to be regions of higher density that are most likely transient and may or may not result in the formation of a protostar. Pre-stellar cores are the precursors of protostars and are expected to be gravitationally bound. I denote 'pre-stellar cores' to be a list of SCUBA 850 μm identified cores originally from Johnstone et al. [2004] and remade by Simpson et al. [2008]. 'Starless cores' were identified by Stanke et al. [2006] from 1.2 mm continuum data. Simpson et al. [2008] states these sources are unlikely to be gravitationally bound since many of these sources have low surface brightness and are more extended.

Figure 5.4 shows histograms of 'pre-stellar' and 'starless' cores, 'embedded' sources (Class 0/I protostars with $\alpha > 0.3$ as in Chapter 3) and more evolved 'flat spectrum' sources ($-0.3 < \alpha < 0.3$). These histograms denote the number of sources binned according to the HCO+ emission. Sources with 0 K km s^{-1} integrated intensities had HCO+ peak main-beam temperatures less than 3σ RMS.

A Kolmogorov-Smirnov test (KS test) can be used to test if these sources are from similar distributions. The two-sample KS test compares two one-dimensional distributions and determines if the distributions differ. The null hypothesis states the samples are drawn from the same distribution. The KS statistic quantifies the maximum distance between the empirical distribution function of the two samples. For two samples of n and m members, the KS statistic is

$$D = \max |S_n(x) - S_m(x)| , \tag{5.1}$$

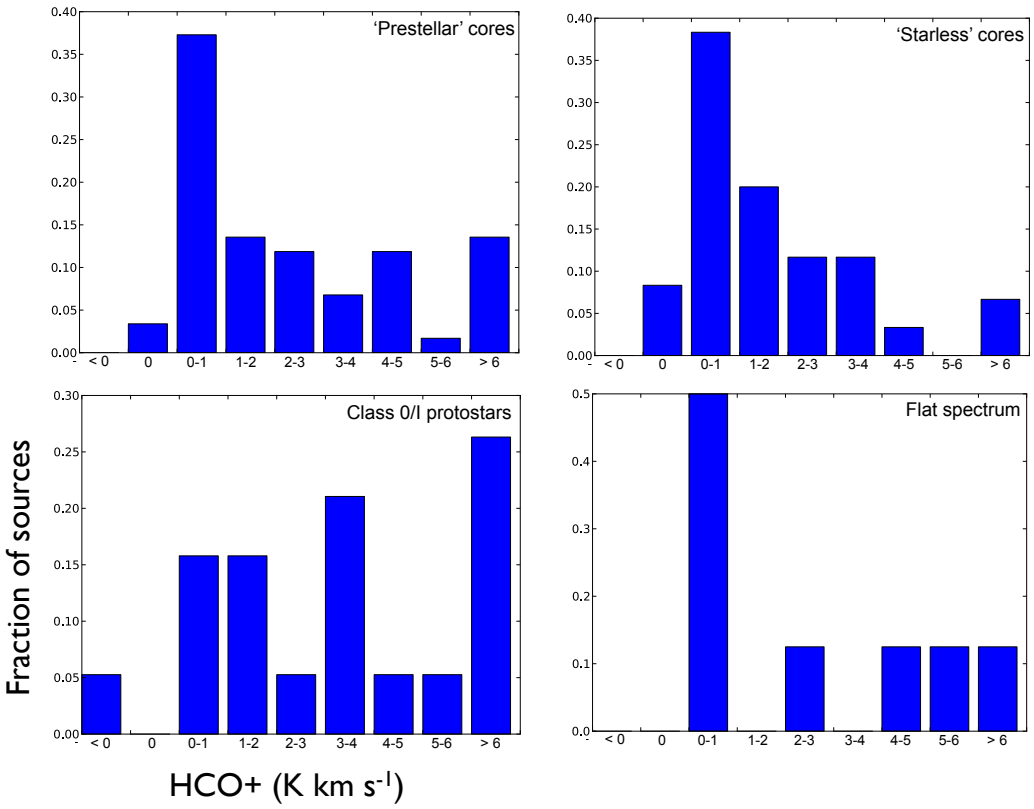

Figure 5.4: Histograms corresponding to the fraction of sources with HCO+ emission.

Source	Pre-stellar	Starless	Flat
Pre-stellar	–	0.603	0.603
Starless	–	–	0.603
Class 0/I	0.603	0.957	0.603

Table 5.1: P-values for the comparison between source distributions, derived using KS tests.

where $S_n(x)$ and $S_m(x)$ are the empirical distributions for n and m members respectively. The KS statistic can be related to the p-value, or the probability the null hypothesis is true and the distributions are the same. Low p-values indicate the null hypothesis is false (distributions are different) and high p-values indicate the null hypothesis is true.

Table 5.1 shows the p-values for the comparison of source distributions between the pre-stellar and starless cores, embedded protostars and flat spectrum sources. The p-values suggest the null hypothesis is true and the sources have the same distribution. I note the pre-stellar cores, starless cores and the flat spectrum sources appear to have HCO+ integrated intensities peaking around 0–1 K km s^{-1}. This trend is not seen in the embedded Class 0/I sources that have a peak at 3–4 K km s^{-1} and $>$ 6 km s^{-1}. This increase of Class 0/I sources with higher HCO+ emission could potentially indicate these regions form in areas with higher densities. Since the KS test compares the empirical distribution functions of the two samples (i.e. redistributing the fraction of sources corresponding to the HCO+ integrated intensity bins), the test can result from two distributions with the same parent distribution appearing different due to random sampling, especially when the sample is small.

5.3 Comparison between HCO+ and column density tracers

To investigate the relationship between density and column density in Ophiuchus, I compare the high density tracer HCO+ to several column density tracers including C^{18}O $J = 3 \rightarrow 2$ from HARP, SCUBA–2 850 μm dust continuum and the visual extinction A$_v$ from the *Spitzer* Space Telescope. Trends in the maps are further analysed to investigate the relation between high density and high column density

regions in the cloud.

5.3.1 Column density tracers

Figure 5.5 shows a comparison of column density tracers $C^{18}O$ (optical depth corrected integrated intensities in K km s^{-1}; see Chapter 4), SCUBA-2 850 μm dust continuum (Jy $beam^{-1}$) with ^{12}CO molecular line emission subtracted from the continuum and *Spitzer* visual extinction A_v data (mag). Black contours denote HCO+ integrated intensities corresponding to 1.5, 3, 5, 8, 10, 15 and 20 K km s^{-1}. Corresponding column densities for each tracer are shown as cyan contours. Contour levels range from $N(H_2) = 1$, 5, 10, 30 and 50 $\times$ 10^{22} cm^{-2} for $C^{18}O$ and 850 μm data and 2 and 3 $\times$ 10^{22} cm^{-2} for the visual extinction data. Methods for calculating the column density from these tracers are described in Section 5.4.2, where ^{13}CO was used to calculate excitation temperatures used in the column densities derived from $C^{18}O$ (Chapter 4) and a constant dust temperature of 10 K was used for the 850 μm derived column densities. SCUBA-2 850 μm data is a part of the Gould Belt Survey (Ward-Thompson et al 2007) and was reduced in 2013 by PhD student Kate Pattle. Molecular line contamination from ^{12}CO was subtracted from the continuum in the reduction process using the recent method described in Chapter 2. Visual extinction data was derived from *Spitzer* Space Telescope observations, taken as a part of the Gould's Belt Survey [Allen et al., 2010]. This data has a 270 arcsec angular resolution, which makes this map not as spatially sensitive as the other column density tracers or HCO+. However, the basic shape of the high extinction regions follows the recognisable outline of the L1688 cloud.

Oph A shows a similar spatial relation between HCO+ and both $C^{18}O$ and 850 μm data. There is an increase in emission on the eastern side of the core, extending into a northern clump-like area. Both $C^{18}O$ and 850 μm show a peak in emission between two peaks at the centre of Oph A, potentially indicating there is a face-on filament at the centre of the clump. The central 'hole' of low HCO+ emission is not reflected in either $C^{18}O$ or 850 μm emission.

The Oph B region appears drastically different in column densities derived from $C^{18}O$ and 850 μm data. The main star forming clump Oph B2 shows a distinct lack of $C^{18}O$ emission in the centre of the region. The 850 μm emission shows an

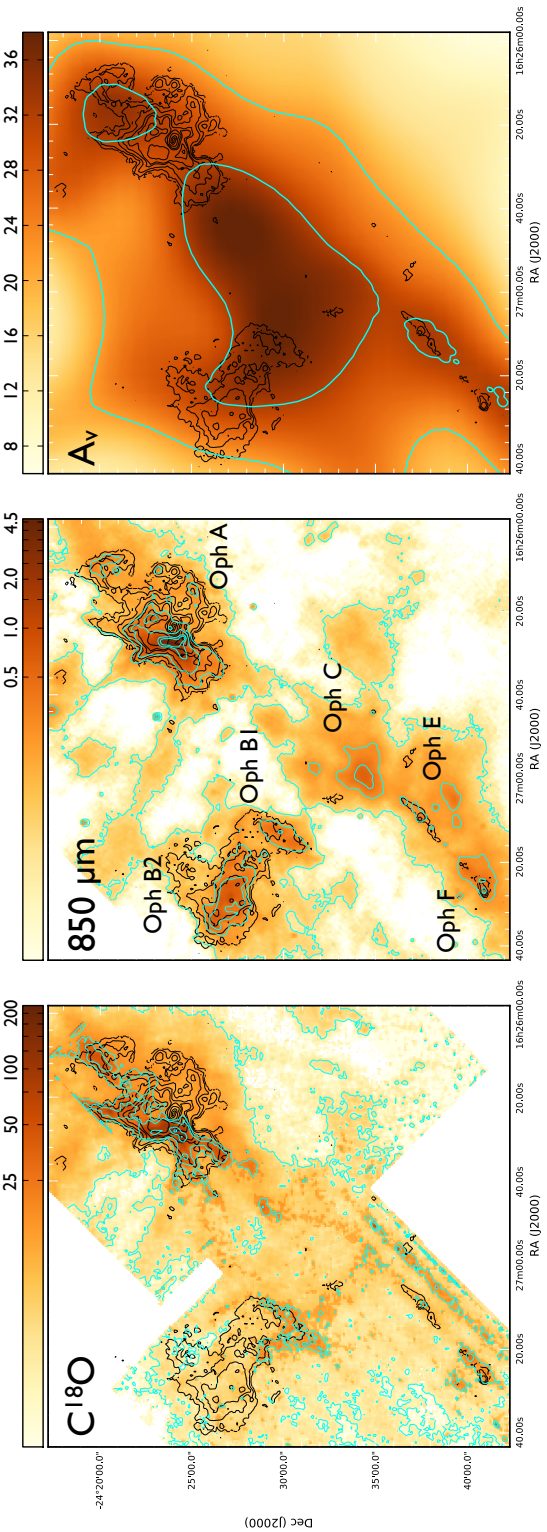

Figure 5.5: Maps of column density tracers. Black contours correspond to HCO+ integrated intensities at 1.5, 3, 5, 8, 10, 15 and 20 K km s^{-1}. *Left:* C^{18}O integrated intensity map with the optical depth correction (K km s^{-1}). Cyan contours correspond to column density $N(H_2)$ at levels 1, 5, 10, 30 and 50 $\times$ 10^{22} cm^{-2}. *Centre:* 850 μm dust continuum map without ^{12}CO molecular line contamination (Jy beam^{-1}. Cyan contours correspond to column density $N(H_2)$ at levels 1, 5, 10, 30 and 50 $\times$ 10^{22} cm^{-2} assuming a 10 K dust temperature. *Right:* Visual extinction A_V map (mag). Cyan contours correspond to column density $N(H_2)$ at levels 2 and 3 $\times$ 10^{22} cm^{-2}.

increase in dust continuum corresponding to the centre of Oph B2 that also relates to increased HCO+ integrated intensities. The lower $C^{18}O$ emission could indicate the molecule is depleted onto dust grains in this region. Conversely, Oph B1 is traced by both $C^{18}O$ and 850 μm emission which corresponds to HCO+ emission.

The main emission seen in the Oph CEF regions in HCO+ emission is a filament-like structure in the southern portion of the cloud, corresponding closely to Oph E and F. Little HCO+ emission is found in the Oph C core. The $C^{18}O$ and 850 μm data show emission in this region that is less defined than the HCO+ filament. Surprisingly, the Oph C region between Oph B and the E/F filament has little to no corresponding HCO+ emission. This region can be seen strongly in 850 μm emission and to a lesser extent in $C^{18}O$. This could indicate that any cores found in this region are transient and lack the density to form protostars.

Figure 5.6 shows a pixel-by-pixel comparison using 6 arcsec pixels in the HCO+ integrated intensity map and maps of the column density tracers ($C^{18}O$ integrated intensity with optical depth correction in K km s^{-1}, SCUBA-2 850 μm continuum with ^{12}CO subtraction in Jy beam^{-1} and visual extinction A_V data in mag). Regions in Ophiuchus, including Oph A, B and CEF, are positions in the map identified as red, green and blue points. Boxes correspond to scenarios that I further examine in Table 5.2. The highest HCO+ integrated intensities are found in the Oph A region (reaching $\sim$26 K km s^{-1}), followed by Oph B and CEF. There are increases in HCO+ emission corresponding to optical depth corrected $C^{18}O$ integrated intensity of $\sim$10 K km s^{-1} ($N(H_2) = 3.3 \times 10^{22}$ cm^{-2} using a constant kinetic temperature of 20 K), visual extinction $\sim$27 ($N(H_2) = 2.5 \times 10^{22}$ cm^{-2}) and SCUBA–2 850 μm dust continuum emission of $\sim$0.3 Jy beam^{-1} ($N(H_2) = 6.5 \times 10^{22}$ or 2.0×10^{22} cm^{-2} assuming constant dust temperature of 10 or 20 K respectively). This is most noticeable in comparisons with $C^{18}O$ and A_v where HCO+ integrated intensities increase above 10 K km s^{-1}. The increase in HCO+ emission could indicate the molecule reaches the critical density for excitation at corresponding column densities.

To examine the possible link between column density and HCO+, I further examine trends seen in Figure 5.6. These scenarios are shown in Table 5.2, where I examine regions of 'low', 'medium' and 'high' levels of HCO+ and column density. Figure 5.7 shows regions in the Ophiuchus cloud that correspond to various trends in the comparison between HCO+ and column density tracers. Protostars from

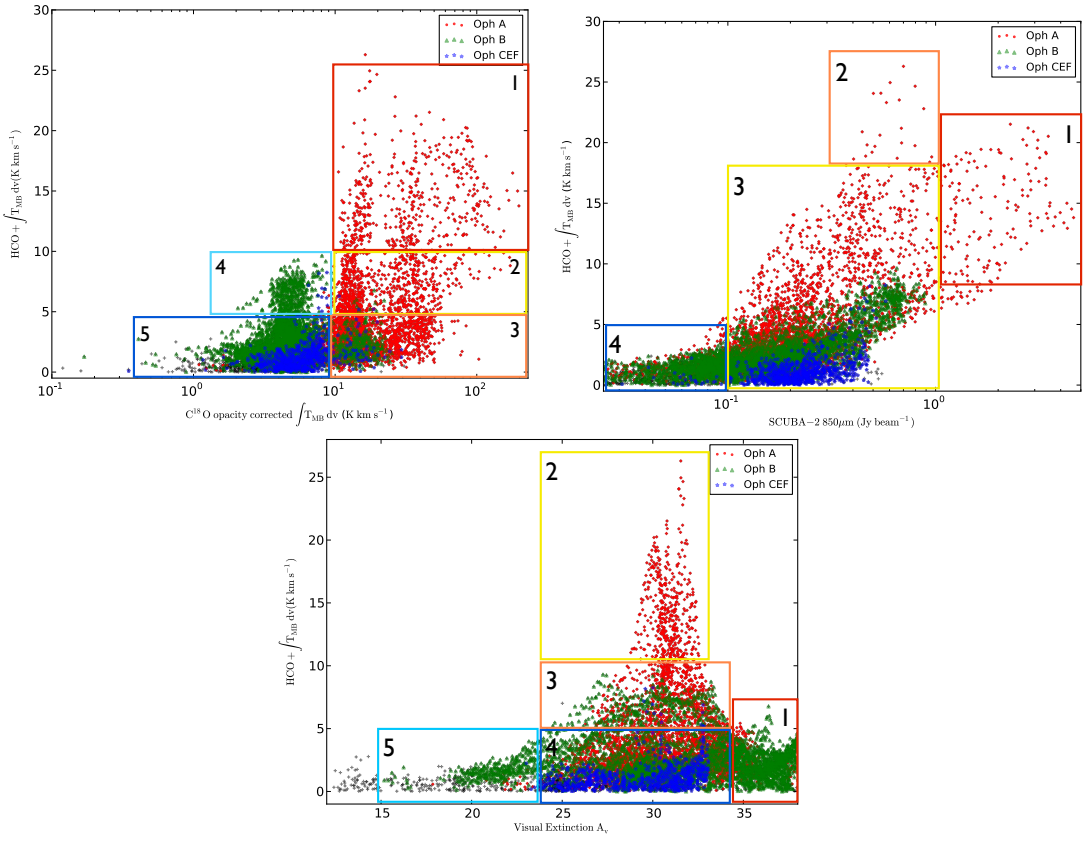

Figure 5.6: Comparison between HCO+ integrated intensity and column density tracers, including opacity corrected $C^{18}O$ integrated intensity (top left), SCUBA-2 850 μm dust continuum (top right) and visual extinction A_v (bottom). Boxes correspond to scenarios listed in Table 5.2.

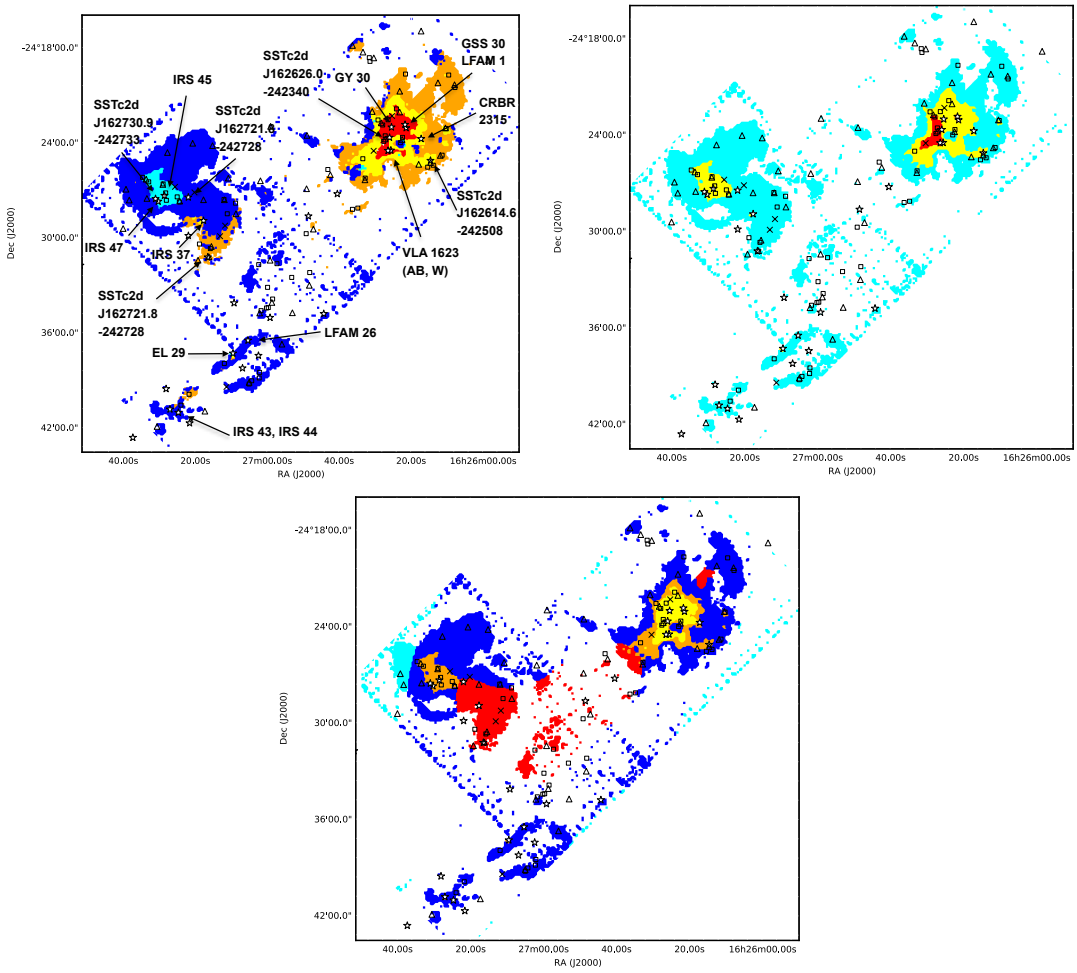

Figure 5.7: Trends in HCO+ $\int T_{\rm MB}$ dv and column density tracers, including opacity corrected $C^{18}O$ integrated intensity (left), SCUBA-2 850 μm dust continuum (right) and visual extinction $A_{\rm v}$ (bottom) corresponding to Table 5.2. A list of protostars from Chapter 3 are shown as '$\star$' and labelled in the top figure. Starless cores from Stanke et al. [2006] starless cores shown as '$\triangle$', pre-stellar cores from Simpson et al. [2008] are shown as '$\square$' and cores that are found in both lists are shown as '$\times$'.

Chapter 3 are shown as '⋆.' Starless cores from Stanke et al. (2006) are shown as '△', pre-stellar cores (assumed to be gravitationally bound starless cores) from [Simpson et al., 2008] are shown as '□' and cores that are found in both lists are shown as '×'.

The scenarios are further discussed in Section 5.3.1.1–5.3.1.3. I note several protostars with confirmed outflows (Chapter 3) do not have corresponding HCO+ data from the comparison between emission from HCO+ and column density tracers. These sources include WL 10 (Class II) and WL 6 (Class I). Additionally, source IRS 54 (flat) is not located in the HCO+ map.

5.3.1.1 HCO+ comparison with $C^{18}O$

In the Oph A region, the centre of the clump has noticeably high HCO+ and $C^{18}O$ emission near 16:26:26 -24:23:16. Protostars in this central region of Oph A include VLA 1623 AB (Class 0) and W (Class I), SSTc2d J162626.0-242340 (flat), GY 30 (Class I), GSS 30 (Class I) and LFAM 1 (Class I). VLA 1623 AB was confirmed to drive an outflow in this region. Moving away from the central portion of Oph A shows a gradual decrease in emission from HCO+ and column density tracers. Protostars SSTc2d J162614.6-242508 (Class 0) and CRBR 2315 (Class I) are included in this section of the clump.

The majority of the Oph B clump has quite low $C^{18}O$ emission (1–10 K km s^{-1}) with HCO+ emission that increases towards the centre of the B2 region. In the central portion of the Oph B2 clump, protostars include SSTc2d J162730.9–242733 (Class I), IRS 47 (flat) and IRS 45 (flat), where IRS 47 was confirmed to drive a molecular outflow in Chapter 3. Protostar SSTc2d J162721.8–242728 (flat) is near this region. Like Oph A, the outer regions of the clump correspond to lower HCO+ and $C^{18}O$ integrated intensities. Protostars IRS 37 (Class I) noticeably has higher HCO+ emission than the surrounding material with the same levels of $C^{18}O$ emission. Lastly, the B1 region has high emission from $C^{18}O$ but low HCO+ emission, which includes protostar SSTc2d J162716.4–2423114 (flat). This is nearly the opposite of the central portions of B2 with higher HCO+ and low $C^{18}O$ emission.

The Oph C, E and F regions primarily have low emission from both $C^{18}O$ and HCO+, similar to the outer portions of Oph B. Two protostars in the region with

$N(H_2)$ Tracer	Scenario	Colour	Range	HCO+ range	Comment
$C^{18}O$	1	red	> 10 K km s^{-1}	> 10 K km s^{-1}	High $C^{18}O$, high HCO+
	2	yellow	5–10 K km s^{-1}	$>$ 5–10 K km s^{-1}	Mid $C^{18}O$, mid HCO+
	3	orange	> 10 K km s^{-1}	< 5 K km s^{-1}	High $C^{18}O$, low HCO+
	4	cyan	1–10 K km s^{-1}	5–10 K km s^{-1}	Low/mid $C^{18}O$, mid HCO+
	5	blue	1–10 K km s^{-1}	0–5 K km s^{-1}	Low/mid $C^{18}O$, low HCO+
850 μm	1	red	> 1 Jy beam^{-1}	7–22 K km s^{-1}	High dust, mid/high HCO+
	2	orange	0.3–0.8 Jy beam^{-1}	18–26 K km s^{-1}	Mid dust, high HCO+
	3	yellow	0.1–1.0 Jy beam^{-1}	< 18 K km s^{-1}	Mid dust, mid/low HCO+
	4	blue	0–0.1 Jy beam^{-1}	< 5 K km s^{-1}	Low dust, low HCO+
A_v	1	red	> 34	0–5 K km s^{-1}	High A_v, low HCO+
	2	yellow	24–34	> 10 K km s^{-1}	Mid A_v, high HCO+
	3	orange	24–34	5–10 K km s^{-1}	Mid A_v, mid HCO+
	4	blue	24–34	0–5 K km s^{-1}	Mid A_v, low HCO+
	5	cyan	< 24	< 5 K km s^{-1}	Low A_v, low HCO+

Table 5.2: Scenarios corresponding to Figure 5.7.

confirmed outflows consistently have higher HCO+ emission in the region (Class I protostars IRS 43 and EL 29).

5.3.1.2 HCO+ comparison with 850 μm dust continuum

Like the comparison with $C^{18}O$, the centre of the Oph A clump has the highest emission from both HCO+ and the 850 μm dust continuum. Protostars VLA 1623 AB (Class 0) and W (Class I), SSTc2d J162626.0-242340 (flat) and GY 30 (Class I) correspond to regions with high levels of HCO+ emission and the highest levels of 850 μm dust continuum. Similarly, GSS 30 and LFAM 1 correspond to the highest levels of HCO+ but more mid-values of 850 μm dust continuum.

The Oph B, C, E and F regions are all fairly consistent. The majority of the region can be defined with low HCO+ and mid/low levels of 850 μm dust continuum. The Oph B2 core has increased levels of HCO+ (similar to regions in Oph A) with mid-levels of 850 μm continuum emission, corresponding to protostars SSTc2d J162730.9–242733 (Class I), IRS 47 (flat) and IRS 45 (flat). Additionally, protostars IRS 37 (Class I), EL 29 (Class I) and IRS 43 have similarly mid-levels of HCO+ and 850 μm emission. The remainder of the clumps have both low HCO+ and 850 μm emission. I note there were fewer scenarios examined for this comparison, which could lead to the decreased variation in these cloud regions.

5.3.1.3 HCO+ comparison with A_V

As explained above, the the visual extinction A_v map has a 270 arcsec angular resolution, which is a factor $\sim$18 larger than the beam for the $C^{18}O$, HCO+ and SCUBA-2 850 μm maps. The visual extinction is the only column density tracer suggesting other regions in the cloud may have higher column densities than the central region of Oph A (for example, the Oph B1 regions has low HCO+ emission with high extinction $A_v > 34$). The central region of Oph A showed the highest levels of HCO+ emission with corresponding mid-levels of visual extinction. Protostars included in this region are VLA 1623 AB (Class 0) and W (Class I), SSTc2d J162626.0-242340 (flat), GY 30 (Class I), LFAM 1 (Class I) and GSS 30 (Class I).

Like the comparisons with the other column density tracers, the centre of the Oph B2 clump corresponds to a mid-level of HCO+ emission and mid extinction (24–

34 mag), corresponding to protostars SSTc2d J162730.9–242733 (Class I), IRS 47 (flat) and IRS 45 (flat). There is a northeastern portion of the clump with a lower extinction than the rest of the cloud (A_v ∼9–24). As discussed above, the B1 region has the highest levels of extinction with low levels of HCO+ (< 7 K km s^{-1}) which includes protostars IRS 37 (Class I), SST2721.8-242728 (flat) and SSTc2d J162716.4-2423114 (flat).

The Oph C, E and F region is similar to the outer portions of the Oph B clump with lower extinction and HCO+ emission. Increased HCO+ emission with mid extinction levels are found near protostars EL 29 (Class I) and IRS 43.

5.4 Non-LTE modelling using RADEX

To interpret the HCO+ line emission in the cloud, it is necessary to understand how the physical cloud conditions contribute to the production of radiation. This process is known as radiative transfer. In Chapter 1, I described the radiative transfer equation and derived molecular line excitation temperatures ($T_{ex} = T_{kin}$), molecular hydrogen column density $N(H_2)$ and molecular hydrogen cloud mass assuming LTE. LTE is a poor approximation on cloud scales where a high density tracers like HCO+ may be subthermally excited ($T_{ex} < T_{kin}$) and trace lower densities than the critical density. Non-LTE radiative transfer codes are a useful tool in understanding these regions without assuming LTE. These codes solve the level populations iteratively with inputs of the column density, density, FWHM velocity (or non-thermal, turbulent velocities) and kinetic temperature. The codes output the molecular line peak temperature (main-beam temperature) and corresponding excitation temperatures and optical depths. Using the HCO+ data to constrain peak main-beam temperatures and FWHM velocities, ^{13}CO data to constrain kinetic temperatures and C^{18}O to constrain column densities (see Chapter 4) these codes can be used to model the densities traced by the HCO+ molecule and better understand the link between column density and density in the cloud.

The simplest density model assumes the density remains constant along the line-of-sight which is implemented in the non-LTE radiative transfer code RADEX. In this section, I use this code to analyse the densities traced by the HCO+ emission assuming constant density. I further develop the density model to vary along the line-

of-sight in Sections 5.5 and 5.6 and implement the profiles into a more sophisticated Monte Carlo non-LTE code TORUS.

5.4.1 RADEX

RADEX[1] [van der Tak et al., 2007], originally written by J. H. Black, is a one-dimensional non-LTE radiative transfer code that assumes an isothermal and homogeneous medium without large-scale velocity fields using the escape probability method. The escape probability, or the probability a photon will break out of the surrounding medium, can use three different geometries: a uniform sphere, an expanding sphere and a plane-parallel slab. The program is iterative, finding a solution for the level populations using the following method:

1. The following parameters are input to RADEX: molecular data file from LAMDA[2] (including term energies, statistical weights, Einstein coefficients and rate coefficients for collisional de-excitation), frequency range of the transition, kinetic temperature of the cloud, number of collision partners (typically H_2 as the only collision partner), H_2 density, temperature of the background radiation field, column density of the molecule being modelled and FWHM line width.

2. An initial estimate of the level populations is made by assuming optically thin emission and statistical equilibrium considering the background radiation field (typically 2.73 K blackbody representing the cosmic microwave background or CMB).

3. The optical depths are then calculated for the molecular line.

4. The program iteratively continues to calculate new level populations with new optical depth values until both converge on a consistent solution.

5. The program outputs are: background-subtracted main-beam line intensities, excitation temperature and optical depth.

[1] http://www.sron.rug.nl/~vdtak/radex/radex.php
[2] http://home.strw.leidenuniv.nl/~moldata/

5.4.2 Methods for calculating density

My initial constant density model uses RADEX with the uniform sphere geometry for the escape probability. This geometry assumes the cloud is static, spherically symmetric and a homogeneous medium. A Python script reads in observationally-derived maps pixel-by-pixel of kinetic temperature, HCO+ column density, observed HCO+ peak main-beam temperature and HCO+ FWHM velocity. The program extracts the kinetic temperature, HCO+ column density and HCO+ FWHM velocity of the first pixel from each map and inputs these parameters into RADEX with an initial guess of the H_2 density (typically the critical density of HCO+ ($n_{\rm crit} = 8 \times 10^6$ cm^{-3}). RADEX makes a preliminary calculation of the HCO+ line strength from these parameters and the the Python script compares this output to the corresponding pixel from the observed HCO+ peak main-beam temperature map. This program will iterate and change the density input until the ratio of the model and observed line strengths agrees to within 1%. The program then outputs the best-fit H_2 density and corresponding excitation temperature and optical depth and writes these values into two-dimensional arrays. The program moves onto the next pixel in the kinetic temperature, HCO+ column density and HCO+ FWHM velocity maps and does a new radiative transfer calculation. Once all of the pixels have been extracted and ran through RADEX, the result is corresponding H_2 density, HCO+ excitation temperature and HCO+ optical depth maps.

The HCO+ column density N(HCO+) was calculated using several methods. Using C^{18}O (see Chapter 4) observations, the molecular hydrogen column density $N(H_2)$ was calculated using the relation

$$N(H_2) = 5.82 \times 10^{12} \ \frac{T_{\rm ex}}{\exp\left(-31.6/T_{\rm ex}\right)} \left(\int T_{\rm MB} \ {\rm dv} \right) \frac{\tau_o}{1 - \exp\left(-\tau_o\right)} \ [{\rm cm}^{-2}] \quad (5.2)$$

assuming LTE where $T_{\rm ex}$ is the excitation temperature calculated from ^{13}CO emission, $\int T_{\rm MB}$ dv is the main-beam integrated intensity and τ_o is the optical depth calculated in Chapter 4. Molecular hydrogen column density can also be calculated from visual extinction data using Spitzer. The dust is responsible for the high extinction of clouds through the absorption of both ultraviolet and visible wavelength light. Extinction is related to column density using the relation [Bohlin et al., 1978]

$$N(\mathrm{H_2}) = \frac{9.4 \times 10^{20}}{\text{molecules cm}^{-2}\ \text{mag}^{-1}} \frac{A_\mathrm{v}}{\text{mag}}\ [\text{cm}^{-2}] \tag{5.3}$$

where A_v is the visual extinction from the *Spitzer* Gould Belt project. Lastly, sub-millimetre dust continuum emission can also be used to calculate the beam averaged molecular hydrogen column density,

$$\begin{aligned} N(\mathrm{H_2}) &= \frac{F_\nu}{\Omega_\mathrm{beam}\ \mu m_{\mathrm{H_2}} \kappa_\nu B_\nu(T_\mathrm{D})} \\ &= 4.91 \times 10^{22} \frac{F_{850}}{\text{Jy beam}^{-1}} \left(\exp\left(\frac{16.93\ \text{K}}{T_\mathrm{D}}\right) - 1\right) \left(\frac{\kappa_{850}}{0.012\ \text{cm}^2\ \text{g}^{-1}}\right) [\text{cm}^{-2}] \end{aligned} \tag{5.4}$$

where Ω_beam is the solid angle in steradians subtended by the beam, $m_{\mathrm{H_2}}$ is the mass of a molecular hydrogen molecule, μ is the mean molecular weight per $\mathrm{H_2}$ molecule assuming 5 $\mathrm{H_2}$ for every He (assumed to be 1.4) and κ_ν is the dust opacity assumed to be 0.012 cm^2 g^{-1}. Past studies have assumed similar dust opacities at 0.02 cm^2 g^{-1} [Johnstone et al., 2000] and 0.01 cm^2 g^{-1} [van Kempen et al., 2009]. The column density was calculated at a dust temperature T_D of 10 K and 20 K to account for colder starless cores (see Curtis et al. 2010a) and warmer protostellar cores [Johnstone et al., 2000] in the Ophiuchus region. Specifically, SCUBA-2 850 μm data was used for this particular calculation. Molecular hydrogen column densities $N(\mathrm{H_2})$ were converted to HCO+ column densities N(HCO+) using the relation $N(\text{HCO+}) = X\ N(\mathrm{H_2})$ where X is the abundance factor, assumed to be 8×10^{-9}. HCO+ column density were fixed through the calculation.

The kinetic temperature map used for the model input was calculated from the ^{12}CO data in Chapter 4. Observed HCO+ line strengths and FWHM line widths were calculated by fitting a single Gaussian to the HCO+ data using the `fit1d` algorithm from the `SMURF` software from JAC. Since HCO+ is usually optically thick, some regions will have a double-peaked profile due to the absorption of the emission from the central high temperature gas and potential infall. In regions with double-peaked profiles, the single gaussian fits the centre of the two peaks and estimates the line strength by taking into account the height of the peaks and absorption dips.

The model outputs for molecular hydrogen density $n(\mathrm{H_2})$ can be found in Figure 5.8. In every model, densities typically range from $\sim 10^4$ to 10^6 cm^{-3}, below the HCO+ n_crit ($\sim 8 \times 10^6$ cm^{-3}). This indicates the HCO+ molecule is subthermally

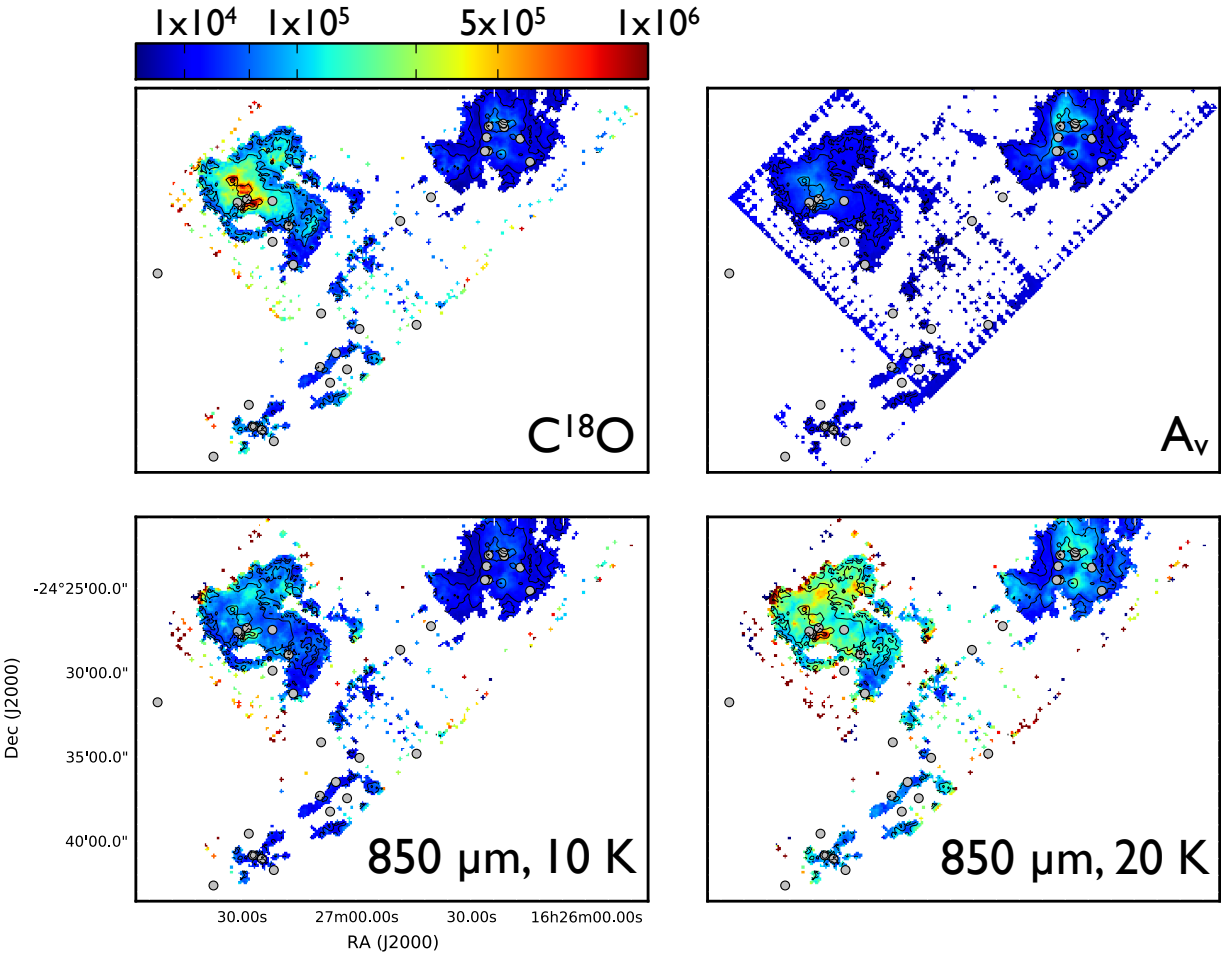

Figure 5.8: Molecular hydrogen density $n(H_2)$ in cm^{-3} calculated using HCO+ emission. HCO+ column densities N(HCO+) were estimated using column densities from $C^{18}O$ (top left), A_v (top right), 850 μm dust continuum with 10 K dust temperature (bottom left) and 20 K dust temperature (bottom right).

Model H_2 peak density (cm^{-3})				
Region	Column density tracer			
	$C^{18}O$	850 μm, 10 K temp	850 μm, 20 K temp	A_V
Oph A	1.4×10^5	7.8×10^4	2.6×10^5	1.9×10^5
Oph B	1.8×10^6	6.4×10^5	2.2×10^6	1.1×10^5
Oph CEF	1.6×10^5	1.3×10^5	4.0×10^5	5.7×10^4

Table 5.3: Peak densities found in Ophiuchus regions using the various RADEX models.

excited. Peak densities for the cloud regions are shown in Table 5.3. Peak densities found in the Oph B region are consistently modelled to be higher than the Oph A clump. An exception to this is the model using column densities derived from the visual extinction data where peak densities are comparable for the two regions. It is possible the larger angular resolution is contributing to this discrepancy. Optical depths, shown in Figure 5.9, indicate HCO+ is optically thick in each model to varying degrees (i.e. $\tau > 1$, reaching $\sim 10^2$). Excitation temperatures range from $\sim$ 6–21 K for each model.

Uncertainty in the density calculations can be examined based on the main-beam temperature noise, discussed in Section 5.1, which vary with kinetic temperature, peak temperature, line width and column density. Figure 5.10 demonstrates the relationship between the peak main-beam temperature of HCO+ and density $n(H_2)$ assuming a range of kinetic temperatures, column densities N(HCO+) and FWHM line widths. Average uncertainties are highest at lower peak main-beam temperatures. For a kinetic temperature of 30 K the uncertainties in density corresponding to 1, 2, 3, 5, 8, 10 and 12 K respectively are: 31, 16, 12, 8, 6, 6, 5 per cent. Similarly, for a 50 K kinetic temperature, corresponding density uncertainties for 1, 2, 3, 5, 8, 10 and 12 K main-beam temperature respectively are: 30, 16, 11, 7, 5, 4 and 4 per cent.

To test the plausibility of the densities calculated using RADEX, the molecular hydrogen column density $N(H_2)$ can be used to estimate the cloud length along the line-of-sight. Column density N is related to density n by integrating $N = \int_0^{L_{max}} n \, ds$ along the line-of-sight 'ds' from the front of the cloud to a distance L_{max}. The range of line-of-sight estimates vary greatly between each density model. Using column densities calculated from $C^{18}O$, line-of-sight lengths range from under 1 pc in Oph A and Oph B, 1–2 pc in portions of Oph B, C, E, and F and up to 40 pc near Oph S1 in Oph A. The A_v model predicts shorter line-of-sight lengths, mainly less than 1 pc but up to 2 pc. Similar to the $C^{18}O$ model, the dust continuum model with $T_D = 10$ K has line-of-sight estimates corresponding to mainly less than 5 pc, but extending greater than 20 pc (50–90 pc) near Oph S1 in Oph A. Estimates are more reasonable using a higher dust temperature ($T_D = 20$ K) where most line-of-sights are under 1 pc and the Oph S1 region is greater than 5 pc (up to $\sim$ 9 pc). Compared to the approximate width of the Oph A and B cores of 0.2 pc, the line-of-sight

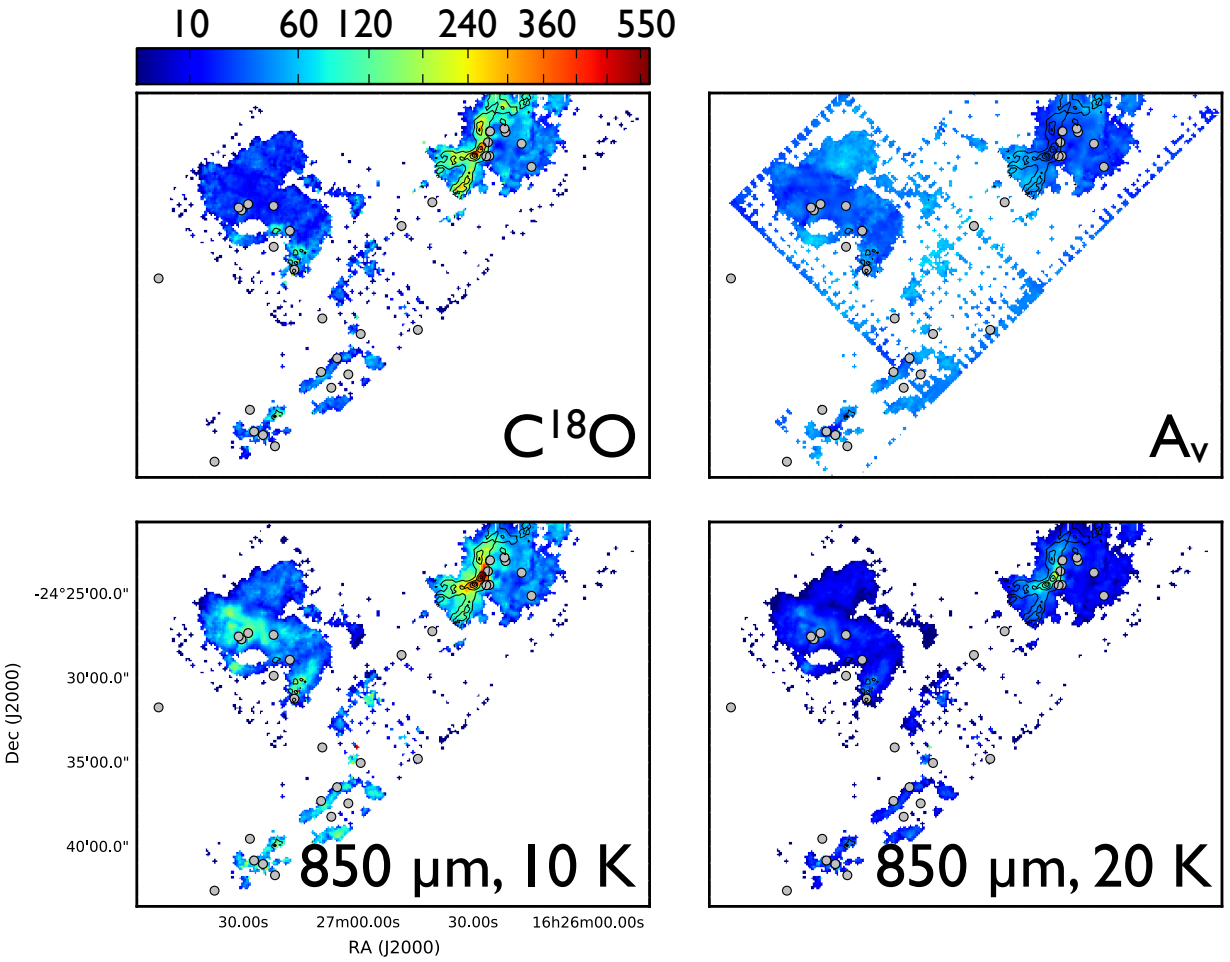

Figure 5.9: HCO+ optical depths. HCO+ column densities N(HCO+) were estimated using column densities from $C^{18}O$ (top left), A_v (top right), 850 μm dust continuum with 10 K dust temperature (bottom left) and 20 K dust temperature (bottom right).

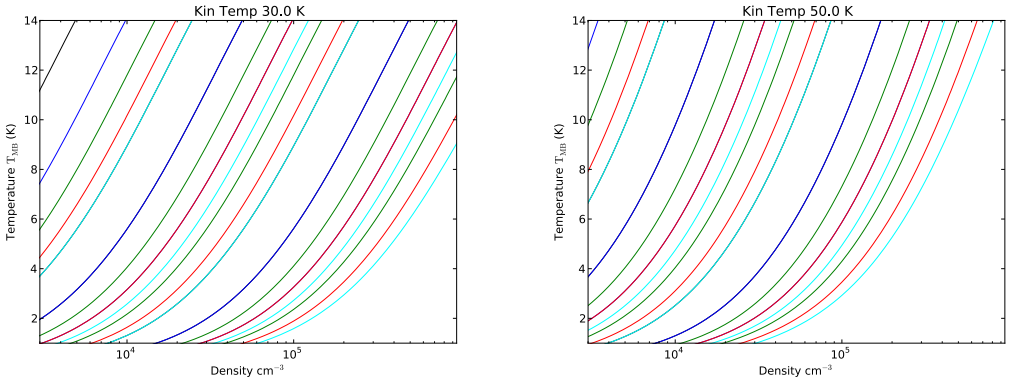

Figure 5.10: Relationship between the peak main-beam temperature of HCO+ and the predicted molecular hydrogen density $n(H_2)$. Inputs include a (left) 30 and (right) 50 K kinetic temperature. Colors denote the FWHM line width input into RADEX: 0.5 (black), 1.0 (blue), 1.5 (green), 2.0 (red) and 2.5 km s^{-1} (cyan). HCO+ column densities are also input into the program and range 5×10^{13}, 1×10^{14}, 5×10^{14}, 1×10^{15} and 5×10^{15} which are shown from left to right for each FWHM line width assumption. Note that only N(HCO+) of 5×10^{15} is shown assuming a 30 K kinetic temperature with 0.5 km s^{-1} and only 5×10^{14}, 1×10^{15} and 5×10^{15} are in range with a 30 K kinetic temperature and 1.0 km s^{-1}. For the 50 K kinetic temperature, the assumption of 0.5 km s^{-1} FWHM line width is out of the range of peak temperatures and densities seen in Ophiuchus and only N(HCO+) of 5×10^{14}, 1×10^{15} and 5×10^{15} are in range when assuming 1.0 km s^{-1} FWHM.

estimates suggest the 850 μm dust continuum model with higher dust temperatures better correlates to expected scales for the line-of-sight. However, each model has produced large line-of-sight lengths that are inconsistent with expected line-of-sight lengths.

The main issue with this method of modelling molecular line densities is the restriction of a constant density, which is unrealistic to assume for a molecular cloud. A peaked-density profile may be able to maintain similar average densities traced by the HCO+ data with a smaller line-of-sight length. In the upcoming sections (Section 5.5), I explore new methods for modelling density using models that vary along the cloud line-of-sight.

5.5 Varying density profile: simple peaked-density model

The assumption of a constant density does not realistically reflect the physical conditions of the cloud. To improve the HCO+ radiative transfer models in Ophiuchus and better understand the densities HCO+ tracers, it is important to develop density profiles that vary along the line-of-sight. The simplest peaked density profile can be described by an isosceles triangle which increases from the front of the cloud at a constant gradient to a peak density at the centre of the cloud and decreases at a constant gradient to the back edge of the cloud. In this section, I discuss the one-dimensional 'triangle' density profile I implement into the Monte Carlo radiative transfer code `TORUS`. I discuss how `TORUS` works and benchmarks I use to test the numerical quality of the code. I then discuss the one-dimensional radiative transfer models developed to model scenarios corresponding to the physical conditions of the cloud. The density results are discussed in Section 5.5.5.

5.5.1 Triangle density profile

The density n along the line-of-sight x is defined by

$$n(x) = \frac{2n_{max}x}{L},\ 0 \leq x \leq \frac{L}{2} \tag{5.5}$$

$$n(x) = \frac{2n_{max}(L-x)}{L},\ \frac{L}{2} \leq x \leq L \tag{5.6}$$

where L is the length of the cloud and n_{max} is the maximum H_2 density of the cloud. The density peaks at the centre of the cloud so that if $x = \frac{L}{2}$, $n = n_{max}$. The column density can then be defined as $N_{H_2} = \frac{1}{2}Ln_{max}$ where the maximum density is related to the average density $\overline{n} = \frac{1}{2}n_{max}$.

The conditions of the overall cloud can be used to constrain the primary density profile. Assuming a maximum cloud line-of-sight length L and an average density defined by $\overline{n} = M/L^3$ where M is the mass of the cloud, both a maximum density and column density of the cloud profile is established. Individual column densities N_i taken using observational data can then be used to infer a corresponding maximum density $n_{i,max}$ and line-of-sight length L_i towards different regions in the cloud using the following relation:

$$N_i = \frac{n_{max}L_i^2}{L} \tag{5.7}$$

$$n_{i,max} = \frac{N_i}{L_i}. \tag{5.8}$$

An example of the triangle density profile is shown in Figure 5.11, where N is the maximum cloud column density that is derived from the assumed maximum line-of-sight length L and the maximum cloud density n_{max} (taken from the cloud mass and length). Individual column densities N_{1-3} have been used to constrain the profiles in yellow, green and blue and correspond to $n_{max,1}$–$n_{max,3}$ and L_1–L_3 respectively. The highest individual column density corresponds to N_1 and column densities decrease with increasing numerical values (i.e N_3 is the lowest individual column density).

Analysing the probability density function (PDF) of this simple peaked-density model yields a constant function, i.e. the probability of finding individual density n, $P(n)$, in the triangle profile is the same for each individual density. Past research (see Kainulainen et al. 2009) suggests the column density PDF across molecular clouds

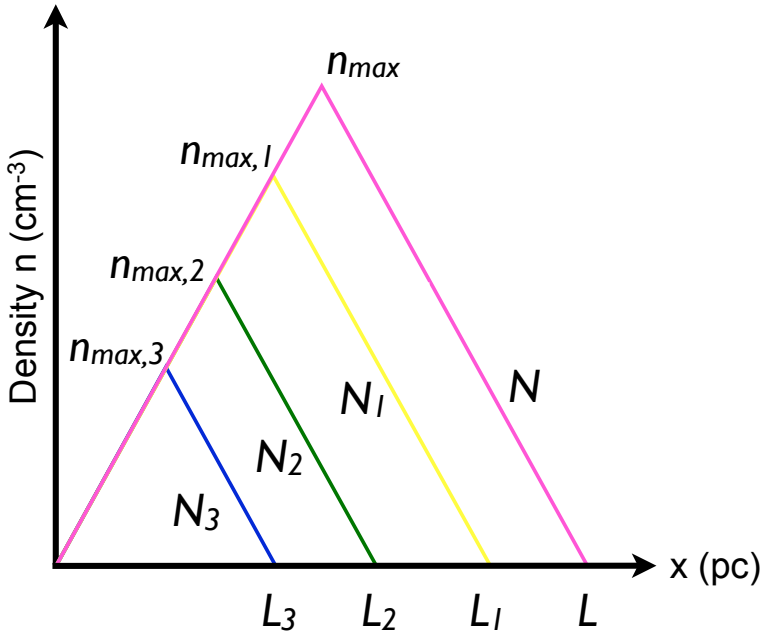

Figure 5.11: Example of the triangle density profile (n) along the line-of-sight (x).

can be defined using a log-normal function. Even though the triangle model does not reflect the log-normal PDF, the profile is the first step in better understanding how a varying density model can be implemented into radiative transfer codes and how the the molecular line radiation is affected by the varying density. Section 5.6 describes the next step in developing a density profile based on the more realistic log-normal PDF.

5.5.2 TORUS

TORUS is a three-dimensional Monte Carlo radiative transfer code short for Transport of Radiation Under Sobolev or Transport of Radiation Using Stokes (see Harries 2000). Though spherically and cylindrically symmetric source models can be used to model cores and filaments respectively, the geometry I use for modelling HCO+ in Ophiuchus is a simple plane-parallel slab with constant density in the x and y directions (RA and Dec) and the density profile implemented in the z direction. Like RADEX, this program is iterative and finds a solution for the level populations (solving the equations of radiative transfer) using the following method:

1. The following parameters are input to TORUS, specifically for the implementation of HCO+ models: molecular data file from LAMBDA (including term energies, statistical weights, Einstein coefficients and rate coefficients for collisional de-excitation), the transition of the molecule, maximum number of transitions to be considered for the calculation of non-LTE populations (typically around 10 in the case of HCO+), molecular abundance (8×10^{-9}), number of initial rays (typically 12800), distance to object (here 120 pc), H_2 density profile, kinetic temperature of the cloud, number of collision partners (typically H_2 as the main collision partner), H_2 maximum density, temperature of the background radiation field, column density of the molecule and turbulent line width. I note these are the parameters for modelling HCO+ in Ophiuchus and these can be changed and more parameters can be added for other purposes (further discussed in Section 5.5.3).

2. An initial guess of the level populations is made, assuming LTE. This allows the calculation of the emission and absorption coefficients, j_ν and α_ν (discussed in Section 1.3.2 using the Einstein coefficients), optical depth τ_ν and the mean intensity J_ν.

3. Using statistical equilibrium and the newly calculated J_ν, the level populations are recalculated.

4. This process is repeated by recalculating emission and absorption coefficients, optical depth and mean intensity until convergence on a solution is achieved.

5. Program outputs include: background-subtracted main-beam temperature data cube (K) along a velocity axis (km/s), excitation temperature (K) along the line-of-sight (pc), and optical depth (τ_ν) peak.

Once convergence is achieved for the level populations, a small set of rays are used to sample the radiation intensity of the model cells. The second stage to this process doubles the number of rays used to sample the radiation field per cell per transition. This increase of rays diminishes potential systematic and random errors by $\sqrt{N}$ where N is the number of rays, i.e. Monte Carlo solution noise (see Rundle, Ph.D. Thesis).

5.5.3 TORUS benchmarks

To test the numerical quality of the TORUS code, it is useful to compare the output to similar non-LTE radiative transfer codes with the same initial parameters. This process is known as 'benchmarking' and is necessary to draw accurate conclusions from modelling. In this section, I test TORUS with other non-LTE codes and test various AMR grid splitting and tolerance parameters to optimise the efficiency and accuracy of the models.

Initially, I compared TORUS to non-LTE codes RADEX (discussed in Section 5.4.1) and the Monte Carlo program RATRAN[1] [Hogerheijde and van der Tak, 2000]. Some discrepancies are expected from these models because both TORUS and RATRAN have finite geometries while RADEX assumes an infinite geometry. I use the benchmark developed by van der Tak et al. [2007] initially used to compare RADEX output from HCO+ $J = 1 \rightarrow 0$ to output from RATRAN. Since I am implementing a plane-parallel slab geometry in TORUS, I use the same geometry for RADEX. The other inputs are the column density of the HCO+ molecule $N(\mathrm{HCO+}) = 10^{12}$, 10^{13}, 10^{14} and 10^{15} cm^{-2}, FWHM line width $\Delta \mathrm{V} = 1.0$ km/s, $T_{\mathrm{kin}} = 10$ K, constant density $n(\mathrm{H_2}) = 10^4$ cm^{-3} and background temperature $T_{\mathrm{CMB}} = 2.73$ K. Figure 5.12 shows the excitation temperature results of HCO+ $J + 1 \rightarrow 0$ models from TORUS (black) with RADEX (red). Excitation temperatures and optical depths of both RATRAN (see Figures 3 and 4 in van der Tak et al. 2007 for RATRAN results) and TORUS agree, including the noticeable shape of the excitation temperatures. This downward slope is due to the geometry of a finite cloud. At the centre of the cloud, the excitation is thermalised through photon trapping; however, emission can escape more easily at the edge of the cloud. At higher column densities, optical depths begin to increase and reach $\tau > 100$ at $N(\mathrm{H_2}) = 10^{15}$ cm^{-2} (found in all models). At these high optical depths, van der Tak et al. [2007] recommends not using RADEX for non-LTE calculations since the excitation temperature may not reflect the true cloud conditions. Differences between RADEX and TORUS range between 4–48% for integrated intensities, 15–72% for peak main-beam temperatures, and 2–22% for optical depths. I note integrated intensities for RADEX are calculated assuming a Gaussian line distribution, i.e. $\int T_{\mathrm{mb}} \mathrm{d}v = T_{\mathrm{mb}}(1.06 v_{\mathrm{fwhm}})$.

[1] http://www.sron.rug.nl/~vdtak/ratran/

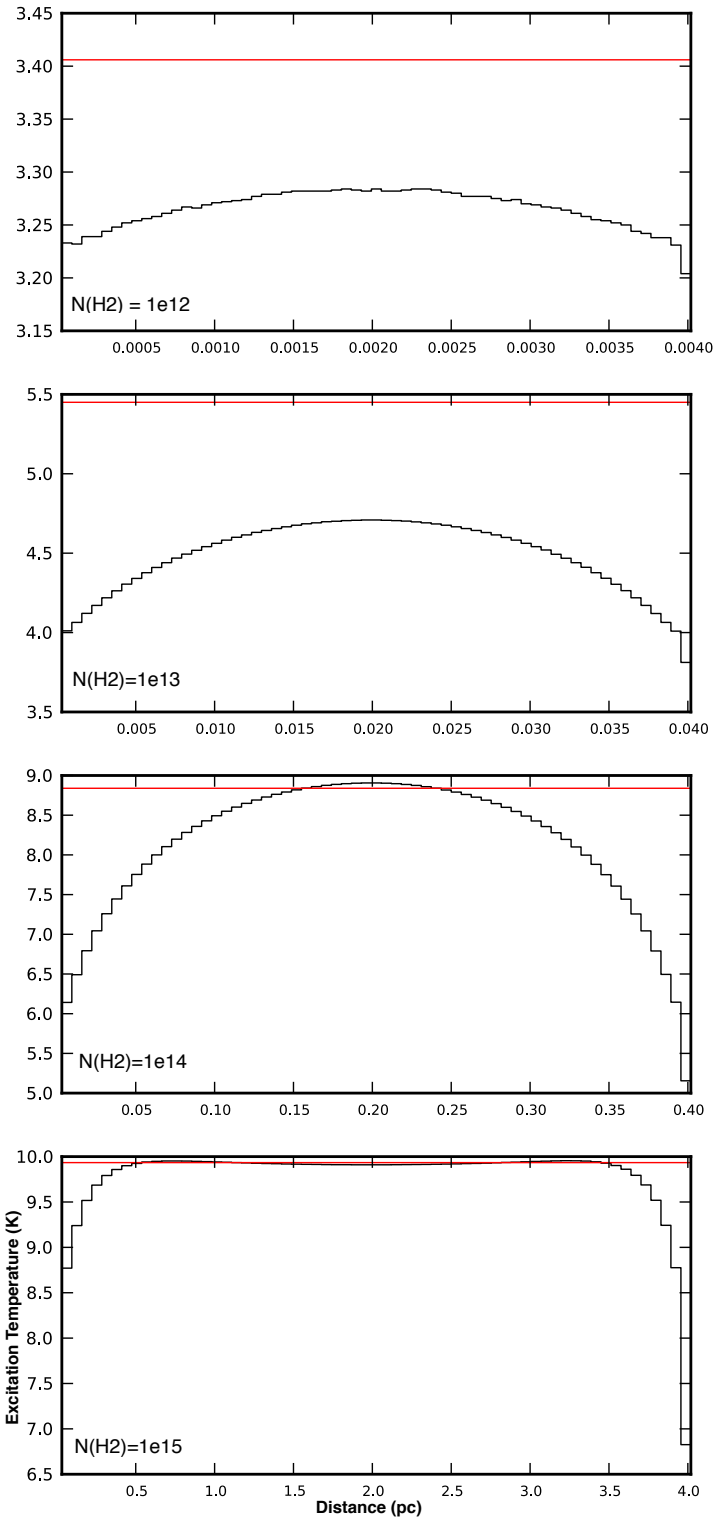

Figure 5.12: HCO+ excitation temperatures (K) from TORUS (black) and RADEX (red) using benchmark parameters.

	Test 1	Test 2	Test 3
Column Density (cm^{-2})	10^{15}	10^{14}	10^{14}
Kinetic Temperature (K)	30	30	50
H_2 Density (cm^{-3})	10^5	5×10^4	5×10^4

Table 5.4: Test scenarios used for TORUS benchmarking.

In addition to benchmarking TORUS against other models, AMR grid splitting and the tolerance levels were optimised for both an efficient run time and accuracy. The AMR splitting, n, determines the minimum and maximum cell depth of the model described by 2^n cells used to generate the density profile in the z-axis. For example, if the grid size is set to be 3×10^{18} cm and $n = 4$, a cell would be 1.88×10^{17} cm or 0.06 pc across. I tested splitting values $n = 4$, 5, 6, and 7 for the constant density scenarios. For each AMR grid splitting values, varying tolerances were also tested. The global convergence of the model is defined by a parameter ξ (see Rundle, PhD thesis), which must be lower than the tolerance input into TORUS. This factor is determined from the old and new level populations in each cell after an iteration of the code for all levels being included in the model. Tolerances of 0.01 ($\sim$1%) and 0.001 ($\sim$0.1%) were tested for both accuracy and run time.

The range of AMR grid splitting and tolerances were tested on three difference scenarios using HCO+ $J = 4 \rightarrow 3$. These scenarios were chosen to test a range of H_2 column densities, kinetic temperatures and densities (continuing to assume a constant density) using TORUS. The test scenarios are listed in Table 5.4, where all of the models had the same line widths ($v_{\rm FWHM}$ = 2.0 km s^{-1}), background temperature ($T_{\rm CMB}$ = 2.73 K) and HCO+ abundance ($X_{\rm HCO+} = 8 \times 10^{-9}$).

As discussed in Rundle [PhD, 2010], the results for the 1% tolerance models show some significant deviation from the 0.1% model. Using the $n = 6$ splitting as a base, the percentage difference between the $n = 6$ model and $n = 4, 5$ and 7 models for the 1% tolerance level show increased variations in integrated intensities, peak main-beam temperatures, excitation temperatures and optical depths. This was particularly noticeable for test 1, which has the highest optical depth (τ $\sim$61–73), where the percentage differences range from 6–32% in integrated intensity, 6–27% in peak temperature, 5–24% in excitation temperatures and 1–15% in optical depths. The other scenarios had much lower percentage differences (peaking at 2%), but

these scenarios have lower optical depths of ∼6–7.

Comparing the splitting values for the 0.1% tolerance, the $n = 6$ and 7 splitting values had the closest results, differing at most 2% when comparing peak temperatures, integrated intensities, excitation temperatures and optical depths. In contrast, $n = 4$ and 5 models were up to 10% different compared to $n = 6$. Taking into account the length of time to run the programs ($n = 7$ can be roughly a factor of 5 greater than $n = 6$), I chose to use the $n = 6$ splitting for the triangle and log-normal models with the 0.1% tolerance.

Since the TORUS outputs were comparable to the other non-LTE radiative transfer codes, I proceeded in implementing a varying density profile into the code and running models of the HCO+ line.

5.5.4 TORUS triangle models

The TORUS models implement the simple 'triangle' density profile described in Section 5.5.1. These models were one-dimensional with a plane-parallel geometry. The model inputs were H_2 column density, kinetic temperature, FWHM velocity, density profile and abundance (assumed to be constant at $X_{\rm HCO+} = 8 \times 10^{-9}$). The model outputs the HCO+ line profile (main-beam temperature as a function of velocity), excitation temperature along the line-of-sight and peak optical depth. The model HCO+ peak main-beam temperature, integrated intensity and FWHM velocity are then compared to the HCO+ observational data.

As described in Section 5.5.1, the triangle density profile was constrained from an assumed maximum line-of-sight cloud length and cloud mass to calculate the corresponding cloud average density. Two maximum cloud lengths were chosen, based on the lengths of the Oph A and B clumps measured in RA and Dec; these cloud lengths were 0.2 and 0.3 pc respectively. The average density of the cloud was estimated from the mass and assumed cloud lengths, $n_{\rm avg} = M/L^3$. From $C^{18}O$ integrated intensities with an optical depth correction, the mass of the cloud was calculated to be 515 $M_\odot$ (see Chapter 4). For the 0.2 and 0.3 pc clouds, the average density of the cloud was 9.6 × 10^5 and 2.8 ×10^5 cm^{-3}. The corresponding peak column densities for the cloud were 5.9 × 10^{23} and 2.6 × 10^{23} cm^{-2}.

As discussed above and in Chapter 4, the cloud has varying physical conditions

N_i (H_2) $\times 10^{22}$ cm^{-2}	T_{kin} K	FWHM velocity km s^{-1}
1	12	0.2
5	15	0.3
10	20	0.4
30	30	0.5
50	40	0.6
	50	1.0
		1.5
		2.0
		2.2

Table 5.5: Parameter grid for TORUS models.

reflected in the observations. The list of input parameters is shown in Table 5.5 and shown in Figure 5.13. These scenarios are not the same as the previous scenarios detailed in Table 5.2 in order to better reflect the range of input parameters were needed to reflect the variety of kinetic temperatures, column densities and HCO+ FWHM velocities found across the cloud. Individual column densities (N_i) were constrained by $C^{18}O$ data with the optical depth correction described in Chapter 4. I note models with the 0.3 pc cloud length were unable to model regions with the high column densities (3–5 $\times$ 10^{23} cm^{-2}) due to the maximum cloud column density constraint discussed above. $C^{18}O$ was chosen over the *Spitzer* A_v extinction and SCUBA-2 850 μm dust continuum data due to the larger angular resolution of the extinction map and the dust continuum data is limited by a constant dust temperature across the cloud. Kinetic temperatures were constrained using the ^{13}CO data from Chapter 4. Lastly, the FWHM velocities were based on the HCO+ observations. In models with kinetic temperatures reaching 40 and 50 K with column densities reaching 1–5 $\times$ 10^{23} cm^{-2}, it was common for TORUS to be unable to converge due to issues with population inversions or masing. The inversions in level population lead to negative optical depth. Since these models would not converge due to the population inversions, some models with kinetic temperature reaching 40 and 50 K were not included in the analysis.

The output main-beam temperature profiles can be found in Section 5.9 in Figures 5.36 and 5.37. The models were fit to the data by defining scenarios corresponding to the range of column densities and kinetic temperatures found across

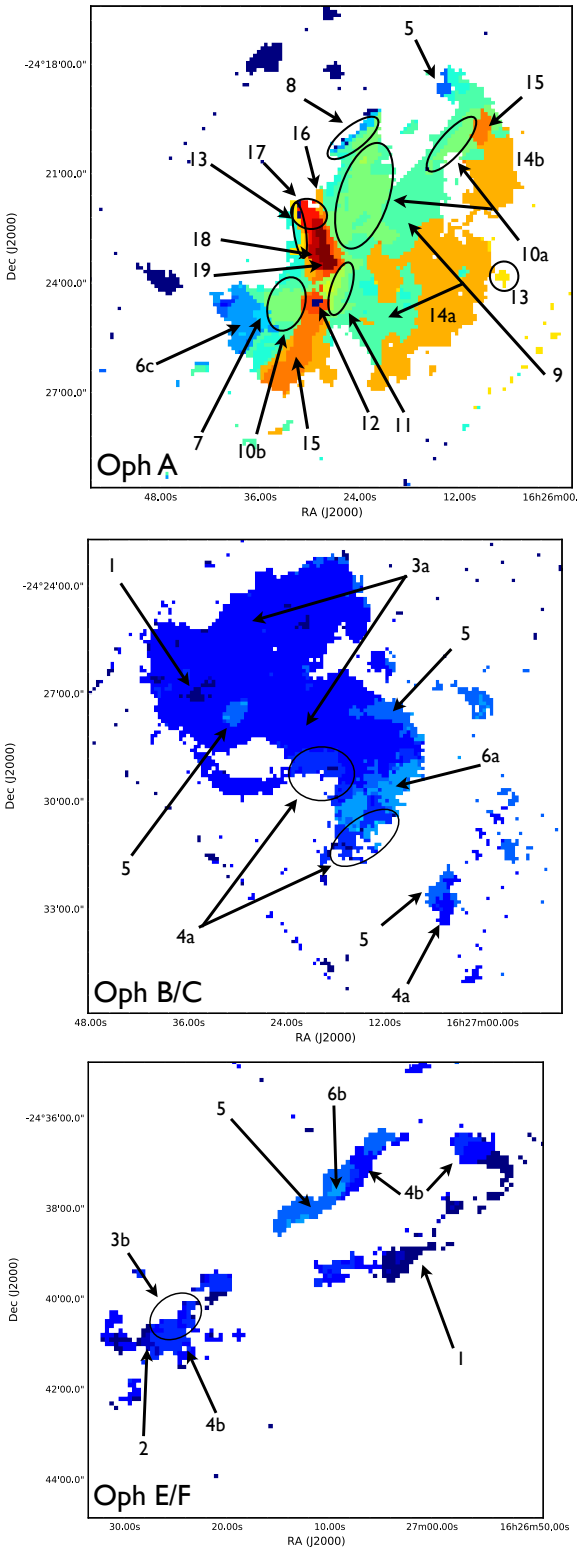

Figure 5.13: Scenarios corresponding to Table 5.6.

the cloud. Column densities calculated from the optical depth corrected $C^{18}O$ integrated intensities ranged from 0.5–40 $\times$ 10^{22} cm^{-2}. Kinetic temperatures from the ^{13}CO data ranged from 10–60 K. Column densities and kinetic temperatures were grouped into smaller ranges that covered the variety of column densities and kinetic temperatures used as model inputs described above. Each scenario had a corresponding range of FWHM velocities calculated from the HCO+ observational data. Initially, all of the models were fit to the individual scenarios, independent of the expected column density, kinetic temperature and FWHM velocity ranges. The criterion for fitting the scenario was the model line profile must have a peak temperature and integrated intensity within 20% of the minimum and maximum temperatures and integrated intensities found in the scenarios. The FWHM velocity must also be within 0.1 km s^{-1} of the minimum and maximum FWHM velocities found in the data. Uncertainties are based on standard HARP calibration uncertainties (see Buckle et al. 2009) and the 0.2 km s^{-1} velocity channel binning for the HCO+ maps.

The fitting process was further refined by choosing 'best-fits' or models that had column density inputs and FWHM velocity outputs matching the ranges found in the scenarios. Since scenario kinetic temperatures were not used to distinguish between the quality of model fit, it is possible these models do not have input kinetic temperatures relating to temperatures found using ^{13}CO data. This issue is further discussed in Section 5.7.2.

In the next section, I describe the fits from the triangle density models. I only include pixels that correspond to HCO+ main-beam temperatures and integrated intensities that have been successfully fit by the models as described above.

5.5.5 Determining density using the triangle model

The range of densities and cloud line-of-sight lengths are shown in Table 5.7 for the triangle model fits. Models produced using the triangle density profile predict peak densities that directly correspond to the input column density of the model, i.e. peak densities are higher for scenarios with higher column densities. Figure 5.14 shows the model column densities and peak densities used to fit each region. Class 0/I protostars are denoted using '$\circ$', pre-stellar cores (Simpson et al 2008) are denoted

Scenario	**Column Density** (cm^{-2})	T_{kin} (K)	v_{FWHM} (km s^{-1})
1	5 $\times 10^{21}$ - 3×10^{22}	10 - 13.5	0.7–1.5
2	3 - 8×10^{22}	10 - 13.5	0.4–2.8
3a	5 $\times 10^{21}$ - 3×10^{22}	13.5 - 17	0.4–1.9
3b	5 $\times 10^{21}$ - 3×10^{22}	13.5 - 17	0.4–2.9
4a	3 - 8×10^{22}	13.5 - 17	0.4–6.2
4b	3 - 8×10^{22}	13.5 - 17	0.4–3.7
5	5 $\times 10^{21}$ - 3×10^{22}	17 - 25	0.4–2.4
6a	3 - 8×10^{22}	17 - 25	0.4–1.5
6b	3 - 8×10^{22}	17 - 25	0.4–1.5
6c	3 - 8×10^{22}	17 - 25	0.4–1.5
7	8×10^{22} - 2×10^{23}	17 - 25	0.2–1.2
8	5 $\times 10^{21}$ - 3×10^{22}	25 - 35	0.4–2.0
9	3 - 8×10^{22}	25 - 35	0.4 –2.0
10a	8×10^{22} - 2×10^{23}	25 - 35	2.0–2.2
10b	8×10^{22} - 2×10^{23}	25 - 35	0.4–2.0
10c	8×10^{22} - 2×10^{23}	25 - 35	0.4–2.0
11	2 - 4×10^{23}	25 - 35	0.9–1.7
12	4 - 8×10^{23}	25 - 35	1.2–1.5
13	5 $\times 10^{21}$ - 3×10^{22}	35 - 45	0.8–1.6
14a	3 - 8×10^{22}	35 - 45	0.4–1.3
14b	3 - 8×10^{22}	35 - 45	0.4–2.1
15	8×10^{22} - 2×10^{23}	35 - 45	0.3–2.1
16	2 - 4×10^{23}	35 - 45	1.1–1.9
17	3 - 8×10^{22}	45 - 60	0.8–1.8
18	8×10^{22} - 2×10^{23}	45 - 60	1.0-2.0
19	2 - 4×10^{23}	45 - 60	1.3–2.0

Table 5.6: Scenarios chosen from the data which are fit using the triangle and log-normal models.

Scenario	Column density (cm^{-2})	Density peak (cm^{-3})		Cloud length (pc)	
		0.2 pc	0.3 pc	0.2 pc	0.3 pc
1	1×10^{22}	2×10^5	1×10^5	0.03	0.06
2	5×10^{22}	6×10^5	2×10^5	0.06	0.13
3a	1×10^{22}	2×10^5	1×10^5	0.03	0.06
3b	1×10^{22}	2×10^5	1×10^5	0.03	0.06
4a	5×10^{22}	6×10^5	2×10^5	0.06	0.13
4b	5×10^{22}	6×10^5	2×10^5	0.06	0.13
5	1×10^{22}	2×10^5	1×10^5	0.03	0.06
6a	5×10^{22}	6×10^5	2×10^5	0.06	0.13
6b	5×10^{22}	6×10^5	2×10^5	0.06	0.13
6c	5×10^{22}	6×10^5	2×10^5	0.06	0.13
7	1×10^{23}	8×10^5	3×10^5	0.08	0.19
8	1×10^{22}	2×10^5	1×10^5	0.03	0.06
9	5×10^{22}	6×10^5	2×10^5	0.06	0.13
10a	1×10^{23}	8×10^5	3×10^5	0.86	0.19
10b	1×10^{23}	8×10^5	3×10^5	0.08	0.19
10c	1×10^{23}	8×10^5	3×10^5	0.08	0.19
11	3×10^{23}	1×10^6	–	0.14	–
12	5×10^{23}	2×10^6	–	0.18	–
13	1×10^{22}	2×10^5	1×10^5	0.03	0.06
14a	5×10^{22}	6×10^5	2×10^5	0.06	0.13
14b	5×10^{22}	6×10^5	2×10^5	0.06	0.13
15	1×10^{23}	8×10^5	3×10^5	0.08	0.19
16	3×10^{23}	1×10^6	–	0.14	–
17	5×10^{22}	6×10^5	2×10^5	0.06	0.13
18	1×10^{23}	8×10^5	3×10^5	0.08	0.19
19	3×10^{23}	1×10^6	–	0.14	–

Table 5.7: Model fits to triangle scenarios for HCO+ data. Corresponding peak densities and cloud lengths for each fit are shown. Scenarios without fits are shown as '–'.

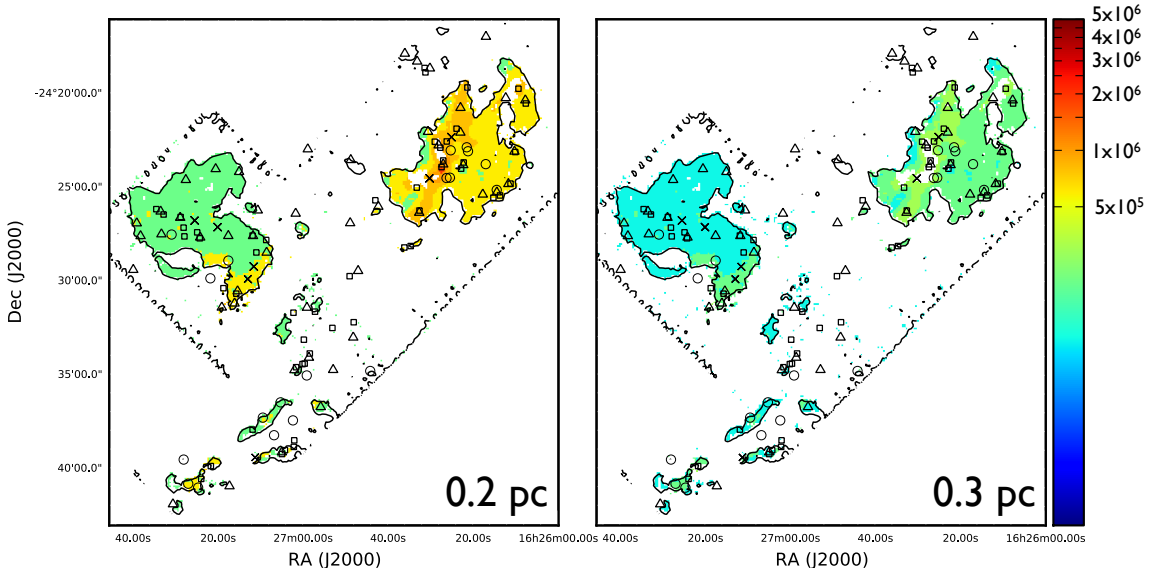

Figure 5.14: Densities (cm^{-3}) measured by the 0.2 and 0.3 pc triangle models. Contours denote the 5σ HCO+ peak main-beam temperature detection.

with '△', 'starless' cores (Stanke et al 2004) are denoted with '□', and duplicate cores found in both lists are denoted using '×'. The peak density ranges from 0.2–2.0×10^6 and 0.1–0.3×10^6 cm^{-3} for the 0.2 and 0.3 pc models respectively. The triangle models fit the majority of the regions with HCO+ emission across the cloud. I note the peak densities do not fully reach the critical density of 8×10^6 cm^{-3}. Additionally, some of the high column density emission primarily from the Oph A region has no corresponding density information in the 0.3 pc model due to the lower maximum column density range this model was able to fit.

The most noticeable features in these density plots are the more uniform densities in Oph B in comparison to Oph A, where Oph B does not show as high of column densities as the Oph A region. The more uniform densities in the Oph B region are the result of the choice in model scenarios. If the TORUS models had more closely spaced column density inputs, more variation in density would have detected. However, the range of Oph B densities would always be smaller than Oph A. Higher densities are seen near a Class I source SSTc2d J162730.9-242733 ($n = 6 \times 10^5$ and 2×10^5 cm^{-3} for the 0.2 and 0.3 pc models), which is close to the flat spectrum sources IRS 45 and 47, where IRS 45 drives the main Oph B outflow (determined

in Chapter 3). Additionally the Oph B1 region, which is further south than the main Oph B clump, has higher column densities and thus a higher model density ($n = 6 \times 10^5$ and 2×10^5 cm^{-3} for the 0.2 and 0.3 pc models) than the main clump. Oph B1 has only one Class I protostar (IRS 37) and several starless and pre-stellar cores previously identified.

The Oph CEF region has a similar density distribution to Oph B, where there is an increase in column density and thus density around Class I protostars EL 29, IRS 43 and IRS 44 ($n = 6 \times 10^5$ and 2×10^5 cm^{-3} for the 0.2 and 0.3 pc models), where these three sources are known to drive outflows (determined in Chapter 3). The filament itself has similar density to the majority of the Oph B region.

The Oph A region shows the greatest range of column densities and densities, with an increasing density in the central region, corresponding to a stripe down the centre of the clump where the peak column density and density are found. The highest densities at the centre of this stripe correspond to increased ^{13}CO kinetic temperatures (calculated in Chapter 4), further discussed in Section 5.7.2. The Class 0/I protostars are mainly clustered in the centre of the region, but do not necessarily correspond to the higher densities located in the stripe across the clump. Some starless and pre-stellar cores are located directly on the stripe of higher column density in addition to being spread along the south-western and northern edge of the cloud.

5.5.6 Understanding the three-dimensional cloud: triangle model

Line-of-sight lengths can be further inferred from the triangle models, shown in Figure 5.15. The lengths along the line-of-sight corresponding to the models are shown in parsecs (pc). Like the peak density maps, lengths along the z-axis follow column density. Therefore, line-of-sight lengths remain fairly constant across the Oph B core due less variation in the column densities. The x and y-axis lengths at the widest sections of the Oph B core taken from the 5σ HCO+ emission range from 0.220-0.280 pc. Line-of-sight lengths are, for the majority of the region, only 0.021 and 0.065 pc for the 0.2 and 0.3 pc triangle models respectively. This indicates the three-dimensional Oph B region is 5–10 times broader than it is deep. The z-axis

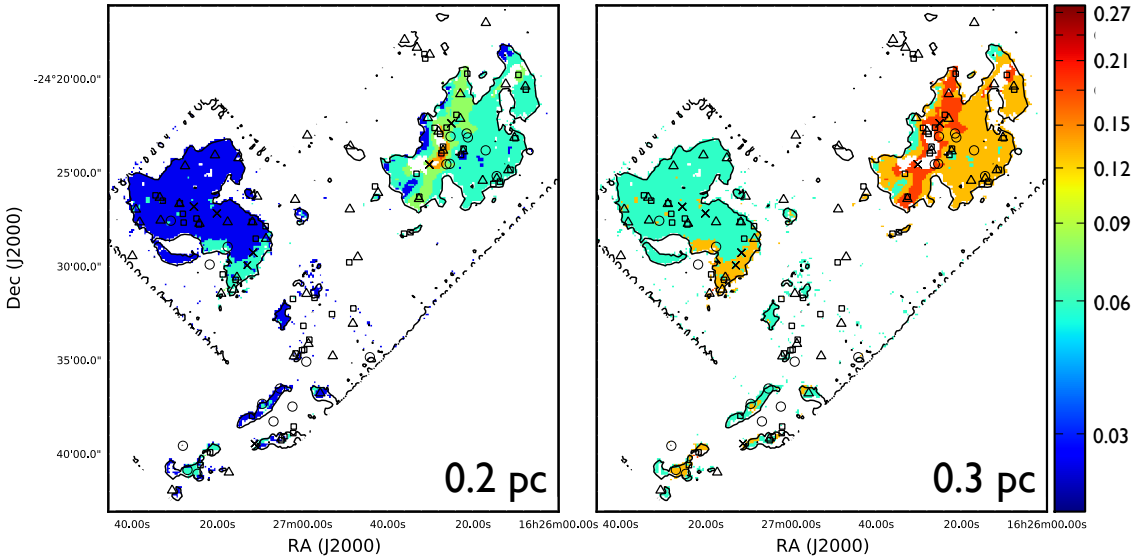

Figure 5.15: Line-of-sight lengths (pc) measured by the 0.2 and 0.3 pc triangle models. Contours denote the 5σ HCO+ peak main-beam temperature detection.

length is roughly 7.5–10% (0.2 pc model) and 23–30% (0.3 pc model) of the longest regions of the cloud, where the 0.2 pc triangle model predicts a thinner, flatter cloud than the 0.3 pc model. There are small portions of the cloud in the main Oph B clump and largely in the Oph B1 region where line-of-sight lengths increase to 0.046 and 0.108 pc (0.2 and 0.3 pc models respectively). In these sections, lengths increase to 16–21% and 39–49% (0.2 and 0.3 pc models) of the largest cloud widths.

Oph CEF has similar line-of-sight lengths to the Oph B region. There appears to be a distinct filament in the region where EL 29 and LFAM 26 are located. Lower in the Oph F region are IRS 44 and 43 driving outflows. From the 5σ HCO+ detections, the filament is around 0.270 pc long (including Oph F) and 0.030 pc wide. The line-of-sight lengths predicted by the models range from 0.022-0.046 pc (0.2 pc model) and 0.065–0.108 pc (0.3 pc model). This indicates the three-dimensional structure of the region is fairly cylindrical or filamentary but increases around the location of protostars for the 0.2 pc triangle model, where the 0.3 pc model predicts the line-of-sight lengths are up to 3 times the filament widths at the location of the protostars.

Oph A has the largest range of lengths along the line-of-sight. At the greatest x

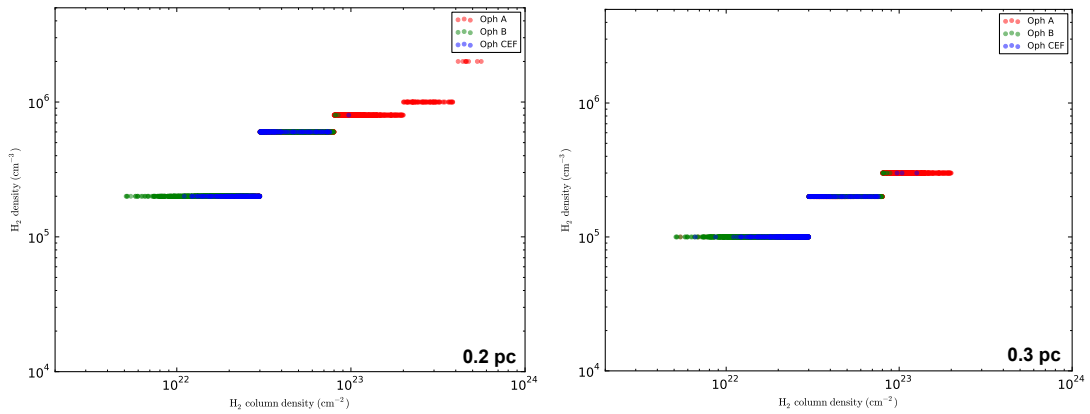

Figure 5.16: Pixel-by-pixel comparison between column density and density of the entire cloud using the triangle models.

and y-axis lengths using 5σ HCO+ emission, Oph A is ∼0.340 pc long and ∼0.190 pc wide. Like the column density and density, line-of-sight lengths predicted by the models increase towards the centre of the core where there is a stripe of increased cloud depth. The models predict z-axis lengths ranging from 0.022–0.162 pc (0.2 pc model) and 0.065–0.280 pc (0.30 pc model). This indicates the centre of the cloud is bulging along the stripe and decreases towards the edge of the cloud. The 0.2 pc triangle model with a peak line-of-sight length of only 48% of the full Oph A length predicts a more 'egg-like' three-dimensional shape to the cloud. Similarly, the 0.3 pc triangle model has a peak line-of-sight length of around 82% of the longest Oph A length, indicating a slightly more rounded cloud. The 0.3 pc model is unable to fit the most central portions of Oph A due to maximum column density constraints.

The regions of the cloud never fully reach the maximum cloud line-of-sight lengths 0.2 and 0.3 pc. The individual column densities from observational data are the main factor used to constrain the individual line-of-sight lengths. From Section 5.5, line-of-sight lengths will reach the maximum cloud lengths when column densities reach the maximum column density constrained by the 0.2 and 0.3 pc models.

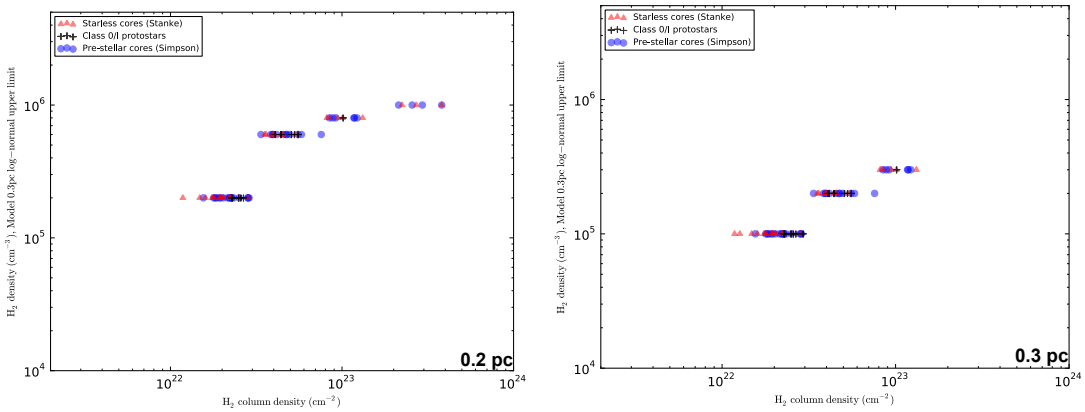

Figure 5.17: Source-by-source comparison between column density and density in the cloud using the triangle models.

5.5.7 Links between column density and density

As discussed in Section 5.3.1, the link between column density and density can be further investigated across the cloud using the density estimates from the above models. Figure 5.16 shows a pixel-by-pixel comparison between column density and density in the cloud. The full map comparison clearly shows the Oph A clump with higher density and column density than the Oph B and CEF regions. Figure 5.17 shows the same comparison for protostars and pre-stellar and starless cores. The source comparison shows a similar distribution to the full map. Column densities and densities range from 0.1–3.0×10^{23} cm^{-2} and 0.2–2.0×10^{6} cm^{-3} (0.2 pc model) and 0.1–0.3×10^{6} cm^{-3} (0.3 pc model) where densities are proportional to the column densities in the cloud.

The majority of cores are evenly distributed over the range of column densities for both the 0.2 and 0.3 pc models except for the high column densities $N(H_2) > 2 \times 10^{23}$ cm^{-2}. The Class 0/I embedded protostars are found primarily at column densities ranging from 2–10 × 10^{22} cm^{-2}, corresponding to density ranges 0.2–1.0 × 10^{6} (0.2 pc model) and 0.1–0.3 × 10^{6} cm^{-3} (0.3 pc model).

Figure 5.18 and 5.19 show histograms of the percentage of pixels and sources at various densities across the cloud. As in Section 5.2, KS tests were used to compare the distribution of pixels and sources in the cloud shown in Table 5.8. P-values indicate there is no difference between the distribution of pixels across the cloud and

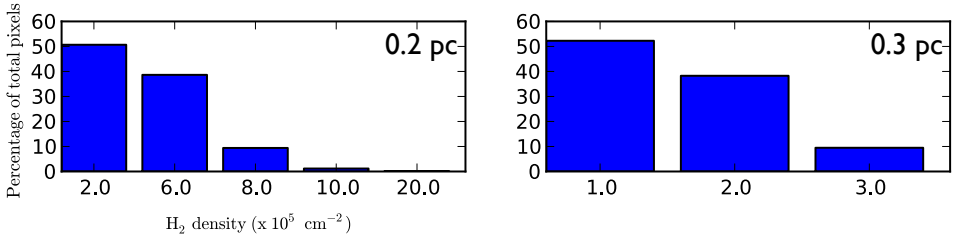

Figure 5.18: Histogram of the percentage of total pixels at different densities across the entire cloud using the triangle models.

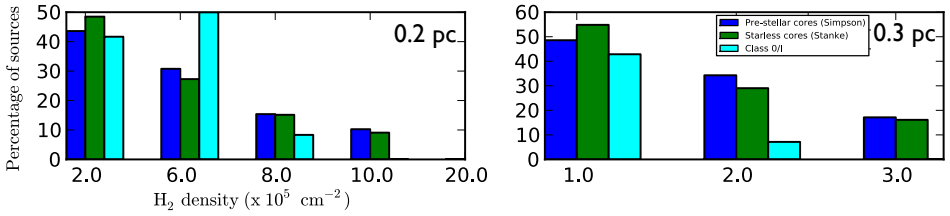

Figure 5.19: Histogram of the percentage of total sources at different densities across the entire cloud using the triangle models.

the sources (i.e. starless cores, pre-stellar cores and embedded protostars). There are slightly lower p-values for the comparison of embedded Class 0/I protostars to the total cloud and the other sources, but these values are not low enough to suggest the distributions are different.

Increased $C^{18}O$ emission may not necessarily be the result of higher column densities. Molecular abundances and gas temperatures also affected $C^{18}O$ emission that can inevitably bias column density calculations. These effects are further discussed in Section 5.7.

	0.2 pc triangle model			0.3 pc triangle model		
Source	Tot. Cloud	Pre-stellar	Starless	Tot. Cloud	Pre-stellar	Starless
Tot. Cloud	–	0.697	0.999	–	0.976	0.976
Pre-stellar	–	–	0.999	–	–	0.976
Class 0/I	0.697	0.697	0.697	0.320	0.320	0.320

Table 5.8: KS test results (p-values) for the distribution of densities across the cloud and for the pre-stellar, starless and protostellar cores.

5.6 Varying density profile: log-normal PDF model

As discussed in Section 5.5, past research suggests the column density probability density function or PDF has a log-normal distribution formed from supersonic turbulence in the cloud. Lombardi et al. [2008] showed the Ophiuchus molecular cloud to have a log-normal column density PDF, calculated from IR extinction at 2.2 μm $A_{\rm K}$, where $A_{\rm K} \approx 0.112 A_{\rm V}$ [Rieke and Lebofsky, 1985] However, this work was undertaken at $A_{\rm K} < 0.6$ or $A_{\rm V} \leq 5.36$ mag ($\sim$5 $\times 10^{21}$ cm^{-2}). These column densities are much lower than peak column densities calculated using C^{18}O optical depth corrected emission and 850 μm dust continuum emission with 20 K dust temperatures by 2 orders of magnitude (as discussed in Section 5.3.1).

Similarly, Kainulainen et al. [2009] used visual extinction data to calculate the probability of finding column densities between 0.5–25 $\times 10^{21}$ cm^{-2} of numerous clouds in the Galaxy, including Ophiuchus and other active and dormant star forming regions. This work found all active areas of star formation to have a column density PDF with a log-normal distribution at $A_{\rm V} \leq$ 2–5 mag and a power-law relation at $A_{\rm V} \geq$ 2–5 mag. In non-star forming regions (e.g. Lupus 5 and Coalsack) or regions with lower star formation activity (e.g. the massive California nebula), the column density PDF can be fit by the log-normal distribution. The log-normal fit to the non-active and low star formation regions suggests the structure of the cloud as it initially evolves is directly related to the supersonic turbulence found in the region. The shape of the log-normal becomes altered as the cloud evolves and local, higher density clumps and cores become self-gravitating. More gas becomes assembled into higher density regions and generates the power-law tail of the column density PDF.

Though the log-normal PDF is typically measured with column densities, the distribution is expected to hold for the three-dimensional density distribution. In the Ophiuchus region, Kainulainen et al. [2009] observed a column density PDF with a power-law tail forming at $A_{\rm v} \sim$5 and a log-normal distribution at lower extinction. The next logical step in developing a more realistic peaked-density profile is to derive a profile with a corresponding log-normal density PDF as opposed to the constant PDF predicted by the previous triangle density profiles. In this section, I discuss the one-dimensional 'log-normal PDF' density profile I implement into `TORUS`, similar to

the methods described in Section 5.5. I detail the implementation of the log-normal PDF density profile into the TORUS radiative transfer code. I discuss the model fitting process to the HCO+ data using similar techniques as the triangle TORUS models. Lastly, I discuss possible relations between column density and density in the cloud using these modelling techniques.

5.6.1 Log-normal PDF density profile

This density model is based on the assumption of a log-normal PDF. The probability of finding a normalised number density $q(x)$ in range $\mathrm{d}q$ is $\mathrm{P}(q)\ \mathrm{d}q \propto \frac{1}{L}\ \mathrm{d}x$ where $q = n/\overline{n}$ is the molecular hydrogen number density n relative to the average density and L is the full length of the cloud. The probability is defined by the log-normal distribution (see Elmegreen and Efremov 1997; Krumholz and Thompson 2007; Mac Low and Klessen 2004),

$$\mathrm{P}(q)\ \mathrm{d}q = \frac{1}{q\sigma\sqrt{2\pi}} \exp\left[\frac{-\left(\ln q - \overline{\ln q}\right)^2}{2\sigma^2}\right] \mathrm{d}q \tag{5.9}$$

where $\overline{\ln q} = \frac{-\sigma^2}{2}$ and σ is the width of the lognormal. Following Price et al. [2011], I define $\sigma^2_{\ln q} = \ln\left(1 + b^2\mathcal{M}^2\right)$ where $\mathcal{M}$ is the three-dimensional supersonic Mach number of the turbulence or $\mathcal{M} = \sqrt{3}\ \mathcal{M}_{1\mathrm{D}}$ and the scaling constant b is assumed to be 1/3. An example of this distribution is shown in Figure 5.20.

To obtain a relation between density and the position along the line-of-sight, I integrate $\int \mathrm{P}(q)\ \mathrm{d}q = \int \frac{1}{L}\ \mathrm{d}x$ and find the density n along the line-of-sight x to be

$$n(x) = \overline{n} \exp\left[\sqrt{2}\sigma \mathrm{erf}^{-1}\left(\frac{4x}{L} - 1\right) - \frac{\sigma^2}{2}\right], 0 \leq x < \frac{L}{2} \tag{5.10}$$

$$n(x) = \overline{n} \exp\left[\sqrt{2}\sigma \mathrm{erf}^{-1}\left(\frac{4\left(L - x\right)}{L} - 1\right) - \frac{\sigma^2}{2}\right], \frac{L}{2} < x \leq L. \tag{5.11}$$

The density diverges to infinity at the centre of the cloud $\left(x = \frac{L}{2}\right)$ unless a maximum density is defined for the above PDF. To find the column density, integrating the two density functions yields the column density relation $N = \overline{n}L$.

Like the triangle model, the global cloud conditions can be used to constrain the

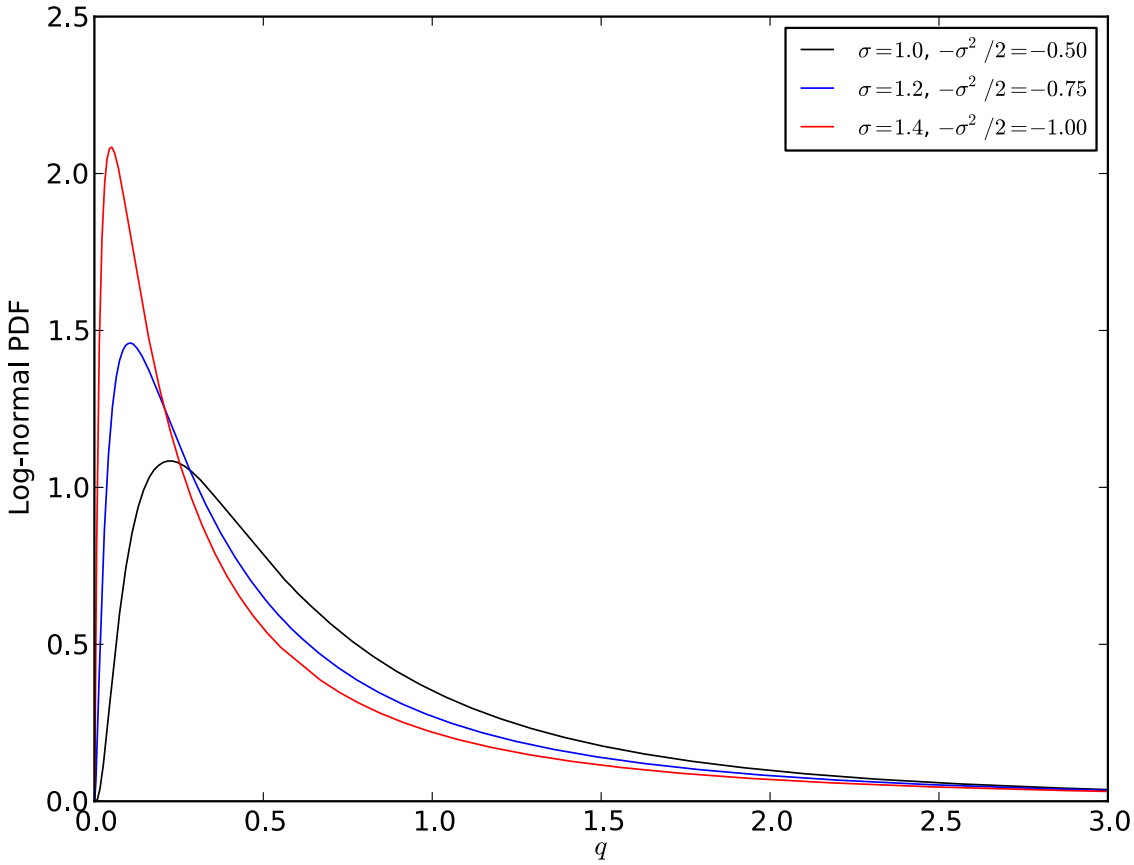

Figure 5.20: Example of a log-normal probability distribution function as described by Equation 5.9 with varying σ and $\overline{\ln q}$.

primary density profile. A maximum line-of-sight cloud length L is assumed and used to calculate the average density n across the cloud by $\overline{n} = M/L^3$ where M is the mass of the cloud (see Chapter 4). The average cloud density and assumed line-of-sight length constrains the maximum column density and density across the cloud. Additionally, the shape of the density profile is affected by the chosen width of the log-normal σ.

The density profile along the line-of-sight is expected to vary across the molecular cloud, dependent on individual column densities calculated from the $C^{18}O$. To investigate the variation of the density profile across the cloud, I use column densities N_i to constrain the corresponding maximum density $n_{i,max}$ and line-of-sight length L_i of the cloud. This is similar to the triangle density profile method. First, the relationship between the individual cloud length L_i and the maximum density $n_{i,max}$ using Equations 5.10 and 5.11 is

$$L_i = \frac{L}{2}\left(\mathrm{erf}\left(\frac{\ln\left(n_{i,max}/\overline{n}\right) + \frac{\sigma^2}{2}}{\sqrt{2}\sigma}\right) + 1\right), \tag{5.12}$$

where I assume $n = n_{i,max}$ when $x = \frac{L_i}{2}$. Integrating Equations 5.10 and 5.11 from $0 \leq \mathrm{x} \leq \frac{L_i}{2}$ (where $\frac{L_i}{2} < \frac{L}{2}$) yields an individual column density related to the maximum cloud column density

$$N_i = N\left(1 + \mathrm{erf}\left[\frac{\ln\left(n_{i,max}/\,\overline{n}\right) - \frac{\sigma^2}{2}}{\sqrt{2}\sigma}\right]\right). \tag{5.13}$$

Rearranging this equation yields the maximum individual density $n_{i,max}$,

$$n_{i,max} = \overline{n}\exp\left[\sqrt{2}\sigma\mathrm{erf}^{-1}\left(\frac{N_i}{N} - 1\right) + \frac{\sigma^2}{2}\right]. \tag{5.14}$$

Inputting these parameters back into Equations 5.10 and 5.11 and deriving the relation between the individual density $n_i(x)$ peaking at the centre of a cloud corresponding to the individual line-of-sight $L_i/2$, the new relation from $0 \leq x \leq \frac{L_i}{2}$

where $L_i < L$ and $N_i < N$ becomes

$$n_i(x) = \overline{n} \exp\left[\sqrt{2}\sigma \mathrm{erf}^{-1}\left(\frac{2x\left(\mathrm{erf}\left(\frac{\ln(n_{i,max}/\overline{n})+\frac{\sigma^2}{2}}{\sqrt{2}\sigma}\right)+1\right)}{L_i} - 1\right) - \frac{\sigma^2}{2}\right], \quad (5.15)$$

and from $\frac{L_i}{2} \leq x \leq L_i$ the relation becomes

$$\begin{aligned} n_i(x) &= \overline{n} \times \\ &\exp\left[\sqrt{2}\sigma \mathrm{erf}^{-1}\left(\frac{2(L_i - x)\left(\mathrm{erf}\left(\frac{\ln(n_{i,max}/\overline{n})+\frac{\sigma^2}{2}}{\sqrt{2}\sigma}\right)+1\right)}{L_i} - 1\right) - \frac{\sigma^2}{2}\right]. \end{aligned} \quad (5.16)$$

Figure 5.21 demonstrates how varying log-normal widths (σ_1–σ_5) and varying column densities (N_1–N_5) affect the shape of the log-normal density profile. Column densities N_i where i = 1–5 (right) correspond to individual column densities as described above in Equation 5.13 and σ_i (left) corresponds to varying σ. Higher i-values correspond to increased column densities or σ. As the width of the profile (σ) increases with constant column density, the maximum individual profile density $n_{i,max}$ decreases and the line-of-sight length increases. As the column density increases with constant profile width (σ), the maximum individual profile density $n_{i,max}$ increases and the line-of-sight length also increases.

Two types of models can be derived from the log-normal PDF density profile. The first is a more simple version where the width of the density profile σ is constant for Equations 5.15 and 5.17 (as in the right-side of Figure 5.21). In this case, σ can be defined from an average FWHM velocity across the cloud to derive the Mach number (as described above). The second case is more complicated and involves a varying density profile width that is defined from a range of FWHM velocities across the cloud. The varying width causes profiles with the same individual column density to have different corresponding individual densities n_i and line-of-sight lengths (L_i) based on the profile width (as in the left-side of Figure 5.21).

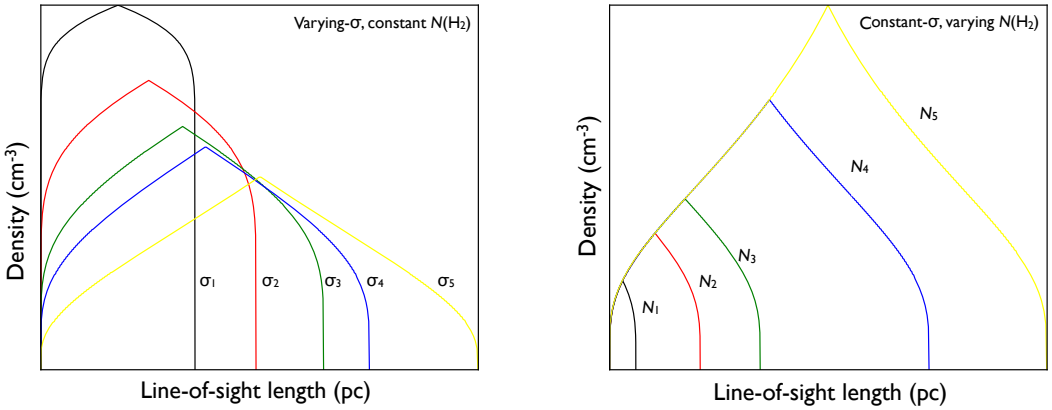

Figure 5.21: Example of a log-normal PDF density profile along the line-of-sight for (left) varying-σ with constant $N(H_2)$ and (right) constant-σ with varying $N(H_2)$.

5.6.2 TORUS models

Like the TORUS models using the triangle density profile described in Section 5.5.4, the log-normal PDF density profiles are implemented into TORUS using a one-dimensional, plane-parallel geometry. The model inputs were H_2 column density, kinetic temperature, FWHM velocity, density profile and HCO+ abundance. The model outputs included HCO+ main-beam temperature as a function of velocity, HCO+ excitation temperature as a function of line-of-sight length and peak HCO+ optical depth. The model main-beam temperature, integrated intensity and FWHM velocity were then compared to the HCO+ observation data to determine if the model fit data.

Two density profiles were developed from the basic log-normal PDF profile described in the previous section. The first profile ('constant-σ') assumed a constant width σ, defined by the average FWHM velocity (i.e. $\mathcal{M}$) across the cloud. The FWHM velocity was 1.7 km s^{-1} using HCO+ data. The second profile ('varying-σ') allowed the width to vary across the cloud. Similar to the triangle models, the maximum cloud lengths 0.2 and 0.3 pc were chosen to calculate the average density of the cloud of 9.6×10^5 and 2.8×10^5 cm^{-3}. The corresponding peak column densities for the cloud were 5.9×10^{23} and 2.6×10^{23} cm^{-2}.

The range of model input parameters (i.e. kinetic temperature, column densities and HCO+ FWHM velocities) are shown in Table 5.9 and match the values used in Section 5.5.4 for the triangle models. For the constant and varying profile widths, the

N_i (H_2)	T_{kin}	FWHM velocity	Mach number	
$\times 10^{22}$ cm^{-2}	K	km s^{-1}	varying-σ	constant-σ
1	12	0.2	1.0	8.5
5	15	0.3	1.5	
10	20	0.4	2.0	
30	30	0.5	2.5	
50	40	0.6	3.0	
	50	1.0	5.0	
		1.5	7.6	
		2.0	10.1	
		2.2	11.1	

Table 5.9: Parameter grid for TORUS models (log-normal density profile).

corresponding Mach numbers are also listed. I note the varying-σ density profile used the input FWHM velocity to constrain the Mach number defining the width of the profile. The relationship between σ^2 and the Mach number depends on supersonic turbulence ($1 \leq \mathcal{M} \leq 20$; Price et al. 2011). The Mach numbers for several of the lower FWHM velocities are low but still fall in this range. The constant -σ Mach number is 8.5. Like the triangle models, TORUS had convergence issues at kinetic temperatures reaching 40–50 K and column densities ranging from 1–5 $\times$ 10^{23} cm^{-2}.

The output main-beam temperature profiles can be found in Section 5.9 in Figures 5.38 to 5.41 for the models. As in Section 5.5.4, the same scenarios defined from the observational data (kinetic temperatures and column densities) were used to fit the models to the data. These scenarios are listed in Table 5.6. The criterion for fitting the scenario was the model line profile must have a peak temperature and integrated intensity within 20% of the minimum and maximum temperatures and integrated intensities found in the scenarios. The FWHM velocity must also be within 0.1 km s^{-1} of the minimum and maximum FWHM velocities found in the data. Uncertainties are based on standard HARP calibration uncertainties (see Buckle et al. 2009) and the 0.2 km s^{-1} velocity channel binning for the HCO+ maps. Only fitted data was included in the density and line-of-sight length analysis.

Scenario	Column density (cm^{-2})	Density peak (cm^{-3})		Cloud length (pc)	
		0.2 pc	0.3 pc	0.2 pc	0.3 pc
1	1×10^{22}	2×10^5	6×10^4	0.02	0.04
2	5×10^{22}	3×10^5	1×10^5	0.05	0.11
3a	1×10^{22}	2×10^5	6×10^4	0.02	0.04
3b	1×10^{22}	2×10^5	6×10^4	0.02	0.04
4a	5×10^{22}	3×10^5	1×10^5	0.05	0.11
4b	5×10^{22}	3×10^5	1×10^5	0.05	0.11
5	1×10^{22}	2×10^5	6×10^4	0.02	0.04
6a	5×10^{22}	3×10^5	1×10^5	0.05	0.11
6b	5×10^{22}	3×10^5	1×10^5	0.05	0.11
6c	5×10^{22}	3×10^5	1×10^5	0.05	0.11
7	1×10^{23}	4×10^5	2×10^5	0.07	0.16
8	1×10^{22}	2×10^5	6×10^4	0.02	0.04
9	5×10^{22}	3×10^5	1×10^5	0.05	0.11
10a	1×10^{23}	4×10^5	2×10^5	0.7	0.16
10b	1×10^{23}	4×10^5	2×10^5	0.07	0.16
10c	1×10^{23}	4×10^5	2×10^5	0.07	0.16
11	3×10^{23}	8×10^5	–	0.12	–
12	5×10^{23}	1×10^6	–	0.16	–
13	1×10^{22}	2×10^5	8×10^4	0.02	0.04
14a	5×10^{22}	3×10^5	1×10^5	0.05	0.11
14b	5×10^{22}	3×10^5	1×10^5	0.05	0.11
15	1×10^{23}	4×10^5	2×10^5	0.07	0.16
16	3×10^{23}	8×10^5	–	0.12	–
17	5×10^{22}	3×10^5	1×10^5	0.05	0.11
18	1×10^{23}	4×10^5	2×10^5	0.07	0.16
19	3×10^{23}	8×10^5	–	0.12	–

Table 5.10: Model fits to constant-σ log-normal scenarios for HCO+ data. Corresponding peak densities and cloud lengths for each fit are shown. Scenarios without fits are shown as '–'.

Scenario	Col. density (cm^{-2})	Density peak (cm^{-3})		Cloud length (pc)	
		0.2 pc	0.3 pc	0.2 pc	0.3 pc
1	1×10^{22}	3–6 $\times 10^5$	0.7–2 $\times 10^5$	0.003–0.080	0.01–0.04
2	5×10^{22}	4–8 $\times 10^5$	1–2 $\times 10^5$	0.01–0.03	0.04–0.10
3a	1×10^{22}	2–7 $\times 10^5$	0.7–2 $\times 10^5$	0.002–0.01	0.01–0.04
3b	1×10^{22}	1–7 $\times 10^5$	0.5–2 $\times 10^5$	0.002–0.02	0.01–0.05
4a	5×10^{22}	4–8 $\times 10^5$	2×10^5	0.01–0.03	0.04–0.08
4b	5×10^{22}	3–8 $\times 10^5$	1–2 $\times 10^5$	0.01–0.04	0.04–0.12
5	1×10^{22}	1–7 $\times 10^5$	0.5–2 $\times 10^5$	0.002–0.02	0.01–0.05
6a	5×10^{22}	5–8 $\times 10^5$	2 $\times 10^5$	0.01–0.02	0.04–0.07
6b	5×10^{22}	5–8 $\times 10^5$	2 $\times 10^5$	0.01–0.02	0.04–0.07
6c	5×10^{22}	6–8 $\times 10^5$	2 $\times 10^5$	0.01–0.02	0.04–0.05
7	1×10^{23}	6–8 $\times 10^5$	2–3 $\times 10^5$	0.02–0.03	0.07–0.09
8	1×10^{22}	2–7 $\times 10^5$	0.7–2 $\times 10^5$	0.002–0.01	0.01–0.04
9	5×10^{22}	4–8 $\times 10^5$	2 $\times 10^5$	0.01–0.03	0.04–0.08
10a	1×10^{23}	5 $\times 10^5$	2 $\times 10^5$	0.05	0.12-
10b	1×10^{23}	5–8 $\times 10^5$	2–3 $\times 10^5$	0.02–0.05	0.07–0.12
10c	1×10^{23}	5–8 $\times 10^5$	2–3 $\times 10^5$	0.02–0.05	0.07–0.12
11	3×10^{23}	8–9 $\times 10^6$	–	0.07–0.08	–
12	5×10^{23}	1×10^6	–	0.11–0.12	–
13	1×10^{22}	3–5 $\times 10^5$	0.9–2 $\times 10^5$	0.004–0.01	0.01–0.02
14a	5×10^{22}	6–8 $\times 10^5$	2 $\times 10^5$	0.01–0.02	0.04–0.05
14b	5×10^{22}	4–8 $\times 10^5$	2 $\times 10^5$	0.01–0.03	0.04–0.08
15	1×10^{23}	5–8 $\times 10^5$	2–3 $\times 10^5$	0.02–0.05	0.07–0.12
16	3×10^{23}	8–9 $\times 10^6$	–	0.07–0.10	–
17	5×10^{22}	4–8 $\times 10^5$	2 $\times 10^5$	0.01–0.03	0.04–0.08
18	1×10^{23}	5–7 $\times 10^5$	2 $\times 10^5$	0.04–0.05	0.08–0.12
19	3×10^{23}	8×10^5	–	0.08–0.10	–

Table 5.11: Model fits to varying-σ log-normal scenarios for HCO+ data. Corresponding peak densities and cloud lengths for each fit are shown. Scenarios without fits are shown as '–'.

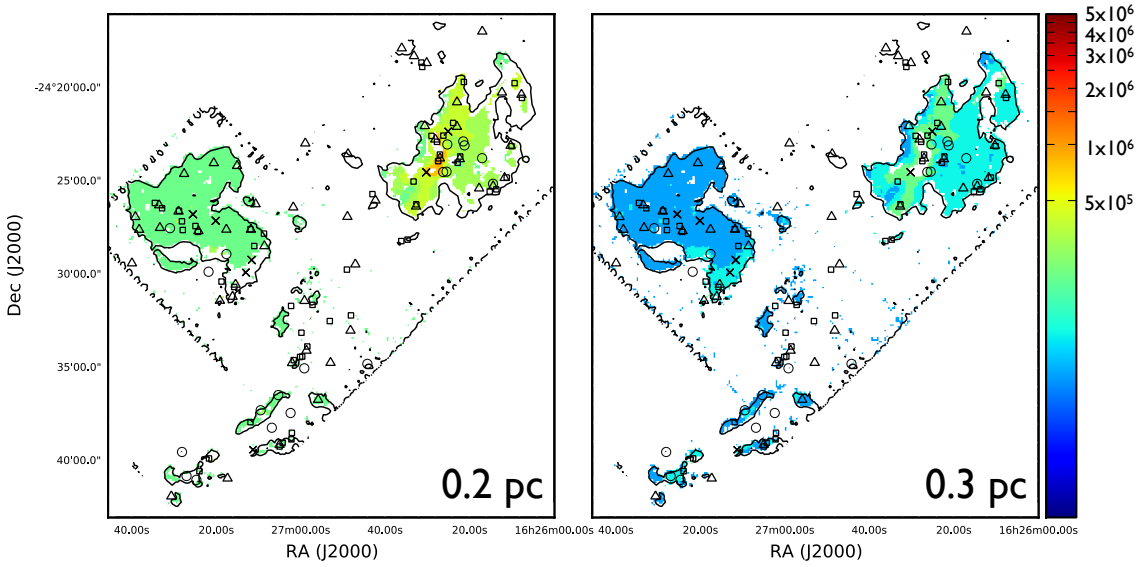

Figure 5.22: Densities (cm^{-3}) measured by the 0.2 and 0.3 pc log-normal models with constant-σ. Contours denote the 5σ HCO+ peak main-beam temperature detection.

5.6.3 Determining density using the constant-σ log-normal model

The range of densities and cloud lengths along the line-of-sight are shown in Table 5.10. Like the triangle models, the log-normal models with constant-σ predict peak densities that are proportional to the column density input parameter of the model (i.e. peak densities are higher for scenarios with higher column densities). The sources shown in the image are the same as the triangle model. Peak densities range from 2–10 $\times$ 10^5 (0.2 pc model) and 0.6–2.0 $\times$ 10^5 cm^{-3} (0.3 pc model). Peak densities are slightly less than those predicted from the triangle model and do not reach the critical density of HCO+. I note the 0.3 pc model is not able to model the higher column densities (i.e. $\sim$3–5 $\times$ 10^{23} cm^{-2}) due to the lower maximum column density of the model.

As in the triangle model, both the 0.2 and 0.3 pc constant-σ models show more uniform densities in the Oph B region. This density uniformity is the result of the column density bin used to fit this region, where more density variation would be detected had more model column density inputs been used. The 0.2 pc model

has been unable to fit the majority of the B1 region, where corresponding models predicted higher integrated intensities and peak main-beam temperatures that did not match the data (lowest model peak main-beam temperature was at 3.8 K while the typical main-beam temperatures found in the data for Oph B1 were ∼1–3 K). This model additionally does not fit the region near Class I source SSTc2d J162730.9-242733 that was found to have slightly higher densities than the rest of the Oph B region. Using the 0.3 pc model, Class I source SSTc2d J162730.9-242733 does have an associated higher density than the rest of the Oph B region (1×10^5 cm^{-3}) and IRS 37 has higher densities found in both models (3×10^5 and 1×10^5 cm^{-3} for the 0.2 and 0.3 pc models respectively) similar to the triangle models.

The Oph CEF region has a similar density range as Oph B. The 0.2 pc model has been unable to map a significant portion of the Oph F clump (corresponding to protostars IRS 43 and IRS 44) and patchy portions of the primary filament in the region. Both the 0.2 and 0.3 pc models show increased density corresponding to the Class I protostar EL 29 (3×10^5 and 1×10^5 cm^{-3}) and the 0.3 pc models show the same increased density corresponding to IRS 43 and IRS 44 in Oph F.

The Oph A region has not been thoroughly fit by either the 0.2 or 0.3 pc models. The 0.2 pc models have not been able to fit large portions of the outer edges of the clump and the 0.3 pc models have not been able to fit the inner portions of the region corresponding to the highest column densities in the cloud. Like the triangle model, the Class 0/I protostars are located in the centre of the clump but do not necessarily correspond to the highest densities. The starless and pre-stellar cores are spread throughout the clump with many of them lining a stripe across the clump corresponding to higher densities.

5.6.4 Determining density using the varying-σ log-normal model

Fits by the varying-σ log-normal models are not as straightforward as the triangle or the constant-σ log-normal models, as shown in Figure 5.21. Unlike the triangle models, regions with higher column density do not automatically correspond to high density due to the inclusion of the three-dimensional Mach number derived from the HCO+ FWHM velocities. The FWHM velocity (through the Mach number)

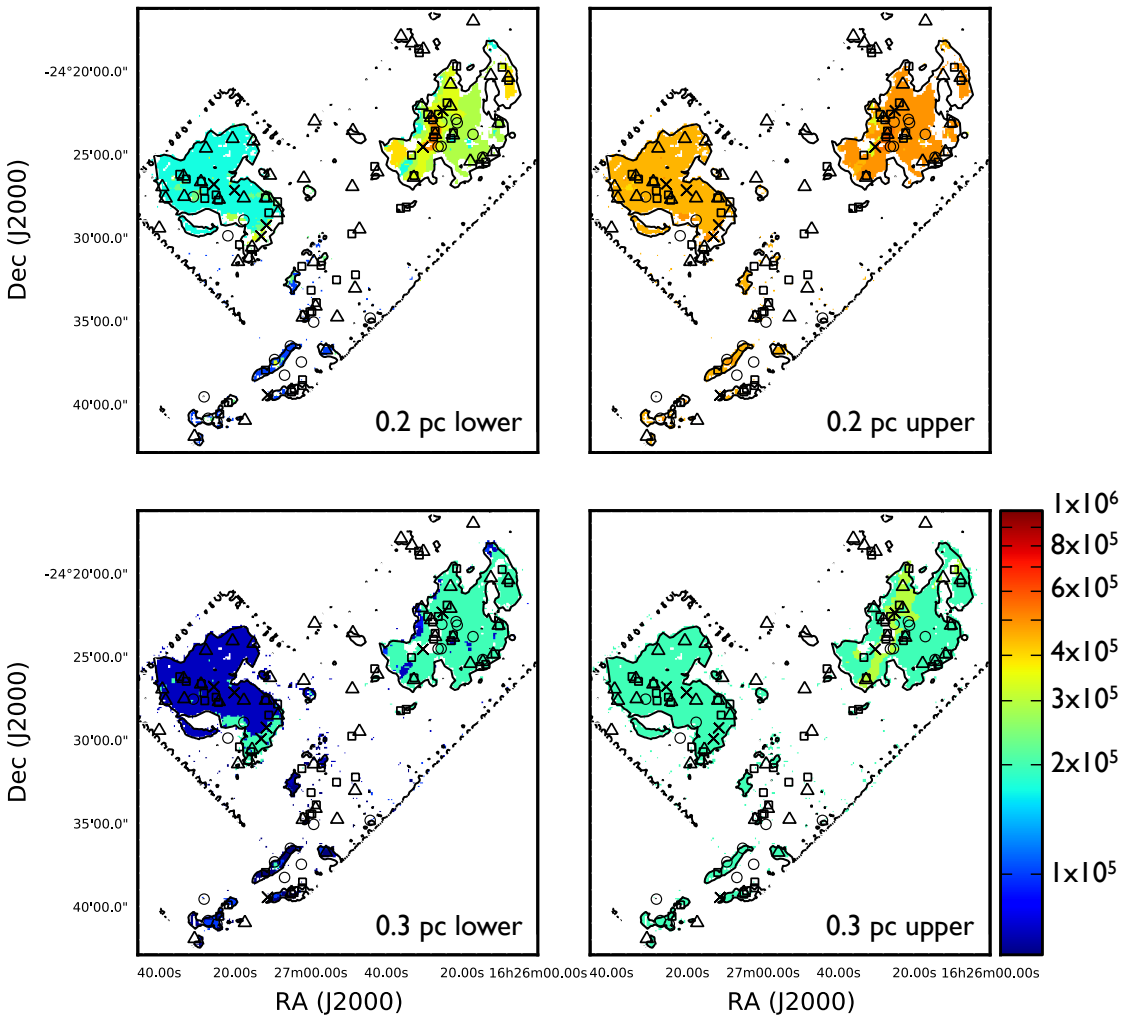

Figure 5.23: Densities (cm^{-3}) measured by the 0.2 and 0.3 pc log-normal models with varying-σ. Contours denote the 5σ HCO+ peak main-beam temperature detection.

determines the width of the log-normal density profile, as discussed in Section 5.5. When the FWHM velocity is fixed, densities predicted by the log-normal models vary with column density and line-of-sight lengths (higher column density and line-of-sight lengths relates to a relatively higher density). However, with a constant column density, the peak density may decrease or increase with increasing FWHM velocity. Lower column densities N_i (relative to the maximum column density N) have corresponding peak densities that decrease with increasing FWHM. Conversely, higher relative column densities have increasing peak densities with higher FWHM velocities. These features are the result of the log-normal density profile shape. With higher FWHM velocity, the density profile has a larger line-of-sight length corresponding to lower density material with the centre of the distribution peaking at a high density. Therefore, lower/moderate column densities with higher FWHM velocities will have lower peak densities and longer line-of-sight lengths (resembling a 'flat' isosceles triangle with a larger base than height). Higher column densities have peak densities continuing to increase with FWHM velocity because a large portion of the material is being pushed to lower densities. The peak densities must therefore be increased to result in the same column densities.

The results from the log-normal models can be found in Figure 5.23, which shows the densities (cm^{-3}) of the regions fit by the models. The log-normal models have not been able to cover the cloud as fully as the triangle models (i.e. on the edges of the Oph A and B regions), but the main portions of the cloud with significant HCO+ emission and regions near protostars and cores have been sufficiently modelled. Due to the more complex nature of the models, there are lower and upper density limits based on the highest and lowest FWHM velocities respectively in each scenario. I note that upper density limits are fairly constant. This is mainly due to low FWHM velocity limits for each scenario that are reasonably similar. Peak densities vary little with column density at low velocities.

Similar to the triangle models, peak densities predicted by the log-normal models are quite constant across the Oph B region, where the lower limits are 2.0×10^5 and $0.7{\times}10^5$ cm^{-3} and upper limits are 7.0 $\times 10^5$ and $1.0{\times}10^5$ cm^{-3}(0.2 and 0.3 pc models). Some variation is found in the Oph B1 region and near Class I sources SSTc2d J162730.9-242733 and IRS 37 where there are narrower or similar but higher density ranges. These slight regions with variation indicate the density (on average)

will be higher than the rest of the region. However, there will be a variety of densities instead of constant density blocks that do follow the FWHM velocity of the individual pixel.

Oph CEF has similar densities as seen in the Oph B region. In both the lower-limit regimes for the 0.2 and 0.3 pc models, the main filament in the region is largely 1.0–7.0 $\times 10^5$ cm^{-3} and 0.5–2.0 $\times 10^5$ cm^{-3} respectively. There is an increase in density near EL 29 at 5.0–8.0 $\times 10^5$ cm^{-3} for the 0.2 pc model while the upper- and lower-limits for the 0.3 pc model are constant at 2.0 $\times$ 10^5 cm^3. Additionally, there is an increase in density around IRS 43 and 44 of $\sim$3.0–8.0$\times 10^5$ cm^{-3} and 1.0–2.0$\times 10^5$ cm^3 for the 0.2 and 0.3 pc models.

Lastly, the Oph A region has a larger range of densities (lower limit) than the rest of the cloud with a fairly constant density range at the upper limit levels. The stripe of higher column densities in the centre of the clump corresponds to a maximum density 1.0 $\times 10^6$ cm^{-3} in the 0.2 pc model (constant lower- and upper-limits). At the 0.3 pc model lower limit, the stripe has the same density as the rest of Oph A; however, this region has a higher density upper limit (2.0–3.0$\times 10^5$ cm^{-3}).

5.6.5 Understanding the three-dimensional cloud: constant-σ model

Figure 5.24 shows the line-of-sight lengths (pc) estimated by the constant-σ models. Similar to the triangle models, the z-axis lengths increase with increasing column density. Line-of-sight lengths continue to remain fairly constant across the Oph B clump and increase towards the B1 region (primarily shown in the 0.3 pc model). For the majority of the region, lengths are 0.01 pc (0.2 pc model) and 0.04 pc (0.3 pc model). With the x- and y-axes lengths ranging from 0.22-0.28 pc at the widest sections of the clump, these models continue to suggest Oph B is quite 'flat' which is similar to the triangle models. The line-of-sight lengths are 4–5 % (0.3 pc model) and 14–18% (0.2 pc model) of the longest regions of the cloud. There are small portions in the B2 region and largely in the B1 region (primarily for the 0.3 pc model) where line-of-sight lengths increase to 0.05 pc and 0.11 pc for the 0.2 and 0.3 pc models respectively. Therefore, lengths increase to 18–23% and 39–50% of the largest cloud widths for the two models.

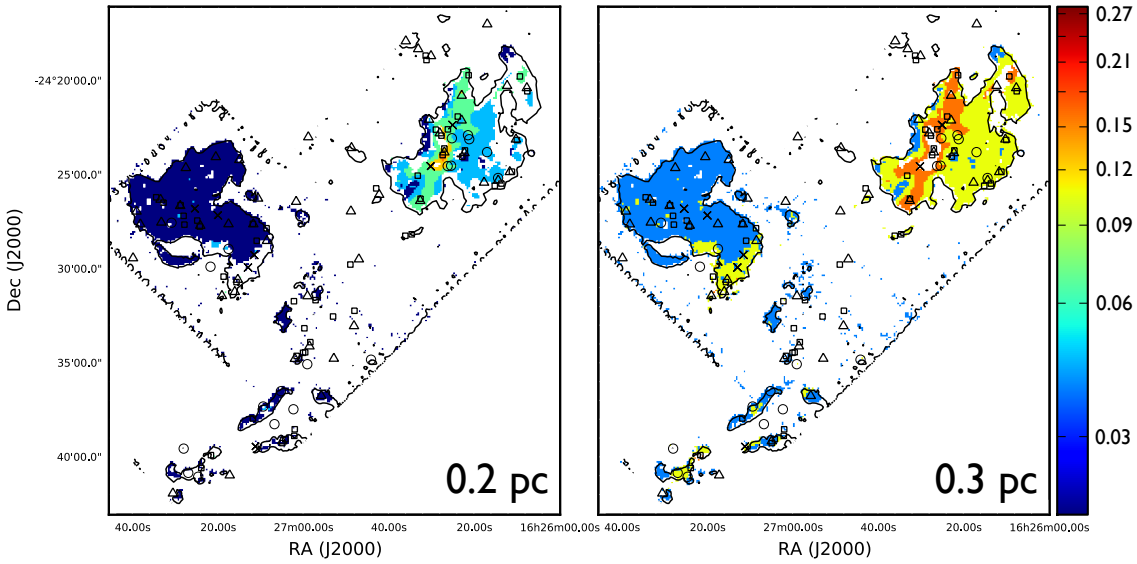

Figure 5.24: Line-of-sight lengths (pc) measured by the 0.2 and 0.3 pc log-normal model with constant-σ. Contours denote the 5σ HCO+ peak main-beam temperature detection.

The range of line-of-sight lengths found in Oph CEF are the same as Oph B. This region has a noticeable filamentary-like structure that is around 0.270 pc long (including the Oph F clump) and 0.030 pc wide. As discussed in Section 5.6.3, the 0.2 pc model does not trace portions of the Oph F region but does trace the main filament near EL 29. The line-of-sight lengths predicted by the models range from 0.01-0.05 pc (0.2 pc models) and 0.04-0.11 pc (0.3 pc models). Like the triangle models, the constant-σ models also indicate the three-dimensional structure of the region is fairly cylindrical or filamentary but increases around the location of the protostars (EL 29 for the 0.2 pc triangle model). The 0.3 pc model predicted the line-of-sight lengths can be 3–4 times the filament width at the location of the protostars.

Like the triangle model, Oph A has the largest line-of-sight length range. The clump is $\sim$ 0.34 pc long and $\sim$0.19 pc width at the largest x and y-axis lengths. Line-of-sight lengths increase towards the centre of the core, near the stripe of higher column densities. The models predict line-of-sight lengths ranging from 0.01–0.16 pc (0.2 pc model) and 0.11-0.16 pc (0.3 pc model). As in Oph B, the 0.2 pc model does not adequately map the edges of the Oph A clump and the 0.3 pc model does not

map the inner portions of the clump corresponding to the highest column densities. In the regions fit by the models, the centre of the cloud seems to bulge along the central stripe and decreases towards the outer edges of the cloud. The inner portions of the cloud covered by the 0.2 pc models suggests the z-axis lengths are $\sim$ 84% of the width of the cloud, suggesting the clump has a similar 'egg-like' three dimension shape of the cloud like the triangle models. The 0.2 pc triangle model finds a similar 0.16 pc z-axis length along the primary stripe in the cloud, indicating the region is somewhat more rounded than the 0.2 pc model.

5.6.6 Understanding the three-dimensional cloud: varying-σ model

The lower and upper-limits on the line-of-sight lengths predicted by the log-normal models are shown in Figure 5.25. Like the triangle models, Oph B and Oph CEF regions have similar line-of-sight lengths. Lengths along the x and y-axis predicted for the majority of Oph B range from 0.002–0.010 pc (up to 4% of the widest part of the cloud) and 0.008–0.040 pc (up to 14% of the widest part of the cloud) for the 0.2 and 0.3 pc models. Compared to the triangle models, the log-normal models predict a similar three-dimensional shape but an even flatter distribution along the z-axis. Even though the 0.2 pc model does not cover the total area of the Oph B1 region, there are still some regions with noticeable longer line-of-sight lengths than the majority of Oph B. These regions range from 0.011–0.027 pc (0.2 pc model) and 0.035–0.075 pc (0.3 pc model), or up to 10% and 27% of the largest Oph B width. This indicates that the lower portion of the Oph B clump including Oph B1 bulges relative to the other sections of the region.

Oph CEF has the same line-of-sight length ranges as Oph B. Increased lengths directly correspond to Class I protostars EL 29 and LFAM 26 along the filament in the region and IRS 43 and 44 in the Oph F region. When the lower and upper line-of-sight limits are compared to the width of the filament, the log-normal models show increased lengths towards the centre of the filaments corresponding up to 67% for the 0.2 pc model and up to 4 times the filament width for the 0.3 pc model. This indicates the filament is cylindrical in shape, narrower on the edges and growing near the location of the protostars.

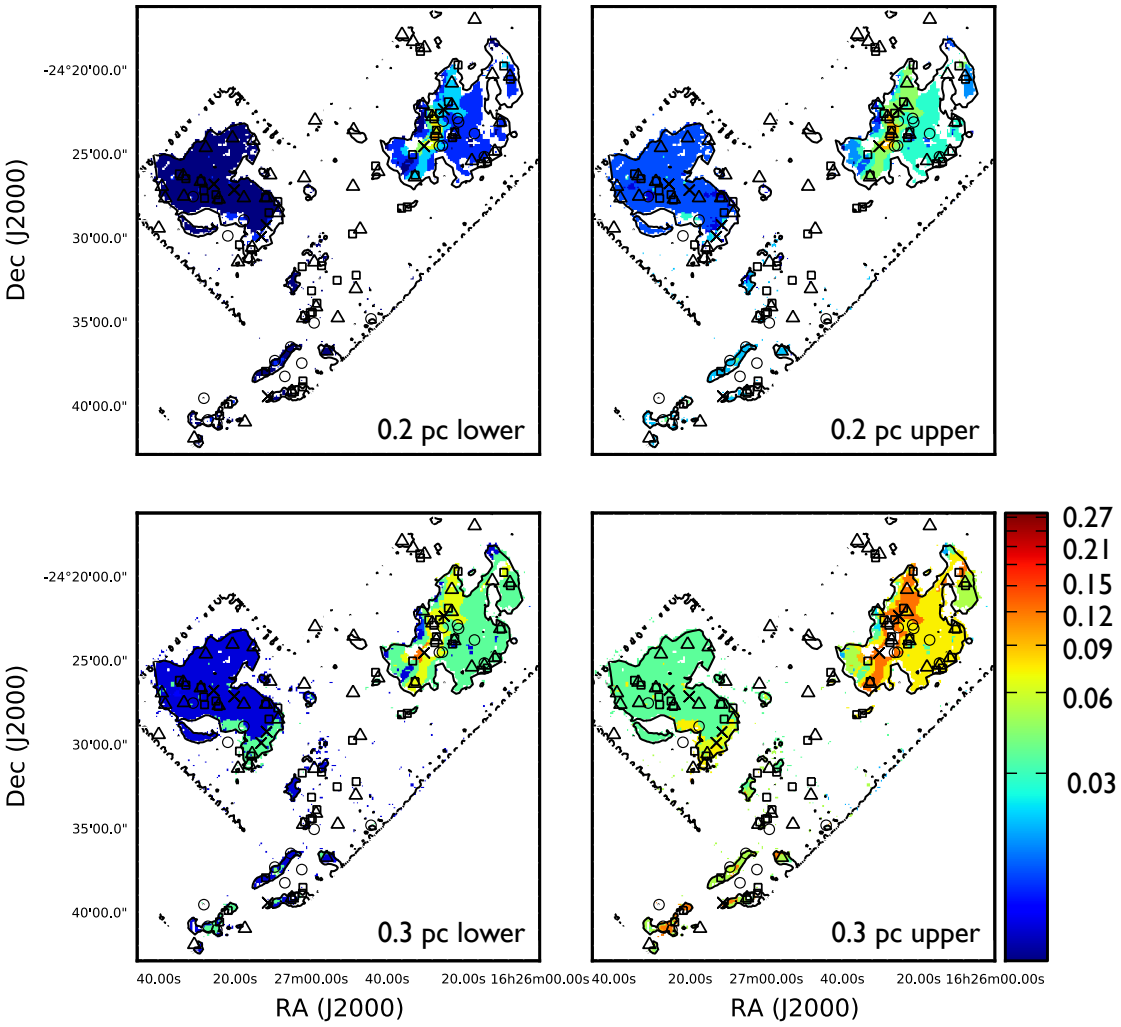

Figure 5.25: Line-of-sight lengths (pc) measured by the 0.2 and 0.3 pc log-normal models (varying-σ). Contours denote the 5σ HCO+ peak main-beam temperature detection.

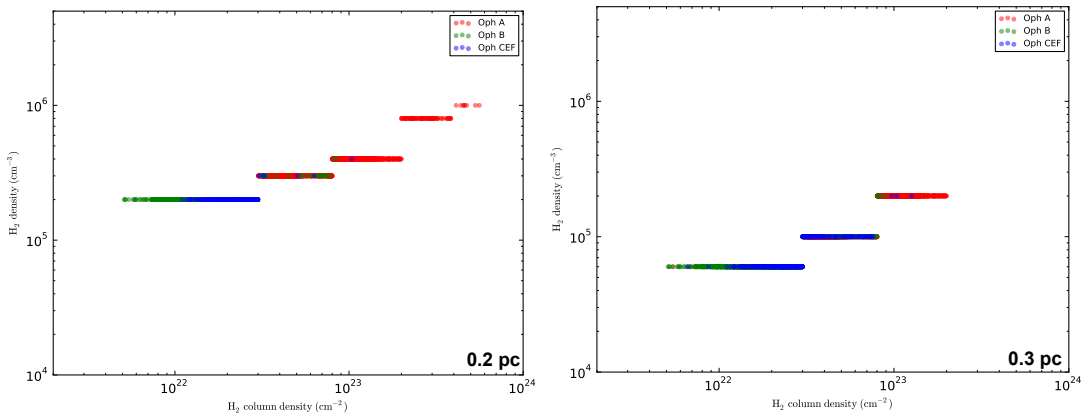

Figure 5.26: Pixel comparison between column density and density of the entire cloud using the log-normal constant-width models.

Lastly, the Oph A region has a large range of line-of-sight lengths, where the lowest lengths are on the edge of the cloud and increase towards the centre of the clump along the central stripe of the region. Lower limits for the region range from 0.011–0.114 (0.2 pc model) and 0.036–0.123 pc (0.3 pc model). Upper limits on the line-of-sight lengths range from 0.028–0.123 and 0.074–0.123 pc respectively. Like the triangle models, the increase of cloud lengths indicates the cloud is more of an 'egg-like' shape with a bulge along the stripe, peaking at the centre of the core. However, this three-dimensional shape is to a much less extent due to the lower length estimates for the region. Additionally, the 0.3 pc model has been unable to map the centre of the region due to constraints on the maximum column density.

5.6.7 Links between column density and density

Using the log-normal profiles to estimate the density corresponding the the HCO+ emission, the link between column density and density can be further explored similar to the triangle density profiles. Figures 5.26 and 5.27 shows the pixel comparison between column density and density across the entire cloud for the log-normal models. Log-normal models with constant-σ show a similar link between high column density and density as the triangle models. This link is also found in the varying-σ models in the lower-limit. Upper-limit cases for the varying-σ models show a more evenly spread density distribution across the entire range of column densities.

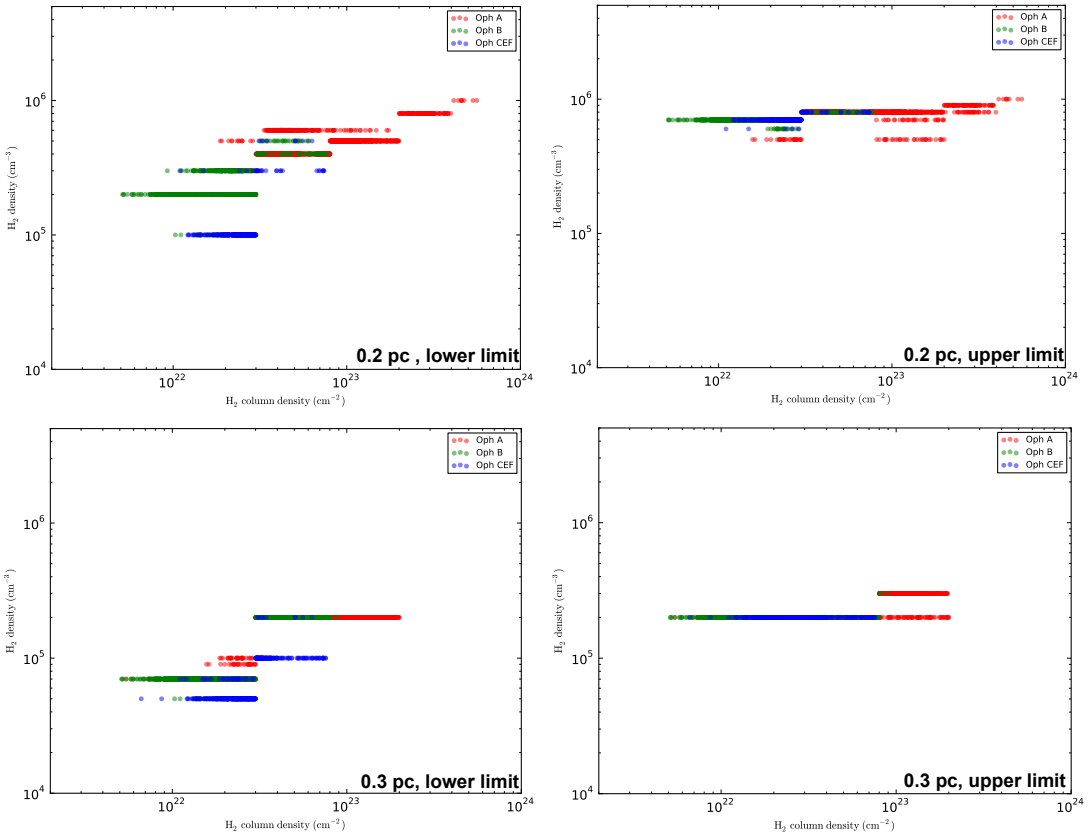

Figure 5.27: Pixel comparison between column density and density of the entire cloud using the log-normal models.

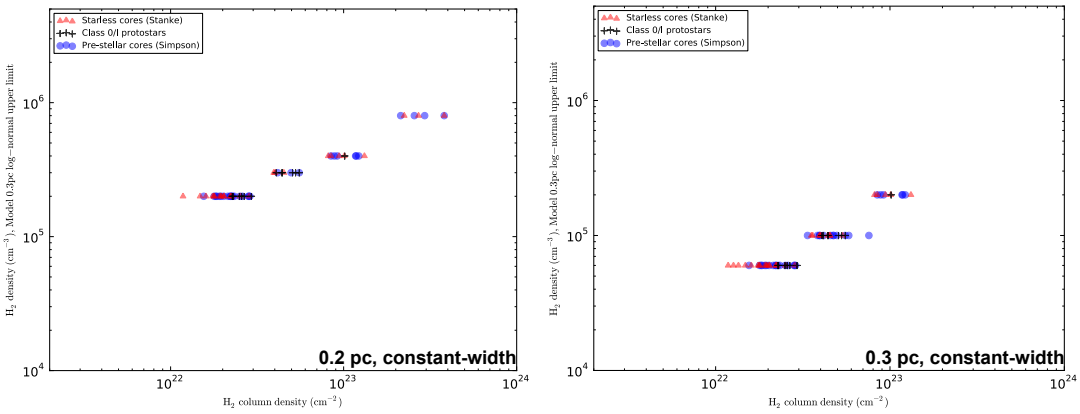

Figure 5.28: Source comparison between column density and density in the entire cloud using the log-normal constant-width models.

Figures 5.28 and 5.29 show the comparison between column density and density for the pre-stellar, starless and protostellar sources in Ophiuchus. The majority of the cores are evenly distributed over the column densities and densities for the constant-σ and varying-σ lower-limit models. Class 0/I protostars are found mainly in the 'middle' column density limits ($\sim$0.2–1.0$\times10^{23}$ cm^{-2}) where pre-stellar and starless cores are found in column densities up to 3 $\times$ 10^{23} cm^{-2}. Therefore, these protostars are not found at the corresponding highest densities in the cloud.

Figures 5.30 and 5.31 show histograms of the percentage of pixels and sources at various densities across the cloud for the various models. KS tests, shown in Table 5.12, comparing the distribution of pixels and sources in the cloud indicate mixed results for the constant- and varying-σ models. The constant-σ models indicate there is no difference between the distribution of pixels across the cloud and the sources (i.e. starless cores, prestellar cores and embedded protostars). This is a similar result for the triangle models. The lower-limit varying-σ models also suggest there is no difference between the distribution of pixels across the cloud and the cores. The upper-limit varying-σ models suggest the total cloud distribution and the Class 0/I embedded protostars are a different distribution for the 0.2 pc model (p-value: 0.077) while the comparison between the total cloud and the other sources suggest a similar distribution. The KS test result in the upper-limit suggesting the Class 0/I protostars have a different distribution than the total cloud is most likely due to a higher percentage of sources at lower column densities and densities (i.e.

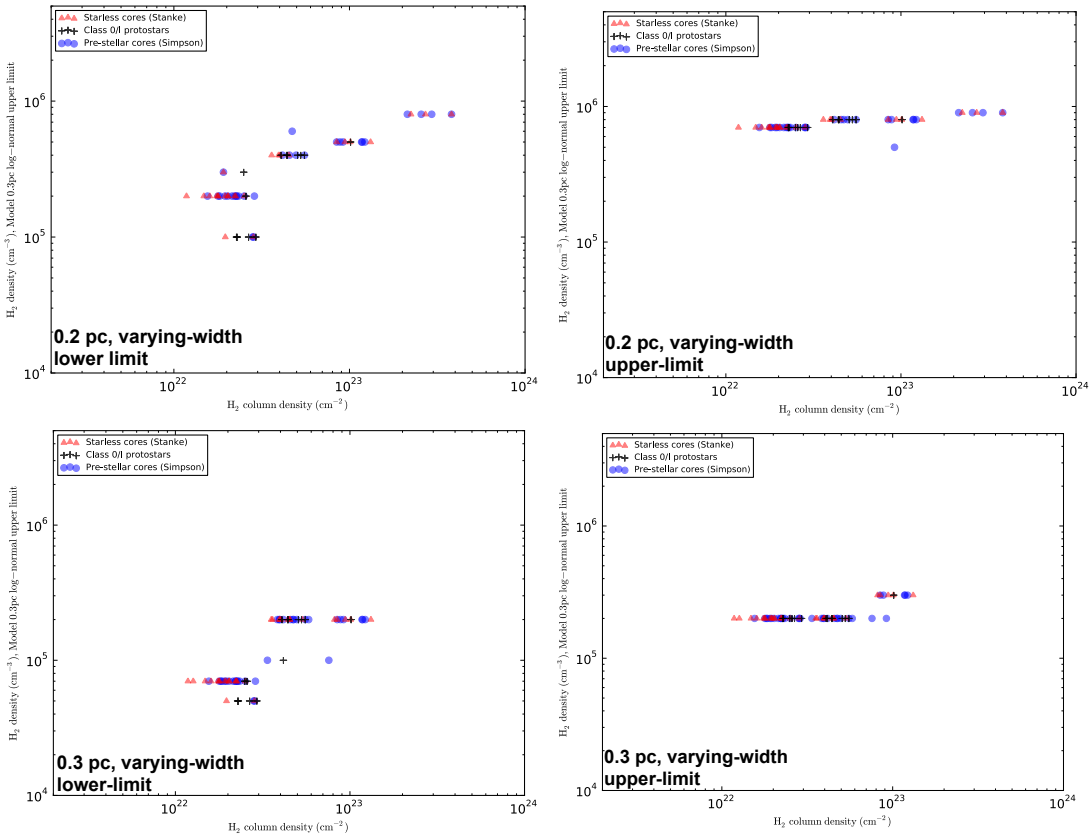

Figure 5.29: Source comparison between column density and density in the entire cloud using the log-normal models.

Log-normal model with constant-σ						
	0.2 pc triangle model			0.3 pc triangle model		
Source	Tot. Cloud	Pre-stellar	Starless	Tot. Cloud	Pre-stellar	Starless
Tot. Cloud	–	0.999	0.999	–	0.976	0.976
Pre-stellar	–	–	0.999	–	–	0.976
Class 0/I	0.697	0.697	0.999	0.976	0.976	0.976
Log-normal model with varying-σ, lower-limit						
Tot. Cloud	–	0.883	0.883	–	0.999	0.697
Pre-stellar	–	–	0.999	–	–	0.999
Class 0/I	0.883	0.883	0.883	0.697	0.697	0.697
Log-normal model with varying-σ, upper-limit						
Tot. Cloud	–	0.810	0.318	–	0.844	0.844
Pre-stellar	–	–	0.999	–	–	0.844
Class 0/I	0.077	0.810	0.999	0.844	0.844	0.844

Table 5.12: KS test results (p-values) for the distribution of densities across the cloud and for the pre-stellar, starless and protostellar cores.

$\leq 10^{23}$ cm^{-2}) than the total cloud or the other sources.

Like the triangle models, protostars are not seen at the highest densities because of the proportionality between column density and density predicted from the models. Other effects resulting in potentially higher C^{18}O emission and thus higher column densities are discussed in Section 5.7, comparing both the triangle and log-normal models. Additionally, gas temperatures are discussed.

5.7 Discussion

The radiative transfer models detailed in this chapter have been relatively successful in modelling the HCO+ emission and resulting in the underlying density traced by the molecule. In this section, I discuss the model results in further detail and the benefits and limitations of the modelling techniques. Additionally, potential issues are detailed including ^{13}CO kinetic temperatures, varying abundances of HCO+ and C^{18}O and beam dilution. Lastly, I discuss methods for improving the models and the next logical step in model development.

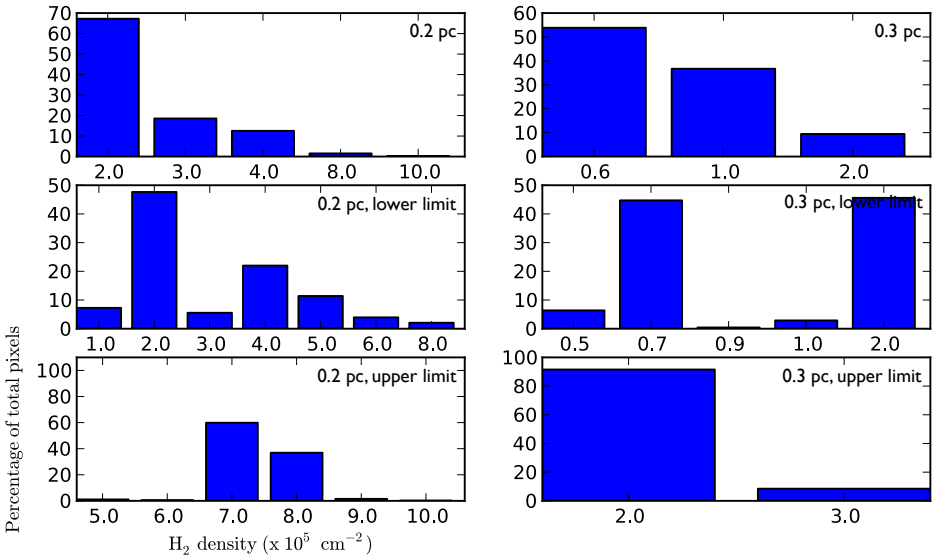

Figure 5.30: Histogram of the percentage of total pixels at different densities across the entire cloud using log-normal models.

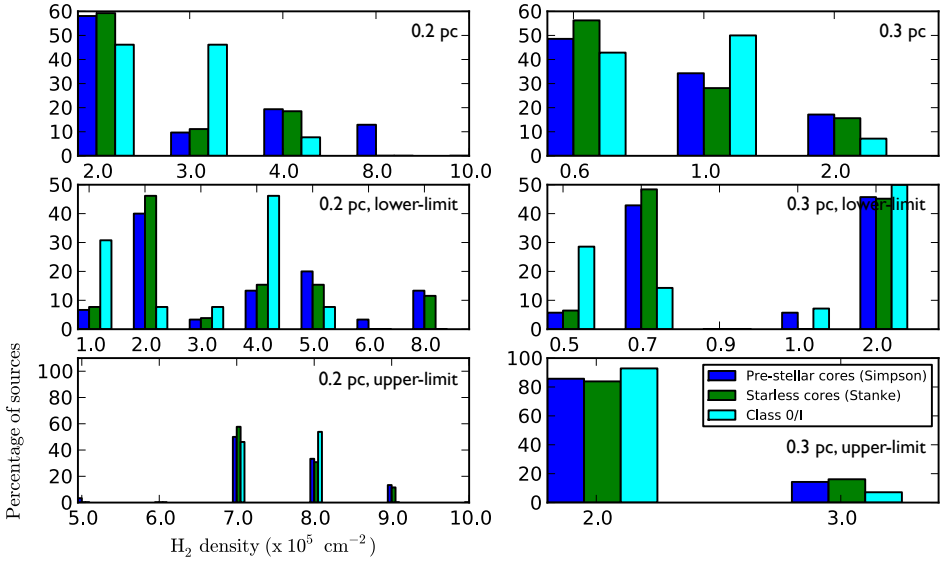

Figure 5.31: Histogram of the percentage of total sources at different densities across the entire cloud using log-normal models.

5.7.1 Model results

In Section 5.4.2, the limitations of a using a constant density profile for radiative transfer models was discussed (for example, large line-of-sight lengths). I do not include the RADEX models in the discussion of the TORUS radiative transfer models because I have ruled out the efficiency of using constant density models for modelling accurate cloud densities.

Both the triangle and log-normal TORUS models predict reasonable densities and line-of-sight lengths constrained by numerous observational cloud properties (cloud mass, observable cloud lengths in RA and Dec, column density, kinetic temperature and FWHM velocity). The 0.2 pc models have been able to model the full range of column densities observed in the cloud calculated from $C^{18}O$ integrated intensities while the 0.3 pc models have not been able to model the highest densities (i.e. $> 2 \times 10^{23}$ cm^{-2}). The two lengths provide two possible maximum line-of-sight lengths based on these observations. Additionally, is possible that some regions of the cloud may be better mapped with a smaller or larger cloud length.

Comparing the spatial coverage of the three TORUS models (triangle, constant-σ log-normal and varying-σ log-normal), the triangle model and the varying-σ models were successful in fitting the majority of the cloud. The 0.2 pc constant-σ log-normal model had some problems modelling lower HCO+ integrated intensities found in the outer portions of the Oph A and B2 clumps and the Class I protostars found in Oph F. The 0.3 pc models were more successful in mapping the outer portions of the clumps but were still constrained by column densities higher than the maximum model column density at the centre of the Oph A core.

It is difficult to distinguish between the model fits and determine the density profile best fitting the HCO+ data. The triangle and constant-σ log-normal profiles are most constrained by column density input due to the proportionality between column density and density in Sections 5.5.1 and 5.6.1. In the physical cloud it is possible higher column density does not yield higher density, e.g. higher column density relative to the total cloud may be detected if a filament is observed down its length but a proportionally high density may not be present. The varying-σ log-normal model begins address this issue, taking a range of Mach numbers found throughout the cloud into account. Using the Mach number or FWHM velocity of

the material, a relative higher density doesn't always result from a higher column density. The drawback to this model is the limitation of fitting scenarios with a range of FWHM velocities. This leads to the lower- and upper-limits in density and line-of-sight lengths described in Section 5.6.2. It would clearly be more useful to fit the map pixel-by-pixel to determine the precise peak density and line-of-sight length associated with the HCO+ emission.

The comparison between the cloud densities associated with different evolutionary stages of the sources remains inconclusive. Apart from the single KS test indicating the Class 0/I embedded protostars had a different density distribution than the total cloud using the 0.2 pc varying-σ log-normal model, the remaining models indicate the density distribution across the total cloud was no different to the distribution for protostellar, pre-stellar and starless cores. Additionally, some pre-stellar and starless cores are found at higher densities than the protostellar cores. Though the protostars are not seen at the highest column densities (2–4$\times10^{23}$ cm^{-2}) in the cloud, they are still found at high column densities in the region ($\sim$0.2–1.0$\times10^{23}$ cm^{-2}). The column densities corresponding to both protostars and the starless/prestellar cores in Ophiuchus are greater than previously derived thresholds for star formation. Onishi et al. (1998) measured C^{18}O column density in Taurus, finding 'young' protostars and starless H^{13}CO^{+} cores to have an average column density $\geq 8 \times 10^{21}$ cm^{-2} (i.e. $A_{\rm v} = 9$). This is a factor of 1.25 lower than the minimum column density for the list of cores further analysed using HCO+. Additionally, Johnstone et al. (2004) found no cores using SCUBA 850 μm continuum data below $A_{\rm v} < 7$ (i.e. column density $\sim$6$\times10^{21}$ cm^{-2}).

Improvements to these density profiles and other potential molecules tracing high density in star forming regions are further discussed below.

5.7.2 Gas temperature

As discussed in Section 5.5.4, the models were fit to the data primarily using the model column density matched to the average of each defined scenario column density in the cloud. This method ignores the kinetic temperature input in the model calculated from ^{13}CO (assuming optically thick emission and LTE; Chapter 4). Therefore, the models fitting the data could have significantly lower or higher ki-

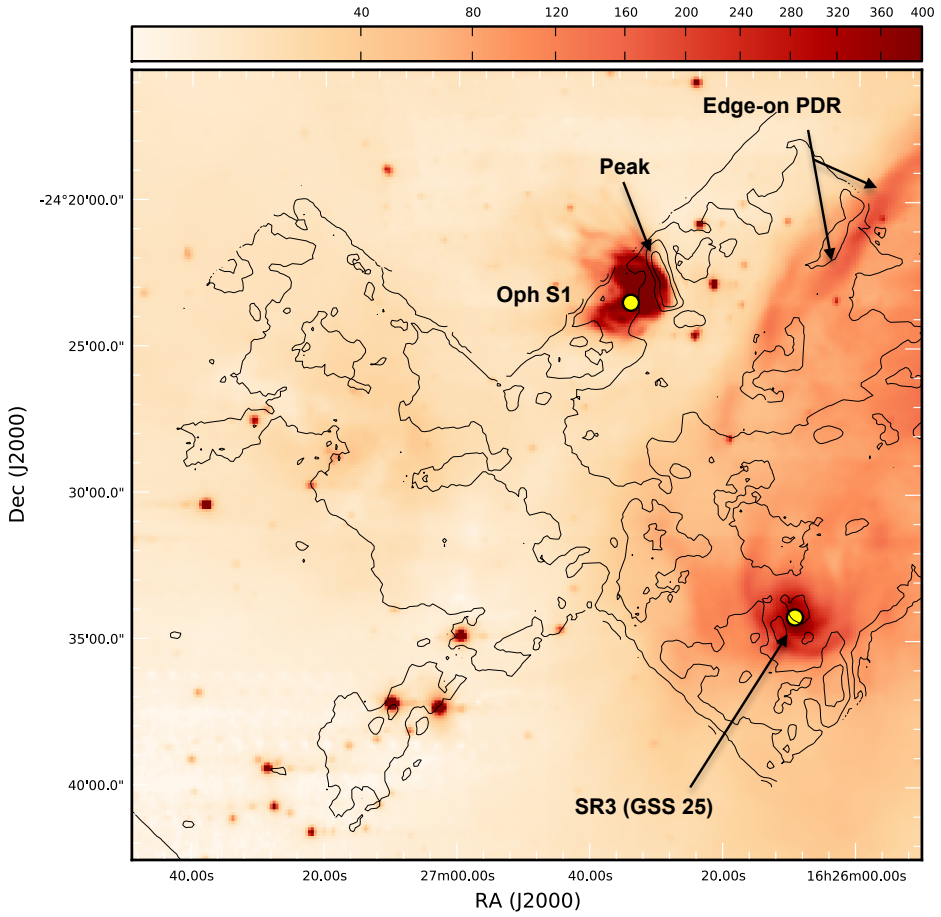

Figure 5.32: ISOCAM 12μm data (MJy sterad^{-1}) with contours of ^{13}CO excitation temperatures, corresponding to 15, 20, 30 40 and 50 K.

netic temperatures than temperatures calculated from ^{13}CO. To validate the models, it is necessary to further investigate the differences between the model and ^{13}CO kinetic temperatures. Additionally, HCO+ excitation temperatures are calculated and compared to excitation temperatures from the output models.

Kinetic temperatures for ^{13}CO are calculated in Chapter 4, where I assume LTE ($T_{\rm kin} = T_{\rm ex}$) and optically thick emission. Figure 5.32 shows the ISOCAM 12 μm dust continuum data in MJy sterad^{-1}, which traces hot dust in the Ophiuchus cloud. Contours correspond to ^{13}CO kinetic temperatures at 12, 20, 30, 40 and 50 K. The Oph A region is noticeably warmer than the rest of the cloud ($>$ 30 K) and temperatures increase to $\sim$40–50 K near B-type star Oph S1 (labelled 'peak').

Scenario	^{13}**CO** $T_{\rm kin}$	$T_{\rm kin}$ **Model Input**					
		Triangle		Constant-σ		Varying-σ	
		0.2 pc	0.3 pc	0.2 pc	0.3 pc	0.2 pc	0.3 pc
1	10–13.5	15	20, 30	20^{+}	40, 50	15	20, 30
2	10–13.5	12	12	–	12, 15	12	12, 15
3a	13.5–17	40	30, 50	40	50^{+}	20	30, 40
3b	13.5–17	40	30, 50	30, 40	50^{+}	20	30, 40
4a	13.5–17	15	15, 20	12, 15	20	15	15, 20
4b	13.5–17	15	15, 20	12, 15	20	15	15, 20
5	13.5–17	40	30, 50	40	50^{+}	20	30, 40
6a	17–25	15, 20	15, 20	15	15^{+}	15	20
6b	17–25	15, 20	15, 20	15	20	15	15, 20
6c	17–25	15, 20	15, 20	15	20	15	20
7	17–25	15	15	15, 20	15, 20	15	15
8	25–35	20, 30	30	30	40, 50	20	30
9	25–35	20, 30	30, 40	20, 30	30, 40	30	30, 40
10a	25–35	20	20	20^{+}	30	20^{+}	20^{+}
10b	25–35	20, 30	20	30	30, 40	20	30
10c	25–35	20, 30	20	30	30, 40	20	30
11	25–35	20, 30	–	20, 30	–	20	–
12	25–35	20	–	20	–	20	–
13	35–45	15, 20	20	20	40	15	20, 30
14a	35–45	30^{+}	30^{+}	20^{+}	50^{+}	30^{+}	40^{+}
14b	35–45	30	30, 40	20, 30	40, 50	30	30, 40
15	35–45	20	20, 30	20, 30	30, 40	20, 30	30
16	35–45	20, 30	–	20, 30	–	20	–
17	45–60	15	12, 15	12	20	15	15, 20
18	45–60	15	15, 20	15, 20	20	15	20
19	45–60	20, 30	–	20	–	20	–

Table 5.13: List of ^{13}CO kinetic (excitation) temperatures. Only kinetic temperatures corresponding to models that were able to fit the peak main-beam temperature and integrated intensity from each scenario are listed. Temperatures marked with the symbol '+' denote the closest fitting model to the scenario but was unable to fully fit the scenario peak main-beam temperature.

Similar heating is seen near the B-type star SR3 (GSS 25). It is possible the B-type stars are biasing the ^{13}CO kinetic temperatures in this region. If ^{13}CO traces a hot, optically thick outer layer of the cloud heated by these young stars, the corresponding kinetic temperatures may not accurately correspond to material traced by HCO+.

This issue with kinetic temperature can be further investigated by comparing ^{13}CO kinetic temperatures and the kinetic temperatures from the model fits. As shown in Table 5.13, kinetic temperatures for the Ophiuchus cloud range from 13.5 to 60 K (the warmest regions are found in Oph A). There is a noticeable issue regarding model kinetic temperature inputs not fitting the scenario ^{13}CO kinetic temperature range. Scenarios 1, 3 (a,b) and 5 consistently have model kinetic temperatures that are higher than ^{13}CO kinetic temperatures. These scenarios correspond to low column density regions (N = 0.5–3 $\times$ 10^{22} cm^{-2}) primarily in Oph B and the EF filament. The need for higher model kinetic temperatures to fit the HCO+ data could suggest the column densities are too low to produce the HCO+ emission detection in these lower column density regions. Depletion, i.e. the freezing of a molecule onto dust grains, could be a possible cause of low column densities predicted by the C^{18}O molecule. This issue is further discussed in Section 5.7.3. Conversely, scenarios 10a, 11, 12, 13, 14a, 15, and 16 have some model kinetic temperatures that are lower than the ^{13}CO kinetic temperature and scenarios 17, 18 and 19 consistently have all model kinetic temperatures lower than the observed temperature. The scenarios involved have ^{13}CO kinetic temperatures at or above 25–35 K and reach 45–60 K. As stated above, the high ^{13}CO kinetic temperatures could potentially result from ^{13}CO emission tracing different features in the cloud (e.g. the front of the cloud or regions near the hot dust) instead of the regions directly corresponding to star formation. In this section, I focus on understanding the models with consistently low model kinetic temperature inputs.

To further investigate the difference between the model and ^{13}CO kinetic temperatures I calculate excitation temperatures from the HCO+ data. The model fits can be further investigated by comparing the HCO+ excitation temperatures to the model output excitation temperatures. I calculate HCO+ excitation temperatures

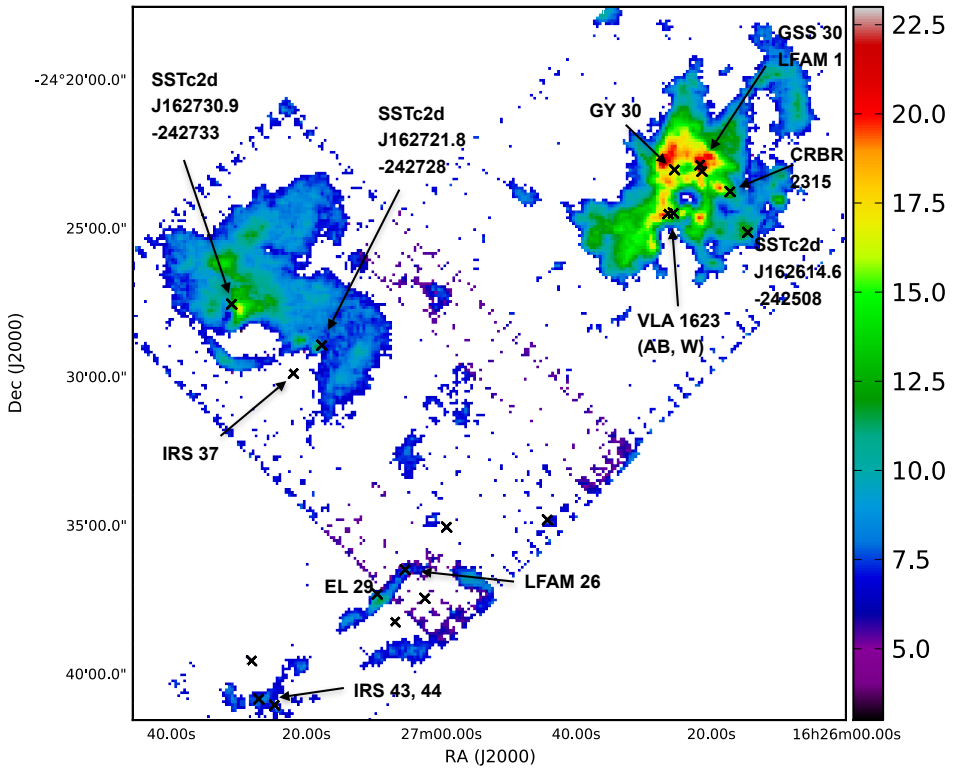

Figure 5.33: HCO+ excitation temperatures (K). Class 0/I protostars are denoted as black '×'.

using a similar method for ^{12}CO and ^{13}CO in Chapter 4,

$$T_{\rm ex}({\rm HCO+}) = \frac{17.1\ {\rm K}}{\ln \frac{17.1\ {\rm K}}{T_{\rm peak}+0.0324\ {\rm K}} + 1} \tag{5.17}$$

where $T_{\rm peak}$ is the peak HCO+ main-beam temperature and 17.1 K is $T_{\rm ul} = h\nu/k$. This equation assumes the gas is optically thick and in LTE. Using the models produced by TORUS, the kinetic temperature and the output excitation temperature can be compared for each scenario to ensure the modelled regions are in LTE (i.e. $T_{\rm kin} = T_{\rm ex}$). While it is likely HCO+ is optically thick, it is possible the excitation temperatures underestimate the gas temperature if the molecule is subthermally excited (i.e. $T_{\rm ex} < T_{\rm kin}$).

The HCO+ excitation temperature map is shown in Figure 5.33. The Oph A region has the largest range of HCO+ excitation temperatures, corresponding to ∼7–

22 K. HCO+ excitation temperatures predominantly trace the regions directly corresponding to Class 0/I protostars (VLA 1623 AB, VLA 1623 W, SSTc2d J162626.0-242340, GY 30, LFAM 1, GSS 30, CRBR 2315 and SSTc2d J162614.6-242508), where there are distinctly higher temperatures (∼15–22 K) located in a 'C-shape' in the centre of the region (shown in Figure 5.33). The main star formation is surrounded by hot material from Oph S1, SR3, and B2V star HD 147889 which drives an 'edge-on' PDR seen in the 12μm dust continuum as a long, filamentary structure. Similarly in Figure 5.34, I point out two distinct peaks in HCO+ excitation temperatures that also correspond to peaks in dust continuum emission. Peak 1 corresponds to VLA 1623 AB and peak 2 corresponds to GSS 30 and LFAM 1.

Other regions in Ophiuchus have a fairly constant HCO+ excitation temperatures of ∼8 K. Higher temperatures are found in the main Oph B clump (∼12–13 K) near Class I protostar IRS 37 and increase to 17 K near the Class I SSTc2d J162730.9-242733 and flat spectrum sources IRS 45 and 47 (not shown in Figure 5.33) driving the main Oph B outflow. Peak 3 in Figure 5.34 shows a correlation between a peak in HCO+ excitation temperature and dust continuum emission corresponding to this region, most likely IRS 47 instead of SSTc2d J162730.9-242733. Oph B1 has fairly low excitation temperatures in comparison (≤10 K), which could potentially correspond to several prestellar and starless cores in the region. Similarly, Oph CEF shows that protostars EL 29, LFAM 26, IRS 44 and 43 have a temperature range of ∼8–12 K, the brightest EL 29 which is shown as peak 4 in Figure 5.34.

Table 5.14 shows the range of HCO+ excitation temperatures for each of the scenarios and the corresponding model excitation temperatures. The model excitation temperature ranges are based on all of the kinetic temperature inputs from Table 5.13 and can vary with the linewidths input into `TORUS`. For a number of the models, $T_{\rm kin} = T_{\rm ex}$ and LTE is a fair assumption. However at lower column densities and depending on the models used, LTE does not necessarily hold (i.e. $T_{\rm ex} < T_{\rm kin}$).

Matching the HCO+ excitation temperatures to the model excitation temperatures yields an interesting insight into the chemistry of HCO+. In cases of high kinetic temperature (as predicted by ^{13}CO) some of the models with lower model kinetic temperatures have excitation temperatures that agree with or are closer to HCO+ excitation temperatures. These are most noticeable in scenarios 17, 18 and 19 where model input kinetic temperatures did not correspond to the ^{13}CO temper-

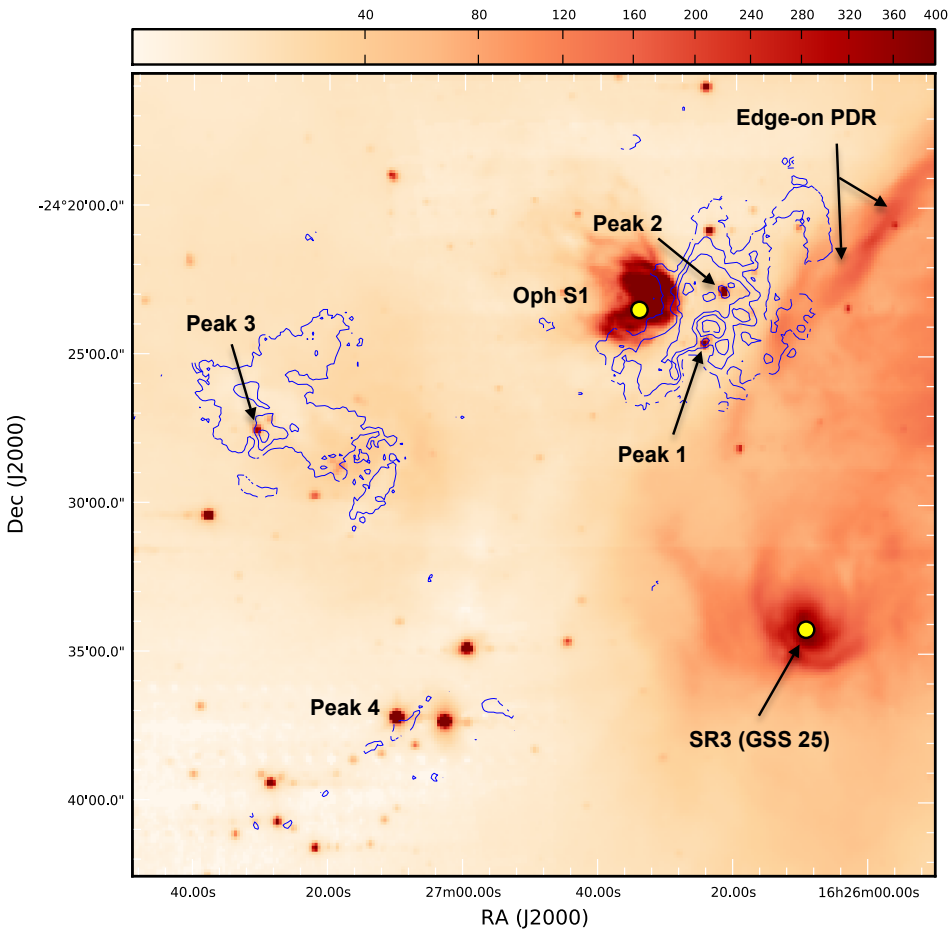

Figure 5.34: ISOCAM 12μm data (MJy sterad^{-1}) with contours of HCO+ excitation temperatures, corresponding to 8, 12, 15, 20 K.

ature range. The remaining scenarios have model excitation temperatures near or overlapping the HCO+ excitation temperatures.

Comparing HCO+ and ^{13}CO kinetic temperatures from Figures 5.32 and 5.34, noticeable discrepancies emerge primarily in the Oph A region. ^{13}CO predicts high kinetic temperatures in the clump $T_{\rm kin} \geq 30$ K. HCO+ kinetic temperatures range only from ∼7–22 K. Even at the peak excitation temperature 22 K, assuming a 20% peak main-beam temperature uncertainty only yields an upper limit of ∼28 K. With the indication that ^{13}CO is tracing regions corresponding to hot dust from Oph S1 instead of the local star formation, higher kinetic temperatures will bias the kinetic temperature parameter input into the TORUS models. This has the effect of increasing output main-beam temperature peaks and integrated intensities for the HCO+ molecule. Additionally, column densities calculated from C^{18}O observations will be altered, though this effect is small. Column densities are dependent on the exponential term $T_{\rm ex}/\exp\left(-31.6\ [\mathrm{K}]/T_{\rm ex}\right)$, which causes column densities to decrease when 0 K $< T_{\rm ex} \leq 31.6$ K and increase when $T_{\rm ex} \geq 31.6$ K. For example, in a region with 50 K excitation temperature, column density would only decrease by a factor of 1.09 if the excitation temperature changed to 35 K.

Accounting for higher kinetic temperatures traced by the ^{13}CO molecules still does not fully address modelling issues with continual high model excitation temperatures compared to the HCO+ temperatures calculated above using the observational data. Additionally, it does not address the problem found in several scenarios regarding high model kinetic temperatures relative to ^{13}CO kinetic temperature. Varying abundances and beam dilution could be potential issues unaccounted for in the modelling of emission.

5.7.3 Abundance

Molecular abundance fluctuations across a cloud can cause corresponding variations in the amount of detected molecular line radiation. When modelling molecular emission using radiative transfer models, it is important to consider the abundance of the molecule when fitting the data.

The simple models developed in this study using TORUS have been chosen to keep a constant abundance. HCO+ is expected to vary through means of CO depletion,

Scenario	**HCO+ T_{ex}** (K)	**T_{ex} Model Output (K)**					
		Triangle		Constant-σ		Varying-σ	
		0.2 pc	0.3 pc	0.2 pc	0.3 pc	0.2 pc	0.3 pc
1	7–11	12	12–16	6–8	11–18, 13–21	9–14	9–16, 6–24
2	5–8.0	12	12	–	8–12, 12–15	11–12	8–12, 14–15
3a	3–17	26–40	15–28, 14–43	17–33	11–30	11–20	7–28, 12–36
3b	5–10	26–40	15–28, 14–43	9–26, 17–33	8–30	7–20	6–28, 12–36
4a	6–13	15	15, 20	12, 15	18–20	15	13–15, 19–20
4b	5–11	15	15, 20	12, 15	18–20	15	13–15, 19–20
5	4–17	26–40	12–28, 36–43	12–33	9–30	8–20	7–28, 7–36
6a	6–13	15, 20	15, 20	15	13–15	15	20
6b	7–12	15, 20	15, 20	15	15–19	15	20
6c	7–14	15, 20	15, 20	15	15–19	15	20
7	5–13	15	15	9–13, 18	15, 20	15	15
8	5–13	20, 30	15–28	12–26	10–26, 12–30	8–20	7–23
9	6–21	20, 30	30, 40	20, 30	23–30, 30–40	29–30	25–30, 32–40
10a	8–16	20	20	20	29	20	20
10b	7-21	20, 30	20	30	29–30, 39–40	20	29–30
10c	7–21	20, 30	20	30	29–30, 39–40	20	29–30
11	13–20	20, 30	–	20, 30	–	20	–
12	15–19	20	–	20, 30	–	20	–
13	7–10	15, 20	13–16	9–15	10–19	15	8–14, 23
14a	7–12	30	30	20	46–49	9–30	39–40
14b	5–22	30	30, 40	20, 30	30–40, 46–49	29–30	25–30, 32–40
15	7–21	20	20, 30	20, 30	29–30, 39–40	20, 30	29–30
16	14–21	20, 30	–	20, 30	–	20	–
17	7–12	15	12, 15	12	17–20	15	13–15, 19
18	9–15	15	15, 20	15, 20	19–20	15	20
19	14–19	20, 30	–	20	–	20	–

Table 5.14: List of HCO+ kinetic (excitation) temperatures for each scenario. The model excitation temperatures are shown for each model (i.e. ranges of excitation temperatures correspond to the ranges of kinetic temperatures shown in Table 5.13.

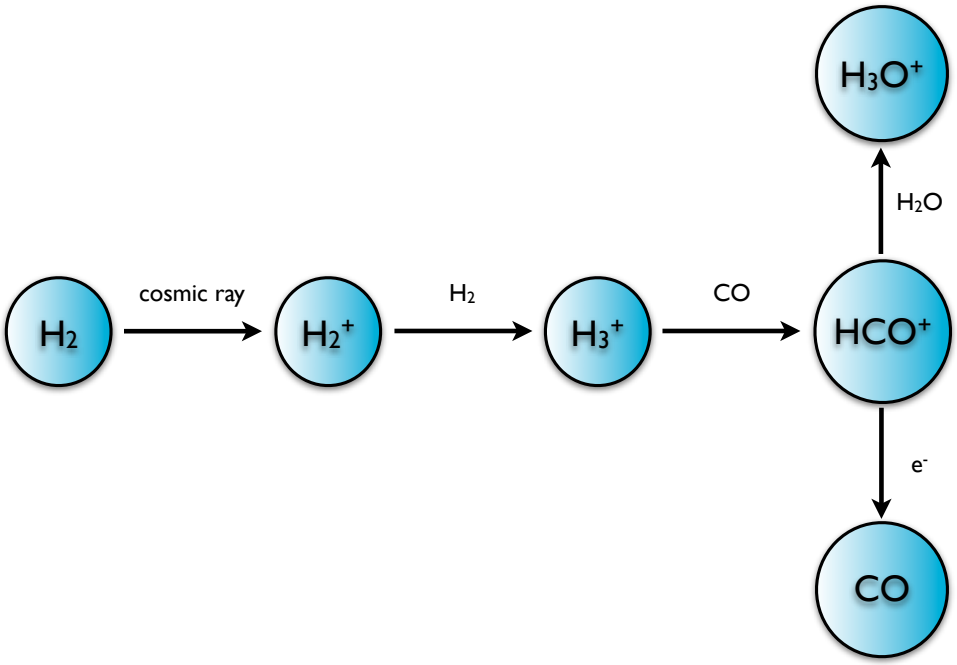

Figure 5.35: Typical chemistry of HCO+ in molecular clouds.

photodissociation due to nearby hot stars, recombination with other molecules or electrons, or enhanced ionisation due to magnetic fields. The HCO+ abundance used in the TORUS models was 8×10^{-9} (Irvine et al 1987), but varies by a factor of 2–4 in other studies (e.g. Blake et al. 1987; Kulesa et al. 2005). The chemical cycle of HCO+ abundance is expected to follow CO, where CO depletion occurs at temperatures ∼20 K [Nakagawa, 1980]. The typical lifecycle of HCO+ is shown in Figure 5.35, where HCO+ is made from the combination of H_3^+ and CO. Additionally, in the outer envelopes of stars and PDRs, HCO+ can also be created from the combination of C^+ and H_2O. Destruction of HCO+ typically occurs through several main processes, including electron dissociative recombination forming CO or proton transfer to water creating H_3O^+ in higher temperatures (> 100 K). Additionally, HCO+ can be destroyed through combination with neutral metallic atoms (i.e. Na and Mg to form Na^+ and Mg^+).

CO depletion could be an issue in high density regions, i.e. starless cores which have densities $\sim 10^5$ cm^{-3} and lower temperatures ∼10 K [Di Francesco et al., 2008]. Christie et al. [2012] found Ophiuchus to have the lowest average CO depletion levels

in comparison to other GBS clouds (including Serpens, NGC 2024, NGC 2071 and Taurus). In this study, CO depletion levels were defined as the ratio of 850 μm and $C^{18}O$ dust column densities,

$$F_{\rm dep} = \frac{N(H_2)_{\rm dust}}{N(H_2)_{\rm CO}}, \tag{5.18}$$

where depletion factors were estimated to be a mean of 7 in starless cores and 4 in protostellar cores. I note these values were not corrected for optically thick $C^{18}O$ emission, where depletion factors would decrease because the column densities estimated by $C^{18}O$ would increase with the optical depth correction. The abundance of $C^{18}O$ was assumed to be $X_{\rm C^{18}O} \simeq 1.7 \times 10^{-7}$ from Frerking et al. [1982]. In my analysis, I use a $C^{18}O$ abundance of 10^{-7}, which would change the depletion values calculated by Christie et al. [2012] to 4 and 2 for the starless and protostellar cores respectively in my data. Assuming the main method of creating HCO+ is from the combination of H_3^+ and CO and the abundance of CO and HCO+ have a linear relation, HCO+ abundances would decrease by the same factor to 2–4 $\times$ 10^{-9} (assuming the original HCO+ abundance is 8 $\times$ 10^{-9}). These values are similar to values found in other clouds, for example OMC-1 [Blake et al., 1987].

Depletion would result in important consequences needed for modelling the cloud. First, the input column density for each model would be a factor 2–4 too low. In the optically thin scenario, increased column densities would cause the HCO+ main-beam temperature output to increase proportionally. Second, $C^{18}O$ depletion could indicate corresponding HCO+ depletion by the same factor (if the two molecular abundances are linearly related). The increase in column density by the depletion factor would then result in the HCO+ main-beam temperature outputs remaining the same in the optically thin limit (due to the decreasing the HCO+ abundance).

It is unlikely depletion will affect regions like Oph A with model main-beam temperatures which were found to surpass the corresponding cloud main-beam temperatures. However, Oph B has model main-beam temperatures that are found to be consistently lower than what is found in the cloud. To understand how depletion may affect a region with lower column density and kinetic temperature like Oph B, it is important to understand HCO+ optical depth and excitation temperatures. The

models predict a varying range of optical depths dependent on the column density, density and line width of the molecules. The majority of these molecules indicate that at the column densities and kinetic temperatures corresponding to the $C^{18}O$ and ^{13}CO integrated intensities, optical depths range from $<$ 1–10 in the Oph B1, B2 and CEF regions. In thermalised and optically thick emission, the HCO+ integrated intensities will saturate and remain constant with increasing or decreasing column density. The optical depth is then proportional to column density, where $N(H_2) \propto \frac{\tau}{1-\exp(-\tau)} \int T_{\rm MB}\ {\rm d}v$. Therefore, varying abundance due to depletion will not affect the corresponding main-beam temperatures of a thermalised and optically thick molecule.

The scenarios primarily affected by low model main-beam temperatures are found to have low column densities ($\sim 10^{22}$ cm^{-2}), a range of optical depths and non-LTE conditions (i.e. $T_{\rm ex} < T_{\rm kin}$). Scenarios include 1, 3 ab, and 5, primarily found in Oph B, C, E and F. The molecule appears to primarily be optically thick but not thermalised. In the optically thick regime, the main-beam temperature of the molecule is equivalent to the excitation temperature as discussed in the above section. Since the molecule is not thermalised, the excitation temperature will increase a higher column density that has been corrected for lower $C^{18}O$ abundance. Even though the molecule is optically thick, the main-beam temperature will still increase with the higher excitation temperature and column density. This would allow the models to produce higher main-beam temperatures that may match the HCO+ data better in these particular regions.

Past studies of the Oph A clump indicate an enhanced ionisation rate from magnetic fields may affect HCO+ abundances in the region. Using HCO+ $J = 3 \rightarrow 2$ and $H^{13}CO$ $J = 3 \rightarrow 2$ data, Kulesa et al. [2005] describe a 'ring-like' structure at the centre of Oph A and calculate a varying HCO+ abundance for the region ranging from 3×10^{-9} on the south-side of the ring to 1.2×10^{-8} on the eastern portion of the ring near VLA 1623. Both values are higher than the HCO+ abundances inferred from CO depletion. This increase in abundance is theorised to be the result of an enhanced ionisation rate from the nearby magnetic B star S1 and three other nearby sources. The potential for HCO+ destruction through gaseous H_2O was ruled out due to low abundance of H_2O in the cloud, taken from the Submillimetre Wave Astronomy Satellite [Ashby et al., 2000; Snell et al., 2000]. I note my observations of

Ophiuchus find increased column densities and gas temperatures in Oph A compared to those found in Kulesa et al. [2005], where they use a column density $N(H_2) \simeq 1$–5×10^{22} cm^{-2} and kinetic temperature 25 K. However, the abundance I use for the HCO+ models is comparable to the upper limit on abundance found in this study (smaller by a factor of 1.5).

Using the lower limit of $X(\text{HCO+}) = 3 \times 10^{-9}$ from Kulesa et al. [2005], the integrated intensities would decrease at most by a factor of 0.375 (assuming optically thin emission). In particular, the edges of the Oph A, B and CEF cores have less prominent emission than the centres of the regions and these areas are not fully covered by the existing models. Decreasing peak main-beam temperatures by 0.375 would allow more of these regions to be covered in the optically thin scenario. However, these regions are modelled to have high optical depths reaching $\tau \sim 10^2$. Using the upper abundance limit 1.2×10^{-8}, the HCO+ abundance and thus the main-beam temperatures will increase at most by a factor of 1.5. With emission predicted to be widely optically thick, it is likely the HCO+ line is saturated and increasing the abundance would not drastically affect output main-beam temperatures.

There is a distinct possibility that multiple issues are the cause of the TORUS models not fitting all (or some) of the data. For example, optically thick ^{13}CO may still trace outer cloud layers directly heated by the early B-type stars surrounding the inner star-forming regions and inevitably predict high kinetic temperatures. Additionally, abundance variations across the cloud due to depletion and an enhanced ionisation rate may require separate models for each region to be developed with different abundances.

5.7.4 Beam dilution

Lastly, beam dilution can lead to decreased main-beam temperature measurements, occurring when the material being observed is clumped on scales smaller than the size of the beam, $\Omega_s << \Omega_B$. The main-beam temperature will fall with the ratio of the solid angle subtended by the source and telescope beam. Additionally, this can

be related to the FWHM or the angular size modelling the source as a Gaussian,

$$T_{\mathrm{MB,corr}} = T_{\mathrm{MB,s}} \left(\frac{\theta_{\mathrm{s}}}{\theta_{\mathrm{B}}} \right)^2 , \tag{5.19}$$

where θ_{s} is the FWHM corresponding to the source and θ_{B} is the FWHM of the beam. The JCMT beam is $\sim$15″ FWHM for HARP at 356 GHz. While cores are typically comparable or larger than the JCMT beam size [Christie et al., 2012], it is possible that Ophiuchus largely consists of clumpy material smaller than the size of the beam. In this scenario, the main-beam temperature will be reduced by beam dilution.

As discussed in Section 5.7.2 and 5.7.3, the region where HCO+ main-beam temperatures are overpredicted by the models is Oph A. Models with kinetic temperature inputs corresponding to ^{13}CO predict main-beam temperatures that range up to 20 K. Main-beam temperatures in the Oph A region range up to 13–14 K. This would mean the main-beam temperature of the source would decrease by 0.7, or the corresponding FWHM size of the source would be $\sim$ 13″.

Though it is possible material in the cloud has a clumpy distribution smaller than the beam, it is more likely beam dilution would affect individual sources like cores since the Oph A region doesn't particularly appear to be a series of small clumps/cores from HCO+ observations. Additionally, Oph A consistently has high main-beam temperatures predicted using the `TORUS` modelling, which would be better described from abundance variations across the cloud or high kinetic temperature inputs.

5.7.5 Improvements and future work

Using radiative transfer models to investigate the underlying densities traced by molecular line emission has much room for improvement. In addition to accounting for depletion or high kinetic temperatures and further developing the one-dimensional density profile (and eventually adding more complex geometries), other molecules with high critical densities can be further explored for potential application. In this section, I discuss the next steps for the log-normal density models, developing new density profiles and other useful molecules tracing high densities.

As discussed above, the varying-σ log-normal models primarily had an issue with the range of FWHM velocities. The resulting fits had lower- and upper-limits on density and line-of-sight lengths. It would be more appropriate to fit the HCO+ emission pixel-by-pixel, similar to the method introduced using the RADEX models to have a better idea of the density and line-of-sight variations across the cloud. Additionally, this would allow a better comparison of the distribution of densities associated with the sources and total cloud.

The next step in developing the density profile is to include the observed power-law tail in the log-normal density distribution, described in Section 5.6.1 and observed by Kainulainen et al. [2009] from the column density PDF. The inclusion of the power-law tail in the density PDF and the derived density profile along the cloud line-of-sight would effectively increase the peak densities suggested by the log-normal profile and potentially solve the issue that none of the current density profiles predict HCO+ emission reaching its critical density based on the conditions in the cloud. This may also allow the log-normal density profile and the log-normal with the power-law density profile to be tested on different types of molecular clouds, i.e. the log-normal density profile should better fit regions with little to no active star formation and the power-law profile should better fit regions with active star formation.

Other molecules with high critical densities can also be used to explore the relationship between high density and column density in molecular clouds. Friesen et al. [2009, 2010a,b] concluded the N_2H^+ 1–0 with a critical density close to the HCO+ line (2×10^5 cm^{-3}) traced the dense gas in the Oph B and CEF regions and was resilient to depletion at high densities and older temperatures ($n > 10^5$ cm^{-3}). Deuterated molecules were also used in this study, including N_2D^+ $J = 3 \rightarrow 2$ ($n_{\rm crit} \sim 8 \times 10^5$ cm^{-3}) and H_2D^+ $J_{K_{-1}K_1} = 1_{11} - 1_{10}$ ($n_{\rm crit} \sim 10^5$ cm^{-3}). Deuterated species are thought to be abundant in cold cores where significant depletion has occurred. Additionally, another high density tracer HCN 4–3 has a frequency similar to HCO+ (354.505 GHz) and traces similar densities. Variations in emission from multiple dense gas tracers would give a more complete view of higher densities found in the cloud which would facilitate the development of accurate density profiles.

5.8 Summary

This chapter aimed to make a comparison between column density and density in the Ophiuchus molecular cloud (L1668) by modelling the densities traced by HCO+ $J = 4 \rightarrow 3$ using non-LTE radiative transfer codes RADEX and TORUS. Each method results in a density map corresponding to HCO+ emission used to compare densities at positions of embedded Class 0/I protostars, prestellar cores [Simpson et al., 2008] and 'starless' cores [Stanke et al., 2006]. The main conclusions are summarised:

1. **Trends in HCO+ and column density comparison.** Trends can be seen in the comparison between HCO+ integrated intensities and the various column density tracers ($C^{18}O$ integrated intensities, SCUBA-2 850 μm dust continuum and extinction maps A_v). In each comparison, there is a drastic increase in HCO+ emission (> 10 K km s^{-1}) corresponding to values ($C^{18}O$) 10 K km s^{-1}, (850 μm) 0.1 Jy beam^{-1} and (A_v) 27 mag. The increased HCO+ integrated intensities were found in the Oph A region and were thought to potentially correspond to the region reaching the critical density for HCO+.

2. RADEX **non-LTE modelling.** RADEX was used to model densities traced by HCO+ in the cloud using the column density tracers listed above. The program was modified to input an initial density into the offline program and compare the output HCO+ line peak to HCO+ data. The program would vary the density input based on the ratio of HCO+ model output and HCO+ data. Results indicated HCO+ was widely subthermally excited (densities ranging from 10^3–10^5) and line-of-sight estimates ranged from several parsecs to 90 pc which is unrealistic for a cloud like Ophiuchus with clumps on scales of 0.2 pc in length. This suggested the need for an improved density profile varying along the line-of-sight.

3. TORUS **non-LTE modelling using varying density profiles.** To improve upon a constant density model, the TORUS non-LTE Monte Carlo code was used to implement varying density profiles for modelling HCO+ emission. One-dimensional density profiles were developed for a plane-parallel slab geometry, including a 'triangle' density profile and 'log-normal PDF' density profile based

on the assumption the density probability density function (PDF) follows a log-normal distribution. The density models were constant along the x- and y-axes and varied along the z-axis. Models were constrained using an average cloud density (derived from the cloud mass) and an assumed cloud length (corresponding to the length of the Oph A and B clumps). Input parameters included the column density (derived from $C^{18}O$), kinetic temperature (derived from ^{13}CO), line width, density profile and abundance.

4. **Modelling Results.** Models were fit to scenarios in the data, defined as regions with similar column density and kinetic temperature within the cloud. Initially, the column densities for each model were fit to the scenarios, allowing a range of kinetic temperatures to fit the data. For the triangle models, density fits ranged from 0.2–2.0 $\times 10^6$ cm^{-3} and 0.1 $-$ $-$0.3 $\times 10^6$ cm^{-3} for the 0.2 and 0.3 pc models respectively. Log-normal models with constant-σ show density ranges from 0.2–1.0 $\times$ 10^5 cm^{-3} and 0.6–2.0 $\times$ 10^5 cm^{-3} for 0.2 and 0.3 pc models. Log-normal models with varying-σ have lower and upper density limits corresponding to the range of FWHM velocities that constrain the density profile. Densities (lower and upper limits) range from 0.1–1.0 $\times 10^6$ and 0.5–3.0 $\times 10^5$ cm^{-3} for the 0.2 and 0.3 pc models respectively. Upper and lower density limits are the result of fitting a range of FWHM velocities in the scenarios of the data. Using a pixel-by-pixel fitting method, these limits would be replaced with a single fit to each individual pixel in the map. Implementation of the pixel-by-pixel fitting method is expected in the future.

5. **Source Densities.** Densities corresponding to embedded Class 0/I protostars, starless cores and prestellar cores were determined from the model results. The distribution of peak densities at the positions of the protostars do not differ for the majority of the scenarios with the exception of the upper density limit using the log-normal varying-σ models. The density distributions most likely vary because the protostars are not found at the highest column densities in the cloud (2–4 $\times 10^{23}$ cm^{-2}), though they are found at high column densities within column density thresholds found in previous studies [Johnstone et al., 2004; Onishi et al., 1998].

5.9 Appendix: Model main-beam temperature profiles

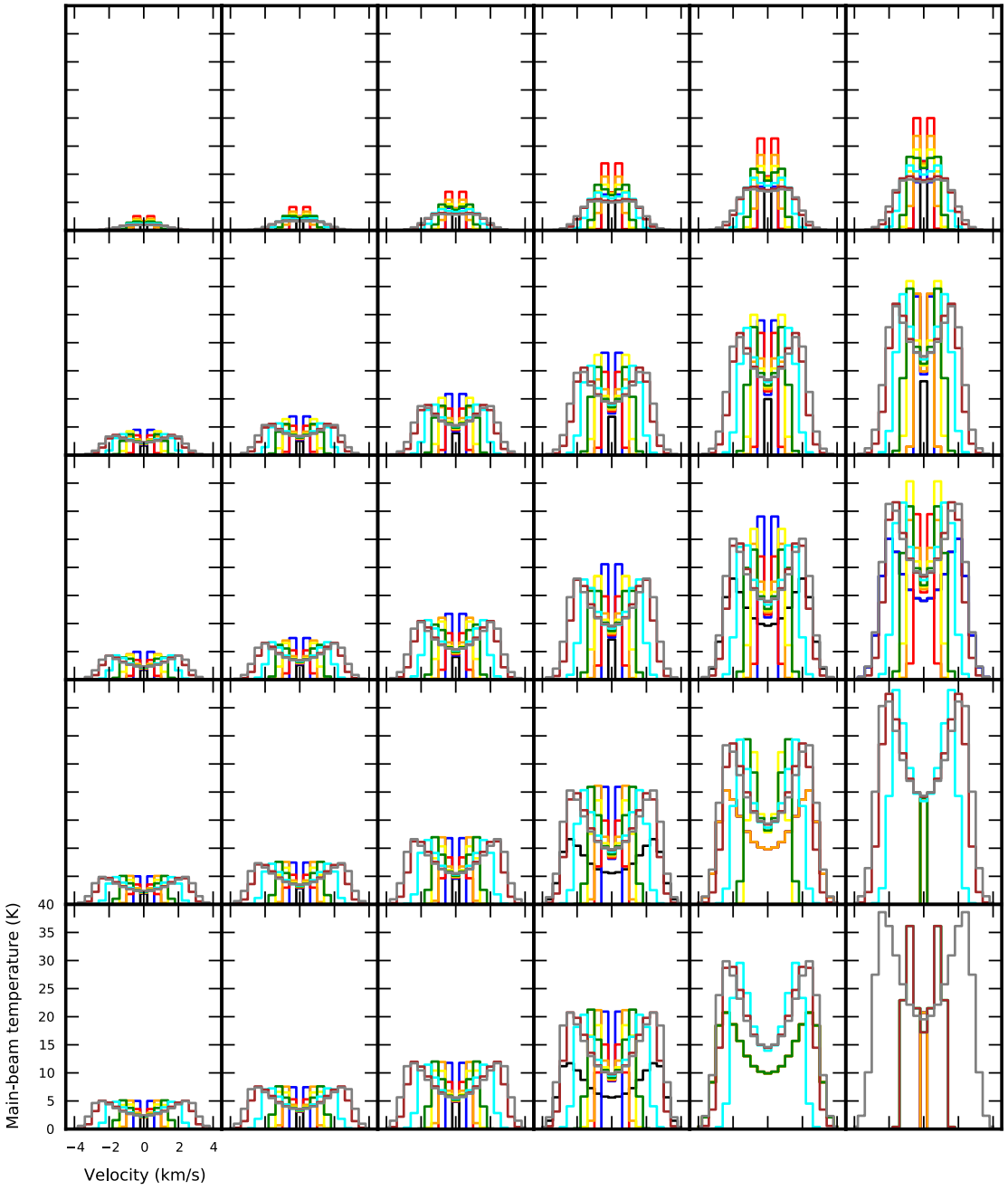

Figure 5.36: HCO+ main-beam temperature models assuming the triangle density profile with a maximum cloud length of 0.2 pc. Column densities increase from left to right (1×10^{22}, 5×10^{22}, 1×10^{23}, 3×10^{23} and 5×10^{23} cm^{-2}). Kinetic temperature increases from top to bottom (12, 15, 20, 30, 40 K). Colours correspond to input model velocities: (black) 0.2, (blue) 0.3, (red) 0.5, (orange) 0.7, (yellow) 0.8, (green) 1.0, (cyan) 1.5, (brown) 2.0 and (gray) 2.2 km s^{-1}.

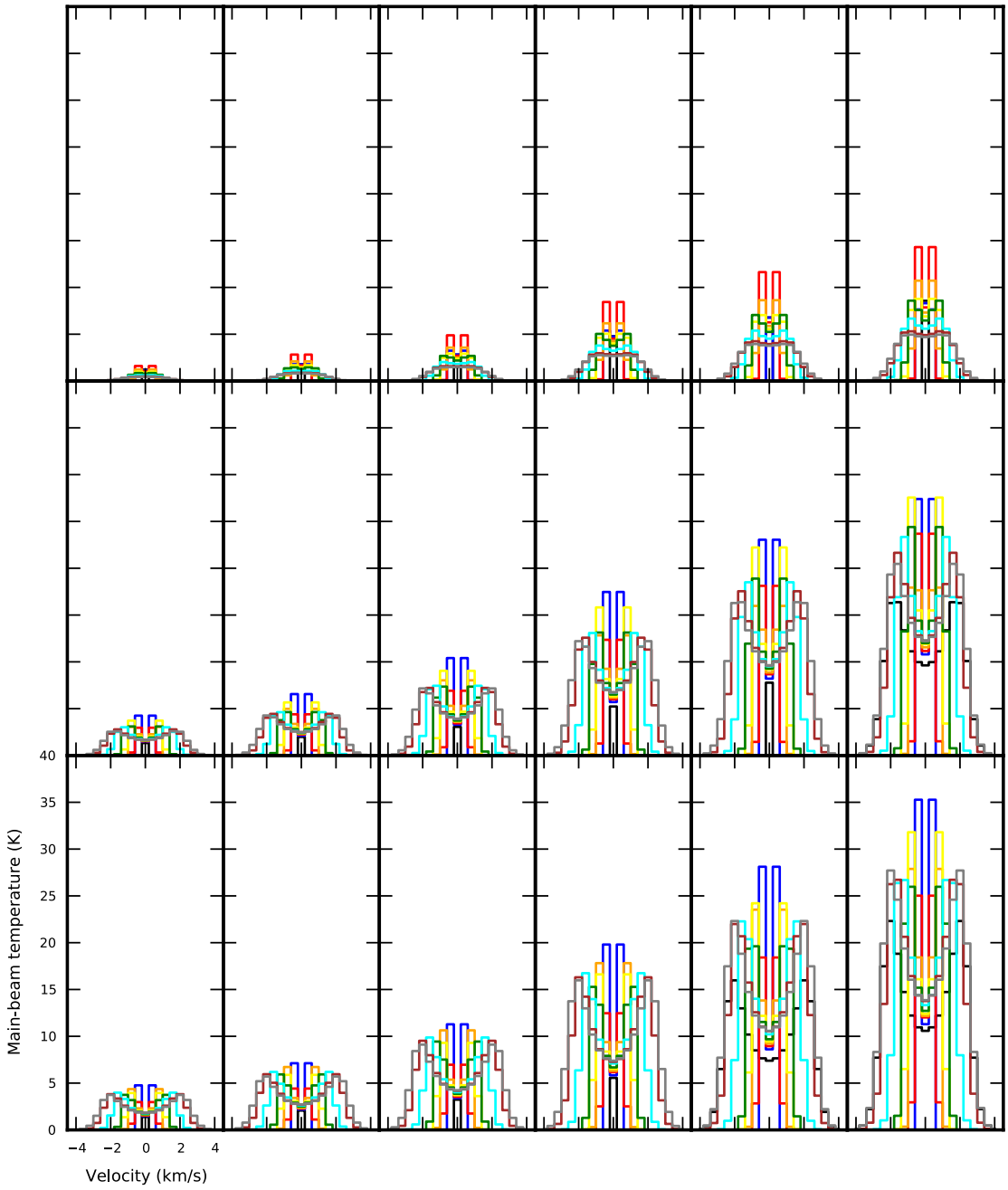

Figure 5.37: HCO+ main-beam temperature models assuming the triangle density profile with a maximum cloud length of 0.3 pc, as in Figure 5.36. I note that column densities 3 and 5 $\times$ 10^{23} cm^{-2} are not constrained using these models.

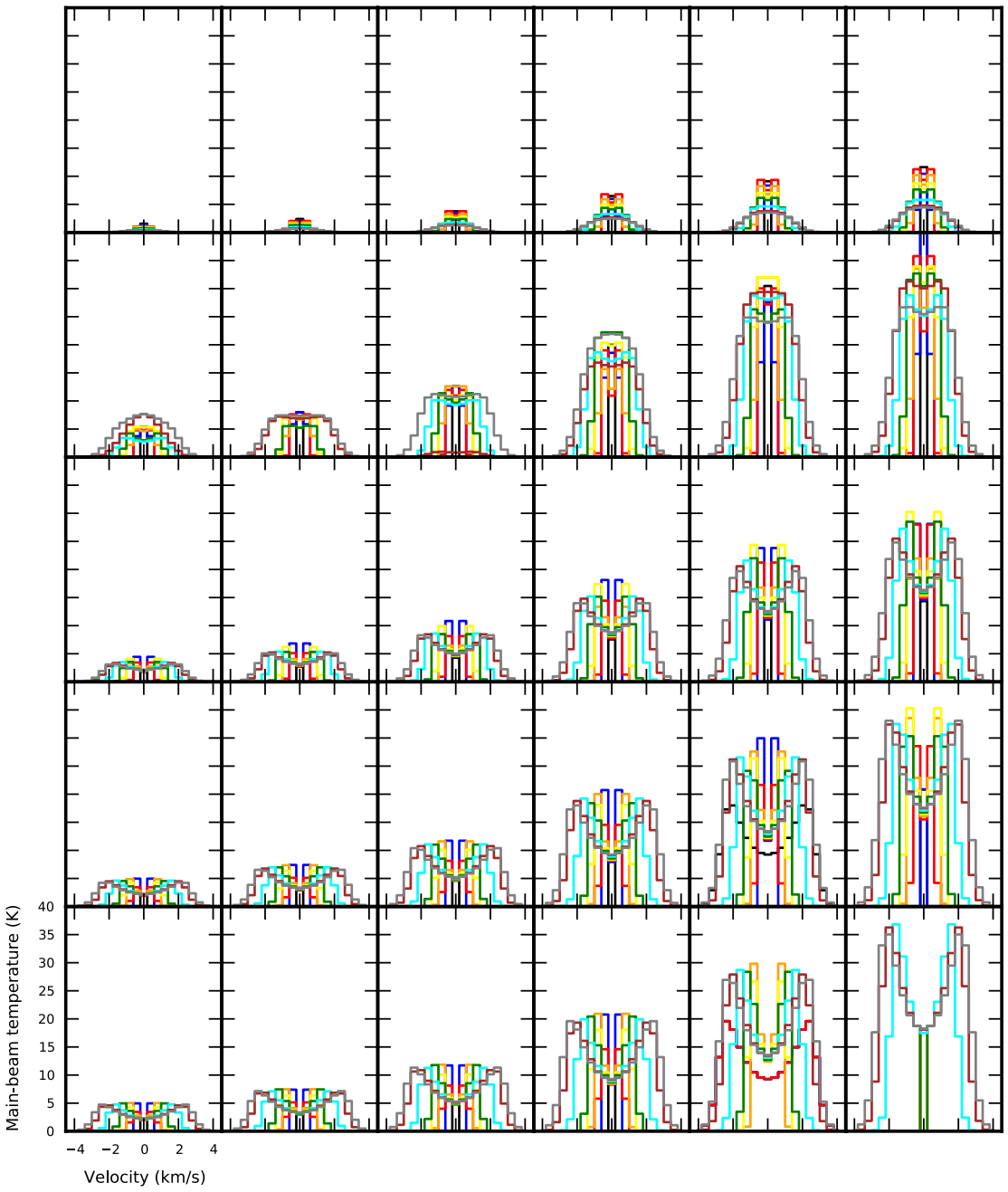

Figure 5.38: HCO+ main-beam temperature models assuming the constant-σ log-normal PDF density profile with a maximum cloud length of 0.2 pc, as in Figure 5.36.

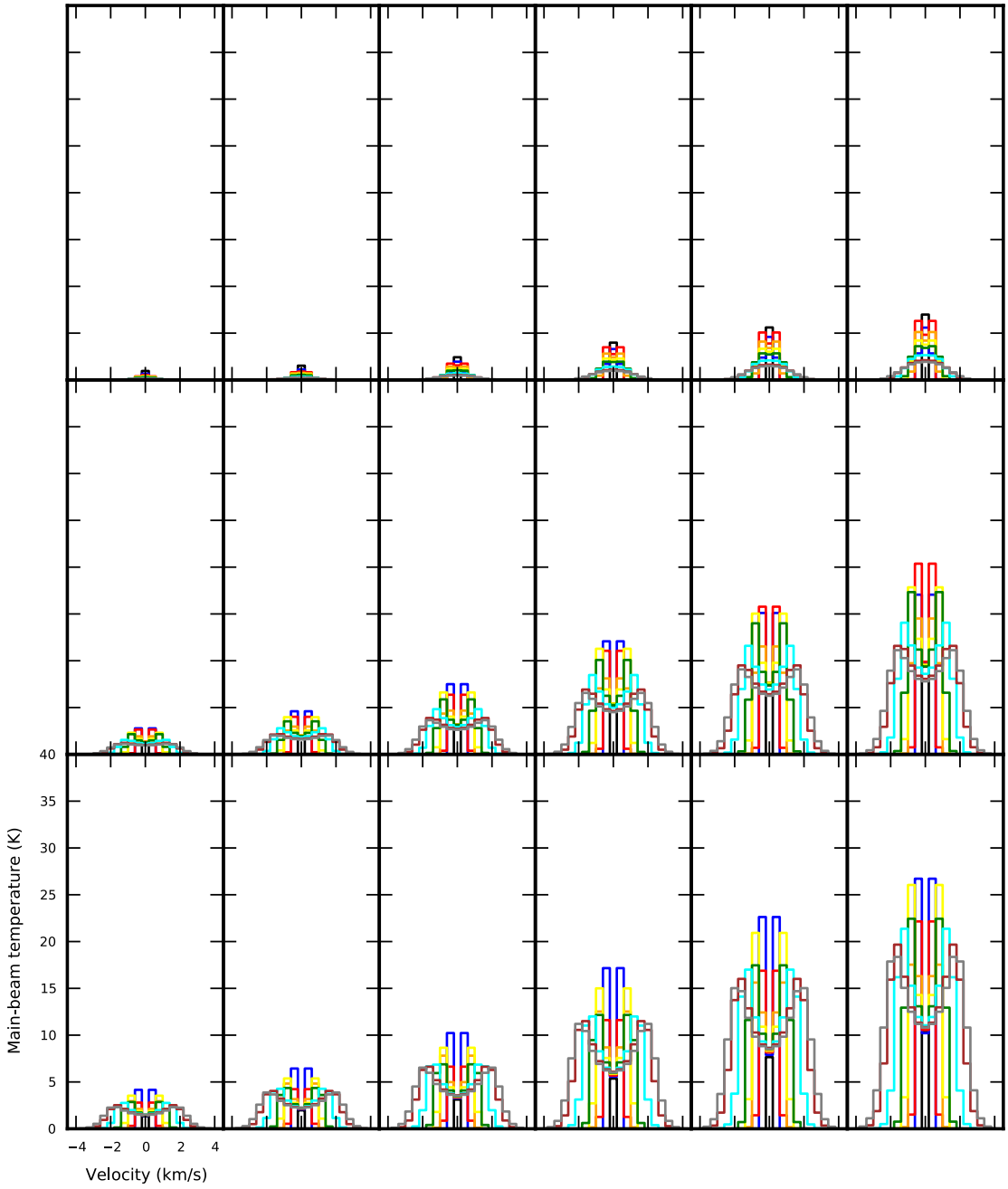

Figure 5.39: HCO+ main-beam temperature models assuming the constant-σ log-normal PDF density profile with a maximum cloud length of 0.3 pc, as in Figure 5.36. I note that column densities 3 and 5 $\times$ 10^{23} cm^{-2} are not constrained using these models.

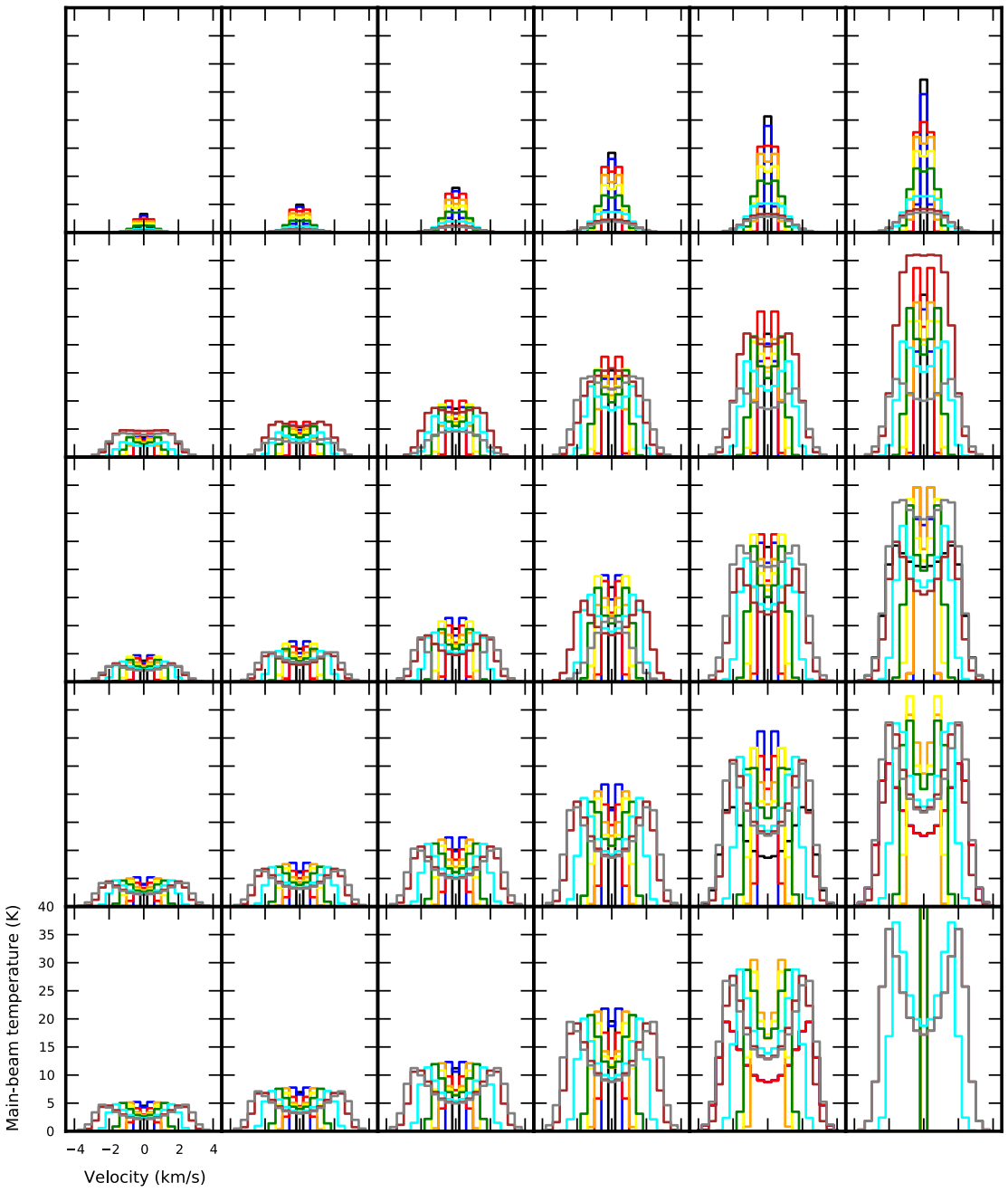

Figure 5.40: HCO+ main-beam temperature models assuming the varying-σ log-normal PDF density profile with a maximum cloud length of 0.2 pc, as in Figure 5.36.

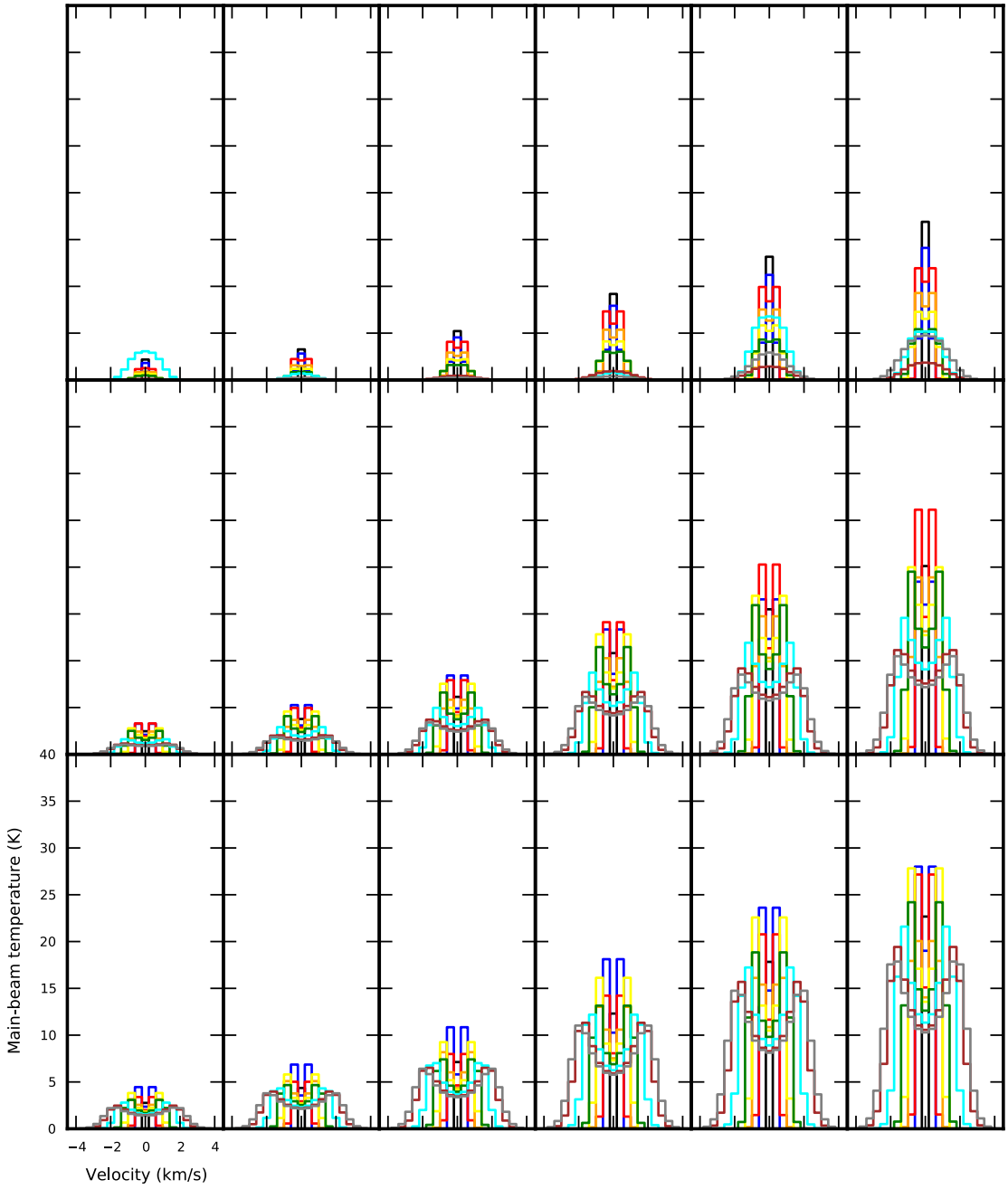

Figure 5.41: HCO+ main-beam temperature models assuming the varying-σ log-normal PDF density profile with a maximum cloud length of 0.3 pc, as in Figure 5.36. I note that column densities 3 and 5 $\times$ 10^{23} cm^{-2} are not constrained using these models.

Chapter 6

Conclusions

I stepped from plank to plank
So slow and cautiously;
The stars about my head I felt,
About my feet the sea.

I knew not but the next
Would be my final inch,–
This gave me that precarious gait
Some call experience.

— Emily Dickinson

This thesis primarily focused on using submillimetre observations of molecular lines to improve our understanding of nearby low-mass star formation. It demonstrated the variety of properties that can be traced by molecular lines like CO $J = 3 \rightarrow 2$ isotopologues and the dense gas tracer HCO+ $J = 4 \rightarrow 3$ and their significance in addressing current questions in star formation research. In this chapter, I review the conclusions from my work and discuss potential areas for future research.

6.1 Molecular line contamination

The first part of this thesis introduced SCUBA-2, a bolometer array on the JCMT that began full operations in Fall 2011. SCUBA-2 observes dust continuum emission

at 450 and 850 μm. In Chapter 2, I described a method used to calculate molecular line contamination in the SCUBA-2 dust continuum observations. Observations of continuum emission can be contaminated by molecular line flux, potentially biasing the fluxes and masses of protostellar sources. This line contamination can be quantified by comparing observations of the continuum to line emission. The brightest molecule in the submillimetre wavelength range is ^{12}CO, where ^{12}CO $J = 3 \rightarrow 2$ and $J = 6 \rightarrow 5$ transitions have corresponding wavelengths to the 850 and 450 μm SCUBA-2 bands respectively. Therefore, I derived line contamination (or conversion) factors used to convert ^{12}CO molecular line emission maps in K km s^{-1}to molecular line flux in mJy beam^{-1} contaminating the dust continuum emission of SCUBA-2.

I applied these conversion factors to HARP ^{12}CO $J = 3 \rightarrow 2$ maps of NGC 1333 of Perseus and NGC 2071 and NGC 2024 of Orion B to quantify the ^{12}CO contamination found in corresponding SCUBA-2 850 μm maps. Noticeable line contamination was seen near sources with known outflows, including SVS13 in NGC 1333, LBS-MM18 of NGC 2071 and FIR 1–7 of NGC 2024. Fluxes and masses were quantified for a list of submillimetre sources in the SCUBA-2 850 μm and ^{12}CO line contamination maps, where the majority of sources had line contamination $< 20\%$. Substantial contamination was found for sources driving or near molecular outflows, where contamination ranged from 24–79%. ^{12}CO $J = 6 \rightarrow 5$ contamination to the 450 μm data was concluded to be insignificant compared to the dust continuum RMS value.

Since some star forming regions have molecular line contamination that dominates the dust continuum emission, my work emphasised the importance of removing this flux from the 850 μm continuum. Dust continuum is used for a variety of analyses, including core detection, core mass, dust temperature and dust emissivity. Without subtracting the ^{12}CO line flux from the 850 μm emission, it is possible dust temperatures and core masses would be biased due to higher continuum fluxes. Similarly, outflow lobes seen in the continuum from ^{12}CO line contamination can easily be mistake for starless cores (e.g. Figure 2.4 in Section 2.4).

Since my initial work incorporated in Drabek et al. [2012], the filtering process for the HARP maps was improved [Hatchell et al., 2013] and new beam sizes have been measured [Dempsey et al., 2013] which changes the initial line conversion factors

by a factor of 1.06 higher (new effective beam size) or lower (primary beam only). This work contributed to dust temperature estimates of NGC 1333 in Hatchell et al. [2013] and dust emissivity β calculations of B1 in Sadavoy et al. [2013] . Additionally, the method for applying conversion factors to ^{12}CO $J = 3 \rightarrow 2$ HARP data and subtracting this line contamination has now been implemented into the SCUBA-2 reduction process for 850 μm maps used in the JCMT Gould Belt Survey [Ward-Thompson et al., 2007b].

6.2 Outflows and global properties of Ophiuchus L1688

Molecular outflows are thought to be ubiquitous in star formation, where each protostar is expected to undergo a period of mass-loss. Outflows provide a mass-loss history of the protostar and potentially solve issues regarding excess angular momentum for matter to accrete onto the central protostar. Additionally, there are disputes regarding the role of turbulence in the molecular cloud and the ability of turbulence to provide support against gravitational collapse.

Understanding turbulence and its driving source is important for understanding the cloud conditions leading to star formation. Observational evidence shows star formation efficiency in molecular clouds to be lower than expected if the cloud is collapsing under gravity in a free-fall timescale (as discussed in Chapter 1). Turbulence can act as a support mechanism against gravity for the cloud, allowing smaller scales to collapse and form stars [Mac Low and Klessen, 2004]. If molecular outflows drive turbulence in star forming regions, this may suggest self-regulated star formation and explain the support mechanism for longer cloud lifetimes and lower star formation efficiency.

In Chapter 3, I further analysed a catalogue of sources from the *Spitzer* survey, "From Molecular Cores to Planet-Forming Disks" or 'c2d' [Evans et al., 2009] for the presence of molecular outflows in the Ophiuchus L1688 cloud. This list consisted of 30 source ranging from Class 0, Class I and flat spectrum sources (Class II source WL 10 was included with research from Sekimoto et al. 1997 suggesting an outflow was present). The source list included 6 new protostellar sources found in the c2d

survey that had never been analysed for molecular outflows. A HARP ^{12}CO $J = 3 \rightarrow 2$ map was used to search for high-velocity blue and redshifted emission characteristic of bipolar outflows driven by embedded protostars. Out of the 30 sources analysed, 8 had firm molecular outflow detections, 20 were 'confused' detections and 2 sources had non-detections. Additionally, outflow directions were further investigated with H_2 data taken by UKIRT. From this study, the location of confirmed outflows was determined and the velocity range associated with molecular outflows in the region was defined which is important for quantifying the outflow mass and energetics.

The Ophiuchus L1688 cloud has an active history of star formation that was thought to be triggered by a supernova explosion of the ζ Oph binary companion. My work found the L1688 cloud to be gravitationally bound, where the virial mass is 27% of the cloud mass and the turbulence is a factor of 7 smaller than the cloud binding energy. Additionally, the energy driven by outflows was found to be only 21% of the turbulent kinetic energy, suggesting outflows are significant but not the dominant source of turbulence in the cloud. This conclusion is contrary to results from Nakamura et al. [2011], who suggested outflows drive turbulence in the region after comparing the outflow injection rate to the turbulent dissipation rate. I showed that using a longer outflow timescale that reflected the lifetime of a Class I protostar (0.5 Myr; Evans et al. 2009) and recalculating the turbulent dissipation rate using the updated masses from the optical depth corrected C^{18}O emission, the outflow injection rate is lower than the dissipation rate by a factor of 2.4–6.0. This result agreed with my conclusion that global outflows in the region are significant but not the dominant driver of turbulence.

One issue with my comparison between the outflow and turbulent kinetic energies was the uncertainty that outflows are the source driving the global high-velocity emission. In Section 4.1.8, I further examined the physical regions corresponding to this global high-velocity emission and used masks to quantify the amount of energy from confirmed molecular outflows, hot dust from the nearby B-type stars Oph S1 and SR3 and regions that have energies with sources unaccounted for. Using the ambient velocity range $v_o = 3.3 \pm 2.5$ km s^{-1}, outflows were found to be 33% of the global high-velocity energy and regions with hot dust were 26%. This left ∼41% of the high-velocity energy unaccounted for. It is possible this emission is the result of several factors, including outflow remnants from less embedded sources, Class II

jets with corresponding H_2 knots that excite the molecular medium or stellar winds from the nearby Upper Sco OB association.

The low outflow-driven turbulence is not surprising in a region like Ophiuchus with relatively fewer embedded Class 0/I protostars compared to the less embedded Class II/III sources. Evans et al. [2009] noted the region seems to have a star formation rate that has declined relative to the lifetime of the cloud. The decline in star formation could similarly relate to a decline in outflow-driven turbulence in the region.

What are the implications of the declining star formation rate and low turbulence in the Ophiuchus L1688 cloud? As the cloud collapses under gravity, there is a possibility the region could undergo a second generation of star formation. Jørgensen et al. [2008] noted a higher fraction of starless cores relative to protostellar cores in L1688. These cores could go on to form protostars in the cloud. Turbulence may then be renewed in the region with this new generation of protostars. Similarly, the molecular cloud associated with IC 348 is similar to Ophiuchus, where outflow energy is only 38% of the turbulent kinetic energy. This region is a remnant of a larger cloud that has formed the IC 348 cluster. The stars that now produce the Flying Ghost Nebula are likely the sources of past outflows that created strong velocity gradients in the region. The cores in the region are primarily starless and will likely go on to collapse and form protostars [Curtis et al., 2010b]. Like Ophiuchus, the lack of outflow-driven turbulence in IC 348 is likely due to the lack of embedded protostars able to drive molecular outflows and turbulence is likely driven by the nearby IC 348 cluster that initially triggered star formation in the region.

One aspect of this study was to use different methods to calculate both the mass and energetics of the cloud and global molecular outflows to further investigate how different methods can affect the calculations. For the mass and energetics of the molecular cloud, I used $C^{18}O$ and ^{13}CO observations with optical depth corrections and compared the results. The cloud was gravitationally bound in both cases where the kinetic turbulent energy is smaller than the gravitational binding energy by factors of 7 and 5 for the respective isotopolgues and potentially in a state of collapse. I chose to continue using cloud mass and energetics derived from $C^{18}O$ observations to match past studies of Gould Belt clouds (e.g. Curtis et al. 2010b; Graves et al. 2010) and to avoid potentially including outflowing gas from the ^{13}CO FWHM

velocity 2.0 km s^{-1}.

Similarly, the global molecular outflow properties were calculated using two ambient velocity ranges based on the outflow criterion ($v_o \pm 2.5$ km s^{-1}) as described above and the ^{13}CO optical depths (2.5–4.7 km s^{-1}). The small ambient velocity range defined by the ^{13}CO optical depths ($\tau > 1$)had a corresponding outflow kinetic energy a factor 6 larger than the original outflow energy and a factor 1.2 larger than the turbulent kinetic energy from C^{18}O measurements. Unlike the original calculations, this indicated the outflows have enough energy to drive turbulence in the molecular cloud. I chose to continue using the ambient velocity range derived from the outflow criterion to prevent ambient velocities from being included in the calculation of outflow properties. However, the difference between the outflow kinetic energies and the contrasting conclusions indicates the need for the ambient velocities to be explored further. This method of using the ^{13}CO can be revisited in the future and lower optical depths could be used as a limit for the ambient velocity range. Alternatively, ambient velocity ranges could be defined using velocities with a 3σ detectable C^{18}O measurements since the molecule is expected to trace the bulk motions of the cloud.

6.3 Non-LTE modelling of density using HCO+

Lastly in Chapter 5, I further investigated the relationship between column density and density in the Ophiuchus molecular cloud. This work involved developing density models using non-LTE radiative transfer codes to model HARP HCO+ $J = 4 \rightarrow 3$. Past work (e.g. André et al. 2010; Johnstone et al. 2000; Onishi et al. 1998) indicates there is a column density threshold for star formation that may link to a density threshold. This can lead to further understanding why a small percentage of the cloud mass proceeds to form stars and the low star-formation efficiencies. As a dense gas tracer ($n_{\rm crit} \sim 8 \times 10^6$ cm^{-3}), HCO+ emission may indicate regions of high density in molecular clouds. Modelling the densities traced by the HCO+ emission allowed me to compare these densities to column density tracers and examine the potential density threshold of star formation.

Densities traced by HCO+ were first traced using the non-LTE radiative transfer code RADEX [van der Tak et al., 2007]. This code assumes an isothermal and homoge-

neous medium with a constant density model along the cloud line-of-sight. Kinetic temperatures were constrained using ^{13}CO data, column densities were constrained by three different tracers (C^{18}O, 850 μm dust continuum and visual extinction $A_{\rm v}$) and FWHM velocities were determined using the HCO+ line maps. I was able to incorporate RADEX into Python code and iterate over the density input to determine the best fitting output HCO+ main-beam temperatures to my data. The result indicated HCO+ was predominantly subthermally excited with densities ranging from 10^3–10^5 and line-of-sight estimates from several parsecs to 90 pc, which is unrealistic for a cloud like Ophiuchus with clumps on scales of 0.2–0.3 pc. Realistically, the physical conditions of the cloud would not have constant line-of-sight densities, suggesting the need for an improved density model.

To improve the HCO+ radiative transfer models and better understand the densities across the cloud, the Monte Carlo non-LTE radiative transfer code TORUS [Harries, 2000] was used to implement density profiles varying along the line-of-sight. The simplest peaked density profile was described by an isosceles triangle, increasing from the front of the cloud at a constant gradient to a peak density at the centre of the cloud and decreasing at a constant gradient to the back edge of the cloud. This model was known as the 'triangle' density profile. The second density profile was more complex than the triangle model and was derived from the density probability density function (PDF), which has been described as log-normal in shape (see Kainulainen et al. 2009; Lombardi et al. 2008). The density profiles varied along the z-axis and remained constant along x- and y-axes. These models were constrained using the average cloud density, derived from the mass calculated by C^{18}O in Chapter 4 and an assumed cloud length (corresponding to the length of Oph A and B clumps). Like the RADEX models, the column density was constrained by C^{18}O, kinetic temperatures were constrained by ^{13}CO and FWHM velocities were constrained using the HCO+ maps.

The peaked-density profiles implemented into TORUS were relatively successful at modelling the primary regions of HCO+ emission found across the Ophiuchus L1688 cloud. The 0.3 pc cloud length models were unable to model regions with column densities $\geq 3.0 \times 10^{23}$ cm^{-2} due to constraints with the maximum column density of the cloud. For the triangle models, density fits ranged from 0.2–2.0$\times 10^6$ cm^{-3} and 0.1–0.3$\times 10^6$ cm^{-3} for the 0.2 and 0.3 pc cloud length models respectively. Log-

normal models with constant-σ (constant width of the log-normal PDF) had peak density ranges from 0.2–1.0 $\times 10^5$ cm^{-3} and 0.6–2.0$\times 10^5$ cm^{-3} for 0.2 and 0.3 pc models respectively. Similarly, log-normal models with varying-σ had lower and upper density limits corresponding to the range of FWHM velocities. Densities (lower and upper limits) ranged from 0.1–1.0 $\times 10^6$ and 0.5–3.0 $\times 10^5$ cm^3 for the 0.2 and 0.3 pc models respectively.

The result of the HCO+ density modelling showed the protostars and starless/prestellar cores do not have a preference for higher densities with respect to the rest of the cloud. This distribution of peak densities for the starless, prestellar and protostellar cores did not differ from the total cloud according to KS tests. This result disagrees with past research suggesting the probability of finding a submillimetre core steeply rises as a function of column density (e.g. Belloche et al. [2011]; Hatchell et al. [2005]). Since it is likely Ophiuchus evolved from a burst of star formation that has since declined, the region represents one particular evolutionary stage in the lifetime of a molecular cloud. The small sample of Class 0/I protostars likely to be embedded in the surrounding dense material of the cloud may not accurately represent the density or column density distribution of protostellar cores in all molecular clouds. Additionally out of the list of 'embedded' protostellar cores, there are only two Class 0 objects. Class I protostars are expected to be less embedded in the surrounding cloud material relative to Class 0 sources. Additionally, Class I sources are likely to have undergone a longer period of outflow activity that could impact the surrounding cloud material (i.e. outflow cavities; see Quillen et al. 2005) and lead to lower corresponding densities. Therefore, it is possible the density distribution of protostellar cores do not favour higher densities in clouds with declining star formation rates like Ophiuchus. I note there are a small number of starless and prestellar cores that are forming at the highest densities and column densities, which could indicate the region will undergo a second generation of star formation in the future [Jørgensen et al., 2008].

Alternatively, it is possible column densities predicted by C^{18}O are affected by depletion, which could potentially affect the densities predicted from the HCO+ modelling (i.e. yielding lower column densities and densities). Using the SCUBA-2 850 μm data to calculate column density could potentially resolve this issue for future models. Additionally, improvements to the density models could be made so

that pixel-by-pixel fitting methods using the log-normal PDF density profiles are applied to the HCO+ data. This method would be similar to the RADEX models so that the lower and upper density limits are eliminated. This would allow density variations to be modelled across the cloud and the density distribution could be further investigated for cores and the total cloud.

Additionally, the density profile can be further improved by incorporating the power-law tail in the log-normal density PDF as described in Section 5.7.5 and observed by Kainulainen et al. [2009]. The log-normal density PDF with the inclusion of the power-law tail better describes the Ophiuchus region and other regions with active, ongoing star formation. This tail would effectively increase the peak densities higher than the log-normal PDF and potentially solve the issue that none of the current density profiles predict HCO+ emission reaching its critical density.

This method for modelling densities traced by molecular lines is not exclusive to HCO+. Other molecules with high critical densities can also be used to explore the relationship between column density and density in molecular clouds (e.g. HCN, DCO+, $H^{13}CO$). Multiple dense gas tracers with a variety of critical densities and optical depths would provide a more rounded view of densities found in the cloud. A more accurate density profile could be better constrained using a variety of molecular lines tracing different densities across the cloud.

References

A. Abergel, J. P. Bernard, F. Boulanger, C. Cesarsky, F. X. Desert, E. Falgarone, G. Lagache, M. Perault, J.-L. Puget, W. T. Reach, L. Nordh, G. Olofsson, M. Huldtgren, A. A. Kaas, P. Andre, S. Bontemps, M. Burgdorf, E. Copet, J. Davies, T. Montmerle, P. Persi, and F. Sibille. ISOCAM mapping of the ρ Ophiuchi main cloud. *A&A*, 315:L329–L332, November 1996. 84

J. E. Aguirre, A. G. Ginsburg, M. K. Dunham, M. M. Drosback, J. Bally, C. Battersby, E. T. Bradley, C. Cyganowski, D. Dowell, N. J. Evans, II, J. Glenn, P. Harvey, E. Rosolowsky, G. S. Stringfellow, J. Walawender, and J. P. Williams. The Bolocam Galactic Plane Survey: Survey Description and Data Reduction. *ApJ*, 192:4, January 2011. doi: 10.1088/0067-0049/192/1/4. 35

D. A. Allen. Infrared Objects in H II Regions. *ApJL*, 172:L55, March 1972. doi: 10.1086/180890. 96

L. Allen, X. Koenig, R. Gutermuth, and T. Megeath. Star Formation in your Back Yard: The Spitzer-Identified Young Stellar Objects within 1 kpc of the Sun. In *American Astronomical Society Meeting Abstracts #215*, volume 42 of *Bulletin of the American Astronomical Society*, page 369.01, January 2010. 165

P. Andre, T. Montmerle, E. D. Feigelson, and H. Steppe. Cold dust around young stellar objects in the Rho Ophiuchi cloud core. *A&A*, 240:321–330, December 1990. 82, 84, 91, 96

P. Andre, D. Ward-Thompson, and M. Barsony. Submillimeter continuum observations of Rho Ophiuchi A - The candidate protostar VLA 1623 and prestellar clumps. *ApJ*, 406:122–141, March 1993. doi: 10.1086/172425. 8, 9

P. Andre, D. Ward-Thompson, and F. Motte. Probing the initial conditions of star formation: the structure of the prestellar core L 1689B. *A&A*, 314:625–635, October 1996. 54

P. Andre, D. Ward-Thompson, and M. Barsony. From Prestellar Cores to Protostars: the Initial Conditions of Star Formation. *Protostars and Planets IV*, page 59, May 2000. 13, 92

P. André, J. Bouwman, A. Belloche, and P. Hennebelle. Submillimeter Studies of Prestellar Cores and Protostars: Probing the Initial Conditions for Protostellar Collapse. In C. L. Curry & M. Fich, editor, *SFChem 2002: Chemistry as a Diagnostic of Star Formation*, pages 127–+, 2003. 54

P. André, A. Men'shchikov, S. Bontemps, V. Könyves, F. Motte, N. Schneider, P. Didelon, V. Minier, P. Saraceno, D. Ward-Thompson, J. di Francesco, and G. White. From filamentary clouds to prestellar cores to the stellar IMF: Initial highlights from the Herschel Gould Belt Survey. *A&A*, 518:L102, July 2010. doi: 10.1051/0004-6361/201014666. 157, 254

H. G. Arce, D. Shepherd, F. Gueth, C.-F. Lee, R. Bachiller, A. Rosen, and H. Beuther. Molecular Outflows in Low- and High-Mass Star-forming Regions. *Protostars and Planets V*, pages 245–260, 2007. xiii, 12, 13, 14, 133

M. L. N. Ashby, E. A. Bergin, R. Plume, J. M. Carpenter, G. J. Melnick, G. Chin, N. R. Erickson, P. F. Goldsmith, M. Harwit, J. E. Howe, S. C. Kleiner, D. G. Koch, D. A. Neufeld, B. M. Patten, R. Schieder, R. L. Snell, J. R. Stauffer, V. Tolls, Z. Wang, G. Winnewisser, and Y. F. Zhang. Water Abundance and Velocity Structure in S140, ρ Oph A, and B335. *ApJL*, 539:L119–L122, August 2000. doi: 10.1086/312845. 235

F. Bacciotti, T. P. Ray, R. Mundt, J. Eislöffel, and J. Solf. Hubble Space Telescope/STIS Spectroscopy of the Optical Outflow from DG Tauri: Indications for Rotation in the Initial Jet Channel. *ApJ*, 576:222–231, September 2002. doi: 10.1086/341725. 81

J. Bally, B. Reipurth, and C. J. Davis. Observations of Jets and Outflows from Young Stars. *Protostars and Planets V*, pages 215–230, 2007. 12

A. Belloche, F. Schuller, B. Parise, P. André, J. Hatchell, J. K. Jørgensen, S. Bontemps, A. Weiß, K. M. Menten, and D. Muders. The end of star formation in Chamaeleon I?. A LABOCA census of starless and protostellar cores. *A&A*, 527: A145, March 2011. doi: 10.1051/0004-6361/201015733. vi, 256

G. A. Blake, E. C. Sutton, C. R. Masson, and T. G. Phillips. Molecular abundances in OMC-1 - The chemical composition of interstellar molecular clouds and the influence of massive star formation. *ApJ*, 315:621–645, April 1987. doi: 10.1086/165165. 136, 233, 234

R. C. Bohlin, B. D. Savage, and J. F. Drake. A survey of interstellar H I from L-alpha absorption measurements. II. *ApJ*, 224:132–142, August 1978. doi: 10.1086/156357. 175

S. Bontemps, P. Andre, S. Terebey, and S. Cabrit. Evolution of outflow activity around low-mass embedded young stellar objects. *A&A*, 311:858–872, July 1996. 84, 91, 100, 110, 116, 117, 137

M.-H. Boulard, E. Caux, J.-L. Monin, D. Nadeau, and N. Rowlands. The Flying Ghost Nebula: a remarkable circumstellar disk. *A&A*, 300:276, August 1995. 152

A. G. A. Brown, E. J. de Geus, and P. T. de Zeeuw. The Orion OB1 association. 1: Stellar content. *A&A*, 289:101–120, September 1994. 54

J. V. Buckle, R. E. Hills, H. Smith, W. R. F. Dent, and G. Bell. HARP/ACSIS: a submillimetre spectral imaging system on the James Clerk Maxwell Telescope. *MNRAS*, 399:1026–1043, October 2009. doi: 10.1111/j.1365-2966.2009.15347.x. 18, 19, 20, 37, 65, 85, 206

J. V. Buckle, E. I. Curtis, J. F. Roberts, G. J. White, J. Hatchell, C. Brunt, H. M. Butner, B. Cavanagh, A. Chrysostomou, C. J. Davis, A. Duarte-Cabral, M. Etxaluze, and J. di Francesco. The JCMT Legacy Survey of the Gould Belt: a first look at Orion B with HARP. *MNRAS*, 401:204–222, January 2010. doi: 10.1111/j.1365-2966.2009.15619.x. 15, 21, 45, 46, 48, 51, 58, 68, 128, 151

REFERENCES

R. S. Bussmann, T. W. Wong, A. S. Hedden, C. A. Kulesa, and C. K. Walker. A CO (J=3-2) Outflow Survey of the Elias 29 Region. *ApJL*, 657:L33–L36, March 2007. doi: 10.1086/513101. 91, 113, 117

S. Cabrit, A. Raga, and F. Gueth. Models of Bipolar Molecular Outflows. In B. Reipurth and C. Bertout, editors, *Herbig-Haro Flows and the Birth of Stars*, volume 182 of *IAU Symposium*, pages 163–180, 1997. 13

A. Caratti o Garatti, T. Giannini, B. Nisini, and D. Lorenzetti. H_2 active jets in the near IR as a probe of protostellar evolution. *A&A*, 449:1077–1088, April 2006. doi: 10.1051/0004-6361:20054313. 93, 100

S. Casassus, C. Dickinson, K. Cleary, R. Paladini, M. Etxaluze, T. Lim, G. J. White, M. Burton, B. Indermuehle, O. Stahl, and P. Roche. Centimetre-wave continuum radiation from the ρ Ophiuchi molecular cloud. *MNRAS*, 391:1075–1090, December 2008. doi: 10.1111/j.1365-2966.2008.13954.x. 84, 123

G. Chabrier and P. Hennebelle. Dimensional argument for the impact of turbulent support on the stellar initial mass function. *A&A*, 534:A106, October 2011. doi: 10.1051/0004-6361/201117285. 12

C. J. Chandler, S. Terebey, M. Barsony, T. J. T. Moore, and T. N. Gautier. Compact Outflows Associated with TMC-1 and TMC-1A. *ApJ*, 471:308, November 1996. doi: 10.1086/177971. 142

E. L. Chapin, D. S. Berry, A. G. Gibb, T. Jenness, D. Scott, R. P. J. Tilanus, F. Economou, and W. S. Holland. SCUBA-2: iterative map-making with the Sub-Millimetre User Reduction Facility. *MNRAS*, 430:2545–2573, April 2013. doi: 10.1093/mnras/stt052. 17

H. Chen, P. C. Myers, E. F. Ladd, and D. O. S. Wood. Bolometric temperature and young stars in the Taurus and Ophiuchus complexes. *ApJ*, 445:377–392, May 1995. doi: 10.1086/175703. 92

H. Christie, S. Viti, J. Yates, J. Hatchell, G. A. Fuller, A. Duarte-Cabral, S. Sadavoy, J. V. Buckle, S. Graves, J. Roberts, D. Nutter, C. Davis, G. J. White, M. Hogerheijde, D. Ward-Thompson, H. Butner, J. Richer, and J. Di Francesco.

CO depletion in the Gould Belt clouds. *MNRAS*, 422:968–980, May 2012. doi: 10.1111/j.1365-2966.2012.20643.x. 131, 233, 234, 237

F. Comeron, G. H. Rieke, A. Burrows, and M. J. Rieke. The Stellar Population in the rho Ophiuchi Cluster. *ApJ*, 416:185, October 1993. doi: 10.1086/173225. 96

E. I. Curtis, J. S. Richer, and J. V. Buckle. A submillimetre survey of the kinematics of the Perseus molecular cloud - I. Data. *MNRAS*, 401:455–472, January 2010a. doi: 10.1111/j.1365-2966.2009.15658.x. 85, 176

E. I. Curtis, J. S. Richer, J. J. Swift, and J. P. Williams. A submillimetre survey of the kinematics of the Perseus molecular cloud - II. Molecular outflows. *MNRAS*, 408:1516–1539, November 2010b. doi: 10.1111/j.1365-2966.2010.17214.x. 15, 48, 68, 127, 128, 131, 134, 136, 137, 151, 152, 154, 155, 253

C. J. Davis and J. Eisloeffel. Near-infrared imaging in H_2_ of molecular (CO) outflows from young stars. *A&A*, 300:851, August 1995. 85

C. J. Davis, W. R. F. Dent, H. E. Matthews, I. M. Coulson, and M. J. McCaughrean. Observations of a curving molecular outflow from V380Ori-NE: further support for prompt entrainment in protostellar outflows. *MNRAS*, 318:952–960, November 2000. doi: 10.1046/j.1365-8711.2000.03836.x. 34, 62, 65

C. J. Davis, A. Chrysostomou, J. Hatchell, J. G. A. Wouterloot, J. V. Buckle, D. Nutter, M. Fich, C. Brunt, H. Butner, B. Cavanagh, E. I. Curtis, A. Duarte-Cabral, J. di Francesco, M. Etxaluze, and P. Friberg. The JCMT Legacy Survey of the Gould Belt: a first look at Taurus with HARP. *MNRAS*, 405:759–776, June 2010a. doi: 10.1111/j.1365-2966.2010.16499.x. 21

C. J. Davis, R. Gell, T. Khanzadyan, M. D. Smith, and T. Jenness. A general catalogue of molecular hydrogen emission-line objects (MHOs) in outflows from young stars. *A&A*, 511:A24, February 2010b. doi: 10.1051/0004-6361/200913561. 85

E. J. de Geus. Interactions of stars and interstellar matter in Scorpio Centaurus. *A&A*, 262:258–270, August 1992. 145, 150

J. T. Dempsey, P. Friberg, T. Jenness, R. P. J. Tilanus, H. S. Thomas, W. S. Holland, D. Bintley, D. S. Berry, E. L. Chapin, A. Chrysostomou, G. R. Davis, A. G. Gibb, H. Parsons, and E. I. Robson. SCUBA-2: on-sky calibration using submillimetre standard sources. *MNRAS*, 430:2534–2544, April 2013. doi: 10.1093/mnras/stt090. 17, 43, 69, 70, 72, 74, 250

W. R. F. Dent, H. E. Matthews, and D. M. Walther. CO and shocked H_2 in the highly collimated outflow from VLA 1623. *MNRAS*, 277:193–209, November 1995. 85

J. Di Francesco, D. Johnstone, H. Kirk, T. MacKenzie, and E. Ledwosinska. The SCUBA Legacy Catalogues: Submillimeter-Continuum Objects Detected by SCUBA. *ApJS*, 175:277–295, March 2008. doi: 10.1086/523645. 39, 233

T. P. Downes and S. Cabrit. The mass-velocity and intensity-velocity relations in jet-driven molecular outflows. *A&A*, 403:135–140, May 2003. doi: 10.1051/0004-6361:20030363. 142, 144

E. Drabek, J. Hatchell, P. Friberg, J. Richer, S. Graves, J. V. Buckle, D. Nutter, D. Johnstone, and J. Di Francesco. Molecular line contamination in the SCUBA-2 450 and 850 μm continuum data. *MNRAS*, 426:23–39, October 2012. doi: 10.1111/j.1365-2966.2012.21140.x. 33, 69, 71, 250

G. Duchêne, J. Bouvier, S. Bontemps, P. André, and F. Motte. Multiple protostellar systems. I. A deep near infrared survey of Taurus and Ophiuchus protostellar objects. *A&A*, 427:651–665, November 2004. doi: 10.1051/0004-6361:20041209. 109

M. Dunham, T. Bourke, M. Enoch, N. Evans, T. Huard, J.-E. Lee, P. Myers, and K. Pontoppidan. A Search for Evidence of Episodic Mass Accretion: IRS and MIPS SED Mode Observations of 21 Low-Luminosity, Embedded Protostars. *Spitzer Proposal*, page 50295, March 2008. 13

J. Eislöffel, M. D. Smith, and C. J. Davis. Spectroscopy of molecular hydrogen in outflows from young stars. *A&A*, 359:1147–1161, July 2000. 93, 100

J. H. Elias. An infrared study of the Ophiuchus dark cloud. *ApJ*, 224:453, September 1978. doi: 10.1086/156393. 96

B. G. Elmegreen and Y. N. Efremov. A Universal Formation Mechanism for Open and Globular Clusters in Turbulent Gas. *ApJ*, 480:235, May 1997. doi: 10.1086/303966. 6, 201

M. L. Enoch, K. E. Young, J. Glenn, N. J. Evans, II, S. Golwala, A. I. Sargent, P. Harvey, J. Aguirre, A. Goldin, D. Haig, T. L. Huard, A. Lange, G. Laurent, P. Maloney, P. Mauskopf, P. Rossinot, and J. Sayers. Bolocam Survey for 1.1 mm Dust Continuum Emission in the c2d Legacy Clouds. I. Perseus. *ApJ*, 638: 293–313, February 2006. doi: 10.1086/498678. 46, 48, 53, 54

M. L. Enoch, N. J. Evans, II, A. I. Sargent, and J. Glenn. Properties of the Youngest Protostars in Perseus, Serpens, and Ophiuchus. *ApJ*, 692:973, February 2009. doi: 10.1088/0004-637X/692/2/973. 96

N. J. Evans, M. M. Dunham, J. K. Jørgensen, M. L. Enoch, B. Merín, E. F. van Dishoeck, J. M. Alcalá, P. C. Myers, and K. R. Stapelfeldt. The Spitzer c2d Legacy Results: Star-Formation Rates and Efficiencies; Evolution and Lifetimes. *ApJS*, 181:321–350, April 2009. doi: 10.1088/0067-0049/181/2/321. iv, 9, 11, 92, 96, 99, 118, 131, 148, 150, 151, 157, 251, 252, 253

N. J. Evans, II. Physical Conditions in Regions of Star Formation. *ARA&A*, 37: 311–362, 1999. doi: 10.1146/annurev.astro.37.1.311. 6

N. J. Evans, II, J. M. C. Rawlings, Y. L. Shirley, and L. G. Mundy. Tracing the Mass during Low-Mass Star Formation. II. Modeling the Submillimeter Emission from Preprotostellar Cores. *ApJ*, 557:193–208, August 2001. doi: 10.1086/321639. 54

J. D. Fiege and R. N. Henriksen. A global model of protostellar bipolar outflow - I. *MNRAS*, 281:1038–1054, August 1996a. 15

J. D. Fiege and R. N. Henriksen. A global model of protostellar bipolar outflow - II. *MNRAS*, 281:1055–1072, August 1996b. 15

REFERENCES

M. A. Frerking, W. D. Langer, and R. W. Wilson. The relationship between carbon monoxide abundance and visual extinction in interstellar clouds. *ApJ*, 262:590–605, November 1982. doi: 10.1086/160451. 3, 86, 121, 125, 127, 133, 234

R. K. Friesen, J. Di Francesco, Y. L. Shirley, and P. C. Myers. The Initial Conditions of Clustered Star Formation. I. NH_3 Observations of Dense Cores in Ophiuchus. *ApJ*, 697:1457–1480, June 2009. doi: 10.1088/0004-637X/697/2/1457. 158, 238

R. K. Friesen, J. Di Francesco, P. C. Myers, A. Belloche, Y. L. Shirley, T. L. Bourke, and P. André. The Initial Conditions of Clustered Star Formation. III. The Deuterium Fractionation of the Ophiuchus B2 Core. *ApJ*, 718:666–682, August 2010a. doi: 10.1088/0004-637X/718/2/666. 158, 238

R. K. Friesen, J. Di Francesco, Y. Shimajiri, and S. Takakuwa. The Initial Conditions of Clustered Star Formation. II. N_2H^+ Observations of the Ophiuchus B Core. *ApJ*, 708:1002–1024, January 2010b. doi: 10.1088/0004-637X/708/2/1002. 158, 238

T. Giannini, B. Nisini, and D. Lorenzetti. Far-Infrared Investigation of Class 0 Sources: Line Cooling. *ApJ*, 555:40–57, July 2001. doi: 10.1086/321451. 123

M. Gómez, D. P. Stark, B. A. Whitney, and E. Churchwell. Jets and Herbig-Haro Objects in the ρ Ophiuchi Embedded Cluster. *AJ*, 126:863–886, August 2003. doi: 10.1086/376741. 85, 93, 97, 99, 100, 109, 110, 113, 115, 116, 119, 150

A. A. Goodman, E. W. Rosolowsky, M. A. Borkin, J. B. Foster, M. Halle, J. Kauffmann, and J. E. Pineda. A role for self-gravity at multiple length scales in the process of star formation. *Nature*, 457:63–66, January 2009. doi: 10.1038/nature07609. 4

M. A. Gordon. Dust emission as a quantitative probe of star-forming regions. *A&A*, 301:853, September 1995. 34

G. L. Grasdalen, K. M. Strom, and S. E. Strom. A 2-MICRON Map of the Ophiuchus Dark-Cloud Region. *ApJL*, 184:L53, September 1973. doi: 10.1086/181287. 96

S. F. Graves, J. S. Richer, J. V. Buckle, and A. Duarte-Cabral. The JCMT Legacy Survey of the Gould Belt: a first look at Serpens with HARP. *MNRAS*, 409: 1412–1428, December 2010. doi: 10.1111/j.1365-2966.2010.17140.x. 15, 21, 127, 128, 131, 134, 136, 151, 153, 154, 155, 253

T. Greene. Infrared Studies of Protostellar Binaries. In M. G. Burton, R. Jayawardhana, & T. L. Bourke, editor, *Star Formation at High Angular Resolution*, volume 221 of *IAU Symposium*, pages 223–+, September 2004. 9, 96

T. P. Greene and E. T. Young. Near-infrared observations of young stellar objects in the Rho Ophiuchi dark cloud. *ApJ*, 395:516–528, August 1992. doi: 10.1086/171672. 96

T. P. Greene, B. A. Wilking, P. Andre, E. T. Young, and C. J. Lada. Further mid-infrared study of the rho Ophiuchi cloud young stellar population: Luminosities and masses of pre-main-sequence stars. *ApJ*, 434:614–626, October 1994. doi: 10.1086/174763. 92

T. D. Groesbeck, T. G. Phillips, and G. A. Blake. The molecular emission-line spectrum of IRC +10216 between 330 and 358 GHz. *ApJS*, 94:147–162, August 1994. doi: 10.1086/192076. 66

N. Grosso, J. Alves, R. Neuhäuser, and T. Montmerle. Discovery of new embedded Herbig-Haro objects in the rho Ophiuchi dark cloud. *A&A*, 380:L1–L4, December 2001. doi: 10.1051/0004-6361:20011503. 85, 93, 97, 109

F. Gueth, R. Bachiller, and M. Tafalla. Dust emission from young outflows: The case of L 1157. *A&A*, 401:L5–L8, April 2003. doi: 10.1051/0004-6361:20030259. 65, 67

K. E. Haisch, Jr., M. Barsony, M. E. Ressler, and T. P. Greene. Mid-Infrared Observations of Class I/Flat-Spectrum Systems in Six Nearby Molecular Clouds. *AJ*, 132:2675–2684, December 2006. doi: 10.1086/508651. 109

T. J. Harries. Synthetic line profiles of rotationally distorted hot-star winds. *MNRAS*, 315:722–734, July 2000. doi: 10.1046/j.1365-8711.2000.03505.x. 183, 255

L. Hartmann. Accretion disks of young stars. In R. Ignace and K. G. Gayley, editors, *The Nature and Evolution of Disks Around Hot Stars*, volume 337 of *Astronomical Society of the Pacific Conference Series*, page 3, November 2005. 11

L. Hartmann. *Accretion Processes in Star Formation: Second Edition*. Cambridge University Press, 2009a. 8

L. Hartmann. *Accretion Processes in Star Formation: Second Edition*. Cambridge University Press, 2009b. 4, 11

J. Hatchell and M. M. Dunham. Star formation in Perseus. V. Outflows detected by HARP. *A&A*, 502:139–153, July 2009. doi: 10.1051/0004-6361/200911818. 34, 59, 65

J. Hatchell, G. A. Fuller, and E. F. Ladd. Temperature predictions for protostellar outflows. *A&A*, 344:687–695, April 1999a. 68, 123, 134

J. Hatchell, H. Roberts, and T. J. Millar. Limits on HDS/H_2S abundance ratios in hot molecular cores. *A&A*, 346:227–232, June 1999b. 123

J. Hatchell, J. S. Richer, G. A. Fuller, C. J. Qualtrough, E. F. Ladd, and C. J. Chandler. Star formation in Perseus. Clusters, filaments and the conditions for star formation. *A&A*, 440:151–161, September 2005. doi: 10.1051/0004-6361:20041836. vi, 48, 69, 162, 256

J. Hatchell, G. A. Fuller, and J. S. Richer. Star formation in Perseus. III. Outflows. *A&A*, 472:187–198, September 2007a. doi: 10.1051/0004-6361:20066467. 58, 59, 92, 136

J. Hatchell, G. A. Fuller, J. S. Richer, T. J. Harries, and E. F. Ladd. Star formation in Perseus. II. SEDs, classification, and lifetimes. *A&A*, 468:1009–1024, June 2007b. doi: 10.1051/0004-6361:20066466. 46, 48, 49, 52, 53, 54, 79

J. Hatchell, S. Terebey, T. Huard, E. E. Mamajek, L. Allen, T. L. Bourke, M. M. Dunham, R. Gutermuth, P. M. Harvey, J. K. Jørgensen, B. Merín, A. Noriega-Crespo, and D. E. Peterson. The Spitzer Survey of Interstellar Clouds in the Gould Belt. V. Ophiuchus North Observed with IRAC and MIPS. *ApJ*, 754:104, August 2012. doi: 10.1088/0004-637X/754/2/104. 145

J. Hatchell, T. Wilson, E. Drabek, E. Curtis, J. Richer, D. Nutter, J. Di Francesco, D. Ward-Thompson, and JCMT GBS Consortium. The JCMT Gould Belt Survey: SCUBA-2 observations of radiative feedback in NGC 1333. *MNRAS*, 429:L10–L14, February 2013. doi: 10.1093/mnrasl/sls015. 33, 70, 71, 72, 75, 250, 251

P. Hennebelle and G. Chabrier. Analytical Theory for the Initial Mass Function: CO Clumps and Prestellar Cores. *ApJ*, 684:395–410, September 2008. doi: 10.1086/589916. 12

P. Hennebelle and G. Chabrier. Analytical Theory for the Initial Mass Function. II. Properties of the Flow. *ApJ*, 702:1428–1442, September 2009. doi: 10.1088/0004-637X/702/2/1428. 12

J. F. W. Herschel, Sir. *Results of astronomical observations made during the years 1834, 5, 6, 7, 8, at the Cape of Good Hope; being the completion of a telescopic survey of the whole surface of the visible heavens, commenced in 1825*. 1847. 3

R. H. Hildebrand. The Determination of Cloud Masses and Dust Characteristics from Submillimetre Thermal Emission. *QJRAS*, 24:267–+, September 1983a. 53

R. H. Hildebrand. The Determination of Cloud Masses and Dust Characteristics from Submillimetre Thermal Emission. *qjras*, 24:267–+, September 1983b. 3

M. R. Hogerheijde and F. F. S. van der Tak. An accelerated Monte Carlo method to solve two-dimensional radiative transfer and molecular excitation. *ArXiv Astrophysics e-prints*, August 2000. 185

W. Holland, W. Duncan, and M. Griffin. Bolometers for Submillimeter and Millimeter Astronomy. In S. Stanimirovic, D. Altschuler, P. Goldsmith, & C. Salter, editor, *Single-Dish Radio Astronomy: Techniques and Applications*, volume 278 of *Astronomical Society of the Pacific Conference Series*, pages 463–491, December 2002. 34

W. S. Holland, D. Bintley, E. L. Chapin, A. Chrysostomou, G. R. Davis, J. T. Dempsey, W. D. Duncan, M. Fich, P. Friberg, M. Halpern, K. D. Irwin, T. Jenness, B. D. Kelly, M. J. MacIntosh, E. I. Robson, D. Scott, P. A. R. Ade, and E. and Atad-Ettedgui. SCUBA-2: the 10 000 pixel bolometer camera on

the James Clerk Maxwell Telescope. *MNRAS*, 430:2513–2533, April 2013. doi: 10.1093/mnras/sts612. 17, 18

T. Jenness, B. Cavanagh, F. Economou, and D. S. Berry. JCMT Science Archive: Advanced Heterodyne Data Products Pipeline. In R. W. Argyle, P. S. Bunclark, and J. R. Lewis, editors, *Astronomical Data Analysis Software and Systems XVII*, volume 394 of *Astronomical Society of the Pacific Conference Series*, page 565, August 2008. 158

D. Johnstone and J. Bally. JCMT/SCUBA Submillimeter Wavelength Imaging of the Integral-shaped Filament in Orion. *ApJL*, 510:L49–L53, January 1999. doi: 10.1086/311792. 34

D. Johnstone and J. Bally. Large-Area Mapping at 850 μm. V. Analysis of the Clump Distribution in the Orion A South Molecular Cloud. *ApJ*, 653:383–397, December 2006. doi: 10.1086/508852. 54

D. Johnstone, C. D. Wilson, G. Moriarty-Schieven, G. Joncas, G. Smith, E. Gregersen, and M. Fich. Large-Area Mapping at 850 Microns. II. Analysis of the Clump Distribution in the ρ Ophiuchi Molecular Cloud. *ApJ*, 545:327–339, December 2000. doi: 10.1086/317790. 52, 176, 254

D. Johnstone, A. M. S. Boonman, and E. F. van Dishoeck. Astrochemistry of submillimeter sources in Orion. Studying the variations of molecular tracers with changing physical conditions. *A&A*, 412:157–174, December 2003. doi: 10.1051/0004-6361:20031370. 34, 62, 65, 66

D. Johnstone, J. Di Francesco, and H. Kirk. An Extinction Threshold for Protostellar Cores in Ophiuchus. *ApJL*, 611:L45–L48, August 2004. doi: 10.1086/423737. 162, 240

J. K. Jørgensen, D. Johnstone, H. Kirk, P. C. Myers, L. E. Allen, and Y. L. Shirley. Current Star Formation in the Ophiuchus and Perseus Molecular Clouds: Constraints and Comparisons from Unbiased Submillimeter and Mid-Infrared Surveys. II. *ApJ*, 683:822–843, August 2008. doi: 10.1086/589956. 253, 256

J. K. Jørgensen, E. F. van Dishoeck, R. Visser, T. L. Bourke, D. J. Wilner, D. Lommen, M. R. Hogerheijde, and P. C. Myers. PROSAC: a submillimeter array survey of low-mass protostars. II. The mass evolution of envelopes, disks, and stars from the Class 0 through I stages. *A&A*, 507:861–879, November 2009. doi: 10.1051/0004-6361/200912325. 84, 91, 109

J. Kainulainen, H. Beuther, T. Henning, and R. Plume. Probing the evolution of molecular cloud structure. From quiescence to birth. *A&A*, 508:L35–L38, December 2009. doi: 10.1051/0004-6361/200913605. 157, 182, 200, 238, 255, 257

Y. Kamata, K. Koyama, Y. Tsuboi, and S. Yamauchi. X-Ray Analysis of the rho Ophiuchi Dark Cloud with ASCA: Source Identification, X-Ray Spectra, and Temporal Variability. *PASJ*, 49:461–470, August 1997. 115

T. Kamazaki, M. Saito, N. Hirano, and R. Kawabe. Millimeter-Wave Interferometric Study of the ρ Ophiuchi A Region. I. Small-Scale Structures of Dust Continuum Sources. *ApJ*, 548:278–287, February 2001. doi: 10.1086/318668. 105

T. Kamazaki, M. Saito, N. Hirano, T. Umemoto, and R. Kawabe. Molecular Outflow Search in the ρ Ophiuchi A and B2 Regions. *ApJ*, 584:357–367, February 2003. doi: 10.1086/345659. 84, 91, 92, 93, 99, 101

T. Khanzadyan, R. Gredel, M. D. Smith, and T. Stanke. An unbiased search for the signatures of protostars in the ρ Ophiuchi A molecular cloud. I. Near-infrared observations. *A&A*, 426:171–183, October 2004. doi: 10.1051/0004-6361:20041241. 93, 97, 100, 106, 109, 110, 117

H. Kirk, D. Johnstone, and J. Di Francesco. The Large- and Small-Scale Structures of Dust in the Star-forming Perseus Molecular Cloud. *ApJ*, 646:1009–1023, August 2006. doi: 10.1086/503193. 52, 54

L. B. G. Knee and G. Sandell. The molecular outflows in NGC 1333. *A&A*, 361: 671–684, September 2000. 152

J. Knude and E. Hog. Interstellar reddening from the HIPPARCOS and TYCHO catalogues. I. Distances to nearby molecular clouds and star forming regions. *A&A*, 338:897–904, October 1998. 82

A. Kolmogorov. The Local Structure of Turbulence in Incompressible Viscous Fluid for Very Large Reynolds' Numbers. *Akademiia Nauk SSSR Doklady*, 30:301–305, 1941. 7

P. Kroupa. The Local Stellar Initial Mass Function. In S. Deiters, B. Fuchs, A. Just, R. Spurzem, and R. Wielen, editors, *Dynamics of Star Clusters and the Milky Way*, volume 228 of *Astronomical Society of the Pacific Conference Series*, page 187, 2001. 12

M. R. Krumholz and T. A. Thompson. The Relationship between Molecular Gas Tracers and Kennicutt-Schmidt Laws. *ApJ*, 669:289–298, November 2007. doi: 10.1086/521642. 201

C. A. Kulesa, A. L. Hungerford, C. K. Walker, X. Zhang, and A. P. Lane. Large-Scale CO and [C I] Emission in the ρ Ophiuchi Molecular Cloud. *ApJ*, 625:194–209, May 2005. doi: 10.1086/426096. 84, 233, 235, 236

C. J. Lada. Star formation - From OB associations to protostars. In M. Peimbert & J. Jugaku, editor, *Star Forming Regions*, volume 115 of *IAU Symposium*, pages 1–17, 1987. 9

C. J. Lada and M. Fich. The Structure and Energetics of a Highly Collimated Bipolar Outflow: NGC 2264G. *ApJ*, 459:638, March 1996. doi: 10.1086/176929. 142

C. J. Lada, J. Alves, and E. A. Lada. Near-Infrared Imaging of Embedded Clusters: NGC 1333. *AJ*, 111:1964–+, May 1996. doi: 10.1086/117933. 48

E. F. Ladd, G. A. Fuller, and J. R. Deane. C 18O and C 17O Observations of Embedded Young Stars in the Taurus Molecular Cloud. I. Integrated Intensities and Column Densities. *ApJ*, 495:871, March 1998. doi: 10.1086/305313. 125

R. B. Larson. Turbulence and star formation in molecular clouds. *MNRAS*, 194: 809–826, March 1981. 8

R. Launhardt, P. G. Mezger, C. G. T. Haslam, E. Kreysa, R. Lemke, A. Sievers, and R. Zylka. Dust emission from star-forming regions. IV. Dense cores in the Orion B molecular cloud. *A&A*, 312:569–584, August 1996. 54

J. A. Leous, E. D. Feigelson, P. Andre, and T. Montmerle. A rich cluster of radio stars in the Rho Ophiuchi cloud cores. *ApJ*, 379:683–688, October 1991. doi: 10.1086/170542. 96

R. Liseau, G. J. White, B. Larsson, S. Sidher, G. Olofsson, A. Kaas, L. Nordh, E. Caux, D. Lorenzetti, S. Molinari, B. Nisini, and F. Sibille. Looking at the bright side of the rho Ophiuchi dark cloud. Far infrared spectrophotometric observations of the rho Oph cloud with the ISO. *A&A*, 344:342–354, April 1999. 84

L. Loinard, R. M. Torres, A. J. Mioduszewski, and L. F. Rodríguez. A Preliminary VLBA Distance to the Core of Ophiuchus, with an Accuracy of 4%. *ApJL*, 675: L29–L32, March 2008. doi: 10.1086/529548. 82

M. Lombardi, C. J. Lada, and J. Alves. 2MASS wide field extinction maps. II. The Ophiuchus and the Lupus cloud complexes. *A&A*, 489:143–156, October 2008. doi: 10.1051/0004-6361:200810070. 82, 200, 255

R. B. Loren. The cobwebs of Ophiuchus. I - Strands of (C-13)O - The mass distribution. *ApJ*, 338:902–924, March 1989. doi: 10.1086/167244. 129, 153

R. B. Loren and A. Wootten. A massive prestellar molecular core and adjacent compression front in the Rho Ophiuchi cloud. *ApJ*, 306:142–159, July 1986. doi: 10.1086/164327. 131, 150

B. T. Lynds. Catalogue of Dark Nebulae. *ApJS*, 7:1, May 1962. doi: 10.1086/190072. 82

M.-M. Mac Low. The Energy Dissipation Rate of Supersonic, Magnetohydrodynamic Turbulence in Molecular Clouds. *ApJ*, 524:169–178, October 1999. doi: 10.1086/307784. 8

M.-M. Mac Low and R. S. Klessen. Control of star formation by supersonic turbulence. *Reviews of Modern Physics*, 76:125–194, January 2004. doi: 10.1103/RevModPhys.76.125. 8, 15, 201, 251

I. MacLaren, K. M. Richardson, and A. W. Wolfendale. Corrections to virial estimates of molecular cloud masses. *ApJ*, 333:821–825, October 1988. doi: 10.1086/166791. 128

E. E. Mamajek. On the distance to the Ophiuchus star-forming region. *Astronomische Nachrichten*, 329:10, January 2008. doi: 10.1002/asna.200710827. 82

H. Maruta, F. Nakamura, R. Nishi, N. Ikeda, and Y. Kitamura. Physical Properties of Dense Cores in the ρ Ophiuchi Main Cloud and a Significant Role of External Pressures in Clustered Star Formation. *ApJ*, 714:680–698, May 2010. doi: 10.1088/0004-637X/714/1/680. 158

C. R. Masson and L. M. Chernin. Properties of jet-driven molecular outflows. *ApJ*, 414:230–241, September 1993. doi: 10.1086/173071. 13, 142

C. D. Matzner. Protostellar Outflow-driven Turbulence. *ApJ*, 659:1394–1403, April 2007. doi: 10.1086/512361. 153

G. E. Miller and J. M. Scalo. The initial mass function and stellar birthrate in the solar neighborhood. *ApJS*, 41:513–547, November 1979. doi: 10.1086/190629. 12

G. F. Mitchell, D. Johnstone, G. Moriarty-Schieven, M. Fich, and N. F. H. Tothill. A Submillimeter Dust and Gas Study of the Orion B Molecular Cloud. *ApJ*, 556: 215–229, July 2001. doi: 10.1086/321574. 54

F. Motte, P. Andre, and R. Neri. The initial conditions of star formation in the rho Ophiuchi main cloud: wide-field millimeter continuum mapping. *A&A*, 336: 150–172, August 1998. xiv, 12, 89, 90

F. Motte, P. André, D. Ward-Thompson, and S. Bontemps. A SCUBA survey of the NGC 2068/2071 protoclusters. *A&A*, 372:L41–L44, June 2001. doi: 10.1051/0004-6361:20010543. 46, 61, 62, 65, 82, 83

T. C. Mouschovias and G. E. Ciolek. Magnetic Fields and Star Formation: A Theory Reaching Adulthood. In C. J. Lada & N. D. Kylafis, editor, *NATO ASIC Proc. 540: The Origin of Stars and Planetary Systems*, pages 305–+, 1999. 7

N. M. Murillo and S.-P. Lai. Disentangling the Entangled: Observations and Analysis of the Triple Non-coeval Protostellar System VLA1623. *ApJL*, 764:L15, February 2013. doi: 10.1088/2041-8205/764/1/L15. 99

P. C. Myers. Growth of an Initial Mass Function Cluster in a Turbulent Dense Core. *ApJL*, 530:L119–L122, February 2000. doi: 10.1086/312495. 7

P. C. Myers and D. Mardones. Young Protostars and Inward Motions in Low-Mass Dense Cores. In J. Yun & L. Liseau, editor, *Star Formation with the Infrared Space Observatory*, volume 132 of *Astronomical Society of the Pacific Conference Series*, pages 173–+, 1998. 7

P. C. Myers, R. A. Linke, and P. J. Benson. Dense cores in dark clouds. I - CO observations and column densities of high-extinction regions. *ApJ*, 264:517–537, January 1983. doi: 10.1086/160619. 122, 125

P. C. Myers, D. Mardones, M. Tafalla, J. P. Williams, and D. J. Wilner. A Simple Model of Spectral-Line Profiles from Contracting Clouds. *ApJL*, 465:L133, July 1996. doi: 10.1086/310146. 157

N. Nakagawa. Interstellar Molecules on Dust Mantles. In B. H. Andrew, editor, *Interstellar Molecules*, volume 87 of *IAU Symposium*, page 365, 1980. 233

F. Nakamura and Z.-Y. Li. Protostellar Turbulence Driven by Collimated Outflows. *ApJ*, 662:395–412, June 2007. doi: 10.1086/517515. 15, 153

F. Nakamura, Y. Kamada, T. Kamazaki, R. Kawabe, Y. Kitamura, Y. Shimajiri, T. Tsukagoshi, K. Tachihara, T. Akashi, K. Azegami, N. Ikeda, Y. Kurono, Z.-Y. Li, T. Miura, R. Nishi, and T. Umemoto. The Molecular Outflows in the ρ Ophiuchi Main Cloud: Implications for Turbulence Generation. *ApJ*, 726:46, January 2011. doi: 10.1088/0004-637X/726/1/46. x, 13, 84, 91, 113, 129, 131, 148, 149, 151, 153, 155, 252

B. Nisini, M. Benedettini, T. Giannini, C. Codella, D. Lorenzetti, A. M. di Giorgio, and J. S. Richer. Far infrared mapping of the gas cooling along the L1448 outflow. *A&A*, 360:297–310, August 2000. 123

D. Nutter and D. Ward-Thompson. A SCUBA survey of Orion - the low-mass end of the core mass function. *MNRAS*, 374:1413–1420, February 2007. doi: 10.1111/j.1365-2966.2006.11246.x. 48, 50, 51, 54, 61, 62, 79

D. Nutter, D. Ward-Thompson, and P. André. A SCUBA survey of L1689 - the dog that didn't bark. *MNRAS*, 368:1833–1842, June 2006. doi: 10.1111/j.1365-2966.2006.10249.x. 145

T. Onishi, A. Mizuno, A. Kawamura, H. Ogawa, and Y. Fukui. A C 18O Survey of Dense Cloud Cores in Taurus: Star Formation. *ApJ*, 502:296–+, July 1998. doi: 10.1086/305867. 157, 240, 254

V. Ossenkopf and T. Henning. Dust opacities for protostellar cores. *A&A*, 291: 943–959, November 1994. 54

J. Ostriker. On the Oscillations and the Stability of a Homogeneous Compressible Cylinder. *ApJ*, 140:1529, November 1964. doi: 10.1086/148057. 157

D. L. Padgett, L. M. Rebull, K. R. Stapelfeldt, N. L. Chapman, S.-P. Lai, L. G. Mundy, N. J. Evans, II, T. Y. Brooke, L. A. Cieza, W. J. Spiesman, A. Noriega-Crespo, C.-E. McCabe, and L. E. Allen. The Spitzer c2d Survey of Large, Nearby, Interstellar Clouds. VII. Ophiuchus Observed with MIPS. *ApJ*, 672:1013–1037, January 2008. doi: 10.1086/523883. 92, 96

P. Padoan and Å. Nordlund. The Stellar Initial Mass Function from Turbulent Fragmentation. *ApJ*, 576:870–879, September 2002. doi: 10.1086/341790. 12

P. Padoan and Å. Nordlund. The "Mysterious" Origin of Brown Dwarfs. *ApJ*, 617: 559–564, December 2004. doi: 10.1086/345413. 12

P. Padoan, A. Goodman, B. T. Draine, M. Juvela, AA. Nordlund, and Ö. E. Rögnvaldsson. Theoretical Models of Polarized Dust Emission from Protostellar Cores. *ApJ*, 559:1005–1018, October 2001. doi: 10.1086/322504. 12

P. P. Papadopoulos and M. L. Allen. Gas and Dust in NGC 7469: Submillimeter Imaging and CO J=3-2. *ApJ*, 537:631–637, July 2000. doi: 10.1086/309066. 34

D. J. Price and M. R. Bate. The effect of magnetic fields on star cluster formation. *MNRAS*, 385:1820–1834, April 2008. doi: 10.1111/j.1365-2966.2008.12976.x. 7

D. J. Price, C. Federrath, and C. M. Brunt. The Density Variance-Mach Number Relation in Supersonic, Isothermal Turbulence. *ApJL*, 727:L21, January 2011. doi: 10.1088/2041-8205/727/1/L21. 201, 206

A. C. Quillen, S. L. Thorndike, A. Cunningham, A. Frank, R. A. Gutermuth, E. G. Blackman, J. L. Pipher, and N. Ridge. Turbulence Driven by Outflow-blown Cavities in the Molecular Cloud of NGC 1333. *ApJ*, 632:941–955, October 2005. doi: 10.1086/444410. 256

A. Raga and S. Cabrit. Molecular outflows entrained by jet bowshocks. *A&A*, 278: 267–278, October 1993. 13

L. M. Rebull, S. C. Wolff, and S. E. Strom. Stellar Rotation in Young Clusters: The First 4 Million Years. *AJ*, 127:1029–1051, February 2004. doi: 10.1086/380931. 82

M. A. Reid and C. D. Wilson. High-Mass Star Formation. I. The Mass Distribution of Submillimeter Clumps in NGC 7538. *ApJ*, 625:891–905, June 2005. doi: 10.1086/429790. 52

J. S. Richer, R. E. Hills, R. Padman, and A. P. G. Russell. High-resolution molecular line observations of the core and outflow in Orion B. *MNRAS*, 241:231–246, November 1989. 46

J. S. Richer, D. S. Shepherd, S. Cabrit, R. Bachiller, and E. Churchwell. Molecular Outflows from Young Stellar Objects. *Protostars and Planets IV*, page 867, May 2000. 13, 142, 145

G. H. Rieke and M. J. Lebofsky. The interstellar extinction law from 1 to 13 microns. *ApJ*, 288:618–621, January 1985. doi: 10.1086/162827. 200

T. P. Robitaille and B. A. Whitney. The Present-Day Star Formation Rate of the Milky Way Determined from Spitzer-Detected Young Stellar Objects. *ApJL*, 710: L11–L15, February 2010. doi: 10.1088/2041-8205/710/1/L11. 6

T. P. Robitaille, B. A. Whitney, R. Indebetouw, K. Wood, and P. Denzmore. Interpreting Spectral Energy Distributions from Young Stellar Objects. I. A

Grid of 200,000 YSO Model SEDs. *ApJS*, 167:256–285, December 2006. doi: 10.1086/508424. 11, 12

L. F. Rodriguez, P. Carral, P. T. P. Ho, and J. M. Moran. Anisotropic mass outflow in regions of star formation. *ApJ*, 260:635–646, September 1982. doi: 10.1086/160285. 142

K. Rohlfs and T. L. Wilson. *Tools of radio astronomy*. 2000. 3, 127

K. Rohlfs and T. L. Wilson. *Tools of radio astronomy*. 2004. 20, 22

S. I. Sadavoy, J. Di Francesco, D. Johnstone, M. J. Currie, E. Drabek, J. Hatchell, D. Nutter, P. André, D. Arzoumanian, M. Benedettini, J.-P. Bernard, A. Duarte-Cabral, C. Fallscheer, R. Friesen, J. Greaves, M. Hennemann, T. Hill, T. Jenness, V. Könyves, B. Matthews, J. C. Mottram, S. Pezzuto, A. Roy, K. Rygl, N. Schneider-Bontemps, L. Spinoglio, L. Testi, N. Tothill, D. Ward-Thompson, G. White, t. JCMT, and Herschel Gould Belt Survey Teams. The Herschel and JCMT Gould Belt Surveys: Constraining Dust Properties in the Perseus B1 Clump with PACS, SPIRE, and SCUBA-2. *ApJ*, 767:126, April 2013. doi: 10.1088/0004-637X/767/2/126. 33, 70, 71, 72, 73, 75, 251

E. E. Salpeter. The Luminosity Function and Stellar Evolution. *ApJ*, 121:161, January 1955. doi: 10.1086/145971. 12

E. Seaquist, L. Yao, L. Dunne, and H. Cameron. Revised masses of dust and gas of SCUBA Local Universe Survey far-infrared bright galaxies based on a recent CO survey. *MNRAS*, 349:1428–1434, April 2004. doi: 10.1111/j.1365-2966.2004.07612.x. 34, 37, 53

Y. Sekimoto, K. Tatematsu, T. Umemoto, K. Koyama, Y. Tsuboi, N. Hirano, and S. Yamamoto. Molecular Outflows from X-Ray–Emitting Protostars in the rho Ophiuchi Dark Cloud. *ApJL*, 489:L63, November 1997. doi: 10.1086/310961. 84, 91, 92, 106, 110, 115, 251

E. Serabyn and E. W. Weisstein. Fourier Transform Spectroscopy of the Orion Molecular Cloud Core. *ApJ*, 451:238–+, September 1995. doi: 10.1086/176215. 66

Y. L. Shirley, N. J. Evans, II, and J. M. C. Rawlings. Tracing the Mass during Low-Mass Star Formation. III. Models of the Submillimeter Dust Continuum Emission from Class 0 Protostars. *ApJ*, 575:337–353, August 2002. doi: 10.1086/341286. 54

F. H. Shu, F. C. Adams, and S. Lizano. Star formation in molecular clouds - Observation and theory. *ARAA*, 25:23–81, 1987. doi: 10.1146/annurev.aa.25.090187.000323. 7

R. J. Simpson, D. Nutter, and D. Ward-Thompson. The initial conditions of star formation - VIII. An observational study of the Ophiuchus cloud L1688 and implications for the pre-stellar core mass function. *MNRAS*, 391:205–214, November 2008. doi: 10.1111/j.1365-2966.2008.13750.x. 162, 169, 170, 239

R. J. Simpson, D. Johnstone, D. Nutter, D. Ward-Thompson, and A. P. Whitworth. The initial conditions of isolated star formation - X. A suggested evolutionary diagram for pre-stellar cores. *MNRAS*, 417:216–227, October 2011. doi: 10.1111/j.1365-2966.2011.19163.x. 158

M. D. Smith, G. Suttner, and H. W. Yorke. Numerical hydrodynamic simulations of jet-driven bipolar outflows. *A&A*, 323:223–230, July 1997. 145

R. L. Snell, J. E. Howe, M. L. N. Ashby, E. A. Bergin, G. Chin, N. R. Erickson, P. F. Goldsmith, M. Harwit, S. C. Kleiner, D. G. Koch, D. A. Neufeld, B. M. Patten, R. Plume, R. Schieder, J. R. Stauffer, V. Tolls, Z. Wang, G. Winnewisser, Y. F. Zhang, and G. J. Melnick. Water Abundance in Molecular Cloud Cores. *ApJL*, 539:L101–L105, August 2000. doi: 10.1086/312848. 235

T. P. Snow, J. D. Destree, and D. E. Welty. A Study of the ρ Ophiuchi Cloud: Mapping the Distribution and the Motions of Interstellar Gas. *ApJ*, 679:512–530, May 2008. doi: 10.1086/587132. 82

S. W. Stahler. The kinematics of molecular outflows. *ApJ*, 422:616–620, February 1994. doi: 10.1086/173754. 13, 142, 144

S. W. Stahler and F. Palla. *The Formation of Stars*. 2005. 22, 26

T. Stanke, M. D. Smith, R. Gredel, and T. Khanzadyan. An unbiased search for the signatures of protostars in the ρ Ophiuchi molecular cloud . II. Millimetre continuum observations. *A&A*, 447:609–622, February 2006. doi: 10.1051/0004-6361:20041331. 162, 169, 239

J. M. Stone, E. C. Ostriker, and C. F. Gammie. Dissipation in Compressible Magnetohydrodynamic Turbulence. *ApJL*, 508:L99–L102, November 1998. doi: 10.1086/311718. 8

K. Tachihara, A. Mizuno, and Y. Fukui. $C^{18}O$ Observations of the Dense Cloud Cores and Star Formation in Ophiuchus. *ApJ*, 528:817–840, January 2000. doi: 10.1086/308189. 129, 153

S. Terebey, S. N. Vogel, and P. C. Myers. High-resolution CO observations of young low-mass stars. *ApJ*, 340:472–478, May 1989. doi: 10.1086/167410. 117

A. G. G. M. Tielens. *Origin and Evolution of the Interstellar Medium*, pages 271–+. 2009. doi: 10.1007/978-1-4020-9457-6_11. 3

R. M. Torres. *Measuring Nearby Star Forming Regions with the VLBA: from the Distance to the Dynamics*. PhD thesis, PhD Thesis, 2010, 2010. 82

N. F. H. Tothill, G. J. White, H. E. Matthews, W. H. McCutcheon, M. J. McCaughrean, and M. A. Kenworthy. The Structure and Evolution of the Lagoon Nebula. I. Submillimeter Continuum and CO Line Mapping. *ApJ*, 580:285–304, November 2002. doi: 10.1086/343068. 34, 66, 67

N. van der Marel, L. E. Kristensen, R. Visser, J. C. Mottram, U. A. Yıldız, and E. F. van Dishoeck. Outflow forces of low-mass embedded objects in Ophiuchus: a quantitative comparison of analysis methods. *A&A*, 556:A76, August 2013. doi: 10.1051/0004-6361/201220717. 84, 91, 106, 110, 113, 115

F. F. S. van der Tak, J. H. Black, F. L. Schöier, D. J. Jansen, and E. F. van Dishoeck. A computer program for fast non-LTE analysis of interstellar line spectra. With diagnostic plots to interpret observed line intensity ratios. *A&A*, 468:627–635, June 2007. doi: 10.1051/0004-6361:20066820. v, 174, 185, 254

T. A. van Kempen, E. F. van Dishoeck, R. Güsten, L. E. Kristensen, P. Schilke, M. R. Hogerheijde, W. Boland, K. M. Menten, and F. Wyrowski. APEX-CHAMP$^+$ high-J CO observations of low-mass young stellar objects. II. Distribution and origin of warm molecular gas. *A&A*, 507:1425–1442, December 2009. doi: 10.1051/0004-6361/200912507. 68, 157, 158, 162, 176

F. J. Vrba. Role of magnetic fields in the evolution of five dark cloud complexes. *AJ*, 82:198–208, March 1977. doi: 10.1086/112031. 131, 150

D. Ward-Thompson. Isolated Star Formation: From Cloud Formation to Core Collapse. *Science*, 295:76–81, January 2002. doi: 10.1126/science.1067354. 3

D. Ward-Thompson, F. Motte, and P. Andre. The initial conditions of isolated star formation - III. Millimetre continuum mapping of pre-stellar cores. *MNRAS*, 305: 143–150, May 1999. doi: 10.1046/j.1365-8711.1999.02412.x. 54

D. Ward-Thompson, J. Di Francesco, J. Hatchell, M. R. Hogerheijde, D. Nutter, P. Bastien, S. Basu, I. Bonnell, J. Bowey, and C. Brunt. The James Clerk Maxwell Telescope Legacy Survey of Nearby Star-forming Regions in the Gould Belt. *PASP*, 119:855–870, August 2007a. doi: 10.1086/521277. 18

D. Ward-Thompson, J. Di Francesco, J. Hatchell, M. R. Hogerheijde, D. Nutter, P. Bastien, S. Basu, I. Bonnell, J. Bowey, C. Brunt, J. Buckle, H. Butner, B. Cavanagh, A. Chrysostomou, E. Curtis, and C. J. Davis. The James Clerk Maxwell Telescope Legacy Survey of Nearby Star-forming Regions in the Gould Belt. *pasp*, 119:855–870, August 2007b. doi: 10.1086/521277. xiii, 4, 21, 251

D. Ward-Thompson, J. M. Kirk, J. S. Greaves, and P. André. The immediate environment of the Class 0 protostar VLA 1623, on scales of 50-100 au, observed at millimetre and centimetre wavelengths. *MNRAS*, 415: 2812–2817, August 2011. doi: 10.1111/j.1365-2966.2011.18898.x. 13, 99

B. A. Whitney, K. Wood, J. E. Bjorkman, and M. J. Wolff. Two-dimensional Radiative Transfer in Protostellar Envelopes. I. Effects of Geometry on Class I Sources. *ApJ*, 591:1049–1063, July 2003. doi: 10.1086/375415. 9, 10, 11

B. A. Wilking and C. J. Lada. The discovery of new embedded sources in the centrally condensed core of the Rho Ophiuchi dark cloud - The formation of a bound cluster. *ApJ*, 274:698–716, November 1983. doi: 10.1086/161482. 96

B. A. Wilking, R. D. Schwartz, T. M. Fanetti, and E. D. Friel. Herbig-Haro Objects in the ρ Ophiuchi Cloud. *PASP*, 109:549–553, May 1997. doi: 10.1086/133912. 85

B. A. Wilking, M. R. Meyer, T. P. Greene, A. Mikhail, and G. Carlson. Low-Mass Stars and Substellar Objects in the NGC 1333 Molecular Cloud. *AJ*, 127: 1131–1146, February 2004. doi: 10.1086/381482. 48

T. L. Wilson. Introduction to Millimeter/Sub-Millimeter Astronomy. *ArXiv e-prints*, March 2009. 69

T. L. Wilson and R. Rood. Abundances in the Interstellar Medium. *ARAA*, 32: 191–226, 1994. doi: 10.1146/annurev.aa.32.090194.001203. 86, 121, 133, 134

J. E. Ybarra, M. Barsony, K. E. Haisch, Jr., T. H. Jarrett, R. Sahai, and A. J. Weinberger. First Evidence of a Precessing Jet Excavating a Protostellar Envelope. *ApJL*, 647:L159–L162, August 2006. doi: 10.1086/507449. 93, 97, 110

U. A. Yıldız, E. F. van Dishoeck, L. E. Kristensen, R. Visser, J. K. Jørgensen, G. J. Herczeg, T. A. van Kempen, M. R. Hogerheijde, and S. D. Doty. Herschel/HIFI observations of high-J CO lines in the NGC 1333 low-mass star-forming region. *A&A*, 521:L40+, October 2010. doi: 10.1051/0004-6361/201015119. 68

C. H. Young, Y. L. Shirley, N. J. Evans, II, and J. M. C. Rawlings. Tracing the Mass during Low-Mass Star Formation. IV. Observations and Modeling of the Submillimeter Continuum Emission from Class I Protostars. *ApJS*, 145:111–145, March 2003. doi: 10.1086/345341. 54

M. Zhang, W. Brandner, H. Wang, T. Henning, and R. Gredel. Molecular Hydrogen Outflows and their Exciting Sources in Ophiuchus. In *Stellar Clusters Associations: A RIA Workshop on Gaia*, pages 397–398, 2011. 115, 116, 119

W. Zhang, S. E. Woosley, and A. I. MacFadyen. Relativistic Jets in Collapsars. In G. R. Ricker and R. K. Vanderspek, editors, *Gamma-Ray Burst and Afterglow Astronomy 2001: A Workshop Celebrating the First Year of the HETE Mission*, volume 662 of *American Institute of Physics Conference Series*, pages 226–228, April 2003. doi: 10.1063/1.1579345. 113

M. Zhu, E. R. Seaquist, and N. Kuno. A Multitransition CO Study of the Antennae Galaxies NGC 4038/9. *ApJ*, 588:243–263, May 2003. doi: 10.1086/368353. 34

B. Zuckerman and N. J. Evans, II. Models of massive molecular clouds. *ApJL*, 192: L149–L152, September 1974. doi: 10.1086/181613. 6